Alterations within the structural hierarchy of parchment induced by damage mechanisms

by

Katherine Thomas

A thesis submitted in partial fulfilment of the requirements for the degree of

Doctor of Philosophy

to

School of Optometry and Vision Sciences
Cardiff University
Maindy Road
Cathays
Cardiff
CF24 4LU

September 2009

UMI Number: U585389

UMI

Dissertation Publishing

ProQuest

Abstract

Collagen plays an important role in many biological tissues, including skin, which, once dried and treated, forms parchment and leather. The structural alterations that occur in collagenous materials due to X-ray radiation damage, fluctuation of relative humidity, and mechanical deformation (with a special focus on historical parchment) are the focus of this thesis.

The primary aim of this thesis is to investigate major structural changes to collagen within parchment when exposed to inappropriate levels of relative humidity during conservation treatments, and cyclic-humidity during long-term storage in archives, museums and libraries. This study led to the discovery that each parchment sample reacted to the application and removal of moisture in a different way, indicating the fundamental need to treat individual parchment documents as in-homogeneous materials.

This thesis investigates the changes that fibrillar collagen undergoes and describes the creation of computational models capable of reproducing the X-ray diffraction patterns for collagen. Previous structural models have been created that sufficiently account for native collagen, however, models created as part of this thesis succeed where previous models have failed in explaining the X-ray diffraction patterns collected from damaged collagen.

This study provided the opportunity to contribute towards a large-scale international collaborative project on the hugely important historical resource, the Domesday Book.

X-ray diffraction was used to provide unprecedented analysis of Domesday Book samples, providing a structural survey at a molecular level. This analysis produced the conclusion that the majority of samples displayed the presence of collagen axial structure, and were generally of a degraded state as a consequence of the method used to source them; the samples were scrapings from the surface, which was less intact than the bulk of the parchment.

Thesis Outline

Chapter 1 introduces the objectives of the study, including relevant background information on collagen, skin and parchment. Chapter 2 provides an overview of the techniques used in this thesis; X-ray diffraction and molecular modelling. The methods of data collection in this thesis are described in depth in Chapter 3.

X-ray diffraction is used in Chapter 4 to establish a better understanding of alterations in the hierarchical structure of dry, hydrated and air-dried parchment. Chapter 5 details an investigation into the effect of relative humidity on the structural integrity of parchment, ultimately providing a basis for improved conservation techniques and storage of documents. Changes to the fibrillar structure of collagen are observed using X-ray diffraction when collagen has undergone deformation due to external factors such as drying, X-ray irradiation and mechanical damage. Chapter 6 uses computer-aided model simulations to fit the low angle component of the experimental X-ray fibre diagrams after specific deformations, to the various changes in the fibrillar structure of collagen that could account for such observed changes. In Chapter 7, X-ray diffraction is used as a technique to investigate the structural integrity of the culturally and historically valuable document, the Domesday Book. Chapter 8 summarises and evaluates the results of the study and discusses the scope for further research in this field.

Acknowledgements

I would like to thank Professor Tim Wess for his supervision and guidance over the past four years of this PhD project. I would also like to thank past and present members of the research group for their help and support: Donna Lammie, Lee Gonzalez, Joanna Glab, Craig Kennedy, Clark Maxwell, Jen Hiller and Linda Wess.

I am grateful to my sponsors the National Archives, in particular Nancy Bell and Kostas Ntanos for the support and advice over the years. I would also like to thank Linda Ramsey at the National Archives of Scotland for the contribution of samples, Dr Ira Rabin for providing the humidity cycled parchment samples and David Howell and the Bodleian Library for the donation of the degraded parchment samples.

A main proportion of this work was undertaken at synchrotron radiation sources; therefore, I would like to thank the following people for their help and support: Dr. Günter Grossmann, Dr. Kalotina Geraki (Station 2.1, SRS, Daresbury), Dr. Mike MacDonald (Station 14.1, SRS, Daresbury) and the staff at station ID18F (ESRF).

Finally, I would like to thank my family and friends for their support during this time and special thanks to James Patten for his help and continued support.

Symbols and Abbreviations

CCD	Charge-coupled device
CRL	Compound refractive lenses
ECM	Extra-Cellular Matrix
EM	Electron Microscopy
ESRF	European Synchrotron Radiation Facility
GAG	Glycosaminoglycan
FTIR	Fourier Transform Infrared Spectroscopy
FWHM	Full Width Half Maximum
OCT	Optical Coherence Tomography
RH	Relative Humidity
RTT	Rat Tail Tendon
SAXS	Small-angle X-ray Diffraction
SRS	Synchrotron Radiation Source
TEM	Transmission Electron Microscopy
WAXS	Wide-angle X-ray Diffraction
XRD	X-ray Diffraction
XPCS	X-ray photon correlation spectroscopy
λ	Wavelength
D	Repeating unit of collagen molecule (e.g. 67nm)
d	Lattice plane spacing
q	Scattering Vector
nm	nanometers (1×10^{-9} meters)

Table of Contents

Chapter 2: The Principles of X-ray Diffraction

Chapter 4: An Investigation into the Influence of Hydration on the Structure of Collagen – An X-ray Diffraction Study

Chapter 5: The Effect of Relative Humidity on the Structural Integrity of Parchment

Chapter 6: Molecular Modelling of Changes in Fibrillar Collagen

Chapter 7: Determining the Nanostructural Integrity of the Domesday Book

Chapter 8: Conclusions

List of Figures

List of Tables

Chapter 1: Collagen and its role in Parchment

1.1 Aims and Objectives of Study

Parchment is a collagen-based writing material made from processed, untanned animal skins, mainly calf, sheep or goat (Larsen, 2002). Parchment has been used as a writing material for many centuries and is still used today. Many well known historical documents have been recorded on parchment, the earliest surviving being the Dead Sea Scrolls dating from around 250BC to AD68 (Burton, Poole and Reed, 1959; Larsen, 2002). Other notable examples include the Domesday Book and the Magna Carta (Forde, 1986; Bell and McPhail, 2007). Images of these documents are shown in Figure 1.1.

Figure 1.1: Notable examples of documents written on parchment, clockwise from top left, the Dead Sea Scrolls, the Magna Carta and the Domesday Book.

Parchment is dried treated skin and as with many complex biomaterials over time it can degrade; a process that can be further accelerated by a range of factors, including

inappropriate temperature levels, mechanical damage and radiation damage from ultra-violet (UV) light. One key environmental effect causing severe damage to archival collections is variation in relative humidity (Larsen, 2002; Kite and Thomson, 2006). The introduction of moisture has been known for decades to have a detrimental effect on parchment, but advances in scientific techniques have allowed us to become more adept at identifying degradation (Reed, 1973; Labaki, Torriani and Grigera, 1991; Hansen, Lee and Sobel, 1992; Wess and Orgel, 2000; Larsen, 2002). These advances mean that science has begun to play a crucial part in furthering our understanding of collagen structure and the long-term survival of parchment.

The aim of this thesis is to investigate major structural changes to collagen within parchment when exposed to inappropriate levels of relative humidity during conservation treatments and storage in archives, museums and libraries. In this work, two main techniques will be utilised in the investigations of collagen structure within parchment; X-ray diffraction analysis and molecular modelling. These two methods complement each other and when combined help in understanding the hydration dependent variations in collagen at the molecular level. This project studies the molecular changes in parchment at a variety of relative humidity levels, facilitating a more sophisticated analysis for the structure of dry collagen. The overall aim of this work is to develop and enhance current knowledge of the relationship between parchment, collagen and water in terms of the hydration state, ultimately improving current conservation practice.

Parchment is composed of the structural protein collagen. It is therefore important to have an understanding of the chemical and physical properties of skin and collagen when analysing historical parchment. This chapter introduces the structure of skin, the structural hierarchy of collagen and the manufacture of parchment.

1.2 Introduction to Skin, Collagen and Parchment

1.2.1 *Structure of Skin*

Skin is the largest organ of the body, its primary function is as a tough physical barrier (Monteiro-Riviere et al., 1997; MacNeil, 2007). Skin is comprised of three layers; the epidermis, the collagen-rich dermis layer and the subcutaneous tissue (flesh layer) (Whitton and Everall, 1973). These layers are illustrated in Figure 1.2, which shows a cross-section of mammalian skin. The total thickness of the skin, fibre size and weave of collagen fibres is found to be significantly diverse and depends on the species, age and sex of the animal (Haines, 1999). These inherent properties often lead to the preferred use of specific skins to obtain characteristic features in parchments.
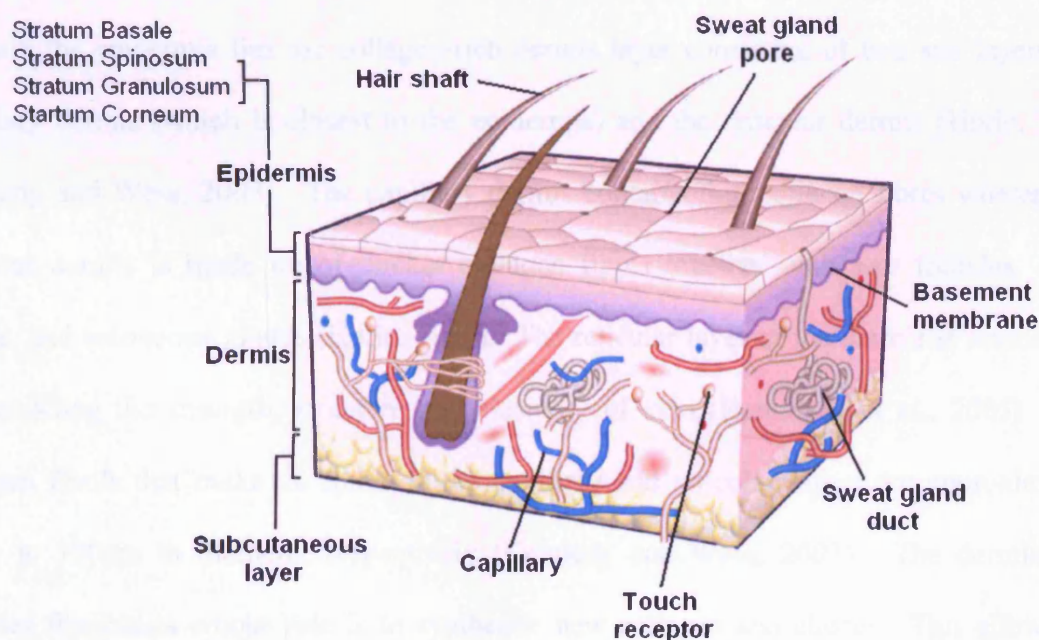
Figure 1.2: Diagrammatic representation of the structure of skin with the key features labeled (MacNeil, 2007). The diagram is not to scale.

1.2.1.1 The Epidermis Layer

The epidermis layer is the outer surface of skin, which acts as a barrier against environmental damage (Monteiro-Riviere et al., 1997). It comprises four structurally distinct layers; the *stratum basale*, the *stratum spinosum*, the *stratum granulosum* and the *stratum corneum* (Whitton and Everall, 1973). The thickness of the epidermis layer is found to vary dramatically across the human body depending on body site, age, sex and environmental factors (Whitton and Everall, 1973). The average thickness of the epidermis layer is 40-50μm, but can be up to 80μm on the wrists and back of hands, around 400μm on the front of the fingers and only 17μm on the face (Whitton and Everall, 1973).

1.2.1.2 The Dermis Layer

Beneath the epidermis lies the collagen-rich dermis layer consisting of two sub layers; the papillary dermis (which is closest to the epidermis) and the reticular dermis (Horie, 1990; Kennedy and Wess, 2003). The papillary dermis contains thin collagen fibres whereas the reticular dermis is made up of thicker collagen fibres together with hair follicles, sweat glands, and sebaceous glands (Horie, 1990). The reticular layer of the dermis is responsible for providing the strength, structure and elasticity of skin (Hendriksa et al., 2005). The collagen fibrils that make up fibres in the papillary and reticular layers are approximately 50nm to 100nm in diameter respectively (Kennedy and Wess, 2003). The dermis also includes fibroblasts whose role is to synthesise new collagen and elastin. This allows the removal of damaged collagen and its replacement with new collagen. It is the dermis layer that constitutes the main part of parchment since the epidermis is removed during processing.

1.2.1.3 The Subcutaneous Tissue

The subcutaneous tissue or the hypodermis is the innermost layer of the skin, which is responsible for fat production (Hendriks et al., 2005). The quantity of fat produced varies depending on age, species and health of the animal. Hair follicles and blood vessels cross through this layer which separates the skin from the underlying muscle (Haines, 1999). The function of the subcutaneous tissue is to act as an insulator, conserving the body's heat, and as a shock-absorber, protecting the inner organs and to store energy (Hendriks et al., 2005).

1.3 Introduction to Collagen

Skin and subsequently parchment are both composed largely of the major architectural protein collagen, the primary constituent of most connective tissue found in all multicellular animals (Bear, 1952). The majority of collagen found in animals is in a fibrillar form where it is predominantly found as long, slender, cylindrical-like structures. There are many different forms of collagen; to date 29 different collagens have been identified (Kadler et al., 2007). Different types of collagen have been assigned Roman numerals based on the order of their discovery, for example type I, type II and type III (Kadler, 1995). The most abundant collagen is type I, which is found predominately in tendon, skin, bone, cornea and the aorta (Traub and Piez, 1971). Collagen types can be classified into one of two main classes, fibril forming collagen or non-fibril forming collagen. From a biomechanical view point, the fibril forming collagen types are of most interest (Kadler, 1995; Hulmes, 2002). Collagen types I, II, III, V, and XI have been identified as fibril forming (Kadler, 1995). The dry weight of skin is approximately 40-50% collagen, the bulk of which (approximately 90%) is made up

of two specific types of collagen; type I and type III (Epstein and Munderloh, 1978; Light, 1985). As discussed in the literature the fibril forming collagens can be further classified as either purely fibril forming collagen (types I, II and III) or fibril-associated collagens (types V, XI) (Burgeson, 1988; van der Rest and Garrone, 1991; Kadler, 1995). Fibril-forming and fibril-associated collagens are detailed in Table 1.1.

Collagen Type	Chain Composition	Distribution/remarks
I	$[\alpha1(I)]_2\,\alpha2(I)$	Non-cartilaginous connective tissues – e.g. tendon, skin, cornea, ligament, bone
II	$[\alpha1(II)]_3$	Cartilage, vitreous humour and nucleus pulposus
III	$[\alpha1(III)]_3$	Co-distributes with collagen I, especially in embryonic skin
V	$\alpha1(V),\alpha2(V),\alpha3(V)$	Co-distributes with collagen I, especially in embryonic tissues and in cornea
XI	$\alpha1(XI),\alpha2(XI),\alpha3(XI)$	Co-distributes with collagen II, cartilage, vitreous body

Table 1.1: Details of the fibril forming collagens; Types I, II, III, V and XI (Kadler, 1995; Kadler et al., 2007).

This thesis will concentrate on the structural behaviour of fibrillar type I collagen, which is the primary constituent of parchment. The term collagen will therefore be used throughout this thesis, which will refer to type I collagen unless otherwise specified.

1.3.1 Collagen Hierarchical Structure

Collagen has a complex structural hierarchy, over a wide length scale. Collagen within skin is fibrous, with an interwoven organization of fibres with diameters of a few hundred microns; this structure defines the biomechanical properties of tissues such as skin, tendon and cornea. The fibres are comprised of fibrils; these are discrete structures with characteristic banded patterns on staining and electron microscopy (EM) along their axis, which in turn are comprised of several thousand collagen molecules, themselves composed of individual peptide chains that constitute a molecular rope like structure. The alignment of collagen fibres is an important factor in the overall mechanical characteristics and behaviour of a tissue (Fratzl et al., 1998). The hierarchical structure of collagen is represented in Figure 1.3.
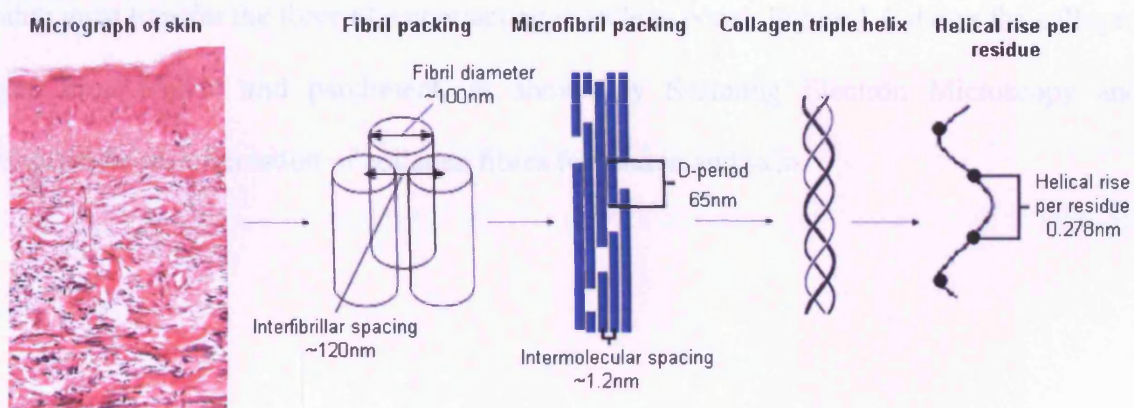
Figure 1.3: **Illustration of the collagen hierarchy. From left to right, shows a micrograph of skin, demonstrates fibril packing within a fibre, illustrates microfibril packing, shows a collagen triple helix and the helical rise per residue. Diagram is for dry skin and is not to scale.**

1.3.1.1 Collagen Fibres

Collagen fibres are composed of between 50 and 100 ordered, tightly packed, approximately cylindrical fibrils the latter having a diameter ranging from 10nm to 500nm (Traub, 1978). In skin, collagen fibres are usually found to be randomly orientated as a feltwork in the plane of the skin surface. In collagen-based tissues such as tendon, the fibres are found to be preferentially aligned with the direction of muscular contraction so that force is transmitted to the articulation of bone (Hansen et al., 1992). The fibre alignment in tendon confers resistance to strain in one direction along the fibre axis, whereas in skin the 'feltwork' accommodates resistance within a lateral plane, in all directions (Provenzano et al., 2002; Kennedy et al., 2003). Such properties are commensurate with the properties required for such tissues. Skin must act as an effective barrier that is resistive to tear and puncture, where tendon must transfer the force of a contracting muscle to bone. Figure 1.4 shows the collagen fibres from tendon and parchment, as shown by Scanning Electron Microscopy and demonstrates the orientation of collagen fibres for tendon and skin.
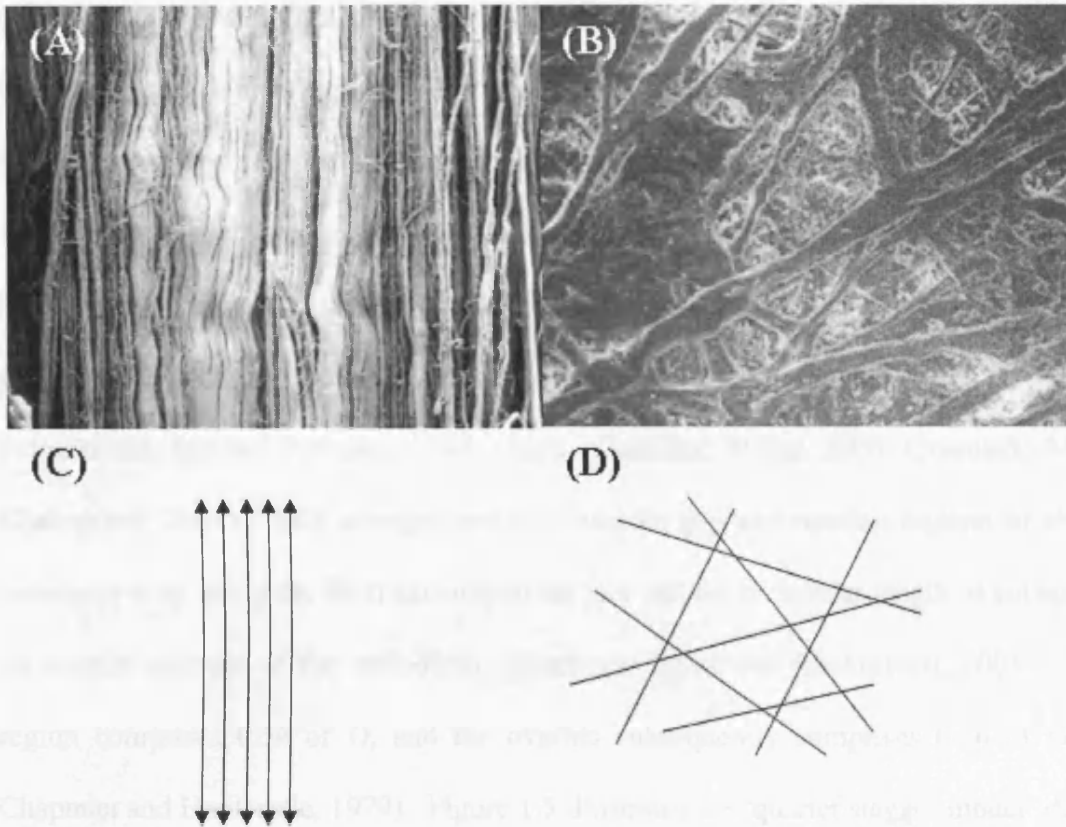
Figure 1.4: Collagen fibres from (A) tendon and (B) parchment, as shown by Scanning Electron Microscopy (Provenzano et al., 2002; Kennedy and Wess, 2003). Diagrammatic representation showing the orientation of collagen fibres. (C) Tendon, which has a preferred orientation. (D) Skin, which is randomly orientated, within the plane of the tissue.

1.3.1.2 Collagen Fibrillar Structure

By mass, most of the collagen found in animals is in a fibrillar form as long slender cylindrical structures with tapered ends. Fibrils have a thickness in the range of 50 to a few hundred nanometers (Fratzl, 2008). The collagen molecules that comprise the fibrils are typically 300nm in length and 1.5nm in diameter, as shown in Figure 1.3 (Brodsky, Eikenberry and Cassidy, 1980; Stinson and Sweeny, 1980; Menon, 2002). The collagen

molecules within a fibril associate with an axial disposition revealing a repeating structural unit (of length D) which is the D-period or the axial periodicity evidenced in electron microscopy as a strong banding pattern upon staining. The 300nm long collagen molecules are staggered axially relative to their nearest neighbours by multiples of a quarter of their length, D ~ 65nm in skin and D ~ 67nm in tendon (Hodge and Petruska, 1963). This arrangement is described as the 'quarter stagger model' and was developed by Hodge and Petruska (Hodge and Petruska, 1963; Orgel, Wess and Miller, 2000; Quantock, Meek and Chakravarti, 2001). This arrangement accounts for gap and overlap regions of alternating density to arise along the fibril axis due to the fact that the molecular length of collagen is not an integer multiple of the periodicity (Quantock, Meek and Chakravarti, 2001). The gap region comprises 0.54 of D, and the overlap subsequently comprises 0.46 of D (Meek, Chapman and Hardcastle, 1979). Figure 1.5 illustrates the 'quarter stagger model' developed by Hodge and Petruska where the gap and overlap regions are shown.
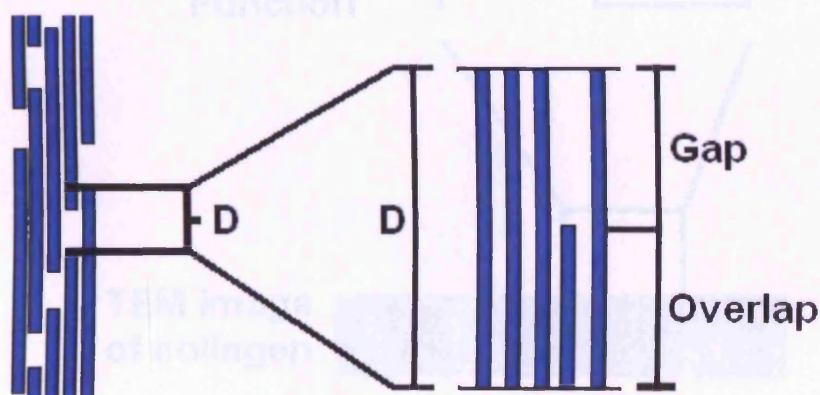
Figure 1.5: Illustration of the axially staggered arrangement of collagen molecules within a fibril. The collagen molecules are represented as blocks. The collagen molecules comprise a repeating structural unit (of length D) which is the D-period or the axial periodicity. This repeating unit forms the characteristic gap and overlap features.

These gap and overlap regions result in fluctuations in the electron density causing a regular banding pattern at intervals of D which is observable by Transmission Electron Microscopy (TEM) of negatively stained collagen (Kadler et al., 1996b). An electron micrograph of native collagen has a banding pattern, which corresponds to regions of high and low electron density where the stain remains and fills the regions of low density more than regions of high density. Figure 1.6 is a graphical representation of the staggering of collagen molecules with a periodicity of D, the resultant projected step function for the structure and a Transmission Electron Microscopy (TEM) image of collagen exhibiting characteristic banding.
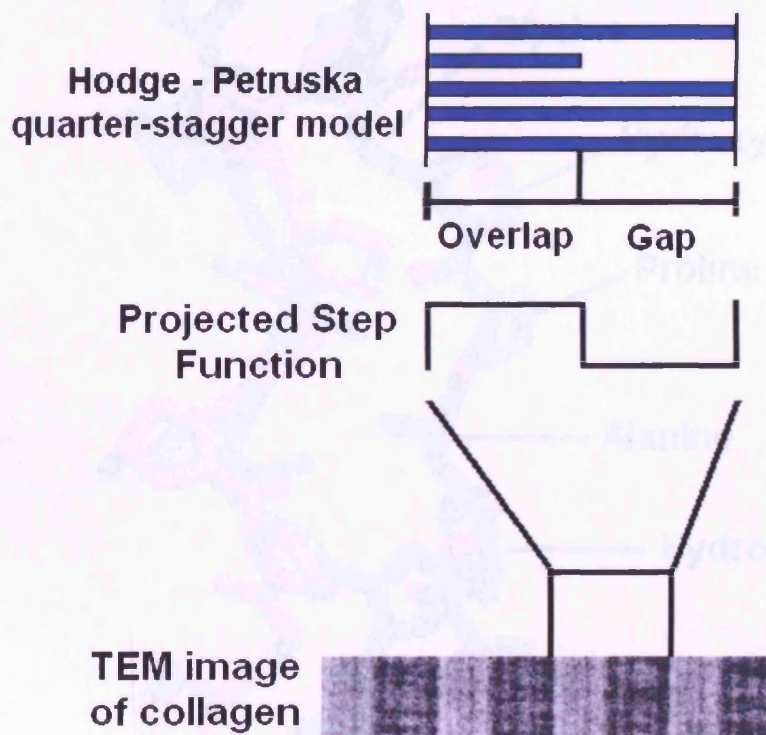
Figure 1.6: Graphical representation of the staggering of collagen molecules with a periodicity of D, the resultant projected step function for the structure and a Transmission Electron Microscopy image of collagen showing the characteristic banding, which corresponds to regions of high and low electron density where the stain remains and fills the regions of low density more than regions of high density (Traub, 1978).

1.3.2 Collagen Triple Helical Structure

Type I collagen is a heteropolymer comprising three polypeptide chains (alpha peptide chains of two gene products $\alpha 1$ and $\alpha 2$). These alpha-chains combine with the stoichiometry ($\alpha 1$, $\alpha 2$, $\alpha 1$) as left-handed helices, and are coiled to give a right-handed superhelix, which contains approximately 1,000 amino acids per polypeptide chain. A triple helix of collagen and the constituents of the polypeptide chains are shown in Figure 1.7.
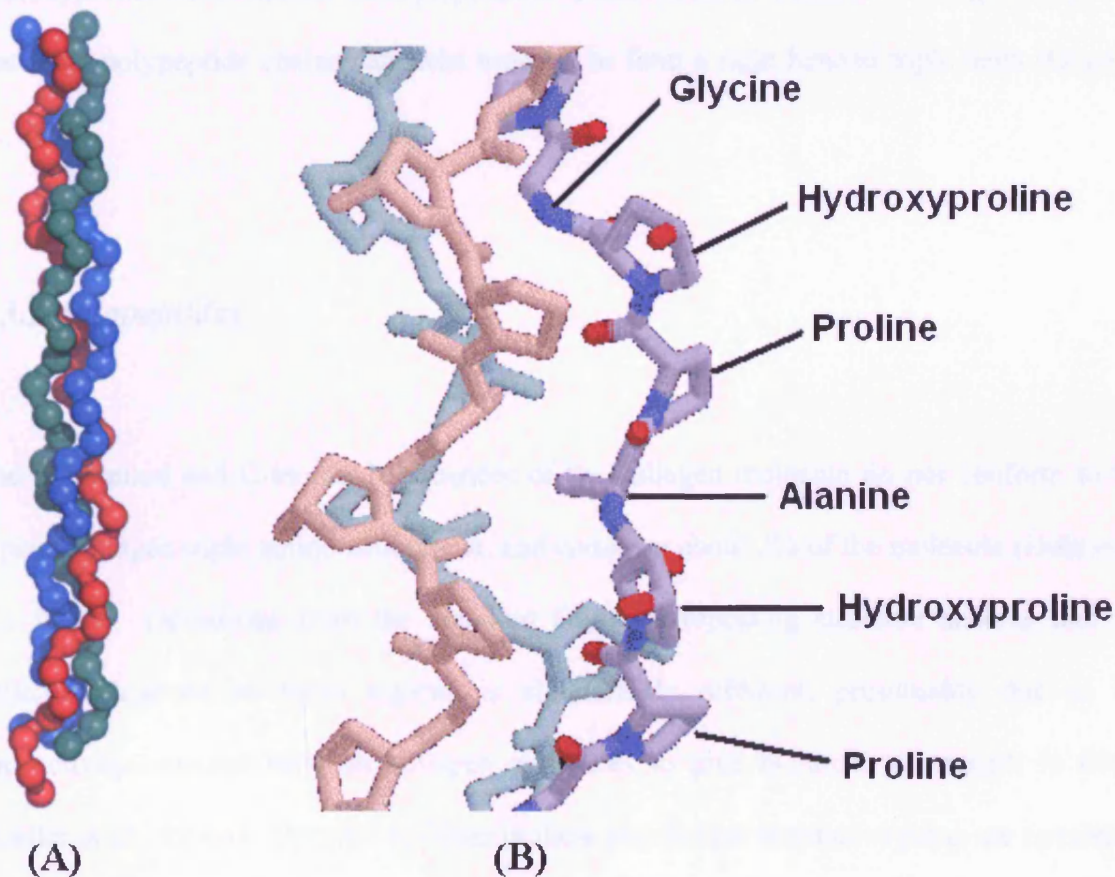
Figure 1.7: (A) Collagen triple helix; B) Collagen polypeptide chain with the [Gly-X-Y] repeating unit. The individual strands have a left handed helical nature which is concatenated to form a right handed suprahelical as individual strands wound around each other, such hierarchical changes in helical handedness stabilise rope like structures from unwinding.

This characteristic conformation provides the collagen molecule with its strength and stability. The three α-chains are largely constituted from the canonical sequence of Gly-Pro-Y or Gly-X-Hyp where X and Y are various other amino acid residues (Haines, 1999). The side chain of glycine, -a hydrogen atom-, is the only amino acid that can be accommodated in the centre of a triple helix (Lodish et al., 2000). Hydrogen bonds linking the peptide bond NH of a glycine residue with a peptide carbonyl (C=O) group in an adjacent polypeptide help hold the three chains together. The fixed angle of the C-N peptidyl-proline or peptidyl-hydroxyproline bond enables each polypeptide chain to fold into a helix with a geometry such that three polypeptide chains can twist together to form a right handed triple helix (Orgel et al., 2000).

1.3.3 Telopeptides

The N-terminal and C-terminal sequences of the collagen molecule do not conform to the typical collagen triple amino acid repeat, and comprise about 2% of the molecule (Hulmes et al., 1980). Deviations from the standard Gly-X-Y repeating structure ensures that the collagen structure in these regions is significantly different, presumably due to the connectivity required between collagen molecules to give hierarchical strength to fibrils (Kadler et al., 1996a). Specific residues in these non-helical terminal regions are covalently bonded to the helical segment of an adjacent collagen molecule. As well as the major cross-linking between neighbouring collagen molecules, cross-linking also occurs between amino acid chains within a triple helix adding further stability to the assemblies (Malone and Veis, 2004). The amino (N-terminal) and carboxyl (C-terminal) telopeptides of type I collagen play crucial roles in the assembly of collagen fibrils, regulating the axial alignment of the molecules within a fibril, orientation of neighbouring molecules, and cross-link formation

(Hulmes et al., 1980). Hulmes et al. (1980) showed that the apparent distance between amino acid residues along the fibril axis is shorter in the telopeptides than in the main triple helix. They showed an average axial rise per residue of 0.286nm in the main triple helix, 0.241nm in the N-terminal telopeptide, and 0.2nm in the C-terminal telopeptide (Hulmes et al., 1980; Orgel et al., 2000). Later studies pointed to the C terminal telopeptide being arranged in a folded conformation while the N terminal telopeptide adopts a structure that appears to be contracted in terms of the average distance between residues when compared to the triple helix (Prockop and Fertala, 1998; Orgel et al., 2000).

1.3.4 Intermolecular Covalent Cross-linking

The strength and stabilisation of collagen fibrils is achieved with the formation of covalent cross-links, at specific points on the collagen molecules (Kjellen and Lindahl, 1991). Type I collagen has four specific cross-linking locations, two of which are in the telopeptide region and two in the helical region. The telopeptide region of one collagen molecule is covalently linked to the helical region of its neighbouring collagen molecule. The linkage is through lysine based crosslinks that form spontaneously after the action of lysyl oxidase (a deaminase) on specific lysine chains (Nagan and Kagan, 1994). The formation of an initial Schiff base is then modulated by a complex maturation process. The spatial distribution of the linkage is demonstrated in Figure 1.8.
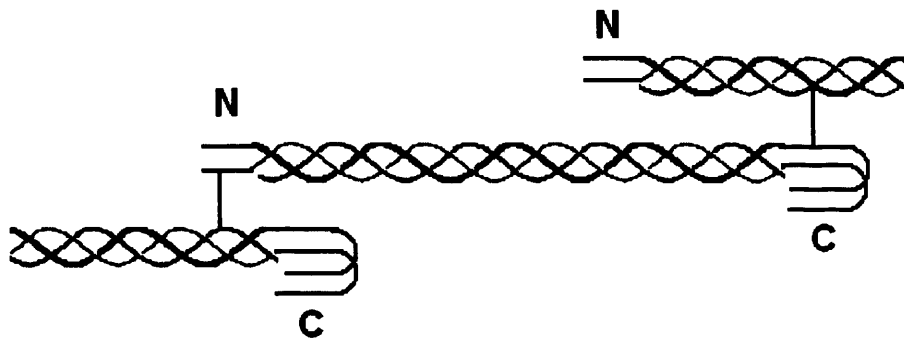
Figure 1.8: Intermolecular covalent cross-links between neighbouring collagen molecules. The non-helical regions (telopeptides) are bound to the helical region of its neighbouring collagen molecules. Such interactions reinforce the stability of the quarter staggered structure.

1.3.5 Collagen-Proteoglycan Interactions

Proteoglycans play a fundamental role in the biomechanical properties of the extra-cellular matrices (ECM). They are essential connecting elements that help to order the hierarchical suprafibrillar structure of the extracellular matrix. They consist of a linear protein backbone with one or more covalently attached glycosaminoglycan (GAG) chains (Scott et al., 1997). Studies have shown that the protein cores of some proteoglycans bind to the GAG chains and the collagen molecules at four sites per D-period, illustrated in Figure 1.9 (Kjellen and Lindahl, 1991).

Collagen fibril

Protein core of
the proteoglycans

Branched GAG chains
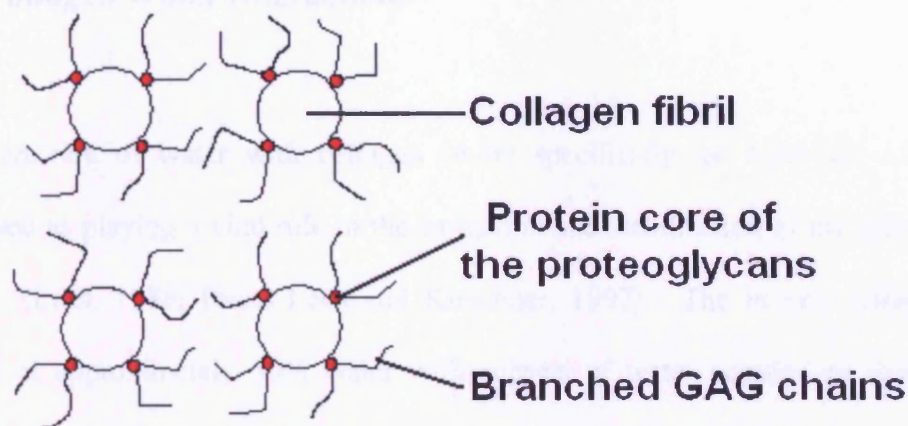
Figure 1.9: Simplistic illustration of the formation of a proteoglycan matrix where the protein cores of the proteoglycans bind to the GAG chains and the collagen molecules at four sites per D-period.

GAG chains are comprised of repeating disaccharides containing hexosamines and hexuronic acids (Scott, Orford and Hughes, 1981). Proteoglycans are therefore water soluble carbohydrate-rich polyanions, which play a role in fibril formation and growth by coating fibrils and supporting suprafibrillar networks (Choi et al., 1989). One suggested role is the assistance in the determination of the distance between collagen fibrils (the interfibrillar spacing). The specific principle glycosaminoglycan associated with type I collagen is composed of dermatan sulphate which is distributed on the surface of collagen fibrils in the skin (Scott and Haigh, 1985). Dermatan sulphate forms filamentous networks that are arranged orthogonally to the fibril axis and is believed to play a key part in prevention of calcification of soft tissues such as skin (Bella, Brodsky and Berman, 1995).

1.3.6 Collagen Water Interactions

The interaction of water with collagen (more specifically the hydration of collagen) is recognised as playing a vital role in the formation and stabilization of the collagen structure *in vivo* (Lees, 1986; Price, Lees and Kirschner, 1997). The *in vivo* collagen structure consists of approximately 50% water with subsets of water populations that 1) surround individual triple helices, 2) fill the gap zone in the hydrated state and 3) surround the fibrils (Labaki et al., 1991). Water may be bound to the collagen molecule, or unbound with layers of "free" molecules (Mogilner, Ruderman and Grigera, 2002). The triple helix of collagen is held together, in part, by the formation of water bridges which act as a stabilising factor in holding the three helical α-chains together (Bella et al., 1995). It was suggested by Bella et al. (1995) that oxygen atoms of water were linked to the peptide chain by water bridges (Bella et al., 1995; Mogilner et al., 2002; Fullerton and Amurao, 2006). The water molecules bind to collagen through hydrogen bonds forming a cylindrical lattice-like structure around collagen (Bella et al., 1995). Three water shells, as shown in Figure 1.10 surround the collagen triple helix. The first level hydration shell (b) contains water molecules that are hydrogen bonded to amino acid groups of the triple helix. The second level hydration shell (c) contains water molecules that are connected by hydrogen bonds to the water molecules in the first shell. The third and final outer hydration shell (d) includes water molecules that are bonded to the inner second shell (Bella et al., 1995).
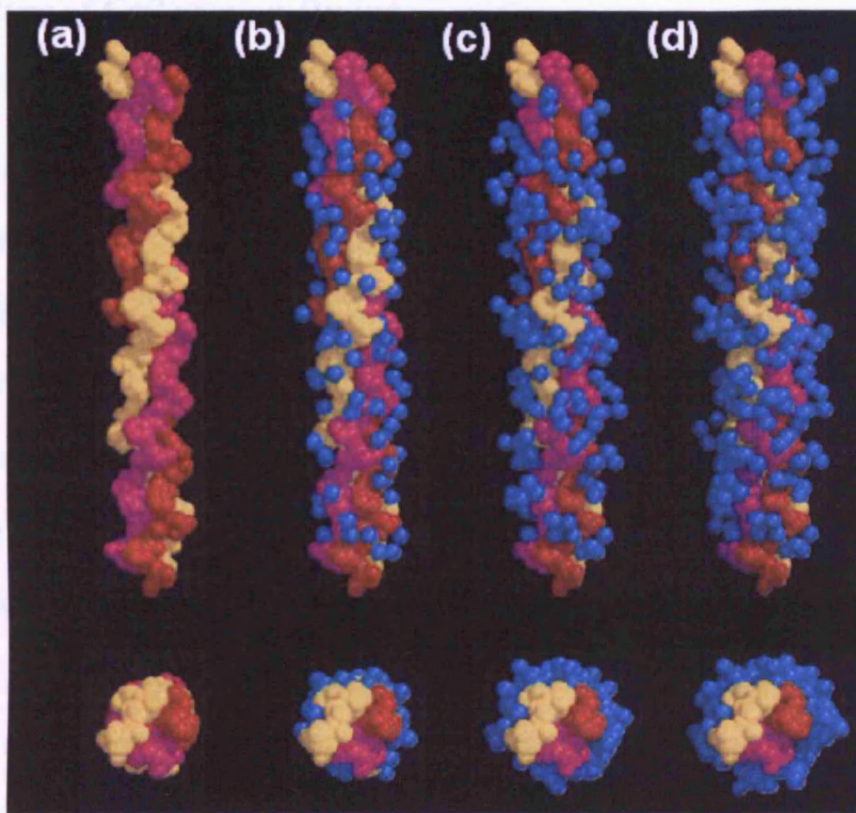
Figure 1.10: Representation of the three water shells surrounding the collagen triple helix, taken from Bella et. al. (1995). (a) The triple helix; where the three peptide chains are shown in different colours. (b) The first shell of water molecules hydrogen bonded to carbonyl, hydroxyl or amide groups on the peptide surface. (c) The second shell of water molecules are hydrogen bonded to those in the first shell. (d) The third shell of water molecules that allow almost complete coverage of the collagen (Gly, Pro, Hyp) helix.

Many studies on the hydration of collagen have shown that the presence of water is essential in maintaining the overall native structure of collagen and the absence of water is known to cause many structural changes in the arrangement of collagen.

1.3.7 Structure of Collagen on Drying

The majority of studies conducted on collagen have been carried out on the native hydrated state, with very few investigations completed on dry collagen. Understanding the structural changes within the hierarchy of collagen on drying is however vital when investigating parchment. The drying of collagen causes large structural changes to occur at a molecular level, these manifest themselves mainly as a shortening in the D-period (Stinson and Sweeny, 1980; Wess and Orgel, 2000). In rat-tail tendon (a more studied type I collagen tissue) the D-period is reduced from 67nm to approximately 65nm (Wess and Orgel, 2000). It was reported that this shortening in the D-period was not entirely dependent on the pitch shortening of the collagen helix, (presumably removal of the water populations that surround and stabilize the triple helix that could cause the helical structure to alter). A shortening of the D period could also arise due to more substantial axial sliding of the collagen molecules relative to each other within a fibril (Bear, 1952; Traub and Piez, 1971; Wess and Orgel, 2000).

X-ray diffraction has been used as a technique to investigate the structure of collagen at a variety of different levels of hydration. Until recently electron microscopy was only able to look at collagen fibrils in the dehydrated state. X-ray diffraction is able to provide structural information at a range of different length scales from submicron to hundreds of microns. Chapter 2 provides a more detailed description of X-ray diffraction, however it is pertinent to highlight some of the features that change in the fibre diagram of collagen are reflective of structural changes within fibrils.

1.3.7.1 Structural Changes to Collagen on Drying Observed by X-ray Diffraction

The X-ray diffraction patterns of collagen in the hydrated and dry states reveal a number of differences (although not fully accounted for by defined structural alterations due to a lack of suitable models) that indicate significant structural conformations between the two states. Structural observations on the drying of collagen show an attenuation in the number of meridional reflections in X-ray diffraction patterns from around 140 in the hydrated state to less than 40 in the dried state (Wess and Orgel, 2000). Two small-angle X-ray diffraction patterns of dry and hydrated rat-tail tendon exhibiting meridional diffraction peaks from the 9th to the 34th order are shown in Figure 1.11. This reduction in the number of clearly visible reflections implies an increase in the disorder of the molecular packing of collagen upon drying.
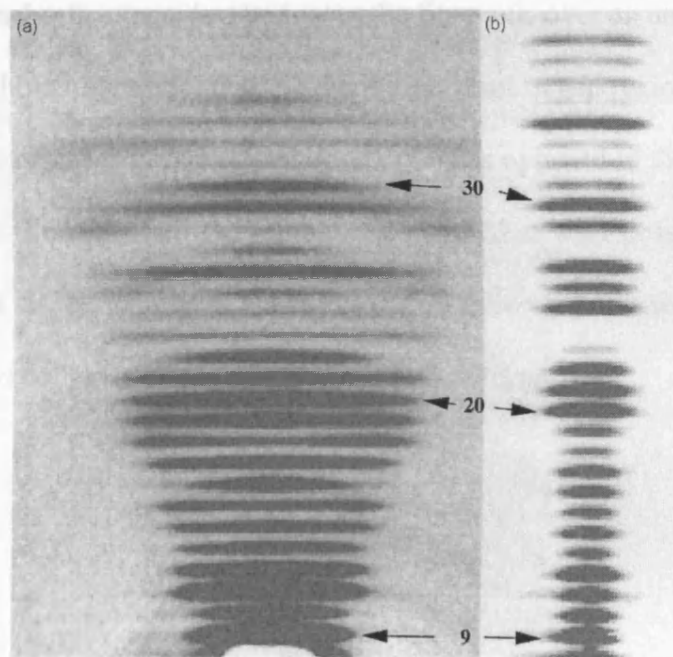
Figure 1.11: Two small-angle meridional X-ray diffraction patterns of collagen taken from Wess and Orgel (2000). (a) Dry rat-tail tendon. (b) Hydrated rat-tail tendon. The meridional peaks shown are for orders 9 to 34 with the 9th, 20th and 30th orders identified.

In the diffraction pattern from dry collagen, the meridional diffraction orders are distributed over a wider arc in azimuth than those in the hydrated state. This "fanning" distributes the diffracted intensity over an angle of 20 degrees as opposed to 5 degrees in the hydrated fibrils. (Bear, 1951; Wess and Orgel, 2000). On drying, collagen fibrils exhibit increased broadening of the X-ray diffraction peaks in the direction perpendicular to the meridian with respect to the diffraction angle. In some orders, the meridional reflections are more intense at the outer edges of the image than at the fibre axis. Some reflections are split into three or more areas of intensity. This phenomenon is observed more easily at the higher orders of X-ray diffraction of collagen.

Wess and Orgel (2000) showed that when water was removed from the collagen fibrils the periodicity of collagen was reduced and postulated that this could occur due to an increased tilting in the collagen chains with respect to the fibre axis (Figure 1.12). They found that the distributed meridional reflections deviated from the fibre axis over an angle of $21.4°\pm2.0°$. It was proposed that this tilting effect may be more prominent in gap regions since there would be a significant loss of water in this region upon drying as opposed to the overlap regions. It was suggested that tilting in the gap region in combination with possible breaking of the chains might result in the axially projected D-period becoming shorter as seen in historic parchment and dried collagen fibrils; this is illustrated in Figure 1.12.

Hydrated Collagen
D=67nm

Air-dried Collagen
D~64.7nm

Historical Parchment
D~63nm

Overlap   Gap   Overlap   Gap   Overlap   Gap
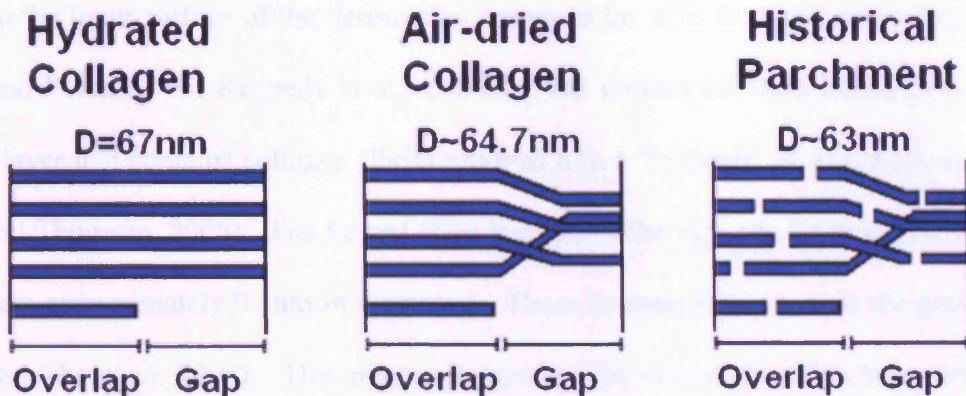
Figure 1.12: **Illustration of the D periodic staggers in hydrated collagen, air-dried collagen and parchment, the approximate D period values are shown. Both air dried collagen and historical parchment have shorter periodicities which results from tilting of molecular chains in the gap regions and breaking of the amino acid chains (Kite and Thomson, 2006). Figure adapted from Wess and Orgel (2000).**

This is one possible explanation for the structural changes that occur in parchment although they have never been fully investigated. The mechanisms by which parchment structure changes during hydration and drying has yet to be sufficiently explained.

1.4 The Structure of Parchment

Parchment is comprised of the architectural protein collagen that is organised into fibrils, which are in turn grouped into bundles or fibres. The production of parchment involves the abstraction of the dermis layer, identified in Figures 1.2 and 1.13, and often the removal of the epidermis using chemical treatments (Haines, 1999). The two sides of parchment; the grain layer and the flesh layer are identified in Figure 1.13. The grain layer refers to the outer

surface of the dermis that contains the hair follicles and sweat glands and the flesh layer refers to the inner surface of the dermis that separates the skin from the underlying muscles (Smit and Porck, 1995; Kennedy et al., 2004b). The corium (or flesh layer), is part of the dermis layer that contains collagen fibrils grouped into a 'feltwork' of interweaving bundles (Kite and Thomson, 2006). The largest fibre bundles in the skin can be found in the corium (fibres are approximately 0.1nm in diameter). These become finer towards the grain surface (Kite and Thomson, 2006). The innermost layer of the skin is the flesh layer where fibre bundles are reorganized into a horizontal arrangement.
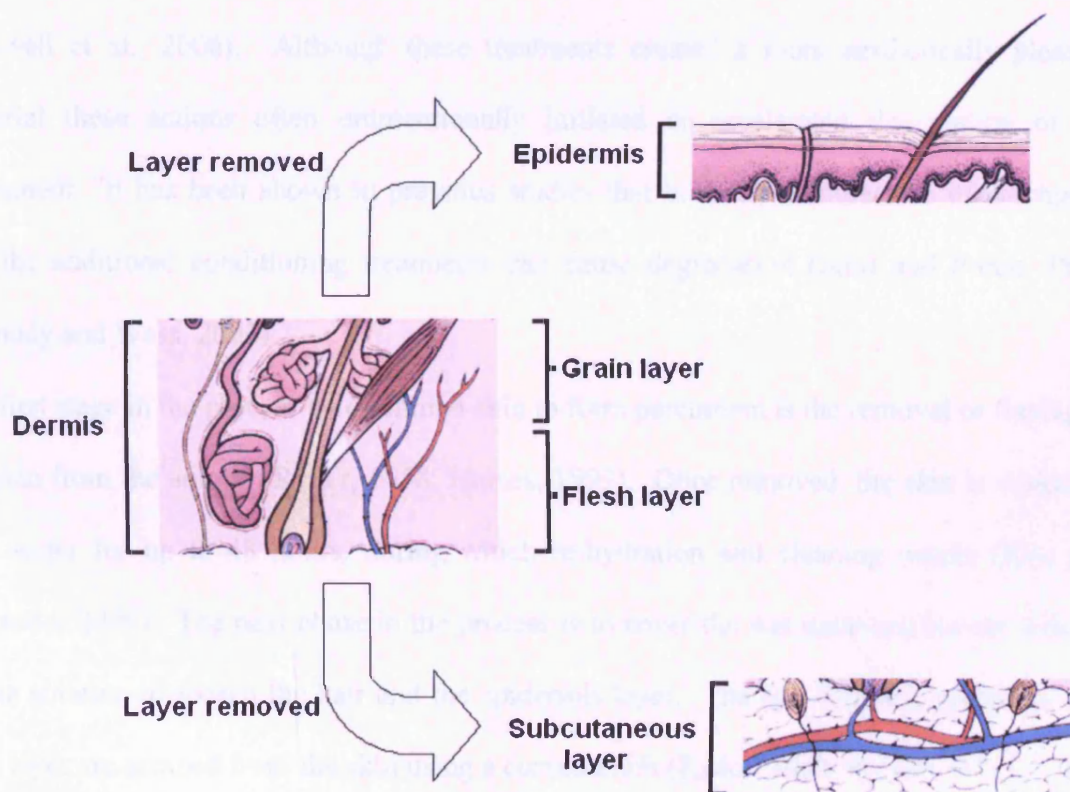
Figure 1.13: A schematic representation of a cross-section of skin, where the grain and flesh layers of the dermis layer are highlighted. The epidermis and subcutaneous layer are removed during the manufacture of parchment.

1.4.1 Parchment Manufacture

The production of parchment has remained relatively unchanged over the centuries with the same essential steps still conducted today. The main objective when producing parchment is to create a smooth, high contrast and adsorptive writing surface (Reed, 1973; Maxwell, Wess and Kennedy, 2006). To make parchment more aesthetically pleasing a number of treatments were used, including the addition of powders and pastes of calcium compounds to remove oils and the application of lime, egg and milk to create a smooth white surface (Haines, 1999; Maxwell et al., 2006). Although these treatments created a more aesthetically pleasing material these actions often unintentionally initiated or accelerated degradation of the parchment. It has been shown in previous studies that both the manufacture of parchment and the additional conditioning treatments can cause degradation (Smit and Porck, 1995; Kennedy and Wess, 2003).

The first stage in the processing of animal skin to form parchment is the removal or flaying of the skin from the animal (Ryder, 1958; Haines, 1999). Once removed, the skin is soaked in cold water for up to 48 hours, during which re-hydration and cleaning occurs (Kite and Thomson, 2006). The next phase in the process is to cover the wet untanned animal skins in a lime solution to loosen the hair and the epidermis layer. The hair follicles, epidermis and flesh layer are scraped from the skin using a curved knife (Ryder, 1960; Woods, 1995). After chemical treatment, the wet skins are air dried under tension on wooden frames allowing for the extraction of water from between the fibres within the skin. It is important that the correct level of tension is applied to prevent the fibres being drawn together once the water is removed. Removing the water from between the fibres causes the skin to dry as a flexible, opaque material (Kennedy and Wess, 2003; Maxwell et al., 2006). The final step is to split the skin between the grain layer and the corium, leaving a uniformly thick parchment without

a glossed surface. The behaviour of parchment in the presence of water during preparation is indicative of their important relationship in subsequent conservation.

The parchment preparation process removes proteoglycans leaving just the insoluble protein and water molecules (Larsen, 2002; Kennedy et al., 2004b; Abil, 2005; Góra et al., 2006; Lee, Mahon and Creagh, 2006; Gonzalez and Wess, 2008a).

New and already established technologies have been used and proposed over the recent years for the interrogation and extraction of data from parchment including X-ray diffraction (XRD), Fourier transform infra-red (FT-IR), nuclear magnetic resonance (NMR), Raman spectroscopy and optical coherence tomography (OCT) (Kennedy et al., 2004c). These methods have proved useful in understanding the structure of parchment as well as monitoring possible degradation.

1.4.2 Degradation of Parchment

Over time parchment degrades which is evidenced by changes in the physical properties leading to fragility. This process can be further accelerated by a range of factors, including temperature, humidity, mechanical damage, radiation damage and bacterial/fungal growth (Quandt, 1996). All of these agents are capable of altering the chemistry of the collagen molecule which destabilizes the native conformation. These factors cause degradation by the process of gelatinisation, and gelatine is frequently found in older parchments. Gelatinisation occurs when the triple helix of collagen molecules unravels to form a random coil. The deterioration of collagen into a gelatine-like state generally leads to irreversible damage. The process of gelatinisation is shown in Figure 1.14. The presence of gelatine is likely to be incompatible with the presence of fibrillar collagen since the latter requires a compact collagen conformation. This therefore presents a major challenge to the maintenance of

recorded history of the Western world.

H$_2$O
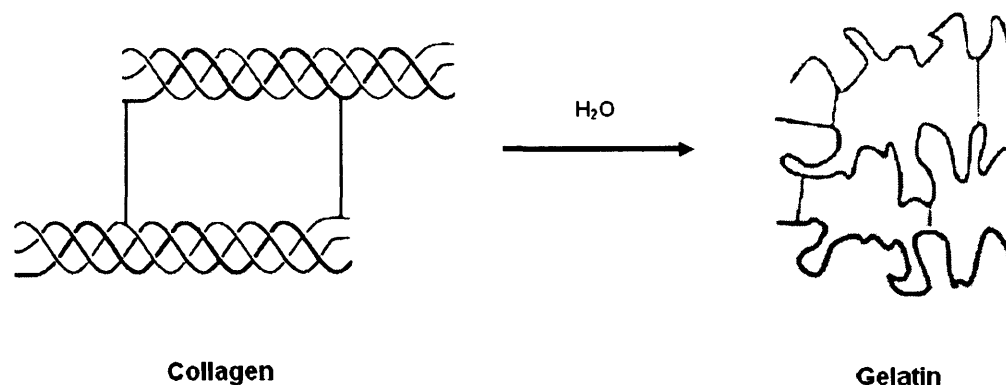
Collagen

Gelatin

Figure 1.14: An illustration of the process of gelatinisation where the triple helix of collagen molecules unravels to form a random coil.

This degradation has created a critical need to conserve parchment to prevent unnecessary damage. Parchment is highly hygroscopic; therefore environmental conditions such as relative humidity must be kept under control. By observation, two external factors known to have a major detrimental effect on parchment collections are hydration/drying and inappropriate levels of relative humidity.

1.4.2.1 Hydration Damage to Parchment

There are three main factors where hydration can give cause for concern in the survival of parchment. 1) The misuse of rehydration strategies to alter the appearance of a document, 2) long term storage at 'inappropriate' relative humidity levels or fluctuation of humidity and 3) accidental damage of parchment through events such as flooding. Although the third factor has to be mitigated for in a different way in terms of disaster management, the first two

factors are considered here.

In parchment characteristic creasing and pleating of the pages can develop as the books are repeatedly opened and closed during use. Repairing these folds and wrinkles is generally desirable for presentation and is achieved by increasing the moisture content, although wetting parchment can cause damage, it is sometimes unavoidable (Quandt, 1996; Kite and Thomson, 2006).

The most traditional smoothing system is the use of stretchers, which pull out the parchment through the action of clamps attached to the edges. The advantage of this system, which is still used today, is that the parchment may be moistened locally using water. Another solution for the removal of creases is pressing the document between blotters after dampening. This system is only effective with parchments that are not too creased as deep wrinkles may worsen and become folds (Haines, 1999). Although conservators use these techniques to remove unwanted folds and creases, very little is known as to what is happening to the parchment structure during hydration and drying.

When hydrated skin is allowed to air dry the water that exists between the fibres migrates to the surface of the parchment and evaporates (Hingley, 2001). It is proposed that the loss of this water causes the fibres to collapse onto each other. It is these large structural changes that make repairing water damage to parchment extremely difficult and time consuming (Hansen et al., 1992; Bowden and Brimblecombe, 1999). One of the major effects of water damage is the distortion and rippling of the parchment. Humidification is the main technique used to correct for this surface distortion.

1.4.2.2 Relative Humidity Damage to Parchment

Relative humidity (RH) is used to describe the amount of water vapour that exists in a gaseous air-water mixture and therefore is a critical descriptor in the interaction between parchment and atmospheric water. The relative humidity of an air-water mixture is defined as the ratio of the partial pressure of water vapour in the mixture to the saturated vapour pressure of water at a prescribed temperature. Relative humidity is normally expressed as a percentage and is defined by Equation 1.1 where RH is the relative humidity of the mixture, $p(H_2O)$ is the pressure of water vapour in the mixture and $p^*(H_2O)$ is the saturated vapour pressure of water at the temperature of the mixture.

$$RH = \frac{p(H_2O)}{p^*(H_2O)} \times 100\%$$ **Equation 1.1**

Variation in relative humidity and water content are serious parameters that affect the structural integrity of archival documents during both conservation treatments and storage. At present, our understanding of how relative humidity misuse affects the structural integrity of historical parchment is limited. In an overly dry environment, parchment will relinquish moisture, causing it to dry out, split and warp. Bowden and Brimblecombe (1999) reported that when parchment is subjected to high relative humidity conditions a significant mass of water is absorbed, causing the parchment to swell possibly leading to rippling and often irreversible distortion of the parchment (Bowden and Brimblecombe, 1999). It has been reported that when parchment is subjected to a change in the RH, unbound water is either lost, which causes an endothermic heat transfer, or gained, resulting in an exothermic heat transfer (Hansen et al., 1992). Hansen et. al. (1992) studied the effects of relative humidity on the physical properties of modern vellum; parchment made from the skin of young or unborn calves (Hansen et al., 1992). They found that variations in the relative humidity

caused the parchment to swell and shrink producing internal strain which eventually results in irreversible damage as judged by mechanical testing. It was noted that a relative humidity value lower than 25% increases the stress induced into the parchment while humidities above 40% increase the process of gelatinisation and allows biological growth (Hansen et al., 1992; Bowden and Brimblecombe, 1999).

Sound housekeeping, in particular the control of environmental factors, plays an essential role in preventing damage to parchment and is therefore an important part of conservation. Cyclic humidity changes of a more restricted nature are typical of the air changes frequently encountered in true library conditions, this causes the parchment to expand and contract causing internal strain, which in some instances can cause irreversible damage. The current recommendations for the storage and display of parchment are in the region of 50% RH to 65% RH but no clear optimal value has been produced (Hansen et al., 1992). One study advises a humidity range from 50% RH to 65% RH (Kite and Thomson, 2006), while others suggest a value between 45%RH and 60%RH (Peters, 1996). Moreover, this standard covers all organic materials, and no current empirical data is available on the effects of relative humidity of parchment. Another study suggested that it is preferable to maintain a consistent relative humidity value in a range as low as possible under ambient conditions to avoid damaging extremes rather than a specific RH value, but no quantitative data was provided to support this claim (Peters, 1996).

The overall process can be summarised as, the greater the percentage RH of the environment, the higher the moisture content of the parchment, the faster the deterioration rate of the parchment due to gelatinisation, the shorter the life expectancy of the parchment. Therefore, a structural study is required to validate and possibly improve current conservation practice and storage recommendations for the conservation of historical documents.

1.4.2.3 Other degradation factors and their effects

External factors that have been shown to induce and accelerate degradation other than the already discussed hydration and relative humidity misuse; are inappropriate temperature levels, mechanical stress, subjection to radiation and bacterial/fungal growth (Reed, 1973). Parchment is extremely sensitive to fluctuations in temperature especially in the presence of elevated levels of relative humidity. The response of parchment heated under dry conditions is less severe (Reed, 1973). One study found that parchment heated in the absence of moisture was able to withstand temperatures of 100°C with no change in colour, dimensions or shape of the parchment sample unlike parchment heated in the presence of moisture (Reed, 1973). Parchment heated in the presence of moisture was found to accelerate degradation, causing possible gelatinisation. The combination of high levels of relative humidity (70%-100%RH) and elevated temperatures (>22°C) have been found to be ideal conditions for deterioration by bacteria or fungi (Reed, 1973).

Ultraviolet (UV) radiation in daylight and artificial light plays an important role in parchment degradation. Parchment is affected by photochemical reactions in which hydrogen peroxide is formed. The parchment is broken down in the process of photochemical degradation causing gelatinisation of the parchment (Cullity, 1978). This causes the parchment to become brittle, fragile and liable to split. However the biomolecular basis for this remains ill defined. The most common damage to parchment is that of mechanical damage caused by everyday use. Tears on edges and folds are a result of frequent handling. Damage caused by wear and tear is mainly macroscopic and does not result in changes in the molecular structure of the material. Mechanical damage in the form of tears and breakage can be exacerbated by excessive dryness, while excessive dampness can cause deformations and warping. Some examples of damaged parchments are shown in Figure 1.15.
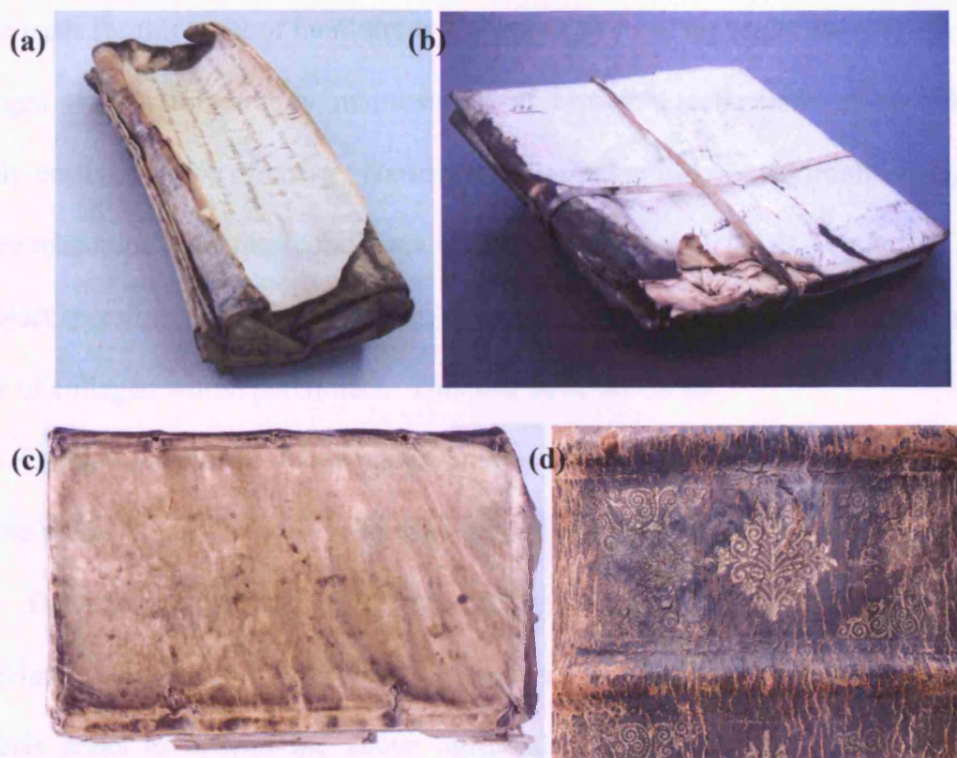
Figure 1.15: **(a) parchment stuck together due to water damage, (b) water and mould damage have caused the parchment to shrink and discolour, in addition there is physical damage to the corner, (c) physico-mechanical damage to parchment bookbinding and (d) physico-mechanical damage to leather bookbinding.**

1.5 Conclusions

This chapter has provided an insight into the background of parchment and the structural protein collagen of which it is comprised. It has been established that very little is known about the structural alterations that occur in the molecular packing of the collagen molecules within parchment at different levels of relative humidity (RH). In the context of library and archive collections, the currently accepted recommendations for the storage and display of

parchment is between 50% to 65% RH; however, no clear value has been produced and the scientific basis for this level of humidity is not informed from the molecular/fibrillar integrity of collagen. Most importantly maintenance of historical collections at specific RH is extremely costly in terms of energy consumption and therefore not environmentally friendly (therefore relaxation of storage conditions is probably necessary).

This project therefore aims to consider in detail the effects of RH on the molecular/fibrillar structure of collagen within parchment. This will be achieved by:

- Obtaining a more detailed understanding of how water and collagen interacts within the preservation and conservation context of historical parchment records.

- Determining the damage caused to historical parchment by inappropriate levels of relative humidity particularly during conservation treatments and storage in archives.

This thesis seeks to answer the above aims using a collection of scientific techniques including X-ray diffraction (XRD) and computational molecular modelling. The principles of X-ray diffraction and molecular modelling will be introduced and the details of the materials and methods used within this work will be presented in Chapter 3. The hydrated and dry structure of parchment will be investigated in Chapter 4 using X-ray diffraction. Chapter 5 will focus on the effect of different levels of relative humidity on parchment. This will be a structural study assessing the integrity of collagen using X-ray diffraction. Chapter 6 will use results from Chapters 4 and 5 to build computational molecular models to explain the structural re-arrangements in X-ray diffraction patterns of hydrated and dry collagen. Chapter 7 will detail an internationally collaborative project on the structural integrity of the Domesday Book using X-ray diffraction.

Chapter 2: The Principles of X-ray Diffraction

2.1 Introduction to X-rays

Since 1895 when W. C. Röntgen discovered X-rays and their ability to be scattered by matter, X-ray diffraction has become an essential technique to study the structure of matter at a molecular and atomic level. X-rays are electromagnetic waves with a wavelength (λ) in the range of 10nm to 0.1nm (approximately 1,000 times shorter than visible light). The wavelength of visible light is in the order of 6.0×10^{-7}m, whereas X-rays used in scattering and diffraction are approximately $0.2 \times 10^{-11} - 2.5 \times 10^{-10}$ m (Hukins, 1981; Glatter and Kratky, 1982). This chapter describes one of the main techniques that will be used in this thesis to investigate the structural changes of collagen; X-ray diffraction. An overview of the physics and mathematics of X-ray diffraction is given, however for a more comprehensive review, books by Hukins (1981) and Glatter and Kratky (1982) are recommended.

2.2 Interaction of X-rays with Matter

All matter scatters X-rays, but the way in which they interact depends on the type of matter. For an ideal gas, where the molecules or atoms are far apart, there are no interactions between the molecules. Therefore, the X-rays are only affected significantly by the intra-molecular or atomic interactions. In a liquid where the molecules are closer together, inter-molecular interference also occurs. The higher the concentration of the liquid, the more interactions occur whereas dilute liquids have fewer interactions and behave similarly to a gas. In

crystalline solids with more regularly spaced molecules, an interference effect occurs, resulting in distinctive scattering in specific directions, diffraction (Glatter and Kratky, 1982). Figure 2.1 demonstrates the X-ray scattering curves observed for a variety of disordered and ordered structures. Collagen is a highly ordered system and gives rise to a rich fibre diagram which contains features of the scattering curves seen in C and D of Figure 2.1.
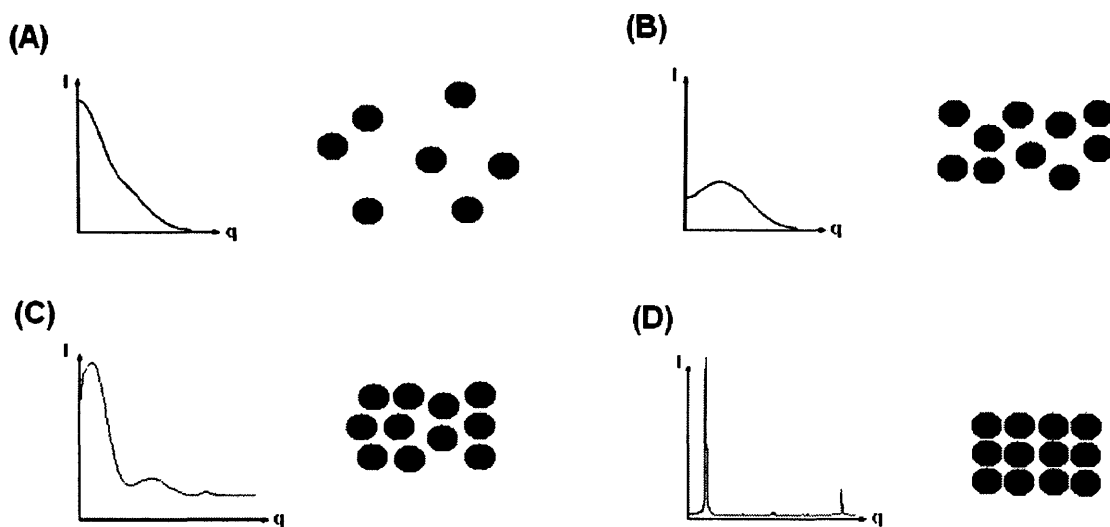
Figure 2.1: **Scattering curves generated from various states of matter: (A) gas-type sample, (B) liquid-type, (C) quasi-crystalline and (D) solid state. Adapted from (Glab, Wess and Thomas, Due to be published in 2009) and (Cullity, 1978).**

2.3 Theory of X-ray Scattering and Diffraction

When a photon collides with matter, they interact with one another. The energy from the incoming photon causes the charge particles within the matter to oscillate with the same frequency as the incident radiation. These oscillations within the matter cause the atom to become unstable resulting in the eventual release of a photon. Usually this photon is released

with the same energy as the incoming incident photon; hence, no energy is lost from the system. This form of scattering is coherent scattering.

2.3.1 Interference between X-rays

X-rays that have been scattered by matter can interfere destructively or constructively. Constructive interference occurs when the waves are in phase where as destructive interference occurs when the waves are out of phase. Constructive and destructive interference is demonstrated in Figure 2.2.
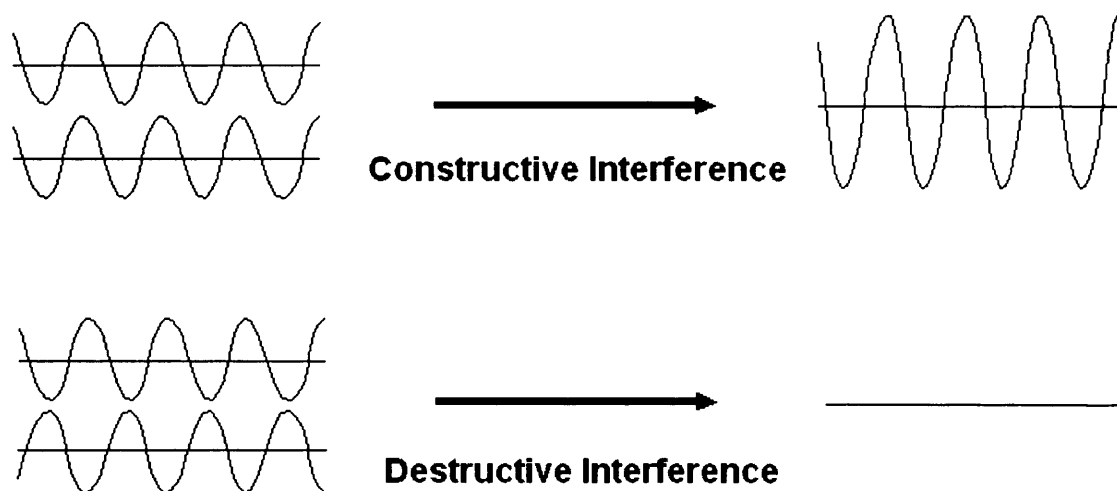
Figure 2.2: Graphical representation of interference between two waves. The scenario at the top of the figure represents constructive interference, where two waves completely in phase are accumulated into a single wave with increased amplitude. The second scenario at the bottom of the figure represents destructive interference where the two waves are completely out of phase with one another resulting in a wave with zero amplitude.

Diffraction is a specific scattering event that leads to interference effects, where incoming X-rays are scattered by atoms in all directions. The majority of X-rays scattered by matter will interfere destructively, however, in some directions, the scattered X-rays will be in phase; therefore, reinforcing each other and forming diffracted beams (Glatter and Kratky, 1982). The constructive interference creates the observed diffraction pattern.

The specific ordering of the material leads to the inference of whether diffraction or scattering dominates. Scattering occurs from all matter, fluctuations in scatter occur when the electron density changes within the sample. These fluctuations can then be analysed to provide structural information about the material under investigation. The intensity of X-ray scattering corresponds to the number of atoms (electrons) present and their relative location. Figure 2.3 shows the interference of two waves scattered from different points with a path difference of λ and at an angle of 2θ.
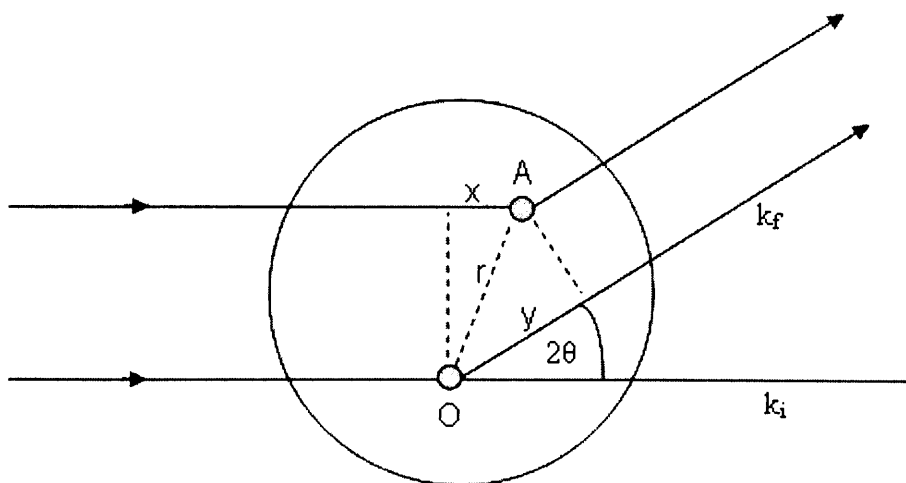
Figure 2.3: Schematic of the interference between two waves scattered from different points, A and O with a path difference of λ and at an angle of 2θ.

54

The incident wave vector k_i and the scattered wave vector k_f are in phase with a scattering angle between them of 2θ. The path difference between the X-rays passing through the points A and O is given in Equation 2.1.

$$x - y = rk_i - rk_f = -r(k_f - k_i)$$

Equation 2.1

The phase is defined as $\Phi = -qr$ when the scattering vector satisfies Equation 2.2.

$$q = (2\pi/\lambda)(k_f - k_i)$$

Equation 2.2

This scattering vector bisects the angle between the incident and scattered beam, k_i and k_f (Stout and Jensen, 1968).

$$q = \frac{4\pi}{\lambda}\sin\theta$$

Equation 2.3

The relative distribution of atoms in a sample corresponds (in terms of scattering) to the distances between scattering (electrons in this case) objects, it is often more appropriate to consider the correlation function between scattering centres in a sample as opposed to the sample itself, and thence infer the structure from the correlation function. The correlation function, $g(r)$ corresponds to the probability density of having two scatterers in the same sample at a specific separation and its Fourier transform (the spatially inverse relationship) is used to calculate the amplitude of the scattering vector, $I(q)$. The scattering of the X-rays within a sample results in a distribution of X-rays continuously over a broad range of angles. If the atomic order within matter tends toward crystallinity then diffraction occurs as a condition of scattering where X-rays interact within well-ordered structures producing a characteristic pattern of sharp peaks collected on a detector due to constructive and destructive interference effects. Many biological samples exhibit the characteristics of a

system that produces both scattering and diffraction. A two-dimensional X-ray diffraction pattern from hydrated rat-tail tendon is shown in Figure 2.4, where the 3rd to 10th orders of collagen axial diffraction are labelled.
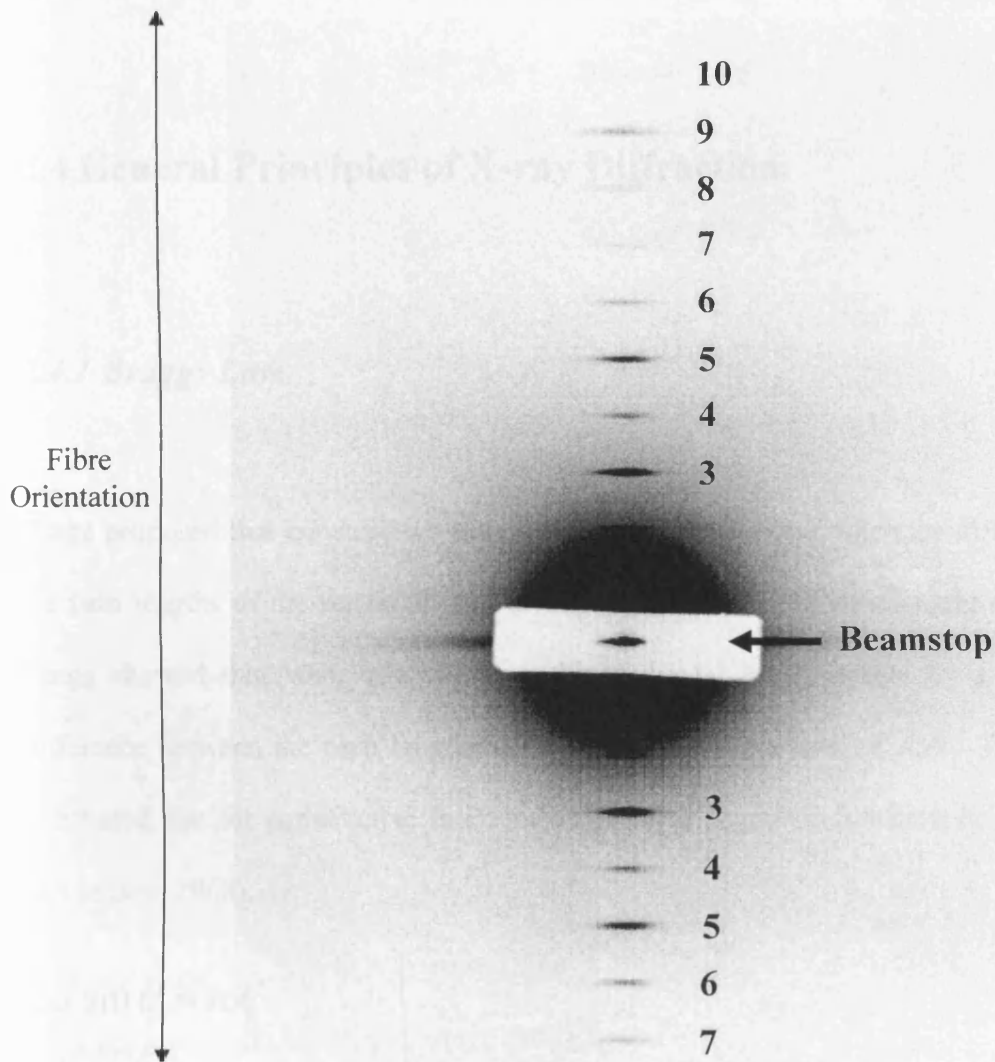
Figure 2.4: An example of the X-ray diffraction pattern from hydrated collagen (rat-tail tendon). The diffraction pattern consists of a series of sharp reflections that reflect a highly regular lattice of molecules in real space; the two-dimensional diffraction pattern shown is from a single fibre. Scattering from the sample due to the fibril structure is a component at low angles, around the beamstop. The fibre orientation and the 3rd to the 10th orders of collagen axial diffraction are labelled.

The diffraction pattern of collagen, a crystalline tissue, consists of a series of sharp Bragg reflections that reflect a highly regular lattice. The deviations from a highly ordered sample give rise to diffuse scatter, which manifests as a continuum of scattering outside the Bragg reflections. Such scatter is important in understanding the nature of the change in materials.

2.4 General Principles of X-ray Diffraction

2.4.1 Braggs Law

Bragg proposed that constructive interference could only occur when the difference between the path lengths of the scattered rays is an integral number of wavelengths of the radiation. Bragg showed that when the planes within a crystal are separated by a distance d, the difference between the path lengths of radiation would become 2d sinθ. Therefore, Bragg concluded that for constructive interference to occur, Equation 2.4 must be withheld (Stout and Jensen, 1968).

$$2d \sin \theta = n\lambda$$ **Equation 2.4**

This condition is Bragg's Law where λ is the wavelength of the incoming X-ray beam, is the angle between the scattered photons and the scattering plane, and n is an integer value (Rhodes, 2000). Therefore, for diffraction to occur the three-dimensional crystal must have the correct orientation with respect to the incoming beam, hence satisfying the diffraction condition or Bragg condition. Bragg's Law is demonstrated in Figure 2.5.

the angle of incidence = the angle of reflection

X-rays

2θ

θ θ

d

layers of crystal lattice

Constructive interference when

$$2d \sin\theta = n\lambda$$
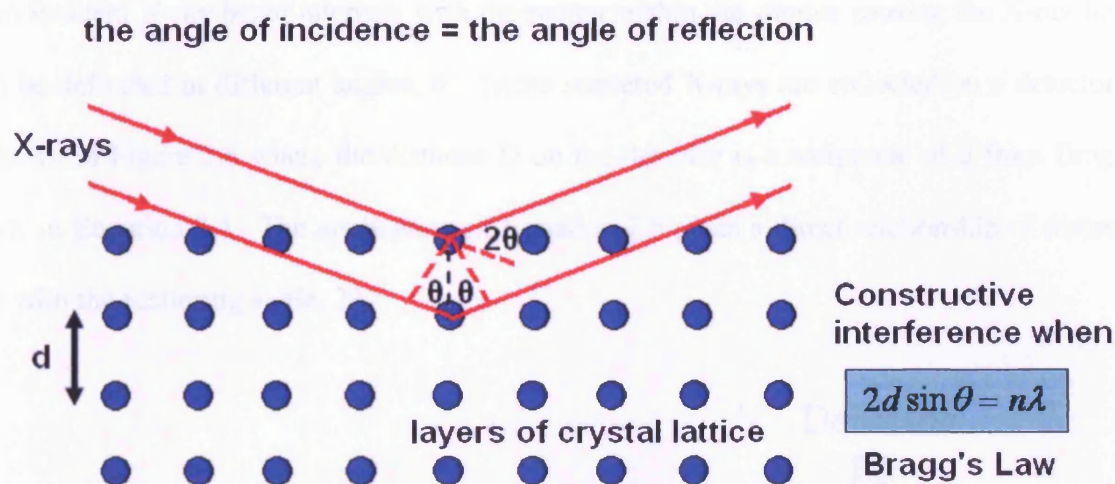
Bragg's Law

Figure 2.5: Diffraction of X-rays by a crystal, demonstrating Bragg's Law. The crystal diffracts the incoming beams of parallel, monochromatic X-rays of wavelength λ if the Bragg condition is satisfied, i.e. path difference λ=2d sinθ.

2.4.2 Reciprocal Lattice

The scattering pattern collected from a group of atoms is related to the internal structure of the crystal and the arrangement of the atoms. The spacing within the unit cell of the crystal is the real lattice, which has a simple inverse relationship with the spacing of the reflections seen in the scattering pattern. The separation of the reflections is equal to the reciprocal of the distance in real space, hence it is the reciprocal lattice (Rhodes, 2000). From this reciprocal relationship, it is possible to calculate the dimensions of the unit cell within the crystal using the spacing of the reciprocal lattice. Reciprocal space lattice constants are calculated using Equation 2.5, which is found by rearranging Braggs Law (Equation 2.4).

$$D = \frac{1}{d} = \frac{2}{n\lambda}\sin\theta$$

Equation 2.5

An incident X-ray beam interacts with the matter within the sample causing the X-ray beam to be deflected at different angles, θ. These scattered X-rays are collected on a detector as shown in Figure 2.6 where the distance D on the detector is a reciprocal of d from Bragg's law in Equation 2.4. The application of Equation 2.5 gives a direct relationship of distance, D with the scattering angle, 2θ.
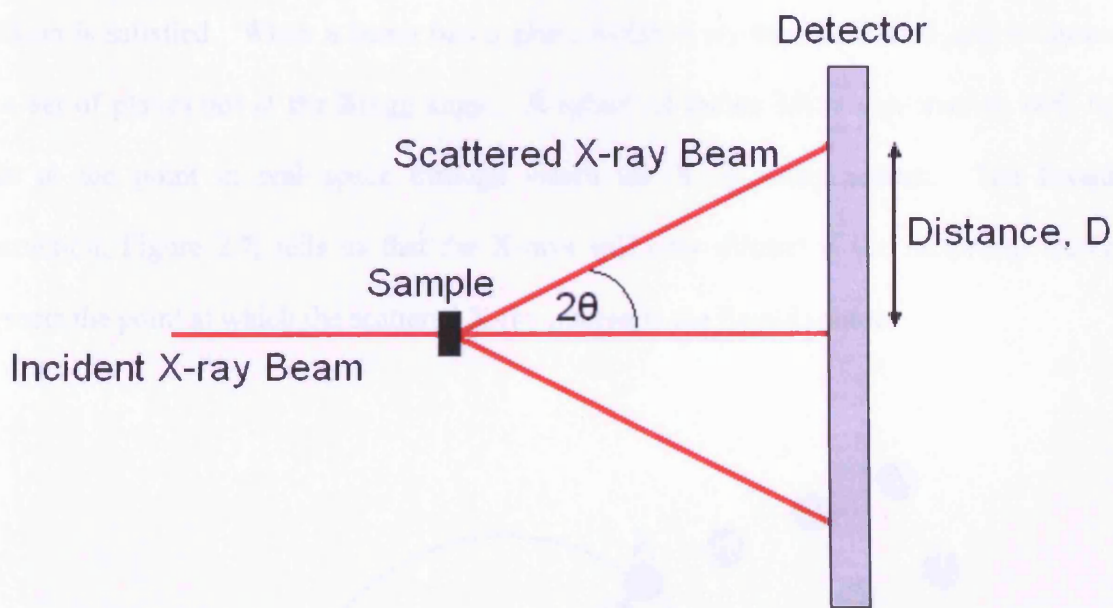
Figure 2.6: An illustration showing an incident X-ray beam scattered by a sample at an angle of 2θ on to a detector. The distance D on the detector is a reciprocal of the distance, d from Bragg's law in Equation 2.4. The application of Equation 2.5 gives a direct relationship of distance, D with the scattering angle, 2θ.

In conclusion, the reciprocal lattice is a set of imaginary points constructed such that the direction of a vector from one point to another coincides with the direction of a normal to the real space planes. The reciprocal lattice is also often referred to as the three-dimensional spatial Fourier transform of the lattice in real space. Fourier transforms will be covered in greater detail later in this chapter (subsection 2.4.6). To relate real space and reciprocal space

a geometrical construction by Peter Ewald was proposed.

2.4.3 Ewald Sphere Construction

The Ewald sphere construction is a way of visualising and determining whether the Bragg condition is satisfied. When a beam hits a plane within a crystal, the Ewald sphere shows that a set of planes are at the Bragg angle. A sphere of radius $1/\lambda$ is constructed, with its origin at the point in real space through which the X-ray beam passes. The Ewald construction, Figure 2.7, tells us that the X-rays will only diffract if the reciprocal lattice intersects the point at which the scattered X-ray intersects the Ewald sphere.
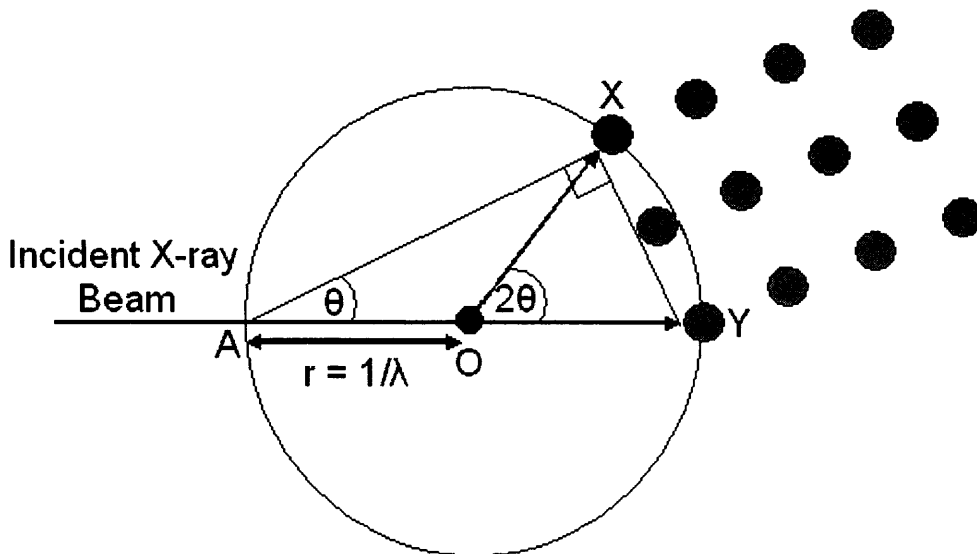
Figure 2.7: The Ewald sphere construction. The Ewald sphere is a way of determining if the Bragg condition is met. For a given wavelength and the unit cell dimensions, it can be used to find the maximum resolution. This shows where $2d \sin \theta = n\lambda$.

2.4.4 Periodic Wave Equations

A simple wave of X-rays can be described as a periodic function and by the equations given in Equation 2.6.

$$f(x) = F \cos 2\pi(hx + \alpha)$$
$$f(x) = F \sin 2\pi(hx + \alpha)$$

Equation 2.6

$f(x)$ is the value of the height of the wave at a position along the horizontal axis x, F is the amplitude of the wave, h is the frequency, x is the variable position along the x-axis and α represents the phase of the wave (Cullity, 1978). These equations describe waves in one-dimensional space only; hence, they are simple periodic wave equations. These periodic functions are too simplistic to explain the diffracted waves of X-ray diffraction, a more complicated description is needed; hence the Fourier series.

2.4.5 Fourier Series

Waves that are more complicated can be described in a similar way to simple waves. They are both described primarily by three constants; the amplitude, the frequency and the phase. These more complicated waves can be described by a sum or integral of sinusoidal functions (a series of sine and cosine functions); a Fourier series. This is used to deconstructing periodic functions into a series of simpler sinusoidal functions (trigonometric functions). This decomposition of functions into one simple sine or cosine function allows easier analysis. Fourier analysis has the advantage of being able to break down even the most complicated periodic functions into simpler and more easily interpreted waveforms.

2.4.6 Fourier Transform

Fourier transforms are used to determine the electron density of an object from the diffraction pattern observed. This is done by the inversion of the Fourier transform of a function. The problem with this mathematical evaluation is that both the amplitude and the phase are needed to calculate the inverse Fourier transform of the diffracted photons, but X-ray diffraction only directly provides the intensity and not the phase. The amplitude is easily calculated using the intensity of the photon scattered, and through recognising that intensity is proportional to the square of the amplitude. However, there is as yet, no direct way to calculate the phase from the diffracted photons, making this a major challenge to X-ray crystallography, since the phase contains most of the structural information.

2.4.7 Structure Factors

A unit cell within a crystal scatters X-rays and the sum of such scattering contributions (the amplitude of each wave) gives the structure factor, F_{hkl} (Azaroff, 1968). The structure factor is more formally defined as complex conjugates that provide information on both the amplitude and the phase (Stout and Jensen, 1968). The relation shown in Equation 2.7 relates the structure factor to the observed intensities (Stout and Jensen, 1968).

$$I(Q) \propto \left| F_{hkl} \right|^2$$

Equation 2.7

The structure factor is used in the calculation of the electron density from determination of the atom positions within the crystal (Riekel, 2000; Tamura et al., 2002).

2.4.8 Electron Density

So far, we have emphasised that when an X-ray beam strikes a crystal, the X-rays are diffracted by point sources. In reality, it is the electrons within the crystal that scatter X-rays. The diffraction pattern provides us with information on the distribution of electrons within the crystal or the electron density of the molecules. Electron density is a complex form of a periodic function that can be described by the mathematical technique of the Fourier series.

2.5 Synchrotron Radiation

2.5.1 Introduction and Development of Synchrotron Radiation

There are many ways to utilise and produce X-rays; however the most appropriate example here is using synchrotron radiation. A synchrotron is a specific type of cyclic particle accelerator in which a magnetic and an electric field are used to circulate and accelerate charged particles. Synchrotron facilities have the ability to emit electromagnetic radiation at wavelengths from X-rays to the far infrared. At present, there are over 100 synchrotron facilities worldwide. The first cyclotrons were built back in the 1930s to investigate the particles that comprise atoms by accelerating particles to relativistic speeds. These accelerated particles caused an atom to break up into its constituent parts when they collided hence allowing Physicists to investigate the inner structure of the atom. These first synchrotrons were known as First generation synchrotrons and although initially radiation was just an unwanted by-product, it soon became a useful property to probe matter.

Synchrotrons have developed over the last few decades with their introduction for the principle application of producing a source of radiation. Second generation synchrotron facilities were used solely to produce radiation for experimental users. An example of a 2nd generation synchrotron is the Synchrotron Radiation Source (SRS) in Daresbury, UK (www.srs.ac.uk). Since the early nineties, synchrotron radiation has reached a new level with the introduction of the 3rd generation synchrotron sources that create radiation with a higher photon flux at specific wavelengths than 2nd generation synchrotrons. These synchrotrons differ from previous ones as they use magnets located around the ring not only to confine the charged particle beam but also causing the accelerated electrons to oscillate hence creating a higher intensity beam. An example of a 3rd generation synchrotron is the Diamond synchrotron source in the UK (www.diamond.ac.uk) and the European Synchrotron Radiation Facility (ESRF) in Grenoble, France (www.esrf.eu). Examples of 2nd and 3rd generation synchrotrons mentioned in this section are shown in Figure 2.8.

Figure 2.8: Examples of 2nd and 3rd generation synchrotrons. From left to right, Synchrotron Radiation Source, SRS (Daresbury,U.K.), Diamond light Source (Oxford, U.K.) and European Synchrotron Radiation Facility, ESRF (Grenoble, France).

2.5.2 Principles of Synchrotron Radiation

Synchrotron radiation sources vary due to their capabilities (such as brightness and detector sensitivity) but the general principles of how synchrotron radiation is produced is the same. Synchrotrons are comprised of a pre-injector, a booster ring and a storage ring. The pre-injector is responsible for firing electrons into the booster ring where the electrons are accelerated to near-relativistic speeds. In the booster ring dipole bending magnets are used to curve the electrons around the bends and the electrons are accelerated in the straight section by passing them through a radio frequency (RF) field. Once the electrons reach sufficient energy they are injected into the storage ring. In the storage ring, the electrons are curved using bending magnets in order to orbit continuously producing synchrotron radiation. Beamlines are placed at tangents to the storage ring to guide narrow beams of light to the experimental stations. Synchrotron radiation is guided to the experimental stations by use of bending magnets and insertion devices. These cause the electron beam to follow a wiggling, or undulating path. Figure 2.9 demonstrates simplistically the main features of a synchrotron.
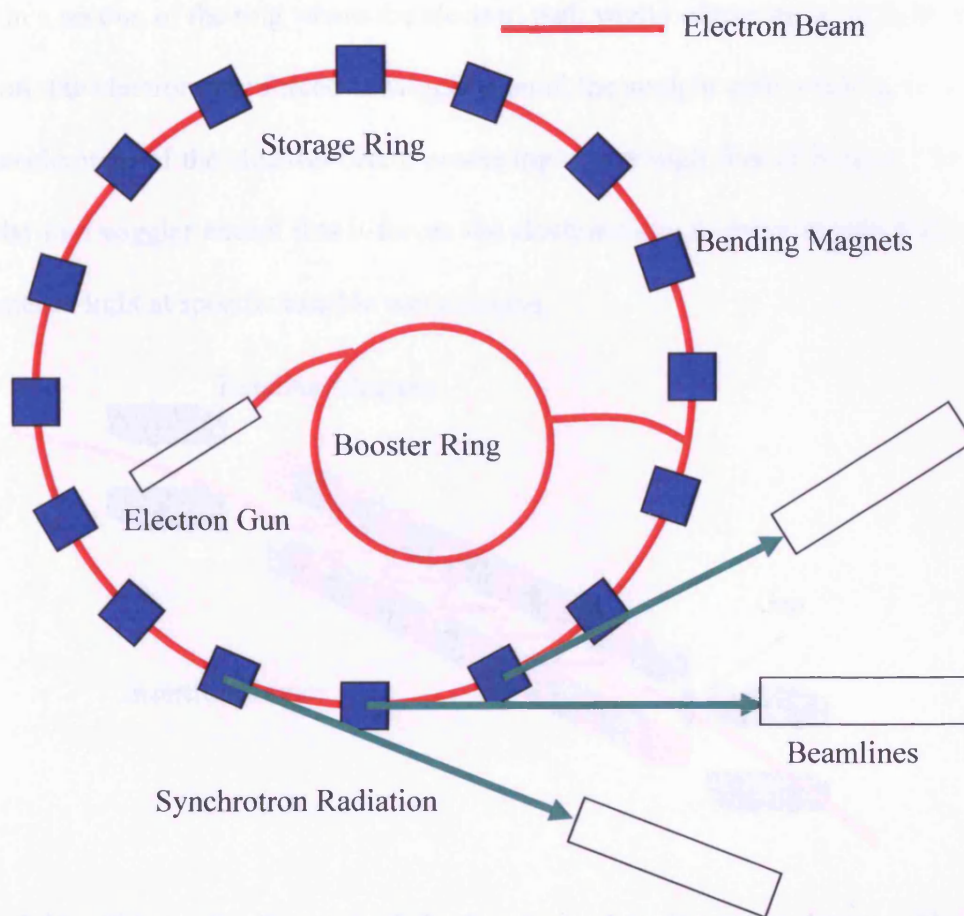
Figure 2.9: **A simplistic diagram showing the main features of a synchrotron. Electrons are injected into the storage ring where they follow a curved path by use of a series of bending magnets. Once the electrons reach a relativistic speed, they produce radiation which is channeled to the beamlines.**

2.5.2.1 Increasing the Intensity of Synchrotron Radiation

Increasing the intensity of synchrotron radiation allows for shorter experiment time. Synchrotron radiation is increased by the insertion devices shown in Figure 2.10, which comprise an array of magnets that produce a spatially periodic magnetic field at the electron beam path. Insertion devices can be configured as either wrigglers or undulators depending on the effect they have on the electron beam. A wiggler consists of an array of magnets,

placed in a section of the ring where the electron path would otherwise be straight; because of its action, the electrons are forced to wiggle around the straight path resulting in an effective local acceleration of the electron beam, producing a very high flux of X-rays. An undulator is similar to a wiggler except that it forces the electrons into a longer meander that results in more intense light at specific tunable wavelengths.
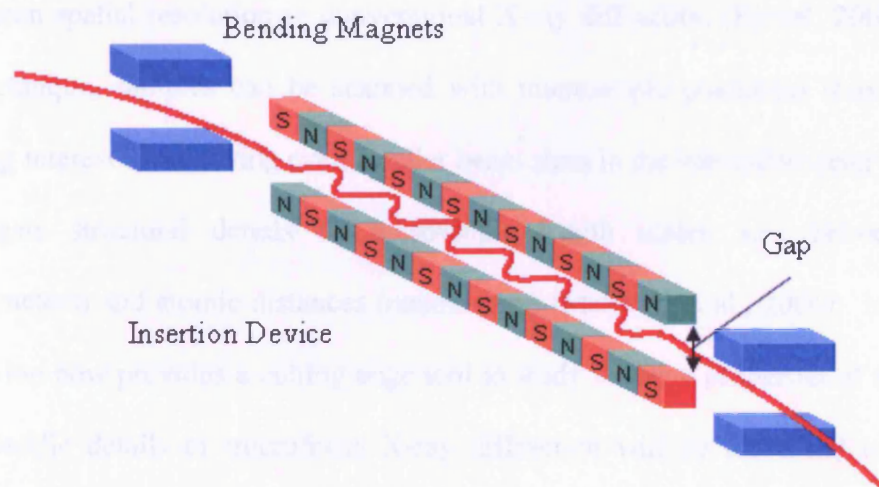
Figure 2.10: Schematic diagram of the function of an insertion device. The electrons follow a trajectory determined by the periodic magnetic field in the insertion device, and synchrotron radiation is emitted. In order to change the wavelength of the resultant radiation, the magnetic field strength is varied by changing the gap between the top and bottom magnet arrays.

2.5.2.2 Microfocus X-ray Diffraction

Increasing the intensity of the radiation obtained from a synchrotron is one modification applied to the X-ray beam at a synchrotron. Many other modifications are made to fully utilise the beam and manipulate the radiation to suit a particular requirement. Another example is the reduction of the beam size to measure a few microns in size whilst

concentrating the X-ray flux (brilliance) using specific optical elements. This is described as microfocus X-ray diffraction and is now utilised at many synchrotron beamlines worldwide, including beamline ID18F at ESRF which is used in this thesis and is discussed in further detail in Chapter 3 and Chapter 7. The availability of high brilliance 3rd generation synchrotron sources together with progress in focusing optics allows the addition of submicron spatial resolution to conventional X-ray diffraction (Riekel, 2000). With this *in situ* technique, samples can be scanned with microscopic positional resolution. There is growing interest in achieving even smaller beam sizes in the sub-micrometer range in order to investigate structural details on mesoscopic length scales, i.e., between microscopic (micrometers) and atomic distances (nanometers) (Maxwell et al., 2006). Microfocus X-ray diffraction now provides a cutting edge tool to study material properties at the micron-scale. The specific details of microfocus X-ray diffraction will be discussed in more detail in Chapter 3 and Chapters 7.

2.6 Data Collection

A simplified model of an X-ray diffraction experiment is shown in Figure 2.11. It comprises an X-ray source that generates X-rays, a detector and a sample placed in the X-ray beam. The X-rays are scattered by the sample under investigation and collected by the detector, which is fixed a selected distance away from the specimen. By altering the distance between the detector and specimen it is possible to collect X-rays scattered at small-angles or wide-angles, as demonstrated in Figure 2.11. Data collection including the correction, reduction and analysis of data is discussed in detail in Chapter 3.

Distance of detector from sample

0.22nm   300nm

Sample

X-ray Source

UWAXS   WAXS   SAXS   USAXS

Wide-angle   Small-angle
X-ray Scattering X-ray Scattering

Ultra Wide-angle   Ultra Small-angle
X-ray Scattering   X-ray Scattering
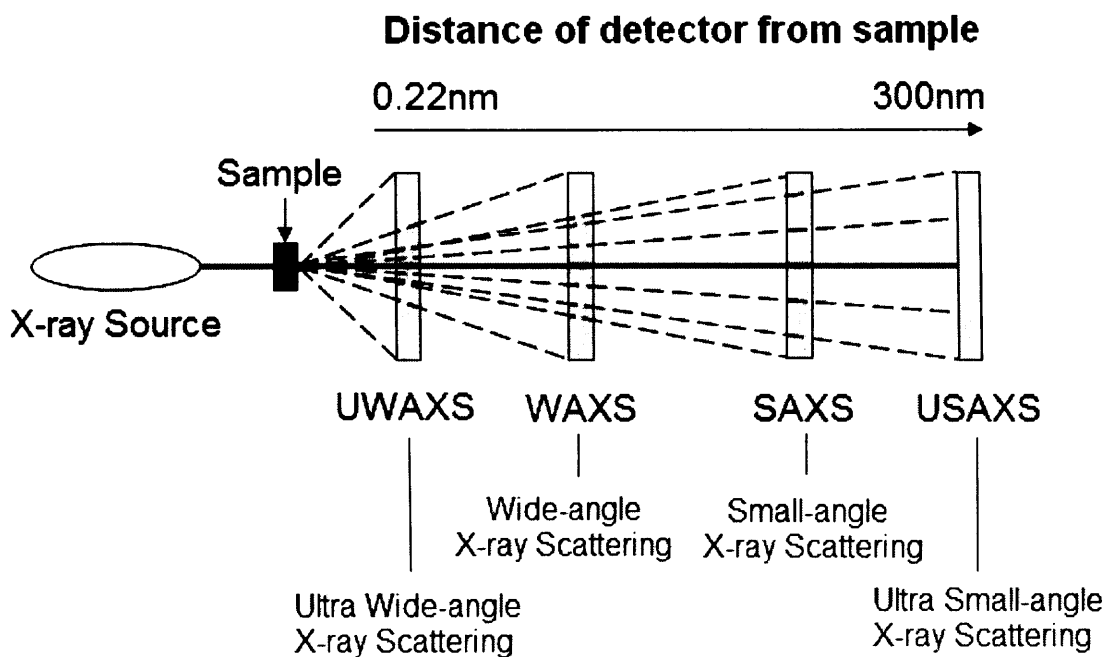
Figure 2.11: **Illustration of sample to detector distances. The main beam is scattered following interaction with the sample. Depending on the position of the detector, different length scales can be investigated. Short sample to detector distances means X-rays scattered at wide-angles can be collected pertaining to structures in the region of a few nanometers. Longer sample to detector distances allow the collection of X-rays scattered at small-angles which provides structural information at lengths scales of a few hundred nanometers. Diagram is not to scale and is adapted from Maxwell et. al., 2006.**

2.7 Fibre Diffraction

The generic principles of X-ray scattering and diffraction, as described previously, can be used to investigate a vast range of materials, including biological tissues. This thesis is interested specifically in the interaction of X-rays with the structural protein, collagen which exhibits structural organisation ranging from the atomic to mesoscopic. The information

revealed by the X-ray diffraction pattern from collagen depends on the collagen type and orientation of the sample. For example, well aligned collagen samples, such as rat-tail tendon, reveals two distinct diffraction regions, the meridian and equator corresponding to axial and lateral molecular arrangements respectively.

2.7.1 Meridional Bragg Reflections

For fibrous proteins such as collagen, a high degree of crystallinity is often present in the direction parallel to the fibre axis. The axial packing of collagen results in the characteristic highly defined D-periodic electron density repeat along the fibril axis. This long-range order gives rise to the meridional reflection series observed on the diffraction pattern. The meridional Bragg reflections have been used to provide information about the axial arrangement of the molecules such as the ratio of the gap region to the overlap region and structural features of the telopeptides (Meek and Quantock, 2001b). Figure 2.11 shows the Bragg orders of the collagen gap and overlap region, known as the D-period which for hydrated rat-tail tendon collagen (Type I) is 67nm. The diffraction image is the reciprocal of the real space structures. Therefore, the position of the reflection due to the 1st order Bragg reflection is at 1/67nm in reciprocal space. The position of the 2nd is at 2/67nm and so on for all of the increasing order numbers.

2.7.2 Equatorial Reflections

The equatorial reflections are found perpendicular to the meridian in the fibre diagram and contain information on the lateral packing and diameters of the molecules and fibrils within a

sample (Orgel et al., 2001). The equatorial reflections give information regarding the quasi-hexagonal packing of collagen molecules within a fibril (Ramachandran, 1967; Brodsky and Ramshaw, 1997). Due to less crystalline packing observed in the direction perpendicular to the fibre axis, diffuse scatter is often observed. A two-dimensional X-ray diffraction pattern for rat-tail tendon collagen is shown in Figure 2.12.
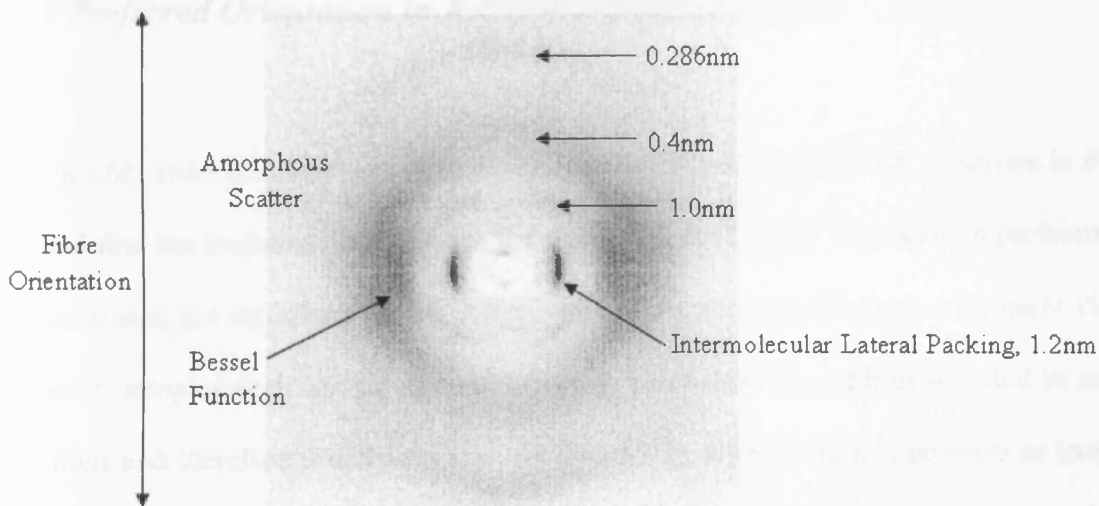
Figure 2.12: A two-dimensional X-ray diffraction pattern for rat-tail tendon collagen. The sample to detector distance was 4cm. The fibre was orientated perpendicular to the X-ray beam. The pattern shows diffraction reflections due to the collagen helix and scattering from the collagen molecules.

The collagen molecules exist in a helical state. Comprehensive reviews of X-ray diffraction analysis from helical structures are given by Ramachandran (1967) and Brodsky (1997) (Wess et al., 2001; Kennedy et al., 2003; Kennedy et al., 2004b). The height shift required to complete one full turn of the helix is termed the helical pitch and the axial repeat (axial rise per residue) is the distance required for two monomers to repeat on the helix. The principal reflection from the collagen helix is shown by the reflection seen at 0.286nm^{-1}. Intermolecular lateral packing between the collagen molecules can be obtained by measuring the position of the reflection which is due to the interference between the collagen molecules.

The combination of disordered material (such as gelatine) and water populations within the sample results in an isotopic ring of amorphous scatter, which exhibits no preferred molecular orientation.

2.7.3 Preferred Orientation in X-ray Diffraction Patterns

Skin, leather and parchment comprise fibres of more than one orientation, as shown in Figure 1.5, and this has important implications for the diffraction image. In tendon, a preferentially aligned tissue, the meridional Bragg reflections and equatorial reflections are clearly visible. However, samples such as skin and subsequently parchment have fibres oriented in several directions and therefore usually exist as a feltwork. In diffraction, this presents as isotropic diffraction and scattering features appear as circles. The meridional Bragg reflection and equatorial reflections for tendon and skin are demonstrated in Figure 2.13.
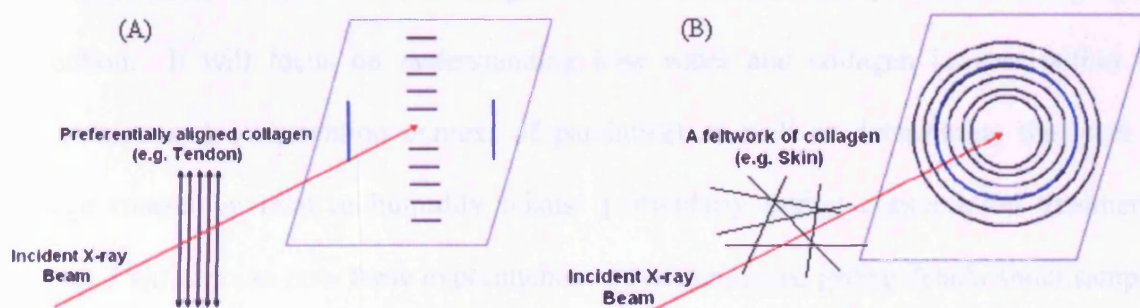
Figure 2.13: (A) Representation of tendon, a preferentially aligned tissue, the meridional Bragg reflections and equatorial reflections are clearly visible. (B) Representation of skin which is not aligned in one direction but exists as a feltwork, smearing of the meridional and equatorial reflections so they appear as arcs or circles is seen.

Figure 2.13 shows that the orientation of collagen fibrils can cause a change in the observed two-dimensional X-ray diffraction images. When there is more than one fibril, the meridional and equatorial reflections appear as arcs or circles, therefore it is more challenging to decouple the meridional from the equatorial reflections in skin and parchment.

2.8 Conclusions

Over recent years X-ray diffraction has become a more readily available tool in the investigation of parchment. X-ray diffraction has been used in many parchment studies including investigation of the collagen structure of parchment (Clark and Curri, 1998; Hochleitner et al., 2003; Creagh et al., 2009), identifying pigments present in parchment (Kennedy et al., 2004c), investigating the effect of laser cleaning on parchment (Kennedy et al., 2004c) and to study the result of liming on collagen structure (Maxwell et al., 2006).

This thesis aims to further the investigative work conducted on parchment using X-ray diffraction. It will focus on understanding how water and collagen interact within the preservation and conservation context of parchment as well as determining the level of damage caused by relative humidity misuse particularly during conservation treatments. Chapter 3 will discuss how these experiments will be conducted giving details about samples and the experimental set-up.

Chapter 3: Materials and Methods

3.1 Introduction

This chapter provides details regarding the utilisation of X-ray diffraction, where the principles of this technique are outlined in Chapter 2. Detailed descriptions of samples used in this thesis are given in this chapter. The following sections will provide details on the X-ray stations used for the collection of scattering images for the samples analysed. The main sources of X-ray diffraction data were three different synchrotron radiation sources (SRS, Daresbury, stations 2.1 and 14.1; ESRF, station ID18F) and the NanoStar, an in-house X-ray diffraction source. Data reduction was achieved using FibreFix software and peak fitting was carried out using PeakFit4 software. Molecular modelling is another technique used in this study and is outlined in Section 3.5 of this chapter.

3.2 Parchment samples

Historical and modern parchment samples were provided for this study from a number of different sources. Table 3.1 provides details of the historical parchment samples gifted by a variety of different sources including the National Archives of Scotland (Edinburgh, U.K.), the Bodleian Library, University of Oxford (Oxford, U.K.), the National Archives (London, U.K.) and samples donated by Dr. Ira Rabin from the Artifacts Treatment and Conservation department at the Israel Antiquities Authority. Table 3.1 provides information on the parchment samples used including their estimated age, size and number of sheets, identification code and any additional information about the sample. Dates of production for

historical samples are estimated from dates inscribed on parchment sheets at the time of initial parchment use. Additional information on the individual parchment samples can be found in the relevant corresponding Result Chapters.

Year	Size	No. of sheets	Name	Notes
1765	30cmx30cm	3	USH01	horny, folded parchment
1769	33cmx25cm	1	USH02	dirty/ coarse feel
1775	54cmx68cm	1	USH03	large folded sheet
1827	65cmx69cm	1	USH04	large folded sheet
1824	30cmx35cm	2	USH05	dirty/ rough feel
1832	25cmx35cm	6	USH06	polished
1828	49cmx36cm	1	USH07	polished
1817	24cmx37cm	6	USH08	tightly folded, several sheets tied together
Unknown	24cmx36cm	1	USH09	book binding
1765	41cmx13cm	1	USH10	small folded single sheet
Unknown	6cmx5cm	1	BOD01	small sample with printed text
Unknown	4cmx5cm	1	BOD02	small sample with hand written text
~2000	-	1	MOD01	modern manufactured
~1086	Sub mm	N/A	1V	Great Domesday, Page 1, verso side
~1086	Sub mm	N/A	LD1V	Little Domesday, Page 1, verso side
~1086	Sub mm	N/A	LD109V	Little Domesday, Page 109, verso side
~1086	Sub mm	N/A	LD183V	Little Domesday, Page 183, verso side
~1086	Sub mm	N/A	LD412V	Little Domesday, Page 412, verso side
~1086	Sub mm	N/A	GD203V	Great Domesday, Page 203, verso side
~1086	Sub mm	N/A	GD202r	Great Domesday, Page 202, recto side
~1086	Sub mm	N/A	382r	Great Domesday, Page 382, recto side
~1086	Sub mm	N/A	LD449r	Little Domesday, Page 449, recto side
Unknown	5cmx2cm	1	LT1d	19°C(±1°C) and 50%RH (±2%)
Unknown	4cmx3cm	1	LT2d	19°C(±1°C) and 50%RH (±2%)
Unknown	2cmx4cm	1	LT3d	19°C(±1°C) and 50%RH (±2%)
Unknown	4cmx3cm	1	LT1L	30-60%RH & varying temp (in the day) 19°C(±1°C) and 50%RH (±2%) (at night)
Unknown	5cmx3cm	1	LT2L	30-60%RH & varying temp (in the day) 19°C(±1°C) and 50%RH (±2%) (at night)
Unknown	4cmx3cm	1	LT3L	30-60%RH & varying temp (in the day) 19°C(±1°C) and 50%RH (±2%) (at night)

Table 3.1:   Detailed information for the historical parchment samples.   The National Archives of Scotland gifted legal documents (USH01-USH10) and the Bodleian Library donated parchment samples identified as being especially degraded (BOD01-BOD02). Samples also include a modern manufactured parchment (MOD01) and the Domesday Book samples provided by the National Archives (1V-LD449r).   Dr Ira Rabin provided the parchment samples subjected to different relative humidity (LT1d-LT3L).

3.2.1 Hydration of Parchment Samples

In order to assess the required amount of time needed to fully hydrate parchment a small study was proposed. Two different parchment sources were used for this study; modern parchment (circa 2000) and historical parchment (dated 1817). Each sample was weighed prior to hydration, and then weighed after hydration at time intervals of 1 minute, 2 minutes, 5 minutes, 30 minutes, 1 hour and 3 days. Figure 3.1 shows the percentage weight change on hydration for both samples. The mean weight and the percentage weight change for these measurements are shown in Table 3.2.
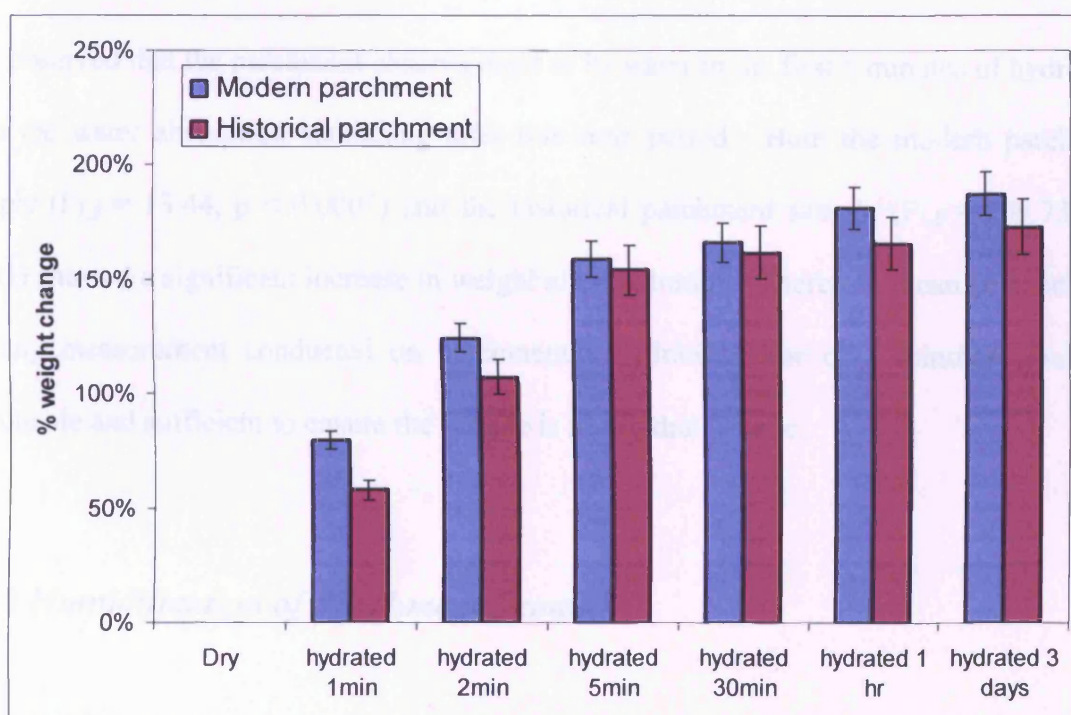
Figure 3.1: The percentage weight change for both samples upon hydration compared with the sample in the dry state. Error bars represent the standard error of the mean where n=5.

	Modern parchment (circa 2000)			Historical parchment (dated 1817)		
	Mean weight (g)	% weight gain	Std dev	Mean weight (g)	% weight gain	Std dev
Dry	0.6068	-	0.0017	0.6774	-	0.0011
hydrated 1min	1.0962	80.06%	0.0178	1.0728	57.96%	0.0296
hydrated 2min	1.3626	124.55%	0.0452	1.4050	107.41%	0.0635
hydrated 5min	1.5691	158.89%	0.0743	1.7228	154.33%	0.0919
hydrated 30min	1.6156	166.25%	0.0040	1.7745	161.96%	0.0353
hydrated 1 hr	1.7081	181.50%	0.0120	1.8102	165.87%	0.0333
hydrated 3 days	1.7436	187.34%	0.0062	1.8498	173.07%	0.0196

Table 3.2: The mean weight and the percentage weight change for modern and historical parchment at different stages of hydration where n =5.

It is observed that the parchment absorbs most of its water in the first 5 minutes of hydration, with the water absorption stabilising after this time period. Both the modern parchment sample ($F_{1,8}$ = 13.44, p < 0.0001) and the historical parchment sample ($F_{1,8}$ = 299.73, p < 0.001) showed a significant increase in weight after hydration. Therefore it can be concluded for any measurement conducted on parchment a hydration time of 5 minutes would be reasonable and sufficient to ensure the sample is in a hydrated state.

3.2.2 Humidification of Parchment Samples

The relative humidity in the laboratory where the samples were stored was monitored over a two week period. The average %RH for the laboratory over a two week period was 43.74%RH (±3.55). Measurements were taken using a humidity probe in both the morning and afternoon at the same time for 2 weeks. Figure 3.2 demonstrates how the %RH changed during this period.
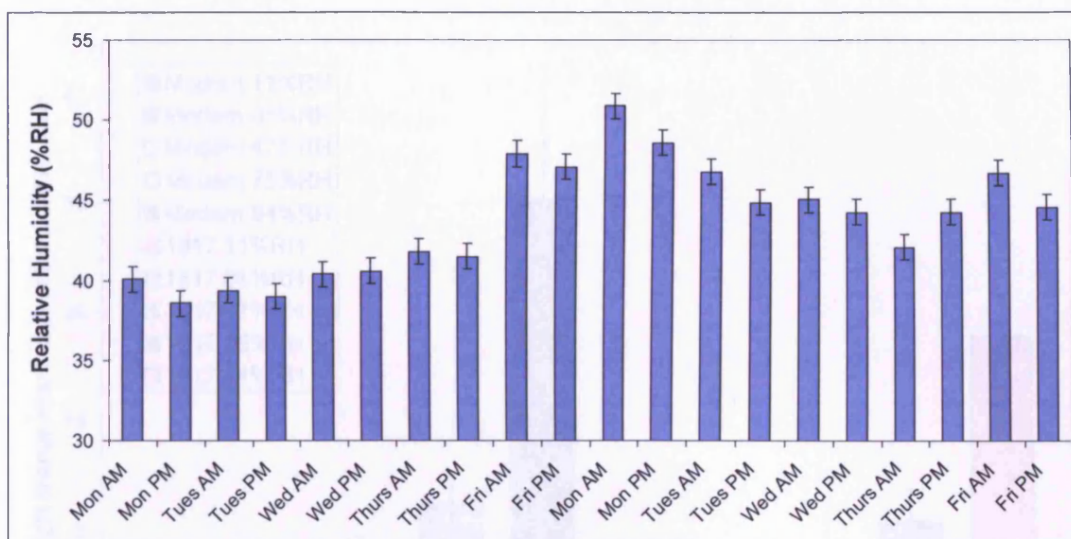
Figure 3.2: Change in the %RH in the laboratory over a two week period. Error bars represent the standard error of the mean where n=5.

Three samples from two different parchment sources were used to assess the amount of water present in parchment at different levels of relative humidity; modern parchment (circa 2000) and historical parchment (dated 1817). Each sample was weighed prior to humidification, and then weighed after humidification at intervals of 1 day to 7 days. The relative humidity (RH) levels used were 11%RH, 31%RH, 47%RH, 75%RH and 84%RH (±5%RH for all measurements). Figure 3.3 shows the mean percentage weight change for both samples at all RH levels. The mean weight and the percentage weight change for all time intervals are shown in Table 3.3.
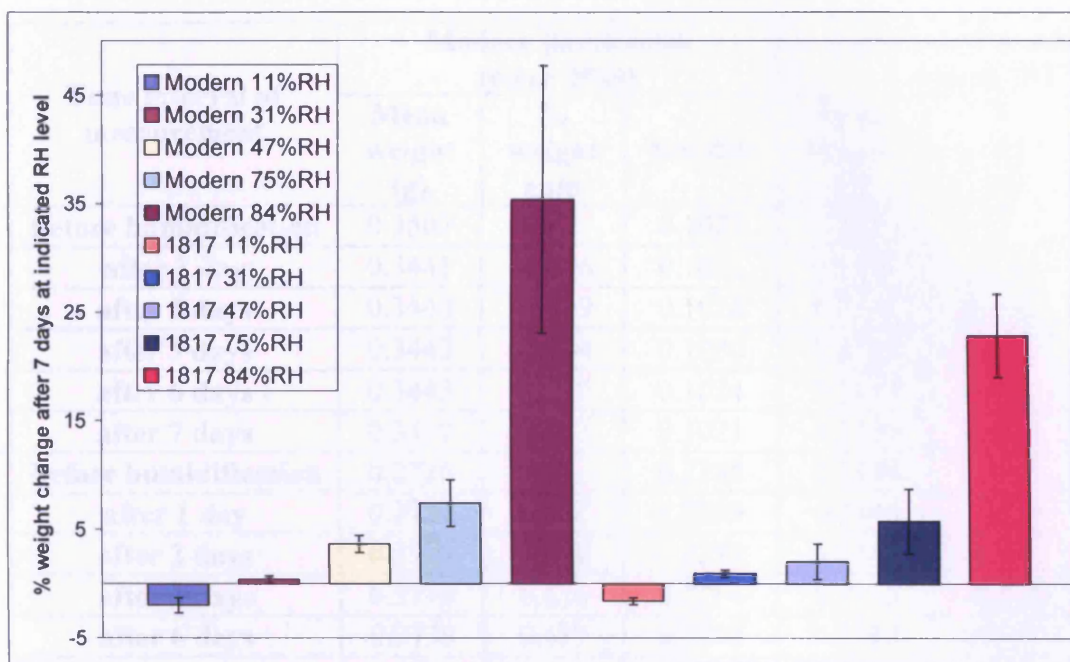
Figure 3.3: The percentage weight change for both samples after 7 days stored at 11%RH, 31%RH, 47%RH, 75%RH and 84%RH. Error bars represent the standard error of the mean where n=5.

Figure 3.3 demonstrates, as expected, for parchment stored at low humidities (11%RH) a decrease in the percentage weight is seen, indicating a loss in water from the parchment structure. At the opposite end of the humidity scale, for parchment stored at higher humidities (84%RH) an increase in the percentage weight is observed, signifying an uptake of water within the structure of the parchment. The relationship for the percentage increase in weight versus increase in relative humidity is non-linear. This suggests than higher humidities cause a larger change in water content present within parchment than lower humidities. The modern parchment sample stored at 84%RH showed a significant increase in weight ($F_{1,8} = 4.30$, $p < 0.05$). While the modern parchment sample stored at 11%RH showed no significant difference in weight ($F_{1,8} = 1.01$, $p = 0.92$).

%RH level	Time interval of measurement	Modern parchment (circa 2000)			Historical parchment (dated 1817)		
		Mean weight (g)	% weight gain	Std dev	Mean weight (g)	% weight gain	Std dev
1%RH	Before humidification	0.3507	-	0.1022	0.2235	-	0.1308
	after 1 day	0.3441	-1.496	0.1032	0.2197	-1.182	0.1302
	after 2 days	0.3443	-1.309	0.1028	0.2195	-1.209	0.1302
	after 3 days	0.3443	-1.384	0.1030	0.2196	-1.343	0.1297
	after 6 days	0.3443	-1.272	0.1024	0.2198	-1.075	0.1304
	after 7 days	0.3438	-1.421	0.1021	0.2199	-1.209	0.1298
1%RH	Before humidification	0.2726	-	0.2288	0.2149	-	0.0988
	after 1 day	0.2727	0.037	0.2289	0.2146	-0.211	0.0980
	after 2 days	0.2731	0.196	0.2289	0.2148	0.105	0.0975
	after 3 days	0.2740	0.526	0.2294	0.2153	-0.158	0.0981
	after 6 days	0.2739	0.489	0.2292	0.2160	0.053	0.0984
	after 7 days	0.2737	0.404	0.2284	0.2169	0.738	0.0990
7%RH	Before humidification	0.2726	-	0.2372	0.2215	-	0.1123
	after 1 day	0.2749	0.832	0.2377	0.2229	0.944	0.1115
	after 2 days	0.2775	1.785	0.2385	0.2247	1.259	0.1120
	after 3 days	0.2788	2.274	0.2398	0.2250	1.206	0.1117
	after 6 days	0.2823	3.558	0.2445	0.2265	1.521	0.1108
	after 7 days	0.2825	3.644	0.2458	0.2261	1.416	0.1105
5%RH	Before humidification	0.2881	-	0.2214	0.2347	-	0.1452
	after 1 day	0.3044	5.646	0.2239	0.2437	1.112	0.1438
	after 2 days	0.3071	6.583	0.2250	0.2452	1.931	0.1442
	after 3 days	0.3094	7.392	0.2276	0.2463	1.755	0.1454
	after 6 days	0.3096	7.462	0.2277	0.2473	3.160	0.1463
	after 7 days	0.3095	7.427	0.2282	0.2482	4.564	0.1463
4%RH	Before humidification	0.3333	-	0.0311	0.1986	-	0.1095
	after 1 day	0.4471	34.130	0.1070	0.2348	23.183	0.1433
	after 2 days	0.4498	34.950	0.1072	0.2424	27.155	0.1479
	after 3 days	0.4528	35.840	0.1069	0.2423	27.248	0.1482
	after 6 days	0.4548	36.430	0.1077	0.2439	28.14	0.1494
	after 7 days	0.4513	35.400	0.1100	0.2440	28.079	0.1490

Table 3.3: The mean weight and the percentage weight change for modern and historical parchment at different stages of humidification where n=5.

3.2.3 Artificial Degradation of Parchment Samples

The parchment samples used throughout the study where assessed by XRD to be in an intact condition with a clear presence of collagen axial structure. Despite substantial effort it was not possible to obtain a spectrum of naturally degraded parchment samples therefore it was necessary to artificially degrade intact parchment to different extents. A number of different methods of artificial degradation were assessed including, steamed, microwaved (energy of 900W) and hydrated then air-dried. XRD images were collected on each of these samples plus a control sample. Figure 3.4 shows the two-dimensional images collected and Figure 3.4 shows the corresponding one-dimensional linear profiles.
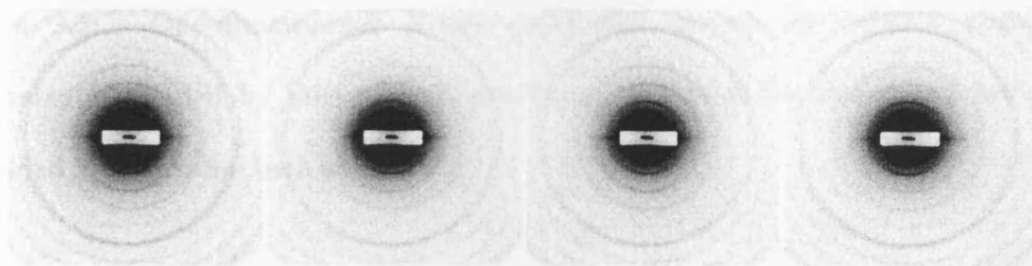
Figure 3.4: **Two-dimensional X-ray diffraction images for control parchment, parchment degraded by microwaves, parchment degraded by steam and parchment degraded by hydration then air-drying (from left to right). The images show a Q range from 0 to 0.15nm^{-1}.**
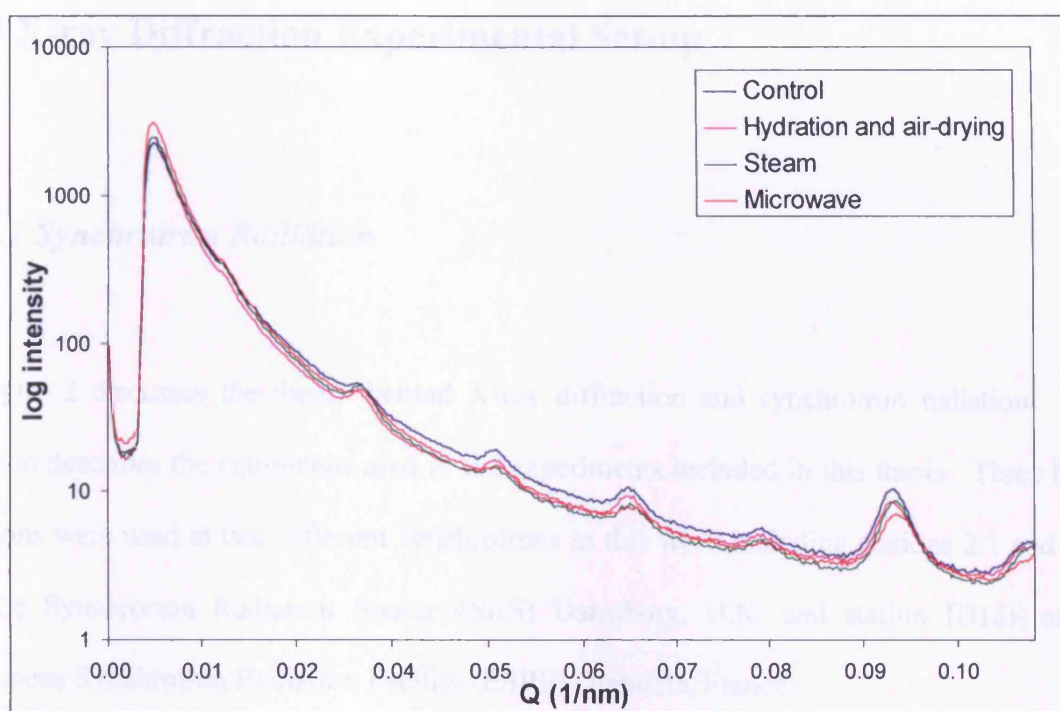
Figure 3.5: One-dimensional X-ray diffraction traces for control parchment, parchment degraded by microwaves, parchment degraded by steam and parchment degraded by hydration then air-drying.

There is very little change to the collagen structure after steaming or hydration then air-drying. A change was observed in the collagen structure after artificial degradation by microwaves; a loss in intensity and a shift in the peak position to a lower D-period. Therefore, the best substitute for naturally degraded parchment is to apply artificial degradation to intact parchment via use of microwaves although naturally degraded parchment is still preferable.

3.3 X-ray Diffraction Experimental Set-up

3.3.1 Synchrotron Radiation

Chapter 2 discusses the theory behind X-ray diffraction and synchrotron radiation. This section describes the equipment used in the experiments included in this thesis. Three beam stations were used at two different synchrotrons in this work including stations 2.1 and 14.1 at the Synchrotron Radiation Source (SRS) Daresbury, U.K. and station ID18F at the European Synchrotron Radiation Facility (ESRF) Grenoble, France.

3.3.1.1 SRS Daresbury, Station 2.1

Station 2.1 at SRS Daresbury is optimised for both small angle X-ray scattering and non-crystalline diffraction. Grossmann (2002) and Andrews, et al. (1989) give comprehensive reviews of this station. Station 2.1 contains a computer controlled sample stage that allows movement of the sample in specific directions and the beam is typically 0.8mm x 3mm. The evacuated camera tube has a variable length between 0.9 and 9.5m making it capable of providing information on the long-range structure of the sample on a length scale between 1-200nm. A schematic representation of station 2.1 is shown in Figure 3.6.
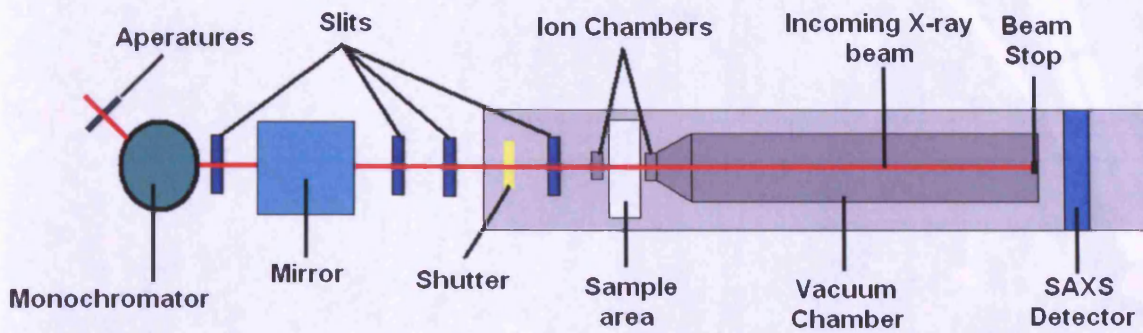
Figure 3.6: Schematic representation of Station 2.1, SRS Daresbury, UK. Adapted from http://srs.dl.ac.uk/ncd/station21/2.1_floorplan.html (Snigirev et al., 1996).

During experiments conducted in this thesis, the camera length used was between 4.25m and 5.5m and samples were exposed for on average 30 seconds (depended on the intensity of the X-ray beam). Samples were mounted in a specially designed Figure 3.7 shows an image of the experimental set-up at a camera length of 5.5m where the detector and sample stage regions are shown in more detail. This allowed the observation of long-range interactions of collagen resulting from axial order (D-period). Hydrated rat-tail tendon was used as a standard calibration providing a characteristic regular axial order of 67nm (D-period).
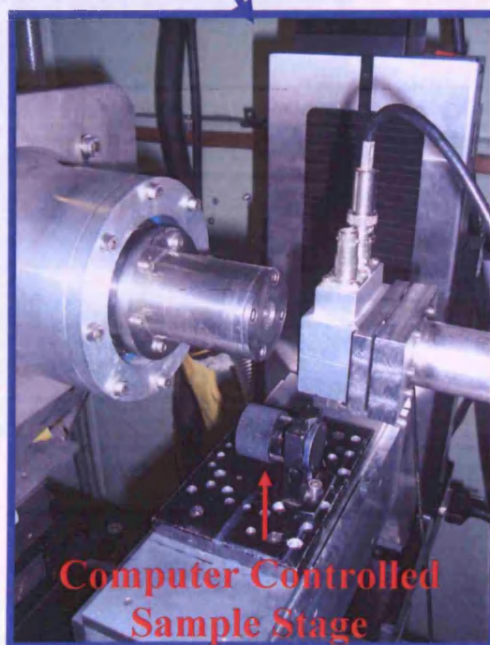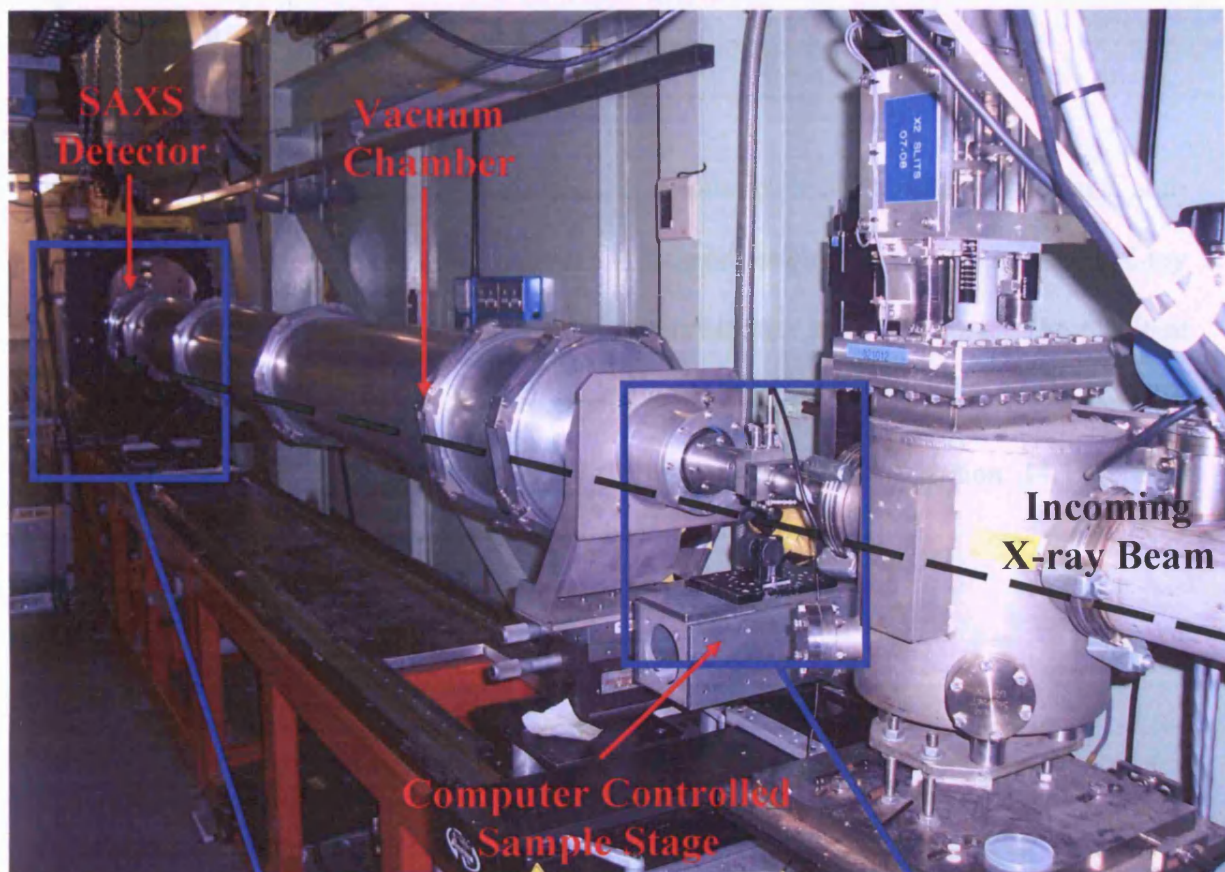
Figure 3.7: Image of station 2.1 at SRS Daresbury, with a sample to detector distance of 5.5m. The detector and sample areas are shown in detail in two additional images below the main image. The black dashed arrow indicates the direction of the incoming X-ray beam.

3.3.1.2 SRS Daresbury, Station 14.1

Station 14.1 at SRS Daresbury is optimised for macromolecular crystallography and non-crystalline diffraction. This station provides a focused, collimated, monochromatic X-ray beam at high energy resolution at wavelengths of 0.1488nm and 0.0977nm. The resultant scattering data is collected on a charge-coupled (CCD) X-ray Quantum 4 ADSC detector (ADSC, Poway, CA). Figure 3.8 shows the equipment used at station 14.1 at SRS Daresbury.
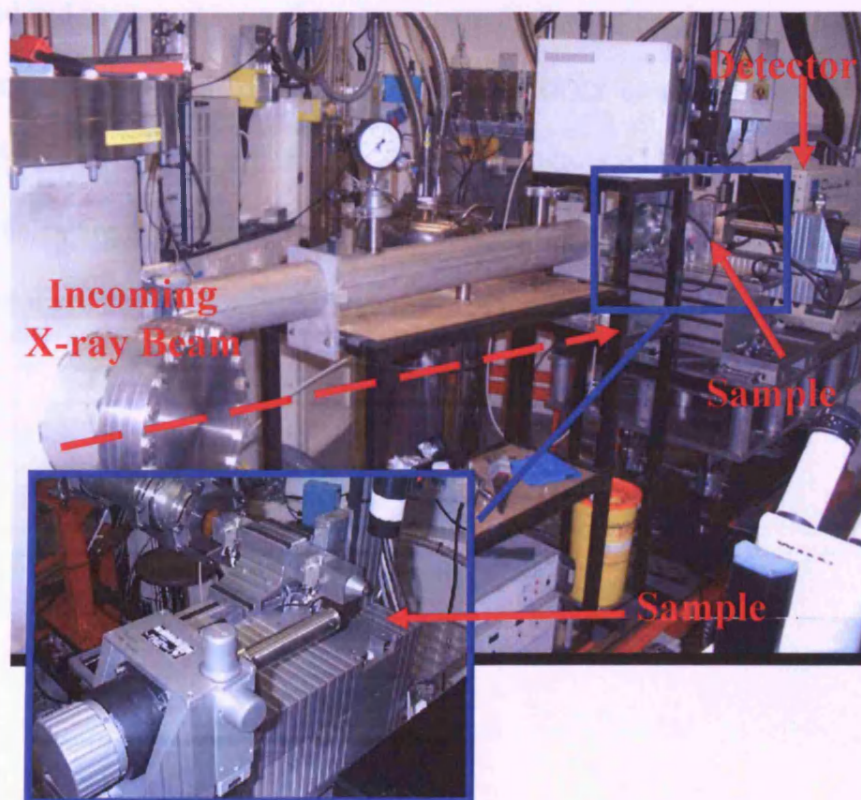
Figure 3.8: Image of station 14.1 at SRS Daresbury at a sample to detector distance of 140mm. The sample area is shown in detail in an additional image (see inset). The red dashed arrow indicates the direction of the incoming X-ray beam.

3.3.1.3 ESRF, Station ID18F

Station ID18F is a microfocus X-ray diffraction source at the high brilliance synchrotron source the European Synchrotron Radiation Facility (ESRF) in Grenoble, France. Compound refractive lenses (CRL) were used to focus the X-ray beam to generate a microbeam of size 2μm (Vertically) x 6μm (Horizontally) (Somogyi et al., 2001). Images of the samples were taken using the defocused X-ray beam in connection with an alignment camera (CCD, a charge-coupled device) prior to starting the microfocus X-ray diffraction scans. The alignment camera was used to locate the sample and region due to be scanned, where images were collected and used to observe the microscopic features of the sample. The set-up allows for the switching of cameras from the diffraction CCD to the alignment CCD. The wavelength of the X-rays was 0.086nm and the sample-to-detector distance was fixed at 213mm. Samples are mounted in the X-ray beam on a goniometer, attached to a computer controlled motorised stage. A schematic of the experimental set-up is shown in Figure 3.9.
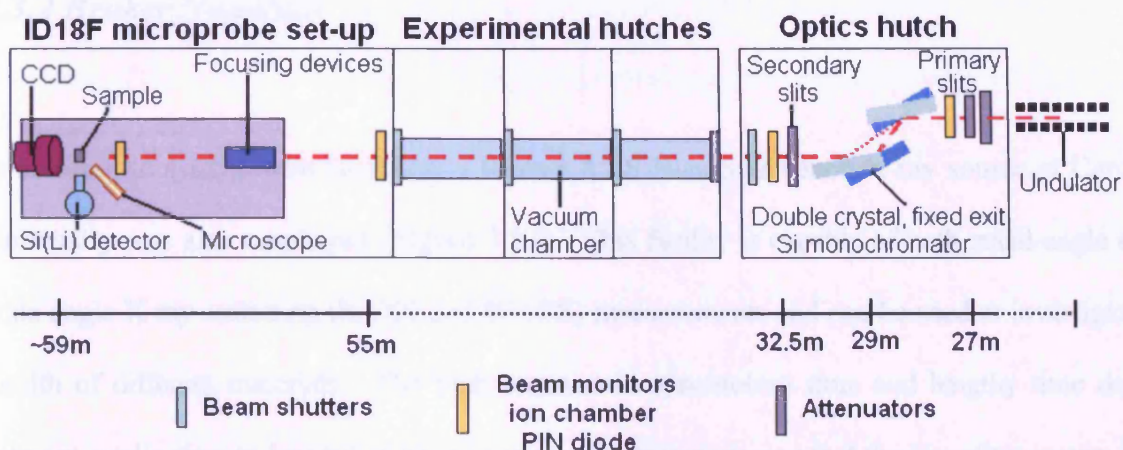
Figure 3.9: A schematic diagram of the microprobe set-up at station ID18F at the ESRF synchrotron. Diagram adapted from Somogyi et al. (2001) and

http://www.esrf.eu/UsersAndScience/Experiments/Imaging/ID18F/BeamlineDescription

Two different types of scans were available as shown in Figure 3.10; the mesh scan and the ascan. The mesh scan is where a series of images are collected in a grid (raster) formation; the sample is moved in both horizontal and vertical directions in relation to the X-ray beam. The ascan is where images are collected in a horizontal direction to the X-ray beam only.
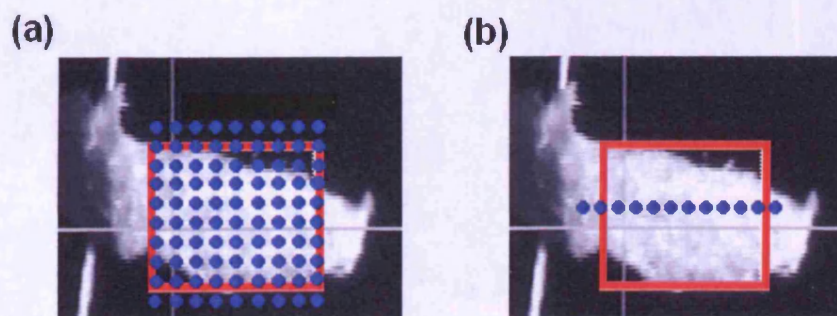
Figure 3.10: Graphical representation of (a) mesh scan where the sample is moved in both horizontal and vertical directions in relation to the X-ray beam and (b) ascan where a collection of images is taken in a horizontal direction to the X-ray beam only.

3.3.2 Bruker NanoStar

In addition to synchrotron facilities, a Bruker AXS NanoStar bench X-ray source at Cardiff University was also employed (Figure 3.11). This facility is capable of both small-angle and wide-angle X-ray scattering (SAXS and WAXS) measurements and can be used to investigate a wealth of different materials. The high demand in synchrotron time and lengthy time delay between application and award of beamtime at synchrotrons means that the NanoStar system is a viable alternative although the NanoStar produces less intense images which therefore require much longer collection times.

Figure 3.11: **An image of the Bruker AXS NanoStar small angle X-ray scattering facility at Cardiff University, U.K.**

Here the X-ray beam is produced by a Kristalloflex 760 X-ray generator (Bruker AXS, Germany) and focused using two cross-coupled Göbel mirrors. The focused beam is reduced in size using a series of three pinholes to produce an X-ray beam of 0.4 mm x 0.8 mm, with a wavelength of 0.154 nm. The NanoStar, (like station 2.1 at the SRS Daresbury), has a vacuum chamber in which the X-ray beam travels. The sample to detector path length is variable between 4cm and 107cm. However, unlike station 2.1 the NanoStar holds the sample in an evacuated chamber to reduce the air absorption of scattered X-rays. The main X-ray beam passes through the sample and is blocked by a gold beam stop. The X-rays scattered by the sample are collected by a HiStar gas filled detector. A schematic of the experimental set-up for the Bruker AXS NanoStar bench X-ray source is shown in Figure 3.12.
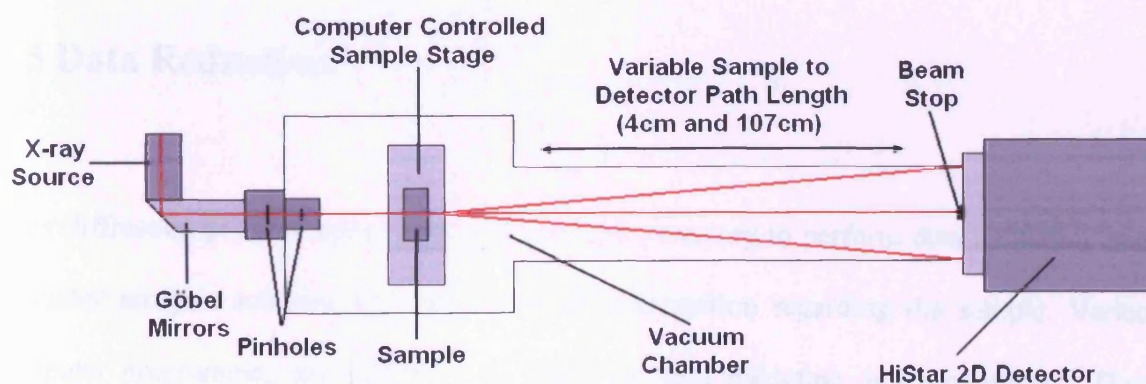
Figure 3.12: A schematic of the experimental set-up for the Bruker AXS NanoStar small angle X-ray scattering station at Cardiff University, U.K.

3.4 Data Correction

X-ray scattering patterns are usually accompanied by other scattered radiation, background radiation that is not due to the interaction with the sample. Before data analysis, it is important to subtract this background radiation from the original data to obtain correct intensity values and a clearer scattering image. This is achieved by repeating the same experimental conditions and recording the image of an empty cell without the specimen present. This background image can then be subtracted from the collected data to remove many artefacts introduced to the original image. Once corrected for the background radiation and artefacts the data can be analysed.

3.5 Data Reduction

After diffraction patterns have been collected it is necessary to perform data reduction using specialist analysis software in order to obtain information regarding the sample. Various computer programmes are currently available for data reduction and processing. These change on an almost year-by-year basis and are frequently updated to account for new modalities of software analysis. The most useful and commonly used are FibreFix (Rajkumar et al., 2005) and PeakFit4.

3.5.1 FibreFix

FibreFix is a software program produced by the non-operational Collaborative Computational Project for Fibre Diffraction and Solution Scattering (CCP13) to determine specific parameters from fibre diffraction patterns (Rajkumar et al., 2005). This program contains various analytical features that allow the X-ray scattering data to be read in and displayed as a two-dimensional image. It also has many additional features, for example, it allows adjustment of the intensity scale and the contrast of the image, estimation and removal of the background radiation, calculation of the diffraction centre of the image and is able to generate one-dimensional intensity profiles. The user can also choose the type of linear intensity plot to be outputted, for example an intensity profile integrated along a line or a scan around an arc. FibreFix is available from the website: www.small-angle.ac.uk/small-angle/Software/FibreFix.

The main aim of data analysis is to extract information from the diffraction images that relates to physical parameters within the sample. Data can be reduced by the conversion of the scattering images into one-dimensional plots as shown in Figure 3.13. The conversion of two-dimensional data to one-dimensional traces allows the intensity distribution of the scattering to be plotted against angular position allowing the quantitative estimation of structural parameters.
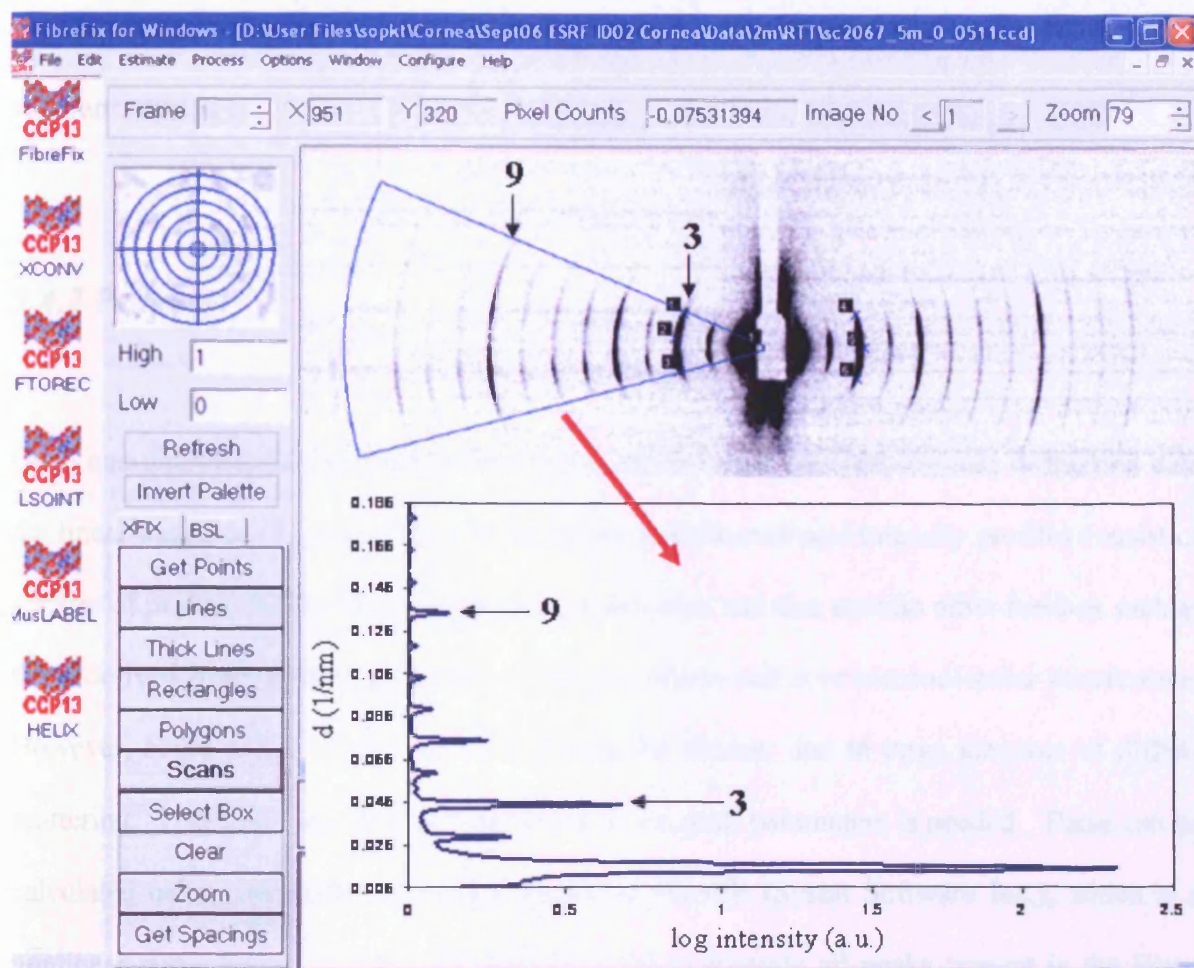
Figure 3.13: Illustration of the spatial conversion of a two-dimensional image to a one-dimensional linear trace. The main image is of the interactive GUI for FibreFix software from CCP13 with a two-dimensional X-ray diffraction image of hydrated rat-tail tendon. The image inset is the corresponding one-dimensional intensity profile for the two-dimensional X-ray diffraction image of hydrated rat-tail tendon. The 3rd and 9th orders of collagen axial diffraction are highlighted on both the two-dimensional X-ray diffraction image and the one-dimensional linear profile.

Figure 3.13 shows an illustration of how two-dimensional data is reduced to a one-dimensional intensity profile using the software, FibreFix. To determine information about the sample from a one-dimensional intensity profile analysis of the peak positions and shapes is required.

Various computer programs for peak fitting are currently available; in this thesis PeakFit4 software was used.

3.4.2 PeakFit4

Once one-dimensional intensity profiles are obtained from two-dimensional diffraction data the linear traces can be analysed. The resultant one-dimensional intensity profiles consist of a series of peaks produced from long-range axial order and also contain other features such as those derived from scattering of objects with a uniform radius or intermolecular interference. However, some peaks in the linear traces can be hidden, due to large amounts of diffuse scattering. Therefore, detailed determination of the peak parameters is needed. These can be calculated using computer programmes such as PeakFit (Systat Software Inc.), which is a nonlinear curve fitting software that can be used to separate all peaks present in the linear plot. It enables the user to fit and subtract a baseline from the traces. It also allows the peaks to be fitted allowing the calculation of the peak parameters such as the peak position, the peak amplitude, the integral area and the peak width (full width half maximum, FWHM). A screenshot from PeakFit software is shown in Figure 3.14. PeakFit is available from the website: http://www.systat.com/products/PeakFit/.

Figure 3.14: **A screenshot from PeakFit software. A two-dimensional diffraction pattern obtained from rat-tail tendon has been converted into a one-dimensional linear trace and transferred into the PeakFit software. The peaks observed correspond to the meridional reflections on the diffraction pattern. The software enables users to fit the peaks and obtain parameters such as peak intensity, position and the full width half maximum (FWHM).**

A number of peak profile parameters can be determined and used to provide information about the structural properties of each sample. One valuable parameter of a peak profile that is utilised in this study is the peak width (full width half maximum, FWHM). The FWHM for a peak is demonstrated in Figure 3.15. When calculating the FWHM in this thesis it was calculated as an average FWHM of the fifth, sixth and ninth orders of collagen axial diffraction. Another parameter used in this study is the integrated intensity.
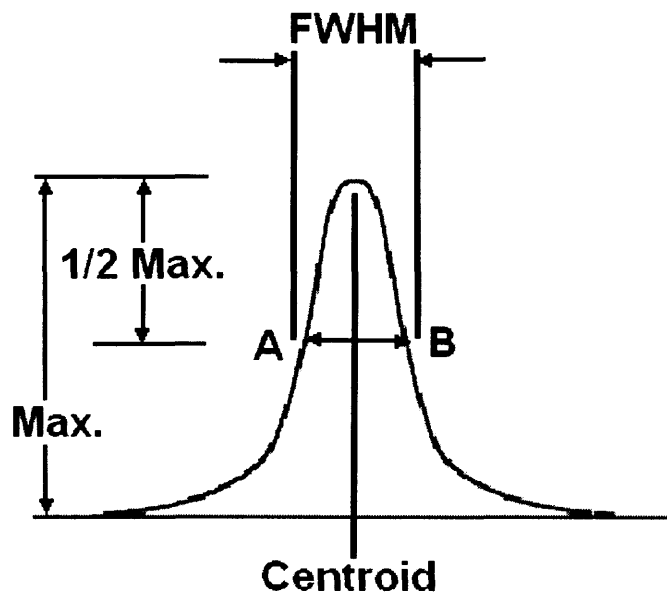
Figure 3.15: Full width at half maximum (FWHM) is given by the difference between the two values of the independent variable (x-axis) at which the dependent variable (y-axis) is equal to half of its maximum value.

3.5 Data Analysis

3.5.1 Small-Angle Diffraction Pattern

Scattering by X-rays at small angles (<6°) gives information regarding the long-range order of structures (Brodsky et al., 1980). Collagen fibrils from skin and subsequently parchment exhibit a fundamental axial periodicity in the region of 65.5nm which is observable within the capacity of SAXS (Hodge and Petruska, 1963).

3.5.1.1 Axial Periodicity of Collagen

The characteristic D-period of collagen is the result of regular fluctuations in the electron density of collagen in the axial direction, which gives rise to meridional X-ray diffraction (a series of Bragg reflections) (Meek and Quantock, 2001b; Sionkowska et al., 2004b). The distances between the meridional reflections correspond to the axial periodicity of the collagen structure allowing the characteristic D-period in real space to be calculated from the peak position on the diffraction pattern.

The breadth of the meridional reflections corresponds to the variation in the D-period within the sample bathed in the X-ray beam or the size of the finite axial crystalline lattice. Collagen fibrils with a highly regulated D-period would produce sharp diffraction peaks with a small width, whereas collagen fibrils with a variation of D-periods could produce broader peaks where peak breadth would increase as a function of diffraction order. A two-dimensional meridional X-ray diffraction pattern of parchment (D-period = 65nm) and the corresponding linear plot are shown in Figure 3.16. The two-dimensional pattern consists of a series of equidistant Bragg reflections where the distance between two peaks is used to calculate the D-period.
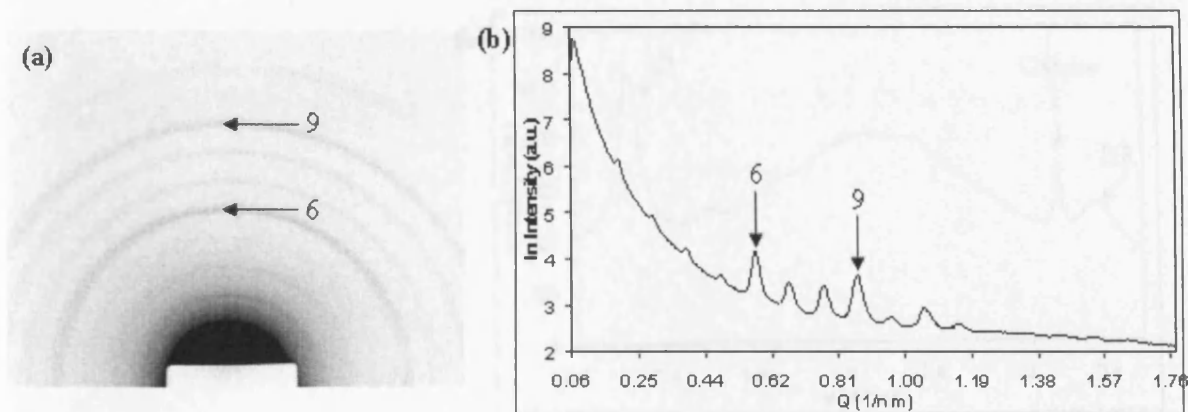
Figure 3.16: (a) Two-dimensional meridional X-ray diffraction pattern of parchment (D-period = 65nm) and (b) the corresponding linear plot. The 6th and 9th diffraction orders of collagen have been indicated by arrows.

3.5.2 Wide-Angle Diffraction Pattern

Scattering at wide-angles provide information on structural features sub-nanometers in size. Two features detected in collagen at wide diffraction angles are the diffraction arising from the intermolecular spacing between triple helices and the helical rise per residue within the collagen triplex. A two-dimensional wide-angle X-ray diffraction pattern of parchment and the corresponding linear plot is shown in Figure 3.17.
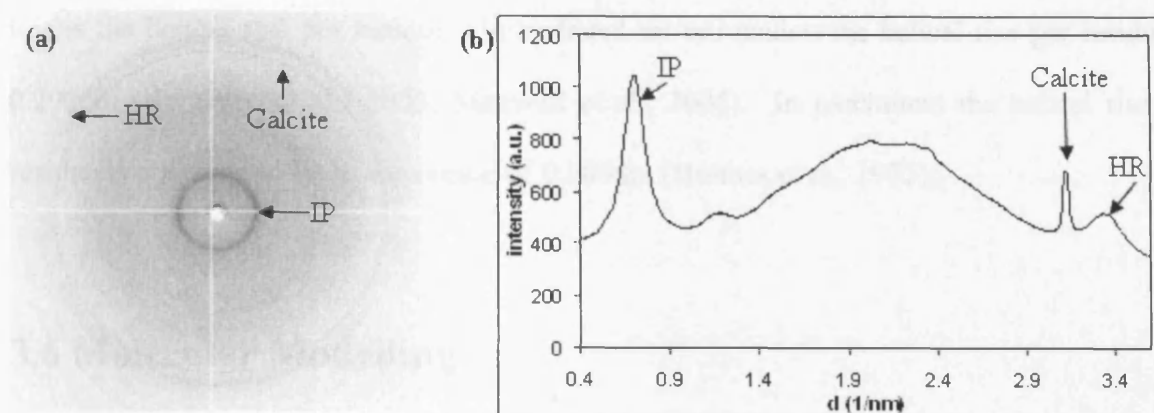
Figure 3.17: (a) A two-dimensional wide-angle X-ray diffraction pattern of parchment and (b) the corresponding linear plot. Arrows indicate the positions of the intermolecular packing (IP) and helical rise per residue (HR).

3.5.2.1 Intermolecular Packing of Collagen

A wide-angle X-ray diffraction pattern of collagen contains a reflection that arises from intermolecular lateral packing, i.e. the distance between collagen molecules within a fibril. The position of this reflection corresponds to the lateral separation of the molecules and in hydrated collagen is found in the region of approximately 1.2nm – 1.6nm, depending on the tissue (Maxwell et al., 2006). In hydrated parchment the intermolecular packing is observed at 1.5nm and in dry parchment it is seen at 1.2nm (Maxwell et al., 2006).

3.5.2.2 The Helical Rise per Residue of Collagen

A wide-angle X-ray diffraction pattern of collagen also contains a reflection that arises from the stepwise distance between amino acid residues along the axis of the collagen triple helix;

this is the helical rise per residue. In hydrated rat-tail tendon the helical rise per residue is 0.290nm (Kennedy et al., 2003; Maxwell et al., 2006). In parchment the helical rise per residue is observed to be in the region of 0.286nm (Hulmes et al., 1977).

3.6 Molecular Modelling

The technique of X-ray diffraction allows a number of different parameters to be extracted from the two-dimensional data. It is possible to build more complex structures if certain limitations and assumptions about the molecular structure can be made.

Molecular models have been used for many decades to interpret results acquired using experimental techniques, for instance X-ray diffraction. The data collected from X-ray diffraction can be used in conjunction with computer-aided model simulations to gain a better understanding of the molecular changes seen within collagen. When constructing molecular models it is important to be aware of their strengths and weaknesses, as no model can explain the results completely, they are simply interpretations of possible solutions. In order to construct molecular models to simulate X-ray diffraction patterns of collagen a series of parameters are essential. These include the amino acid sequence of the protein collagen and the scattering factor value for each amino acid residue.

3.6.1 Calculation of Amino Acid Scattering Factors

The amino acid sequences of the fibril forming collagen molecules used throughout this thesis were taken from a previous study (Hulmes et al., 1977). The molecular models were built using a series of amino acid X-ray scattering factors that were assigned for the

molecular sequence of type I collagen α1 and α2 chains. The scattering factors are an indication of how much an electron is scattered by an amino acid relative to water. The scattering factor is calculated using Equation 3.2, where f_n is the scattering factor, t_n is the total number of electrons, n is the residue, v_n is the total volume occupied by the residue and ρ is the electron density of water (0.33 electron/Å^3) (Hulmes et al., 1977).

$$f_n = t_n - \rho v_n$$

Equation 3.2

The calculated scattering factor values for all the amino acids are given in Table 3.4.

Amino Acid	Residue Volume ($Å^3$)	Scattering Factor
Tyr	209.8	16.766
Met	165.9	15.253
Lys	162.5	16.375
His	163.2	18.441
Pro	123.4	11.278
Gly	67.5	7.725
Hyp	127.2	10.995
Hyl	166.3	16.092
Arg	196.1	12.287
Glu	154.6	16.982
Asp	135.2	15.384
Gln	156.4	16.388
Asn	138.3	14.361
Ser	102.0	12.340
Thr	126.0	12.420
Phe	198.8	12.396
Val	138.4	8.328
Leu	163.4	8.078
Ala	91.5	7.805
Lle	162.6	8.342
Cys	114.4	17.340

Table 3.4: A list of amino acid residues including their corresponding volumes and scattering factors (Hulmes et al., 1977).

When constructing molecular models the scattering factors outlined in Table 3.4 were substituted into the amino acid sequence for type I collagen, where each amino acid residue was represented by its corresponding scattering factor (represented in Figure 3.18). The numerical values represent each amino acid within the Fourier transform calculations.
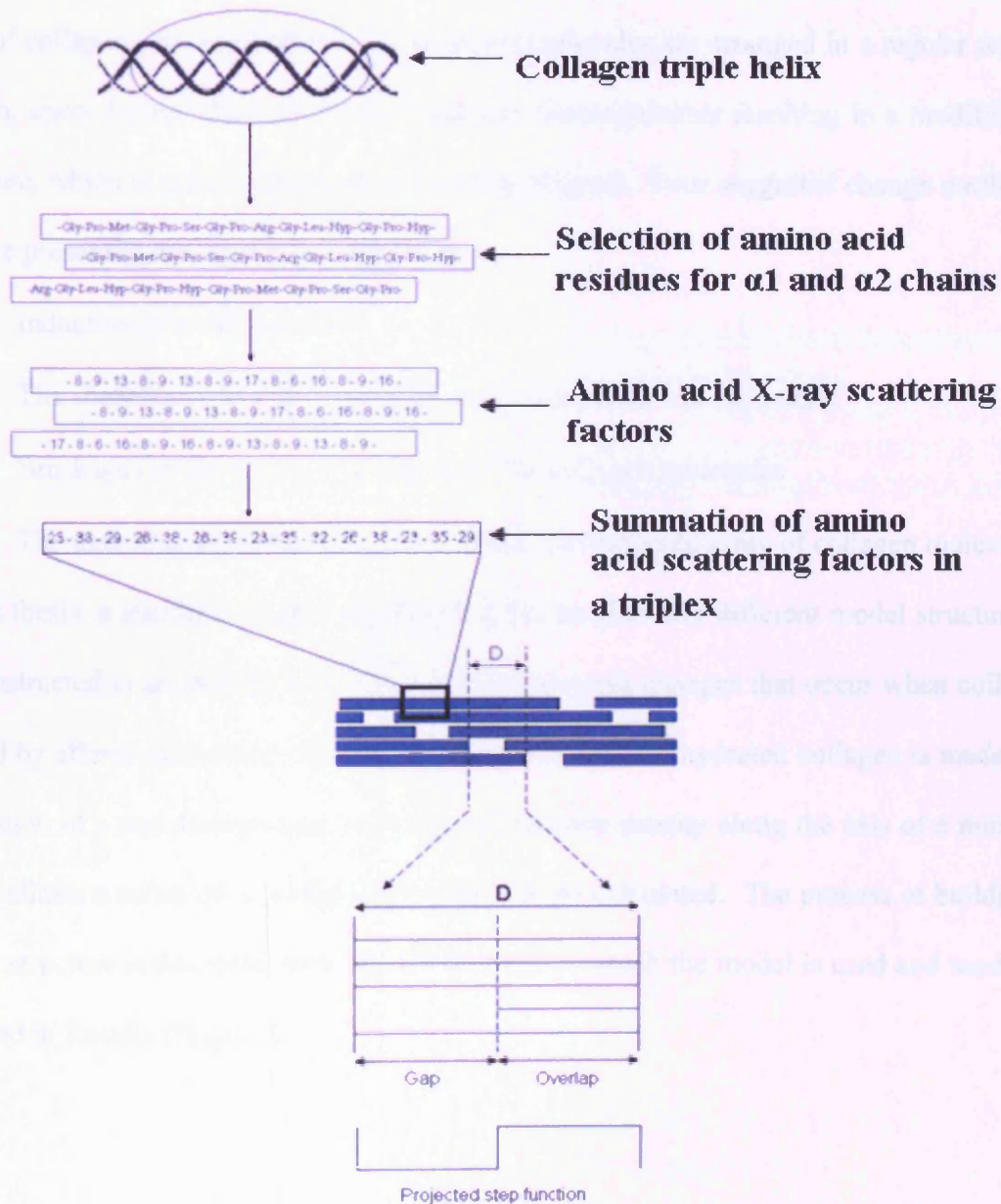
Figure 3.18: Demonstrates the construction from a section of the collagen amino acid sequence to the dynamic collagen model.

3.6.2 Model Structures

Previous computer simulated molecular models have been moderately successful in accounting for the hydrated state of collagen but no model has sufficiently explained the dry state of collagen. In a hydrated state, collagen molecules are arranged in a regular repeating pattern, upon drying, these molecules undergo rearrangements resulting in a modified axial structure, which is readily observed in the fibre diagram. Four suggested change mechanisms that are present in the drying of collagen are:

- Induction of local disorder

- The shearing of laterally adjoined molecules relative to each other

- Breakages in the amino acid chains of the collagen molecules

- The induction of molecular tilting within the staggered array of collagen molecules.

In this thesis, a standard model of hydrated collagen plus four different model structures will be constructed in an attempt to account for the principle changes that occur when collagen is altered by effects such as drying. The 'standard model' for hydrated collagen is made by the estimation of a one-dimensional projection of electron density along the axis of a microfibril which allows a series of meridional reflections to be calculated. The process of building this model structure is described here and the context in which the model is used and modified is reported in Results Chapter 6.

3.6.2.1 The standard model for hydrated collagen

To model a series of meridional reflections from an X-ray diffraction pattern for hydrated collagen it is necessary to simulate the projected electron density of the D-period repeat within the fibril. The projected electron density is Fourier inverted to obtain a series of intensities that correspond to the meridional reflections of the X-ray diffraction pattern. Figure 3.19 demonstrates the creation of a simulated electron density from a D-period collagen structure.
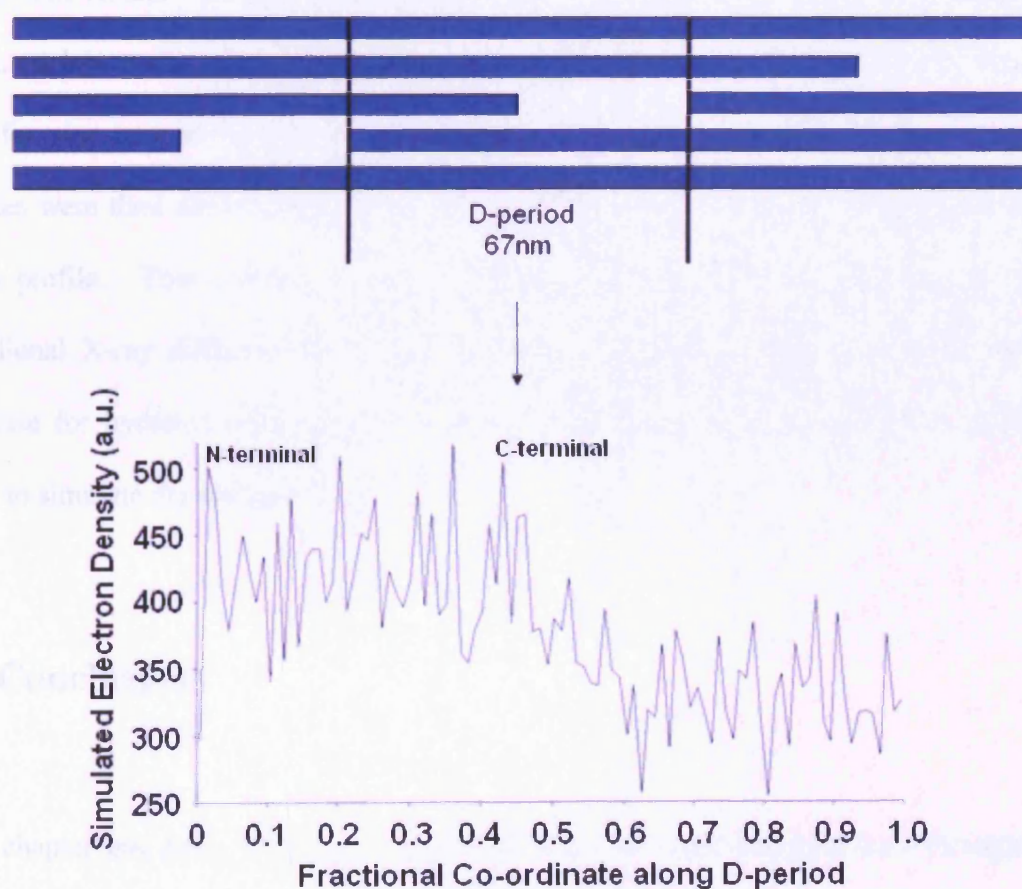
Figure 3.19: The creation of a simulated electron density from a D-period collagen structure. Each amino acid is substituted by its scattering factor from which the electron density is calculated. The electron density is Fourier transformed to produce a series of intensity values for the meridional reflections.

106

A detailed description of how the molecular models were constructed is given by Hulmes et al. (1977) (Haines, 1999; Kite and Thomson, 2006). The scattering density profile produced was used to create a series of axially projected structures. The number of amino acids in the repeating D-period unit of these structures could be varied. The series of produced structures are projected onto a one-dimensional profile exhibiting the characteristic gap and overlap features. The molecular model assumes the average axial rise per residue is fixed at 0.286nm. The models also accounted for the non-helical conformation of the telopeptide regions by using the structures calculated in more detail by a previous study (Orgel et al., 2000). The resultant structure was then Fourier transformed to give a set of structure factors. The model intensity terms were represented graphically as linear intensity profiles with a delta function intensity term at the corresponding reciprocal lattice point. The linear intensity profiles were then convolved with Gaussian profiles that mimicked the broadening due the beam profile. This structure can then be compared to observed linear profiles of the meridional X-ray diffraction data. Chapter 6 will investigate the strength of the model structure for hydrated collagen and study possible modification to the model structure in order to simulate dry collagen.

3.7 Conclusions

This chapter has given a background to the experimental techniques used throughout this thesis. The experimental details and set-ups of the X-ray stations used for the samples in this thesis were provided as well as information regarding data reduction software and the mathematical principles behind data reduction from two-dimensions to one-dimension. This Chapter introduced the technique of molecular modelling as well as providing the principles

behind the use of molecular models to explain X-ray diffraction data.

In the next chapter hydration and drying of parchment was investigated to determine the structural modification collagen undergoes within parchment in the presence or absence of water.

Chapter 4: An Investigation into the Influence of Hydration on the Structure of Collagen – An X-ray Diffraction Study

4.1 Introduction

The conservation and preservation of parchment aims to repair and elongate the lifespan of parchment documents. A wealth of different conservation techniques have been used, although some techniques have been shown to have a detrimental effect on the structural integrity of parchment. One technique used in the preparation of documents for display involves the application of water to parchment by a variety of processes (Woods, 1995). Although it is accepted by the conservation field that the addition of water can cause considerable damage to parchment, the exact effects are not well understood (Smit and Porck, 1995; Woods, 1995). Conservationists wish to understand in detail the damage these treatments cause, and whether the process is irreversible.

4.1.1 Previous investigations conducted on the hydrated and dry molecular structure of collagen

Many studies have been conducted on the hydrated and dry structure of collagen found in tendon (predominately type I collagen) but very few have investigated the hydrated and dry structure of collagen present in parchment (Hansen et al., 1992; Wess and Orgel, 2000;

Larsen, 2002). The native hydrated structure of tendon is found to contain a regular repeating structure with the characteristic 67nm axial D-period (Hodge and Petruska, 1963). On drying there is a reduction in the axial D-period of tendon from 67nm to 64nm (Wess and Orgel, 2000). It has been demonstrated that the axial D-period of skin is 65nm, this is shorter than tendon in the native hydrated state (Brodsky et al., 1980; Stinson and Sweeny, 1980; Menon, 2002). These values differ due to the presence of a mixture of type I and type III collagen within skin and parchment, which produce (by unknown mechanisms) a shorter axial D-period. It has been shown that, in some situations, the axial D-period of collagen may be altered by the processes involved with parchment production (Wess and Orgel, 2000; Maxwell et al., 2006). A study by Wess and Orgel (2000) of the changes in collagen structure which result from drying showed that the mean axial D-period for 12 historical parchment samples was 63.0nm (±0.8). The differences in the D-period between skin and parchment has been proposed to result from the additional treatments that parchment undergoes during manufacture (Smit and Porck, 1995; Woods, 1995; Haines, 1999; Kennedy and Wess, 2003; Maxwell et al., 2006). The manufacture of parchment from skin involves the addition of lime and water where the process of liming has been shown to reduce the axial D-period by approximately 1nm (Maxwell et al., 2006).

When parchment is folded or creased during storage, conservationists use the local application of water to the creases to relax and manipulate the parchment in order to flatten the documents. When hydrated parchment is allowed to air dry the water that exists between the fibres migrates to the surface of the parchment and evaporates (Hingley, 2001). It has been suggested that the loss of this water causes the fibres to "shorten and collapse onto each other". This statement has yet to be investigated from a structural and quantitative point of view. It is proposed that large structural changes similar to these make repairing water damage to parchment extremely difficult and time consuming. This chapter aims to quantify

this statement by investigating the effect of hydration and drying on the fibrillar structure of collagen. The difficulties involved with the reparation of water-damaged parchment have created a need to understand the changing collagen-water interactions that may cause damage. Parchment retains many hierarchical structural features found in skin. At each level, the interaction with water is critical to the structural integrity and survival in parchment. It is necessary to study the structural alterations at different levels of hierarchy, since the interaction with water covers a large number of length scales, from atomic-nanoscopic to macroscopic. This study uses X-ray diffraction to investigate how water and collagen interact within the preservation and conservation contexts of parchment records. This research seeks to study the scale at which irreversible damage occurs to attempt to help conservators understand the application of treatments in greater depth.

4.2 Experimental

4.2.1 Parchment Samples used in this study

During this investigation it has been vital to source a catalogue of parchment samples covering a wealth of different degradation states, from samples considered to be in good condition to samples considered to be in poor condition (both visually and structurally). This has proven extremely difficult, with most conservators unable to provide parchment samples for testing. The National Archives of Scotland (Edinburgh, U.K.) gifted the historical parchment samples used throughout this Chapter. Table 4.1 provides detailed information on these parchment samples including their year of use, size, number of sheets and any additional notes.

Year	Size	No. of sheets	Sample Name	Notes
1765	30cmx30cm	3	USH01	horny, folded parchment
1769	33cmx25cm	1	USH02	dirty/ coarse feel
1775	54cmx68cm	1	USH03	large folded sheet
1827	65cmx69cm	1	USH04	large folded sheet
1824	30cmx35cm	2	USH05	dirty/ rough feel
1832	25cmx35cm	6	USH06	polished
1828	49cmx36cm	1	USH07	polished
1765	41cmx13cm	1	USH10	small folded single sheet

Table 4.1: A detailed description of the parchment samples used in this Chapter.

This study was divided into two different sections shown in the flow diagram in Figure 4.1. The first stage of the study was to collect X-ray diffraction images from all the parchment samples outlined in Table 4.1; patterns were collected from the samples at a variety of different hydration levels. The dry state was the original status of the parchment at room conditions of 20°C (±2°C) and 50%RH (±5%RH). For the hydrated state, the parchment sample was fully immersed in distilled water until fully saturated. The air-dried state was achieved by allowing the hydrated sample to dry (with no tension applied) under standard room conditions of approximately 50%RH and 20°C. The process of wetting parchment and allowing the samples to return to the air-dried state allows the assessment of changes that may occur in terms of gelatinisation during wetting. This continual process of wetting and drying may advance the accumulative damage seen in parchment.

The second stage of the study involved the collection of X-ray diffraction images using parchment samples that were hydrated and allowed to air-dry, with diffraction patterns

recorded at 3 minutes intervals (a drying series experiment). The drying series experiment

was conducted on all parchment samples outlined in Table 4.1 as well as other collagen-

based tissues such as calf skin, rat-tail tendon and modern manufactured parchment.
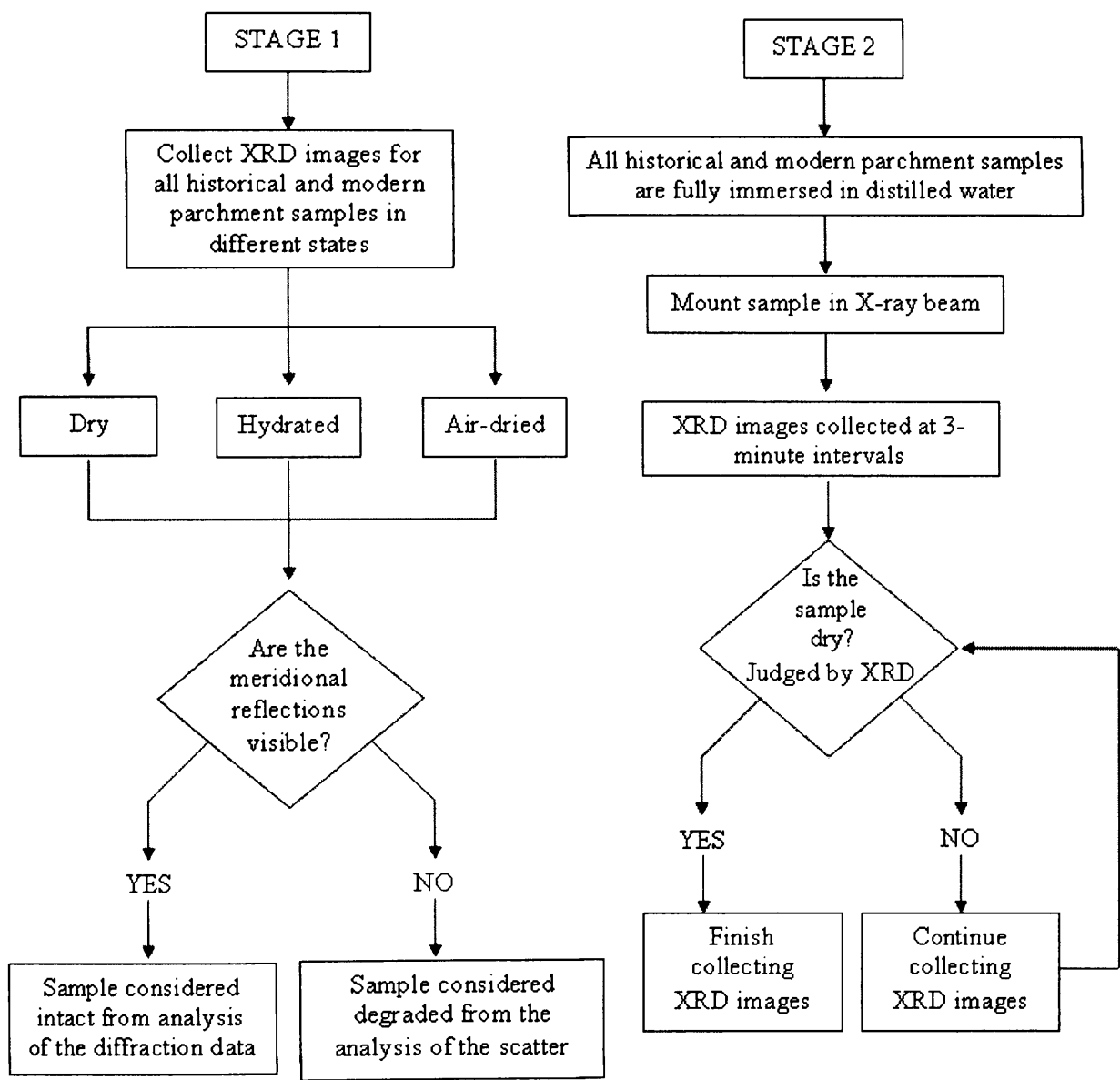
Figure 4.1: A flow diagram showing the key steps involved in the two stages of the study.

4.3 Results for dry, hydrated and air-dried parchment samples

X-ray diffraction data were obtained for the dry, hydrated and air-dried parchment samples outlined in Table 4.1. Structural hierarchies were investigated using two different beam lines; station 14.1 (WAXS) and station 2.1 (SAXS).

4.3.1 Wide-angle X-ray Scattering Data Analysis

Wide-angle X-ray scattering (WAXS) was employed to investigate the structure within and between collagen molecules. An example of a typical WAXS pattern from parchment can be seen in Figure 4.2, where the helical rise per residue (A), amorphous scattering (B) and intermolecular lateral packing (C) are indicated.
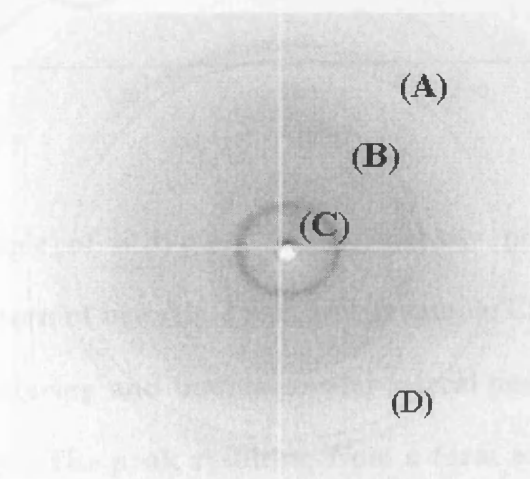
Figure 4.2: An example of a typical WAXS pattern from historical parchment sample USH01, where the helical rise per residue, amorphous scattering and intermolecular lateral packing are indicated as (A), (B) and (C) respectively. The reflection seen at 0.3nm (D) is due to the presence of calcite.

The key features in wide-angle X-ray scattering (WAXS) patterns for parchment are the reflections seen at 0.29nm and 1.2nm (Maxwell et al., 2006). The reflection seen at approximately 0.29nm relates to the helical rise per residue, which is the distance between the amino acid residues along the collagen molecular triple helices. The intermolecular lateral packing corresponds to the distance between one collagen molecule and its nearest neighbour, which is observed at a spacing of approximately 1/1.2nm. To allow for more detailed data analysis of these features, the WAXS patterns were converted to linear traces as shown in Figure 4.3.
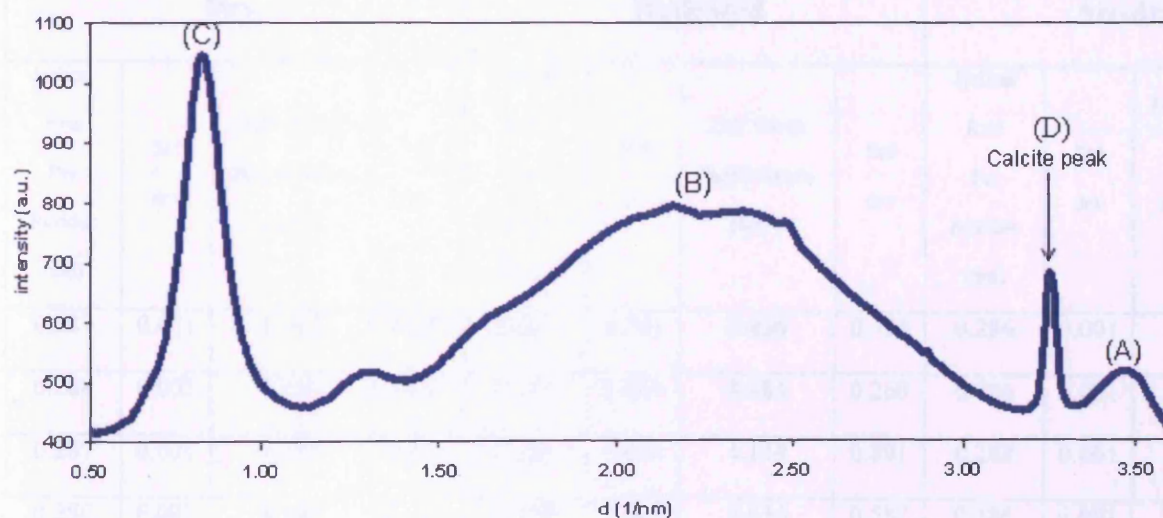
Figure 4.3: An example of a typical linear intensity profile taken from a two-dimensional WAXS pattern of historical parchment sample USH01. The helical rise per residue, amorphous scattering and intermolecular lateral packing are indicated as (A), (B) and (C) respectively. The peak resulting from a form of calcite is seen at 3.3nm^{-1} (D).

4.3.1.1 Analysis of the Helical Rise per Residue Peak

Peak (A) shown in Figure 4.2 and Figure 4.3 corresponds to the helical rise per residue. Peak fitting software PeakFit4 was used to determine the position of peak (A) and also the full width at half maximum (FWHM) value of the peak (explained in section 3.4.3). The beam profile is assumed to be the same throughout the experiment. The result of the peak fitting for all the dry, hydrated and air-dried historical parchment samples are shown in Table 4.2.

	Dry				Hydrated				Air-dried			
ples	Helical Rise Per Residue (nm)	Std dev	Full Width Half Maxima (nm⁻¹)	Std dev	Helical Rise Per Residue (nm)	Std dev	Full Width Half Maxima (nm⁻¹)	Std dev	Helical Rise Per Residue (nm)	Std dev	Full Width Half Maxima (nm⁻¹)	Std dev
H01	0.287	0.001	4.167	0.387	0.287	0.001	3.436	0.451	0.286	0.001	3.448	0.253
H02	0.288	0.001	4.016	0.512	0.288	0.001	3.484	0.268	0.286	0.001	4.274	0.439
H03	0.287	0.001	4.367	0.419	0.286	0.001	4.149	0.891	0.288	0.001	5.181	0.863
H04	0.286	0.001	4.149	0.341	0.289	0.003	3.636	0.587	0.286	0.001	5.814	0.346
H05	0.286	0.001	3.846	0.275	0.288	0.001	3.484	0.695	0.287	0.001	3.215	0.561
H06	0.282	0.002	12.821	3.284	0.282	0.002	3.012	0.986	0.283	0.001	9.804	2.584
H07	0.288	0.001	5.076	0.432	0.288	0.001	4.098	0.252	0.285	0.002	3.484	0.797
H10	0.287	0.001	4.001	0.601	0.287	0.001	3.703	0.314	0.286	0.001	3.247	0.620

Table 4.2: The position and FWHM for the helical rise per residue peak of all dry, hydrated and air-dried historical parchment samples.

As shown in Table 4.2, the peak position of the helical rise per residue remains constant and unaffected for the historical parchment samples whether dry, hydrated or air-dried. Variation is however seen in the helical rise per residue between each parchment sample. This implies

116

that each parchment sample is different from the next and enforces the theory that parchment

is a heterogeneous material and sample to sample variation is significant.

4.3.1.2 Analysis of the Intermolecular Lateral Packing Peak

Peak (C) shown in Figure 4.2 and Figure 4.3 corresponds to the collagen intermolecular

lateral packing which is the distance between one collagen molecule and its nearest

neighbour. The peak position and the FWHM for the intermolecular lateral packing for all

dry, hydrated and air-dried parchment samples are shown in Table 4.3.

ples	Dry				Hydrated				Air-dried			
	Intermolecular lateral packing (nm)	Std dev	Full Width Half Maxima (nm⁻¹)	Std dev	Intermolecular lateral packing (nm)	Std dev	Full Width Half Maxima (nm⁻¹)	Std dev	Intermolecular lateral packing (nm)	Std dev	Full Width Half Maxima (nm⁻¹)	Std d
01	1.195	0.005	4.608	0.405	1.526	0.007	3.257	0.612	1.237	0.006	5.405	0.66
02	1.195	0.003	3.922	0.736	1.518	0.004	4.504	0.496	1.253	0.004	4.651	0.48
03	1.190	0.007	4.367	0.491	1.534	0.009	4.854	0.395	1.237	0.006	5.814	0.77
04	1.205	0.006	3.690	0.824	1.584	0.005	4.854	0.762	1.242	0.008	7.576	0.46
05	1.185	0.007	4.695	0.532	1.584	0.004	4.367	0.621	1.246	0.008	4.831	0.85
06	1.181	0.005	6.944	0.994	1.550	0.008	3.300	0.846	1.235	0.009	6.250	0.70
07	1.205	0.008	5.814	0.671	1.575	0.010	2.725	1.005	1.232	0.100	5.263	0.94
10	1.190	0.004	5.076	0.598	1.534	0.006	3.704	0.680	1.236	0.006	6.173	0.52

Table 4.3: The position and FWHM for the collagen intermolecular lateral packing of all dry, hydrated and air-dried historical parchment samples.

Table 4.3 shows that the collagen intermolecular lateral packing is approximately 1.2nm for all historical parchment samples used in this study in a dry state. Once hydrated the collagen intermolecular lateral packing increases to approximately 1.55nm and decreases when air-dried to approximately 1.24nm. In comparison, a slight increase can be observed in the intermolecular lateral packing reflection for the samples that have been air-dried. This may result from residual moisture in the structure or form the opportunity for molecular rearrangements to occur and gravitate towards an optimal interaction distance.

4.3.1.3 Ratio of the Intermolecular Lateral Packing compared to the Amorphous Scatter

Peak (B) shown in Figure 4.3 and Figure 4.4 corresponds to the amorphous scattering peak that arises from the scatter that results from gelatin, water and other non-collagenous materials. Gelatinisation is caused by a loss of structural order within collagen due to unfolding of the molecules (Weiner et al., 1980; Kennedy et al., 2004a). It is possible to calculate a ratio of collagen to amorphous content from the samples by dividing the integrated intensity of the intermolecular lateral packing peak (C) by the integrated intensity of the amorphous scatter peak (B) (Hodge and Petruska, 1963). This ratio does not give an absolute measure of the amount of collagen or gelatin in the sample, but does provide a means to compare changes between samples.

Table 4.4 shows the ratio for the intermolecular lateral packing compared to the amorphous scatter for the dry, hydrated and air-dried historical parchment samples where the beam profile is assumed to be the same throughout the experiment. The ratios for the dry samples detailed in Table 4.4 are between 0.159 (for USH06) and 0.325 (for USH02). In comparison,

the ratio for the hydrated samples is between 0.106 (for USH04) and 0.373 (for USH07). For the air-dried samples the ratio is between 0.076 (for USH10) and 0.308 (for USH06). Upon hydration the ratio was found to increase for all parchment samples except USH02, USH03 and USH04. When comparing the dry state with the air-dried state the collagen/amorphous ratio is found to decrease for all parchment samples except USH06, where the collagen/amorphous ratio has increased after hydration and air-drying. All these findings seem to enforce the proposed idea that all parchment reacts differently to the addition and removal of water.

Historical Parchment Samples	Collagen / Amorphous ratio					
	Dry	Std dev	Hydrated	Std dev	Air-dried	Std dev
USH01	0.214	0.071	0.330	0.042	0.199	0.063
USH02	0.325	0.098	0.162	0.058	0.198	0.081
USH03	0.254	0.064	0.201	0.052	0.195	0.059
USH04	0.250	0.053	0.106	0.086	0.160	0.067
USH05	0.200	0.075	0.207	0.064	0.193	0.050
USH06	0.159	0.069	0.299	0.070	0.308	0.088
USH07	0.164	0.092	0.373	0.091	0.163	0.073
USH10	0.195	0.055	0.257	0.054	0.076	0.066

Table 4.4: Ratio for the intermolecular lateral packing compared to the amorphous scatter for the dry, hydrated and air-dried parchment samples. This ratio is calculated by dividing the integrated intensity of the peaks that represent the collagen intermolecular lateral packing and the amorphous scatter.

4.3.2 Small-angle X-ray Scattering Data Analysis

Small-angle X-ray scattering (SAXS) was utilised to investigate the long-range interactions resulting from the axial order of the structure. Two typical SAXS patterns from a dry and a hydrated parchment sample (USH01) can be seen in Figure 4.4, where the fifth, sixth and ninth axial orders of collagen diffraction are indicated as (5), (6) and (9) respectively.
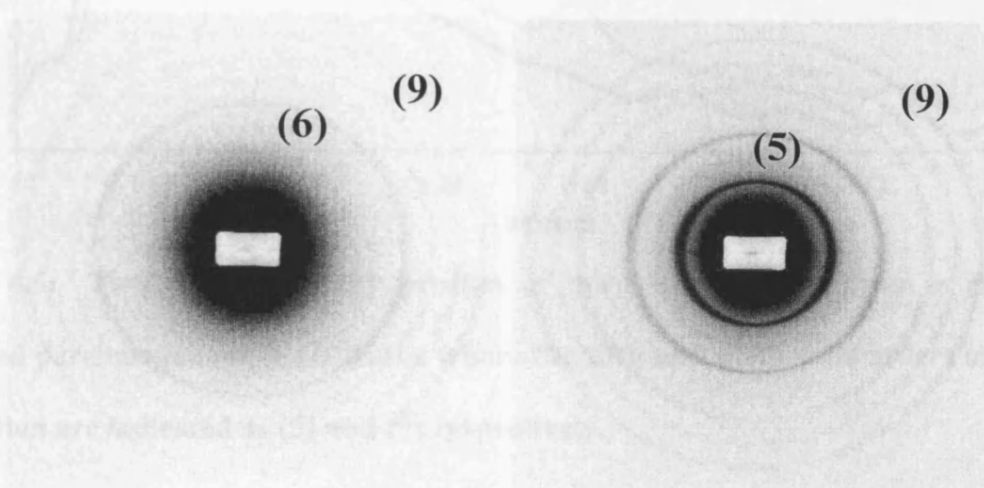
Figure 4.4: Two typical two-dimensional SAXS patterns from a dry (image on left) and a hydrated (image on right) historical parchment sample (USH01), where the fifth, sixth and ninth axial orders of collagen diffraction are indicated as (5), (6) and (9) respectively.

These sharp reflections can be used to determine a change in the D-period of the collagen molecules as the variation in electron density in the axial direction. A useful indicator of sample hydration can be obtained from the reflection intensities, where a strong fifth order of collagen axial diffraction indicates a high level of hydration while a strong sixth order of collagen axial diffraction indicates dehydration as shown in Figure 4.4 and Figure 4.5.
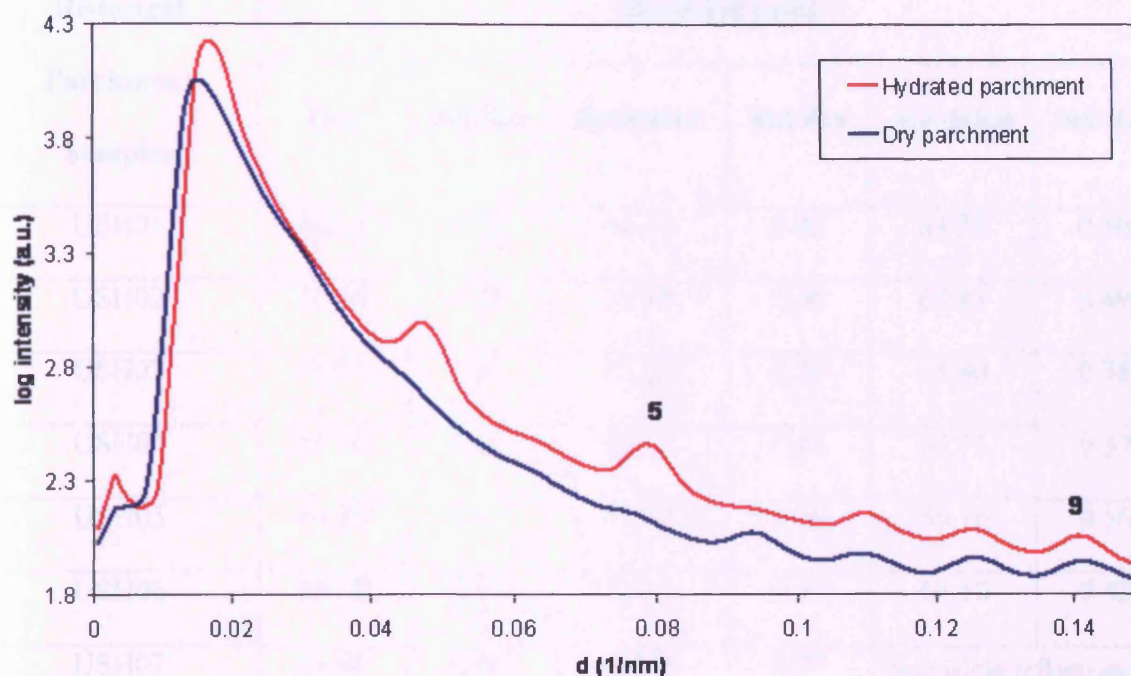
Figure 4.5: **Two linear intensity profiles of the SAXS patterns from a dry and a hydrated parchment sample (USH01), where the fifth and ninth axial orders of collagen diffraction are indicated as (5) and (9) respectively.**

Changes to the axial D-period have been listed in Table 4.5 for all dry, hydrated and air-dried parchment samples.

Historical Parchment Samples	D-period (nm)					
	Dry	Std dev	Hydrated	Std dev	Air-dried	Std dev
USH01	63.84	0.28	64.30	0.43	63.39	0.30
USH02	65.84	0.40	65.98	0.56	65.41	0.49
USH03	64.77	0.38	65.22	0.29	64.80	0.38
USH04	65.30	0.26	65.75	0.41	63.75	0.32
USH05	64.80	0.45	65.27	0.60	64.16	0.56
USH06	64.48	0.31	65.16	0.37	64.50	0.42
USH07	64.80	0.62	63.29	0.77	No visible reflections in 2D or 1D	
USH10	64.29	0.38	65.27	0.44	61.08	0.55

Table 4.5: D-period for all dry, hydrated and air-dried historical parchment samples. For sample USH07 there were no visible reflections in the air-dried state making it not possible to calculate the D-period. The absence of reflections for USH07 may result from a loss of collagen molecular structure after wetting and drying.

For historical parchment samples USH01, USH02, USH03, USH04, USH05, USH06 and USH10, the D-period increased when moving from the dry state to the hydrated state. For historical parchment sample USH07, the D-period decreased when moving from the dry state to the hydrated state. When all hydrated samples were allowed to air dry, the D-period calculated from the samples was found to decrease. Sample USH07 showed the presence of no meridional reflections from which to calculate the D-period for the air-dried sample. This implies that there was a loss of fibrillar structure for sample USH07. Overall, sample USH07 appeared to behave differently to all the other samples investigated.

4.4 Results for Drying Series Samples

In addition to the collection of X-ray diffraction patterns from historical parchment samples in a dry, hydrated and air-dried state, an *in-situ* drying series study was completed. Historical parchment samples and other collagen-based tissues were fully hydrated and allowed to air dry while diffraction patterns were recorded at 3-minute intervals (the beam position was fixed during the experiment). Small-angle X-ray diffraction patterns were collected at the SRS Daresbury Synchrotron on station 2.1. Historical parchment samples outlined in Table 4.1 were used in the drying series study. In addition to historical parchment samples, a modern parchment sample was also investigated.

Figure 4.6 displays X-ray diffraction images for the parchment sample USH01 during the transition from the hydrated state to the dry state. From this figure, it can be observed that as the parchment dried, the fifth order of diffraction weakened and the sixth order of diffraction became more prominent, which is highlighted on the two-dimensional images. This phenomenon was observed for all historical parchment samples.

HYDRATED 3 MIN **HYDRATED 30 MIN** **HYDRATED 60 MIN**

HYDRATED 90 MIN **HYDRATED 120 MIN** **DRY**
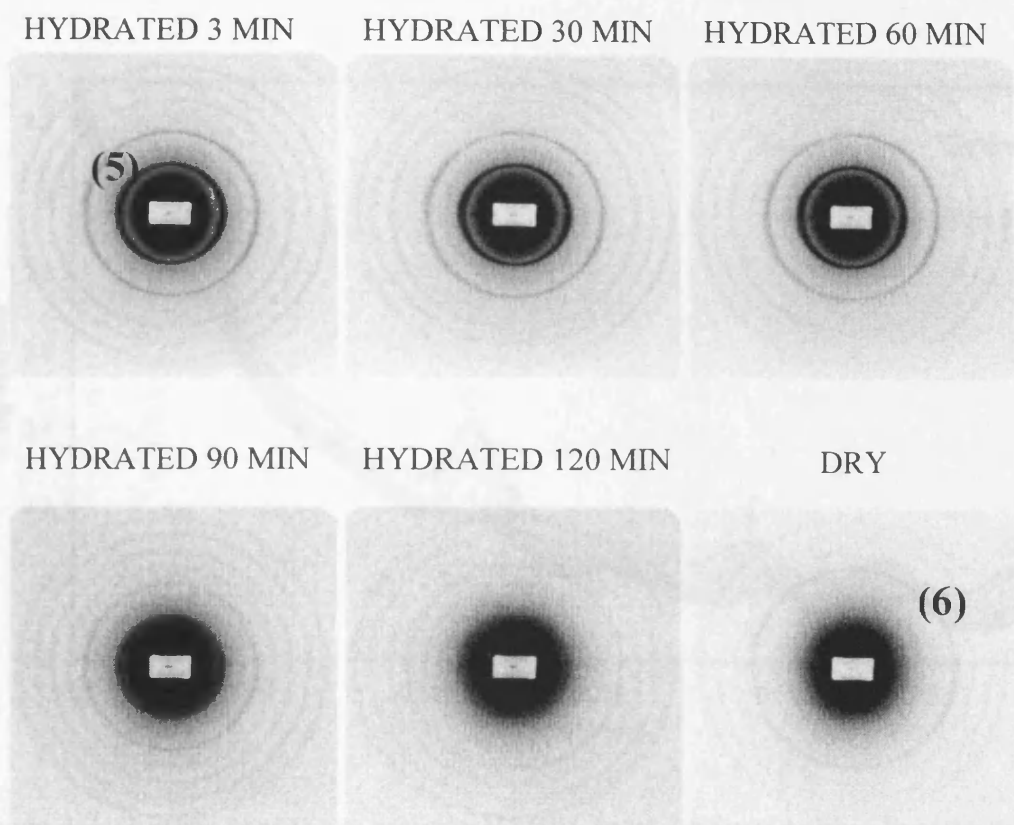
Figure 4.6: Composite of X-ray diffraction images for the drying series of parchment sample USH01. The images show the stages between hydrated and dry, a decreasing level of hydration is seen from top left to bottom right. Working from the top left the X-ray diffraction images are taken at 3, 30, 60, 90, 120 minutes and the final frame is a dry sample (before wetting).

Linear traces have been produced for all parchment samples used in this study and have been smoothed to remove noise fluctuations from the traces. Figure 4.7 shows the linear traces for sample USH01 showing the third to ninth orders of collagen axial diffraction. The decrease in the intensity of the fifth order and the increase in the intensity of the sixth order are seen in the linear traces. It can also be seen that on drying a shift in the peak positions to a higher value of d (1/nm) occurred, corresponding to a decrease in the D-period.
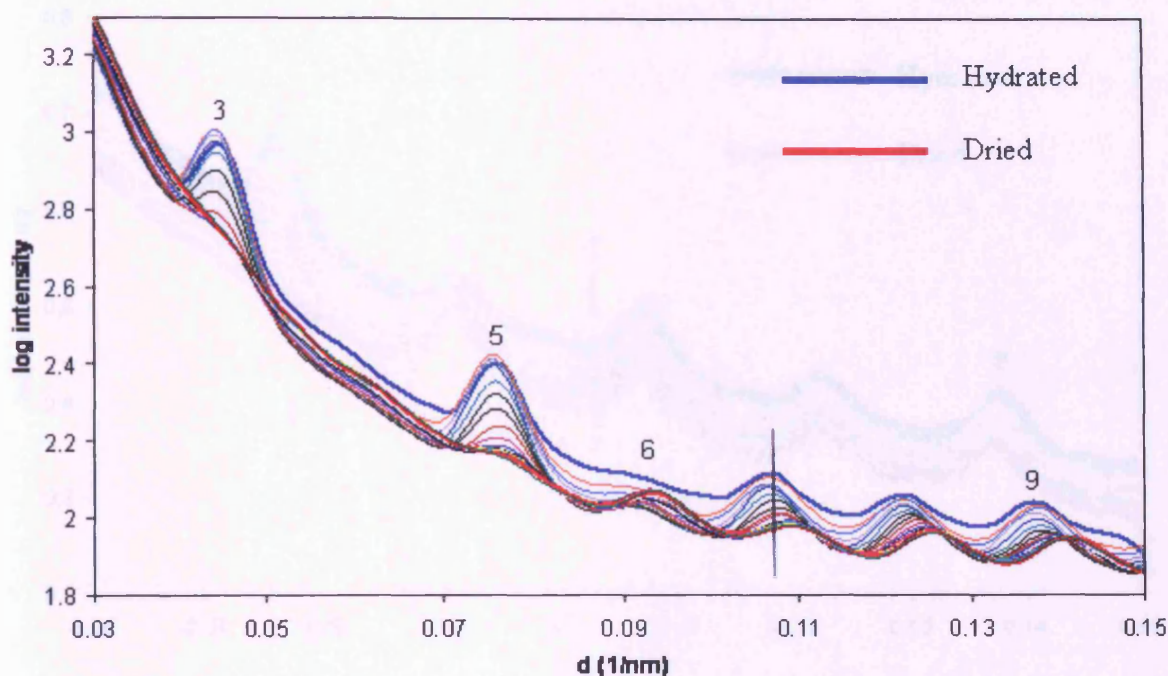
Figure 4.7: Linear traces for sample USH01 from hydrated (blue line) to dry (red line) showing the third to ninth orders of collagen axial diffraction. The fifth, sixth and ninth orders of collagen diffraction are highlighted as (5), (6) and (9) respectively.

Figure 4.8 shows the linear traces for sample USH02 showing the third to ninth orders of collagen axial diffraction. A decrease in the intensity of the fifth order and an increase in the intensity of the sixth order are evident, displaying the same behaviour as sample USH01 shown in Figure 4.7.
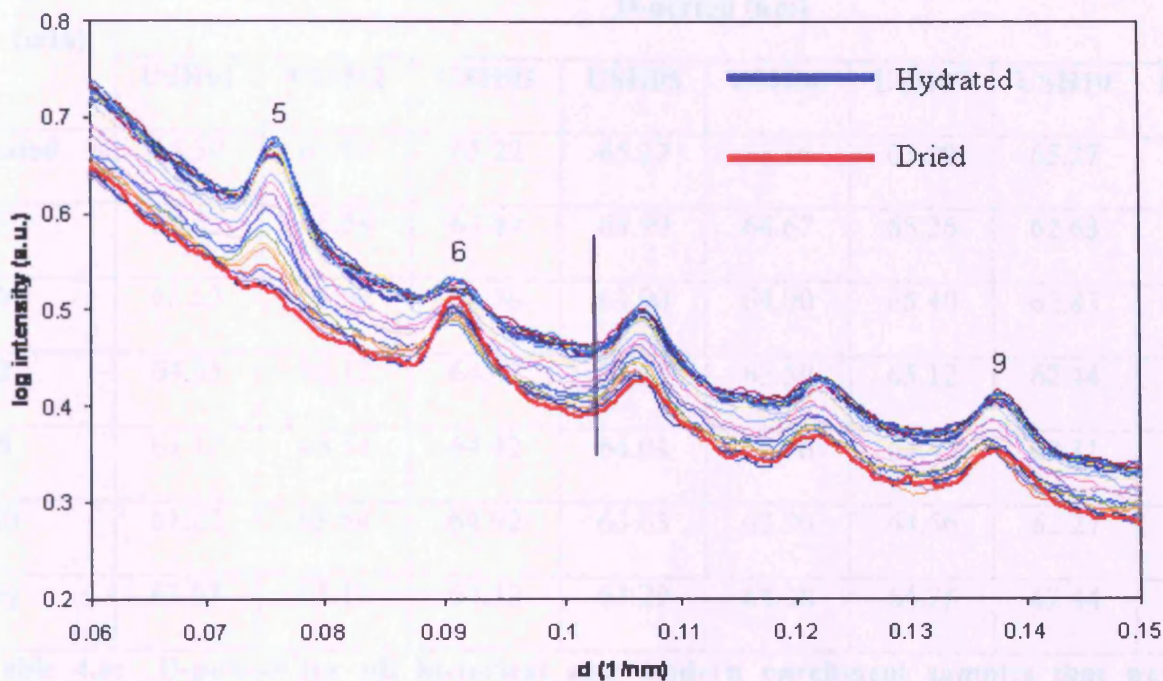
Figure 4.8: Linear traces for sample USH02 from hydrated (blue line) to dry (red line) showing the fifth to ninth orders of collagen axial diffraction. The fifth, sixth and ninth orders of collagen diffraction are highlighted as (5), (6) and (9) respectively.

Table 4.6 includes the calculated D-period values for all historical parchment samples and the modern parchment sample. The D-periods for the hydrated and dry samples are included as well as the D-period at the intervals 3, 30, 60, 90 and 120 minutes after hydration.

Time (min)	D-period (nm)							
	USH01	USH02	USH03	USH05	USH06	USH07	USH10	Modern
Hydrated	64.30	65.98	65.22	65.27	65.16	63.29	65.27	65.12
3	64.39	65.54	64.84	63.90	64.67	65.26	62.63	64.98
30	63.53	65.52	64.70	63.90	64.00	65.40	62.83	64.98
60	64.33	66.12	64.42	64.31	63.59	65.12	62.44	65.26
90	61.17	65.54	64.42	64.04	63.76	64.42	62.31	65.40
120	61.22	65.54	64.92	63.63	63.90	64.56	62.27	64.84
Dry	63.67	65.11	64.32	63.29	64.38	64.75	62.44	64.56

Table 4.6: D-period for all historical and modern parchment samples that were hydrated and allowed to air-dry while a series of X-ray diffraction images were collected. The D-periods for the samples hydrated and dry are included as well as the D-period at the intervals 3, 30, 60, 90 and 120 minutes after hydration.

The D-period for all parchment samples was found to decrease as they dried to near their D-period value for the dry state. An initial increase in the D-period was also seen on drying. This increase is shown in Figure 4.9 where the D-period is plotted as a function of time for all parchment samples where all graphs are plotted using the same y-axis (from 60.5nm to 66.5nm). This allows the variation in the D-period between parchment samples to be observed. Figure 4.10 shows the same data as Figure 4.9 but plotted on varying y-axes allowing the patterns in the D-period for each individual sample to be observed.
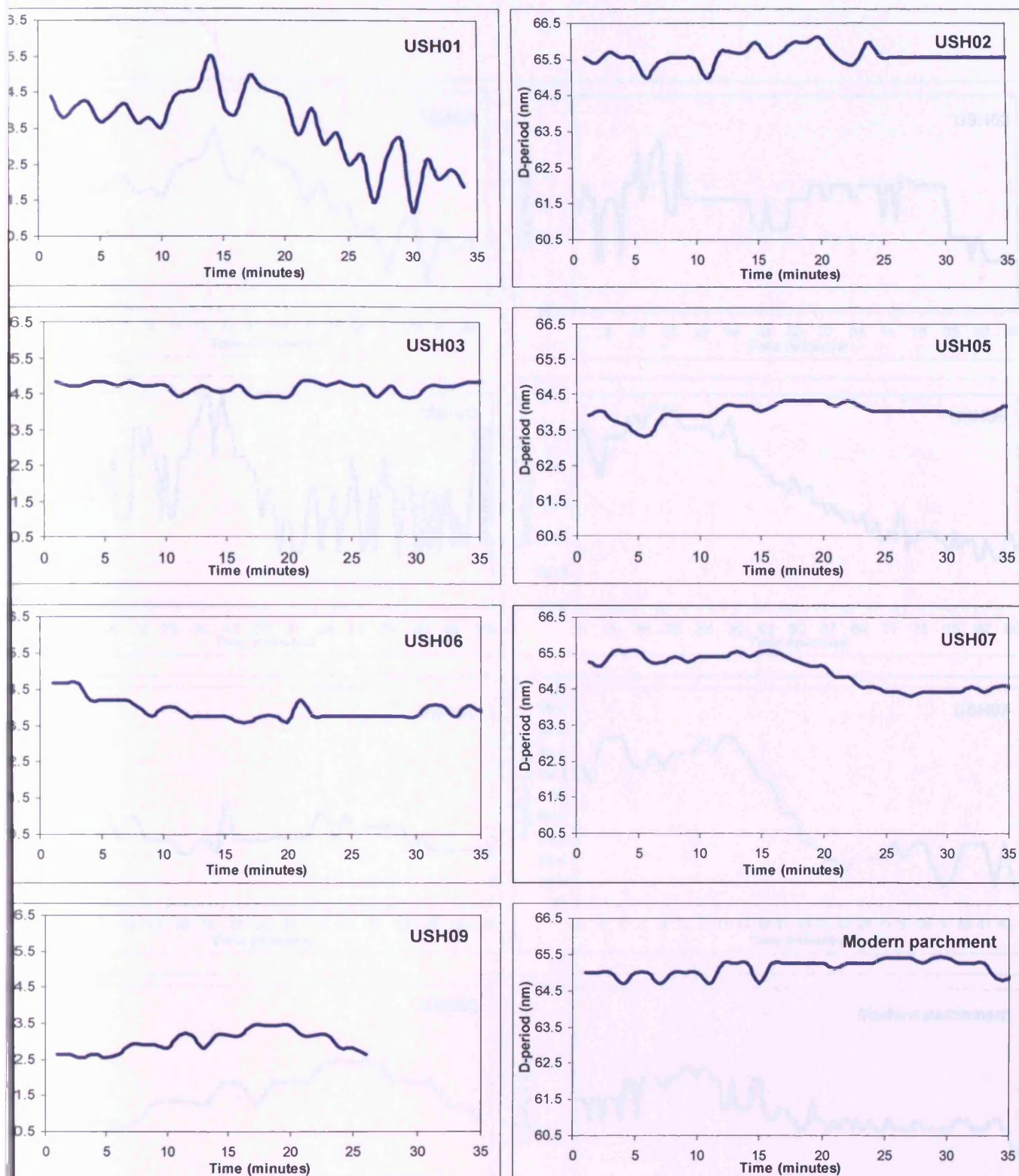
Figure 4.9: The D-period as a function of drying time for all parchment samples that were hydrated and allowed to dry. The x-axis and y-axis are plotted on the same scales for all samples (from 60.5nm to 66.5nm and 0 minutes to 35 minutes).

128
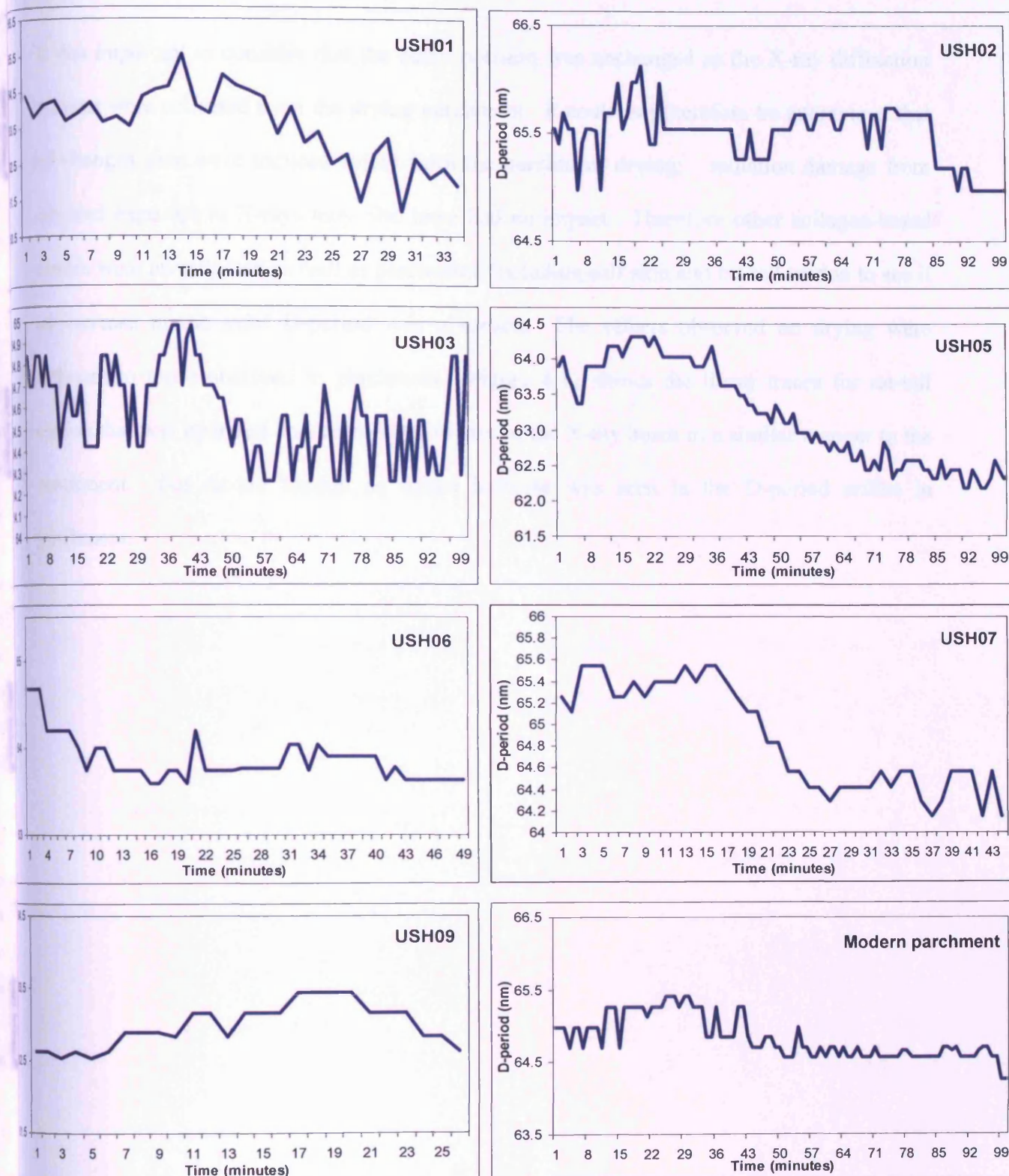
Figure 4.10: The D-period as a function of drying time for all parchment samples that were hydrated and allowed to dry. The x-axis and y-axis are plotted on different scales for all samples.

It was important to consider that the beam position was unchanged as the X-ray diffraction patterns were collected from the drying parchment. It could not therefore be guaranteed that all changes seen were induced solely from the parchment drying; radiation damage from elevated exposure to X-rays may also have had an impact. Therefore other collagen-based tissues were investigated as well as parchment, including calf skin and rat-tail tendon to see if an increase in the axial D-period was observed. The effects observed on drying were different to those observed in parchment. Figure 4.11 shows the linear traces for rat-tail tendon that was hydrated and allowed to air-dry in the X-ray beam in a similar manner to the parchment. For rat-tail tendon no initial increase was seen in the D-period unlike in parchment.
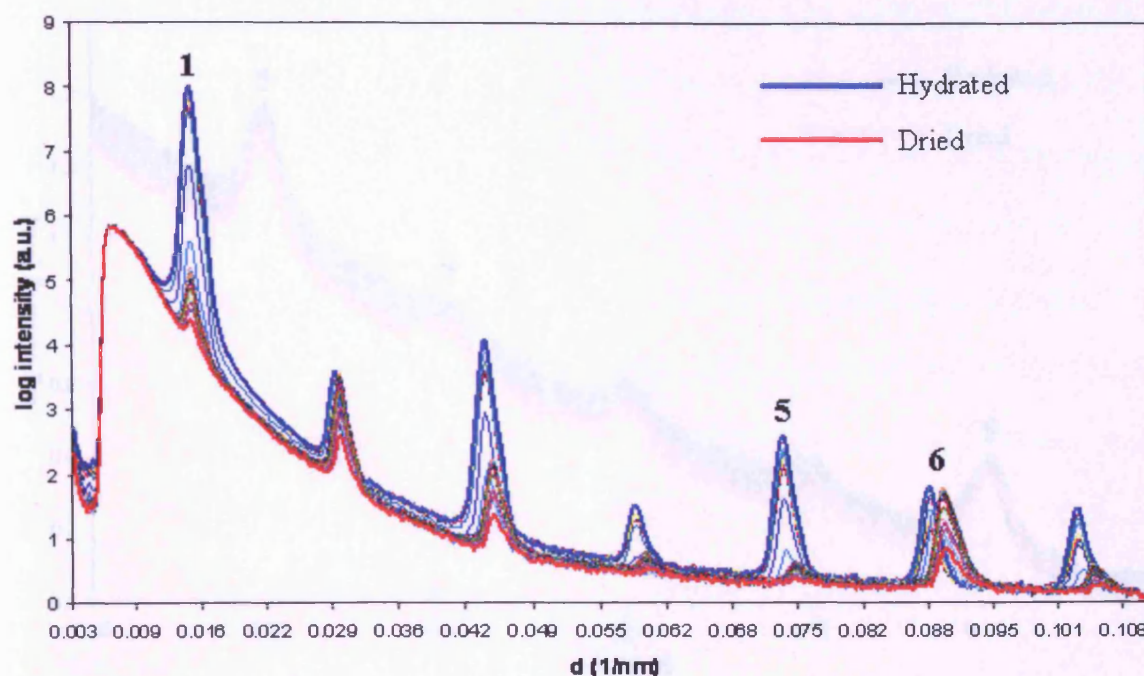
Figure 4.11: Linear traces for rat-tail tendon from hydrated (blue line) to dry (red line) showing the first to seventh orders of collagen axial diffraction. The first, fifth and sixth orders of collagen diffraction are highlighted as (1), (5) and (6) respectively.

In addition to rat-tail tendon, calf skin was also investigated. The linear traces for skin from the hydrated state to the dried state are shown in Figure 4.12. Once again no initial increase was observed in the D-period.

Figure 4.12: Linear traces for skin from hydrated (blue line) to dry (red line) showing the fifth to sixth orders of collagen axial diffraction. The fifth, sixth and ninth orders of collagen diffraction are highlighted as (5), (6) and (9) respectively.

4.5 Discussion

4.5.1 Dry, hydrated and air-dried parchment samples

4.5.1.1 The effect of hydration and air-drying at a molecular level

Results showed that hydration and air-drying has little effect on the helical rise per residue in parchment. The helical rise per residue was found to be constant between 0.282nm and 0.289nm depending on the parchment sample. This is in agreement with other sources that

132

have calculated the helical rise per residue in parchment to be 0.290nm (Maxwell et al., 2006). However, the increase in the peak width after hydration (compared with the dry sample) indicates changes at a molecular level. This broadening may be a product of a decrease in finite crystallite size, or an increase in local disorder, or a combination of the two. The peak width was found to decrease in most samples on air-drying to a value similar to the peak width for the original dry sample. Three samples (USH05, USH07 and USH10) showed an increase in the peak width when compared with both the dry and hydrated sample. Overall, although the helical rise per residue remained constant, the alteration in the peak width may be indicative of a variation at a molecular level, such as breakages in the collagen helix leading to localised relaxation in the structure.

4.5.1.2 The effect of hydration and air-drying on molecular interactions

Previous studies have reported the intermolecular lateral packing in dry parchment to be 1.2nm (Maxwell et al., 2006), however no value for hydrated parchment has been reported. In this study, hydration was found to increase the intermolecular lateral packing in all samples from approximately 1.2nm in the dry state to approximately 1.55nm in the hydrated state. This increase in spacing between the collagen molecules indicates the presence of additional water molecules between the collagen molecules within the fibril causing expansion between the molecules. On drying, the intermolecular lateral packing reflection decreased to approximately 1.24nm due to the loss of water molecules from within the fibrils. The intermolecular lateral packing reflection for the hydrated state did not to return on drying to a similar value for the intermolecular lateral packing of dry collagen. This may have been a consequence of incomplete air-drying of the parchment samples. An increase in the intermolecular lateral packing peak width for most samples from the dry state to the hydrated

state was observed, demonstrating an increase in local disorder. The peak width decreased on air-drying.

It is proposed that the addition and removal of water molecules within a fibril may cause degradation of the parchment. Over time, this repetitive movement induced by the addition and removal of water molecules within a fibril, results in an increase in disorder causing permanent damage and loss of structure.

4.5.1.3 The effect of hydration and air-drying on the axial structure (D-period)

Previous studies have shown that the D-period of parchment varies greatly from sample to sample and is heavily dependent on a number of factors. These include the type of animal skin from which the parchment was made, and the processes and methods involved in parchment manufacture and storage (Wess and Orgel, 2000; Maxwell et al., 2006). The average D-period that has been reported for parchment is approximately 63nm in the dry state and 65.5nm in the hydrated state (Wess and Orgel, 2000; Maxwell et al., 2006). Results from this study showed an increase in the D-period upon the hydration of dry parchment samples. When the hydrated samples were air-dried, the D-period was observed to decrease. The reduction in the D-period on air-drying could result from tilting and breaking of amino acid chains as discussed in section 1.2.8. It is proposed that on drying the collagen molecules experience an increase in intermolecular local tension, giving rise to a breakage of amino acid chains, as well as the collapse and tilting of collagen molecules. It is postulated that the continuous induction of strain in the axial structure could be the basis for irreversible damage.

4.5.2 Drying series samples

The previous experiment investigated the effect of hydration and air-drying on the structure of collagen present in a range of different parchment samples. This gave an insight into the structure in a dry, hydrated and air-dried state but did not provide any information on the transition from hydrated to air-dry. Therefore, a drying series experiment was proposed to investigate the structure of hydrated collagen as it dries.

4.5.2.1 The effect on the axial structure (D-period) during the transition from the hydrated to air-dried state

Results showed a decrease in the D-period for all parchment samples when hydrated and allowed to air-dry. This reduction in the D-period could indicate that during this transition the collagen molecules may move past each other causing an alteration in the quarter-staggered arrangement of the collagen molecules. A variety of alterations may occur including titling or breaking of the collagen molecules. Chapter 6 investigates these modifications in the collagen structure by the use of computer-aided molecular models. As well as the reduction in D-period, an initial increase in the D-period was observed in the samples USH01, USH03, USH05, USH07, USH09 and the modern parchment sample. This effect has not been previously observed.

It is hypothesised that the initial increase in D-period was due to a local increase in the tension of the collagen fibrils during the drying process. It is possible that this type of internal strain could result in irreversible damage to the parchment. The other collagen-based tissues investigated (tendon and skin) showed a decrease in the axial D-period on drying, and

no initial increase in the D-period, as observed in parchment.

4.5.3 Conclusions

Overall, this study indicated that parchment is a heterogeneous material, with each sample reacting in a different way to hydration and air drying. It has shown that parchment is complex and inconsistent, as each sample differs physically from the next. At present conservators often treat all parchment samples as a homogeneous material. Frequently parchment samples are stored under the same conditions and undergo identical treatments. However, this study has underlined the potential need to treat each parchment as an individual item as well as to store and conserve each parchment on an individual basis.

This Chapter has highlighted the need for a larger investigation into how different parchments react to hydration and air-drying. One possible future experiment would be to include more degraded parchments in a much greater sample set.

Overall, this Chapter has shown that X-ray diffraction has proven to be a valuable investigative technique, assisting in the detailed analysis of the collagen structure at various hierarchical levels. This study into hydrated, dry and air-dried parchment has shown that there is a potential need to investigate the effect of relative humidity on parchment. This Chapter provided a platform from which the effect of relative humidity on parchment can be addressed in Chapter 5.

Chapter 5: The Effect of Relative Humidity on the Structural Integrity of Parchment

5.1 Introduction

The structural dynamics of collagen that may lead to its deterioration and the subsequent macroscopic fatigue and brittleness of parchment can be attributed to a range of factors, including inappropriate temperature levels, an unsuitable relative humidity range, mechanical damage, radiation damage and bacterial/fungal growth (Kennedy et al., 2004c). An important factor which is relatively unstudied is the effect of relative humidity (RH) on parchment. High humidity conditions can trigger microbiological growth on the surface of parchment, while low humidity conditions cause the collagen fibres to shrink and harden (Hansen et al., 1992). After centuries of exposure to the fluctuating humidity conditions, often found in collections, it is possible for parchment samples to present significant visual damage. As technology allows us to become more adept at identifying changes in parchment structure at a number of hierarchical levels, we are able to investigate the changes that are critical to long-term survival/deterioration of parchment and allow us to inform conservation from a firm science based approach.

At present, our understanding of how RH misuse affects the structural integrity of historical parchment is qualitative and limited (Hansen et al., 1992; Woods, 1995). A more detailed model of collagen behaviour is required to explain the structural rearrangements that occur in the molecular packing of collagen at various levels of RH. Storage recommendations for parchment seem to vary greatly, with a number of different research reports suggesting an

environment with a variety of ranges of RH as discussed in Chapter 1.

X-ray diffraction is a non-invasive technique that can be utilised to measure changes at different structural levels of the collagen hierarchy. In this study, X-ray diffraction is used to investigate the structural integrity of the collagen within parchment to assess the effect of different levels of RH. Two separate studies have been conducted, the first looking at the effect of a range of fixed humidity levels on a number of different parchment samples, and the second investigating the effect of humidity cycling on the collagen integrity of three scrolls that have been subjected to varying humidity conditions for 6 months.

5.2 Experimental

5.2.1 Parchment Sample preparation

5.2.1.1 Parchment stored at a fixed humidity level

A series of modern and historical parchment samples in varying condition were used in this study. The historical parchment samples donated by the National Archives of Scotland (NAS) have been judged to be in an intact state (both visually and structurally) by conservators at NAS. In addition to these intact samples, parchments considered to be structurally degraded are required in order to fully assess the effects of relative humidity. The Bodleian Library, Oxford University (UK), gifted the historical parchment samples considered to be in a poor condition (as judged by the conservators). It should be noted that visual evaluation of parchment condition is highly subjective as a technique, and conservators

frequently rely on this form of analysis. Parchment that can appear intact on visual inspection can often show no presence of an axial collagen structure and vice versa. This study has therefore used X-ray diffraction as a system to determine the condition of our parchment. All the parchment samples used in this study were allocated as either in a poor condition or in a good condition (as judged by X-ray diffraction). This was based on the parchment evaluation system derived by the Improved Damage Assessment of Parchment project (IDAP), which provided an interactive tool in the form of a database for damage assessment of and research into parchment (Larsen, 2002). Single X-ray diffraction images were collected from all samples that were categorised as degraded or intact. Samples considered degraded showed weak axial meridional reflections whereas the samples considered intact demonstrated clear axial meridional reflections.

The collection of modern and historical parchment samples sourced for the study were stored under different levels of relative humidity using saturated salt solutions. These levels included 11%RH, 31%RH, 47%RH, 75%RH, 85%RH and a control sample kept under room conditions (which fluctuated between 40%RH and 50%RH). The use of saturated salt solutions provides a convenient method for the creation of different relative humidity levels (Hansen et al., 1992; Dubovikov and Podmurnaya, 2001). Saturated salt solutions, with solid salt present, maintain a stable concentration and hence a constant relative humidity (Dubovikov and Podmurnaya, 2001). The parchment samples were enclosed in a sealed plastic chamber with the desired saturated salt solution for a period of one month. A full list of the salts used to create the desired relative humidity values is listed in Table 5.1.

Salt Solution Name, Chemical Formula	Relative Humidity Level from the Literature (±4%RH)	Actual Measured Relative Humidity Level (±5%RH)
Lithium Chloride, LiCl	11%RH	10%RH
Calcium Chloride, $CaCl_2$	31%RH	33%RH
Potassium Thiocyanate, KSCN	47%RH	47%RH
Sodium Chloride, NaCl	75%RH	73%RH
Potassium Bromide, KBr	84%RH	85%RH

Table 5.1: Full list of the salts used to create the desired relative humidity values. The measured relative humidity levels were calculated using a Humidity and Temperature Probe Meter.

All modern and ancient parchment samples were stored under different levels of relative humidity using saturated salt solutions. The sample collection, RH levels and any additional treatments are fully listed in Table 5.2. The measured relative humidity levels were calculated using a Humidity and Temperature Probe Meter. In addition to investigating the parchment samples considered degraded and intact, artificially degraded samples were also produced. This was achieved by subjecting parchment samples to a 60-second dose of microwaves in a fully hydrated state. The use of microwaves causes the collagen within parchment to become partially denatured.

Sample Code	Parchment	Treatment	Humidity (±4%RH)	Sample Code	Parchment	Treatment	Humidity (±4%RH)
Sample Set 1				*Sample Set 2*			
MUC	Modern	Untreated	Control	MMC	Modern	Microwave	Control
MU11	Modern	Untreated	11%	MM11	Modern	Microwave	11%
MU31	Modern	Untreated	31%	MM31	Modern	Microwave	31%
MU47	Modern	Untreated	47%	MM47	Modern	Microwave	47%
MU75	Modern	Untreated	75%	MM75	Modern	Microwave	75%
MU84	Modern	Untreated	84%	MM84	Modern	Microwave	84%
Sample Set 3				*Sample Set 4*			
BaUC	Bodleian a	Untreated	Control	BbUC	Bodleian b	Untreated	Control
BaU11	Bodleian a	Untreated	11%	BbU11	Bodleian b	Untreated	11%
BaU31	Bodleian a	Untreated	31%	BbU31	Bodleian b	Untreated	31%
BaU47	Bodleian a	Untreated	47%	BbU47	Bodleian b	Untreated	47%
BaU75	Bodleian a	Untreated	75%	BbU75	Bodleian b	Untreated	75%
BaU84	Bodleian a	Untreated	84%	BbU84	Bodleian b	Untreated	84%

Table 5.2: Sample list and treatments applied to the parchment samples. All samples were sorted into four different sample sets including 'modern untreated', 'modern artificially degraded', 'Bodleian a untreated' and 'Bodleian b untreated'. Each of these sets were subjected to various levels of relative humidity including 11%RH, 31%RH, 47%RH, 75%RH, 85%RH and a control sample kept at an ambient relative humidity (fluctuated between 40-50%RH).

5.2.1.2 Parchment subjected to humidity cycling

In addition to parchment that was humidified specifically for this study, a collection of parchments that had been subjected to humidity cycling in a library environment were gifted by Dr. Ira Rabin from the Artifacts Treatment and Conservation department at the Israel Antiquities Authority. Two samples were sourced from three different scrolls, LT1, LT2 and LT3. The first sample taken from all three scrolls was stored in the depository at a constant temperature and relative humidity during both night and day. The second sample was placed in the laboratory during the day, and subjected to fluctuating humidity conditions. During the night these second samples were kept in the depository under constant conditions. The scroll samples were stored in this manner for a 6 month time period. Table 5.3 outlines the conditions under which the three scrolls were stored.

Parchment Sample Code	Day Conditions (8-9 hours a day)	Night Conditions (15-16 hours a day)
LT1d	In Depository 19°C (±1°C) 50%RH (±2%)	In Depository 19°C (±1°C) 50%RH (±2%)
LT2d	In Depository 19°C (±1°C) 50%RH (±2%)	In Depository 19°C (±1°C) 50%RH (±2%)
LT3d	In Depository 19°C (±1°C) 50%RH (±2%)	In Depository 19°C (±1°C) 50%RH (±2%)
LT1L	In Laboratory Variable Temperature 30-60%RH	In Depository 19°C (±1°C) 50%RH (±2%)
LT2L	In Laboratory Variable Temperature 30-60%RH	In Depository 19°C (±1°C) 50%RH (±2%)
LT3L	In Laboratory Variable Temperature 30-60%RH	In Depository 19°C (±1°C) 50%RH (±2%)

Table 5.3: Conditions of storage for each of the two samples taken from three different parchment scrolls.

5.2.2 Data Collection at SRS Daresbury, Station 2.1

Small-angle X-ray scattering (SAXS) images were obtained from all parchment sample sets in this study in order to analyse the effects of various relative humidity levels on the structural integrity of parchment. Small Angle X-ray Scattering (SAXS) experiments were carried out at Beamline 2.1, Synchrotron Radiation Source (SRS) Daresbury, UK using a sample to detector length of 4.25m. An X-ray beam with a fixed wavelength of 0.154nm was focused on each sample, which was attached to a computer controlled X-Y elevation stage to provide sample mobility (Grossman, 2002). Hydrated rat-tail tendon was used to calibrate the images and background images were subtracted from all data collected and images were analysed using the CCP13 (Collaborative Computational Project 13) program FibreFix (Rajkumar et al., 2005). Small-angle images were converted from two-dimensional into one-dimensional linear intensity plots. In addition, Peakfit4 (AISL) software was utilised in the analysis of the linear profiles.

5.2.3 Data Collection at SRS Daresbury, Station 14.1

Wide-angle X-ray scattering (WAXS) was also conducted at the Synchrotron Radiation Source (SRS) Daresbury U.K. using station 14.1, with the X-ray wavelength set to 0.148nm, a sample-to-camera length fixed at 140mm and the powder diffraction rings of calcite used to calibrate the data. Full details regarding the experimental set-up of station 14.1 is given in Chapter 3. Station 14.1 was used to collect wide-angle patterns from the parchment subjected to humidity cycling. Background images were removed from data and the wide-angle images were converted, using the same methodology applied to the SAXS data.

5.2.4 Data Collection on the Bruker NanoStar Facility

Wide Angle X-ray Diffraction patterns were also collected on the NanoStar (Bruker AXS, Karlsruhe) X-ray facility at Cardiff University, UK using a sample-to-detector length of 4cm. A Kristalloflex 760 X-ray generator produced an 0.154nm wavelength X-ray beam which was focused using a series of Göbel mirrors and a collimation system (Maxwell et al., 2006). The data was collected on a HI-STAR 2d detector and all images were calibrated using calcite. The NanoStar facility was used to collect wide-angle patterns from the parchment stored at a fixed humidity level. Background images were subtracted from all data collected and images were analysed using the CCP13 (Collaborative Computational Project 13) program FibreFix (Rajkumar et al., 2005). Wide-angle images were converted from two-dimensional into one-dimensional linear intensity plots using the same method as the SAXS data. In addition, Peakfit4 (AISL) software was used in the analysis of the linear profiles.

5.3 Results

5.3.1 Parchment stored at a fixed humidity level

5.3.1.1 Small-angle X-ray Scattering Analysis

Scattering X-rays at small angles (<6°) gives information regarding the long-range order of structures (Glatter and Kratky, 1982). Collagen fibrils from skin exhibit a fundamental axial periodicity of ~65.5nm which is observable within the capacity of SAXS (Brodsky et al.,

1980). The fundamental axial periodicity is the result of regular fluctuations in the electron density of collagen in the axial direction (Hodge and Petruska, 1963), varying from sample to sample and observed to increase upon hydration (Wess and Orgel, 2000). The SAXS images for the modern parchment, both untreated and artificially degraded are shown in Figure 5.1. Figure 5.1 (A) highlights the fifth to tenth orders of collagen diffraction in untreated parchment, where little movement is observed in all the diffraction peaks. Figure 5.1 (B) also shows the fifth to tenth orders of collagen meridional diffraction in degraded parchment, where a variation of the peak positions as a consequence of RH is observed.
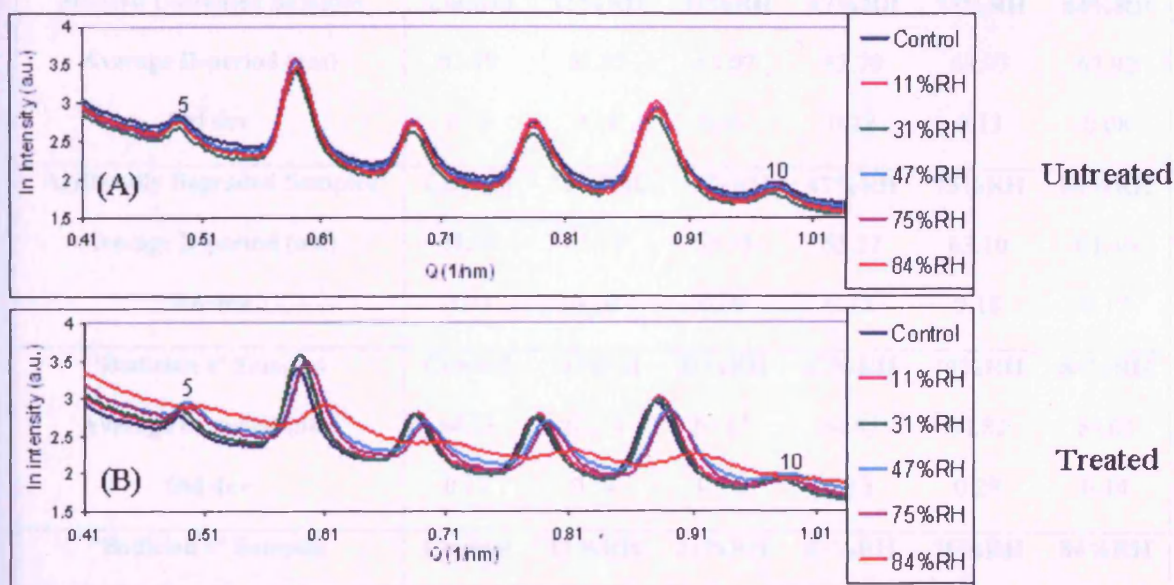
Figure 5.1: (A) Small-angle X-ray scattering image of modern untreated parchment as a function of RH. The fifth to tenth orders of collagen diffraction are shown. (B) Small-angle X-ray scattering image of modern artificially degraded parchment (degraded with a 60 second dose of microwaves with an energy of 900W). The fifth to tenth orders of collagen diffraction are shown with the fifth and tenth orders highlighted.

The largest shift in peak position is seen on the artificially degraded sample subjected to 84%RH. The D-period values for all the parchment samples are shown in Table 5.4. The

145

untreated parchment samples show very little fluctuation in the D-period upon humidification while the artificially degraded parchment samples showed a significant decrease in the D-period. The artificially degraded parchment sample showed a dramatic decrease from 63.86nm for the control sample to 61.40nm for the sample that was stored at 84%RH. In contrast, for the artificially degraded parchment sample, no significant difference was seen in the D-period from 63.86nm for the control sample, to 63.75nm for the sample that was stored at 11%RH. This shows that there is a larger structural variation in collagen at high humidities than found at lower humidities.

Modern Untreated Samples	Control	11%RH	31%RH	47%RH	75%RH	84%RH
Average D-period (nm)	63.79	63.93	64.07	63.79	63.93	63.92
Std dev	0.25	0.10	0.11	0.28	0.13	0.08
Artificially Degraded Samples	Control	11%RH	31%RH	47%RH	75%RH	84%RH
Average D-period (nm)	63.86	63.75	63.75	63.22	63.10	61.40
Std dev	0.09	0.20	0.09	0.15	0.18	0.17
'Bodleian a' Samples	Control	11%RH	31%RH	47%RH	75%RH	84%RH
Average D-period (nm)	64.83	62.98	64.82	64.82	64.82	65.04
Std dev	0.17	0.14	0.15	0.13	0.29	0.14
'Bodleian b' Samples	Control	11%RH	31%RH	47%RH	75%RH	84%RH
Average D-period (nm)	65.25	65.04	65.04	65.25	65.25	65.25
Std dev	0.19	0.18	0.07	0.16	0.20	0.13

Table 5.4: The calculated average D-period for modern parchment samples (both untreated and artificially degraded). Also provided are the calculated D-period values for the 'Bodleian a' sample set and the 'Bodleian b' sample set.

The modern untreated parchment demonstrated no significant difference in the D-period between the sample stored at 11%RH and the sample stored at 84%RH ($F_{1,8}$ = 1.90, p = 0.91). The modern artificially degraded parchment demonstrated a significant difference in

the D-period between the sample stored at 11%RH and the sample stored at 84%RH ($F_{1,8}$ = 1.30, p < 0.0001). The Bodleian 'a' sample (naturally degraded) also showed a significant difference in the D-period between the sample stored at 11%RH and the sample stored at 84%RH ($F_{1,8}$ = 1.05, p < 0.0001).

The small-angle X-ray scattering images for the proposed degraded samples, 'Bodleian a' and 'Bodleian b' at all humidity ranges are shown in Figure 5.2. These parchment samples demonstrate a greater movement in the diffraction peaks for the low levels of humidity as well as the high levels of humidity. Both 'Bodleian a' and 'Bodleian b' demonstrated a decrease in D-period from the control samples to the samples stored at low humidities while an increase in D-period from the control samples to the samples stored at high humidities. The D-period values for all the parchment samples are shown in Table 5.4.
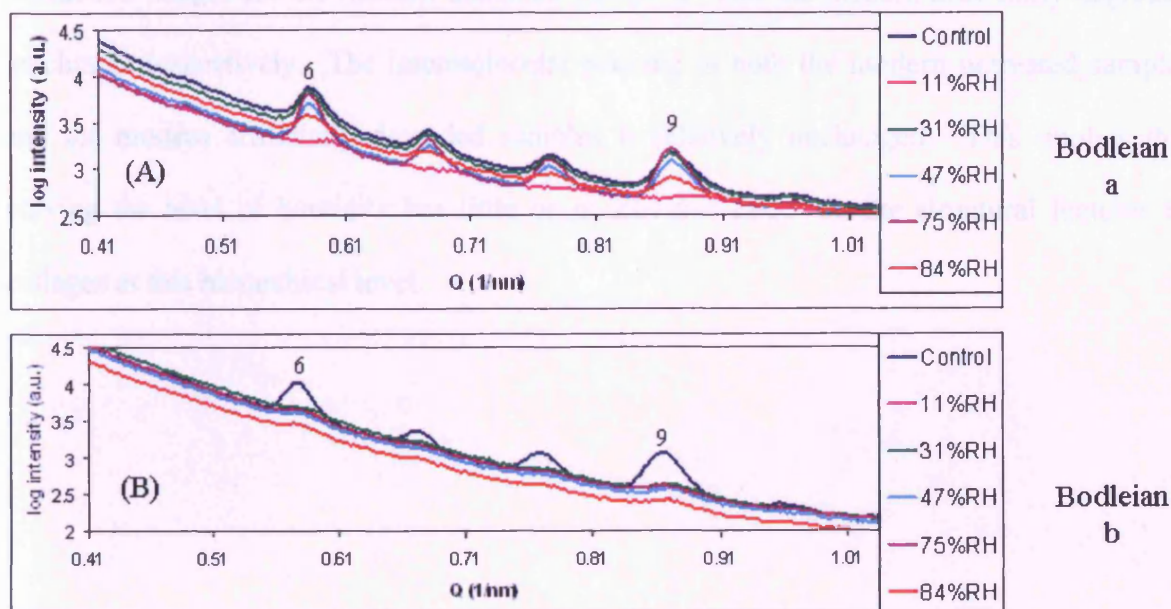
Figure 5.2: (A) Small-angle X-ray scattering image of 'Bodleian a' parchment sample. The fifth to tenth orders of collagen diffraction are shown. (B) Small-angle X-ray scattering image of 'Bodleian b' parchment sample. The fifth to tenth orders of collagen diffraction are shown, where the sixth and ninth orders of axial collagen diffraction are labeled as (6) and (9).

147

5.3.1.2 Wide-angle X-ray scattering Analysis

The key features in collagen at wide-angles are the reflections seen at 0.29nm and 1.2nm (Meek and Quantock, 2001a; Sionkowska et al., 2004a). The reflection seen at approximately 0.29nm relates to the helical rise per residue, which is the distance between the amino acid residues along the collagen triple helices. The intermolecular lateral packing corresponds to the distance between one collagen molecule and its nearest neighbour, which is observed at approximately 1.2nm.

The helical rise per residue value for the collagen molecules in all samples appears to be unchanged. This implies there is little or no alteration to the arrangement of amino acid residues within the collagen triple helix. Figure 5.3 (A) and (B) show the wide-angle X-ray diffraction images for the modern untreated parchment and the modern artificially degraded parchment respectively. The intermolecular packing in both the modern untreated samples and the modern artificially degraded samples is relatively unchanged. This implies that varying the level of humidity has little or no obvious effect on the structural features of collagen at this hierarchical level.
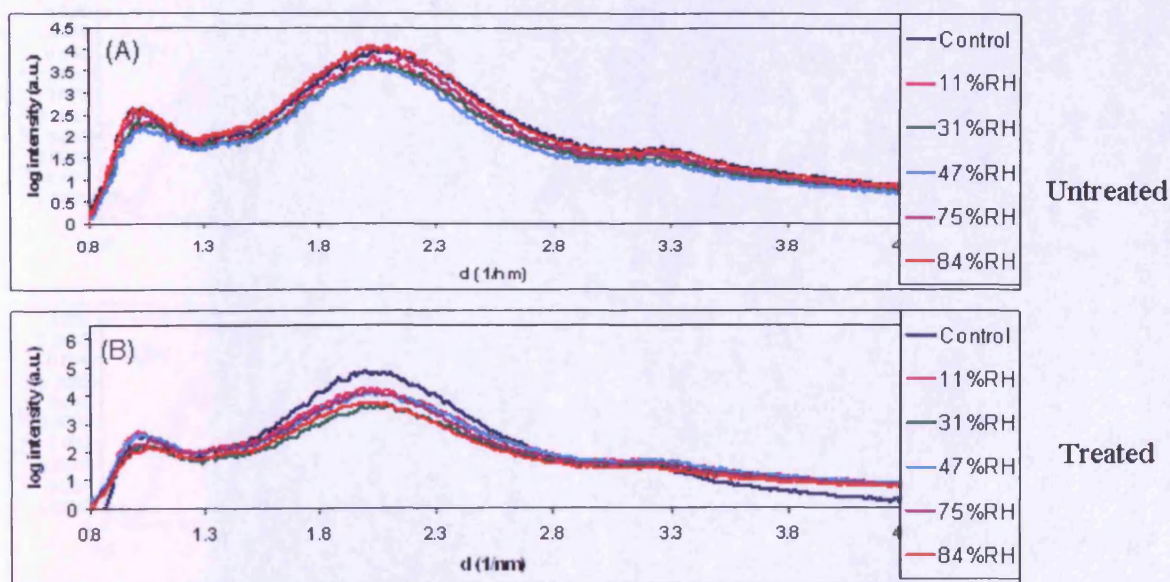
Figure 5.3: **(A) Wide-angle X-ray diffraction image of modern untreated parchment.**
(B) Wide-angle X-ray diffraction image of modern artificially degraded parchment
(degraded with a 60 second dose of microwaves, with an energy of 900W).

Figure 5.4 (A) and (B) show the wide-angle X-ray diffraction of parchment samples
'Bodleian a' and 'Bodleian b'. The helical rise per residue and the intermolecular packing is
unchanged in both samples at all humidity levels. This further enforces the proposal that
varying the level of humidity has little or no obvious effect on the structural features of
collagen at this hierarchical level.
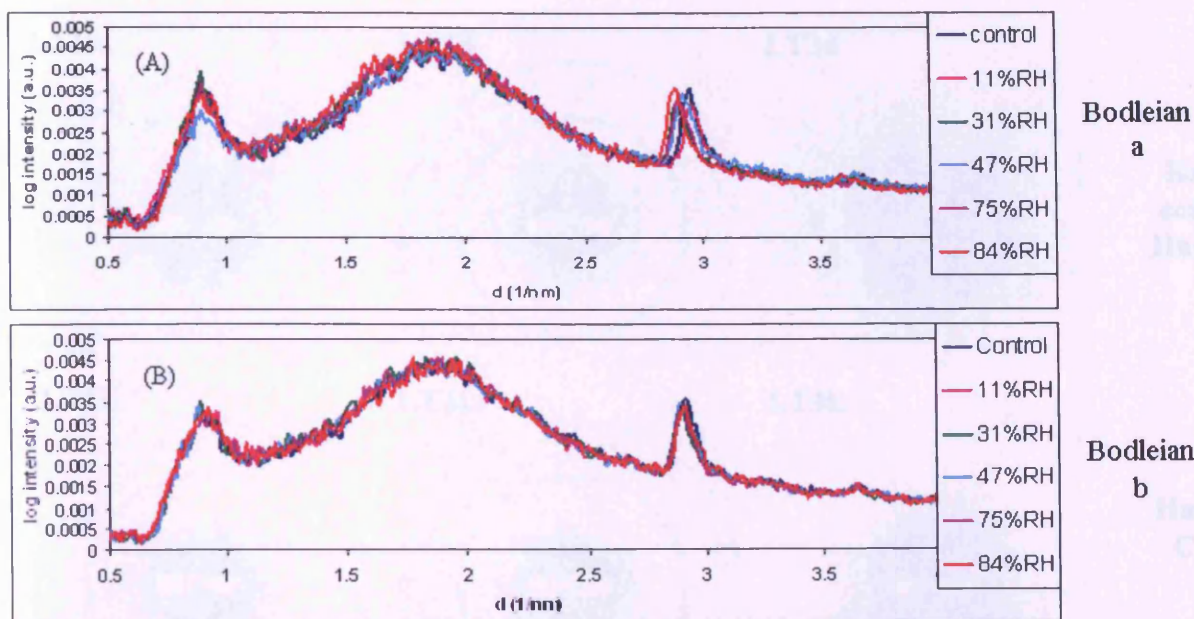
Figure 5.4: (A) Wide-angle X-ray diffraction image of parchment sample 'Bodleian a'. (B) Wide-angle X-ray diffraction image of parchment sample 'Bodleian b'. An undefined peak is seen at approximately 2.9nm^{-1}.

5.3.2 Parchment subjected to humidity cycling

5.3.2.1 Small-angle X-ray Scattering Analysis

Small-angle X-ray diffraction patterns were collected at Station 2.1 for all six samples subjected to humidity cycling. The two-dimensional X-ray diffraction patterns for the six samples are shown in Figure 5.5.
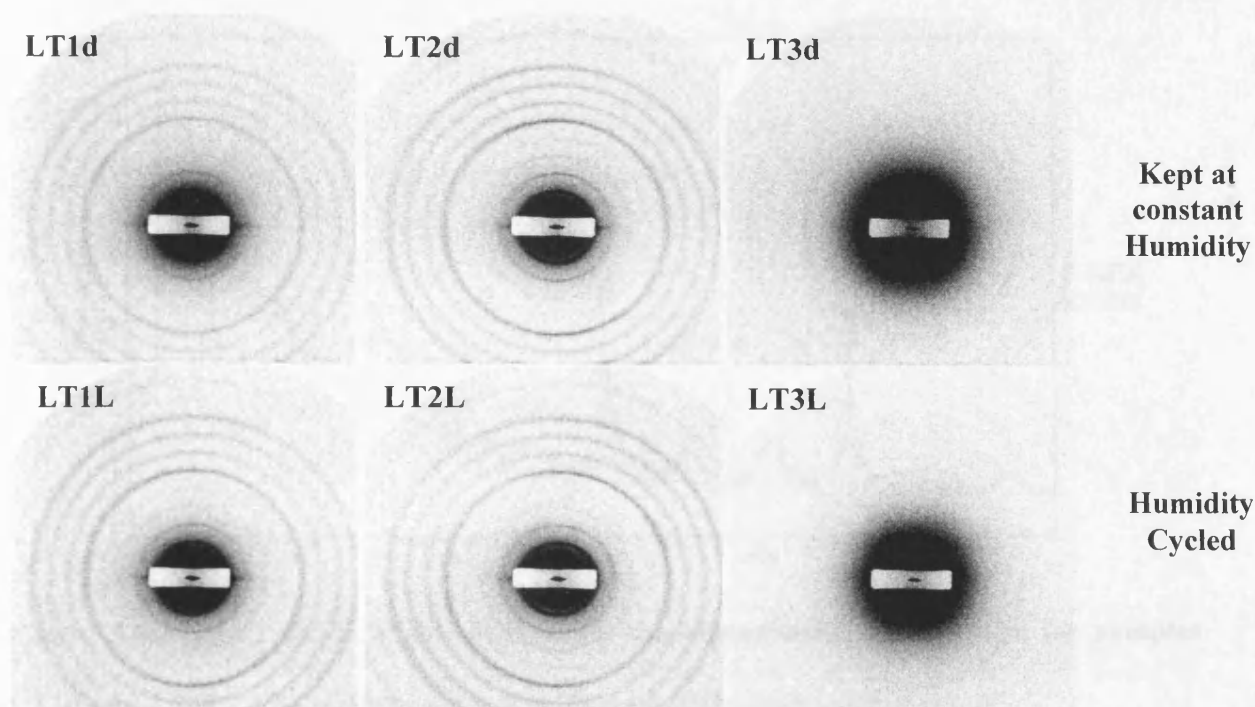
Figure 5.5: Small-angle X-ray diffraction images collected on all samples at SRS Daresbury station 2.1 at a sample to detector distance of 4.25m. LT1d, LT2d and LT3d (top row from left to right). LT1L, LT2L and LT3L (bottom row from left to right).

Samples sourced from the scrolls LT1 and LT2 show very clear reflections from the third to the twelfth orders of collagen axial diffraction when kept under constant conditions and when subjected to humidity cycling. These samples displayed strong sixth and ninth orders of diffraction which is expected in reasonably intact parchment. Samples sourced from the scroll LT3 displayed weaker reflections than the other samples in both sets of conditions. One-dimensional linear traces of samples LT1d and LT1L are shown in Figure 5.6 where the sixth and ninth orders of diffraction are indicated.
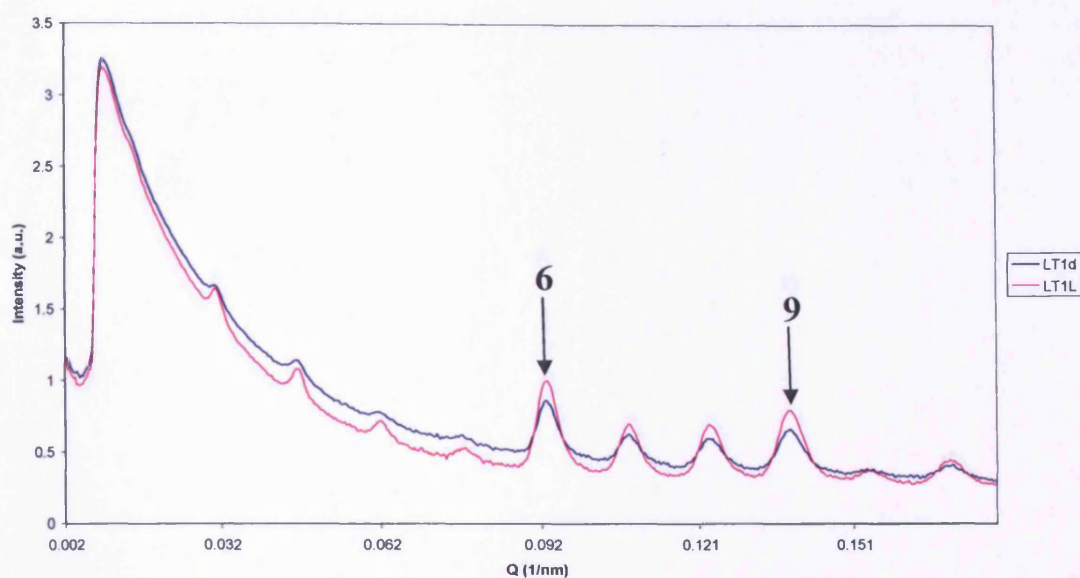
Figure 5.6: **Small angle X-ray diffraction one-dimensional linear trace for samples LT1d and LT1L. The sixth and ninth orders of diffraction are indicated.**

Figure 5.6 shows little difference in the axial D-period between the sample stored under constant conditions (LT1d) and the sample subjected to humidity cycling (LT1L). One-dimensional linear traces of samples LT2d and LT2L are shown in Figure 5.7 where the sixth and ninth orders of diffraction are indicated.
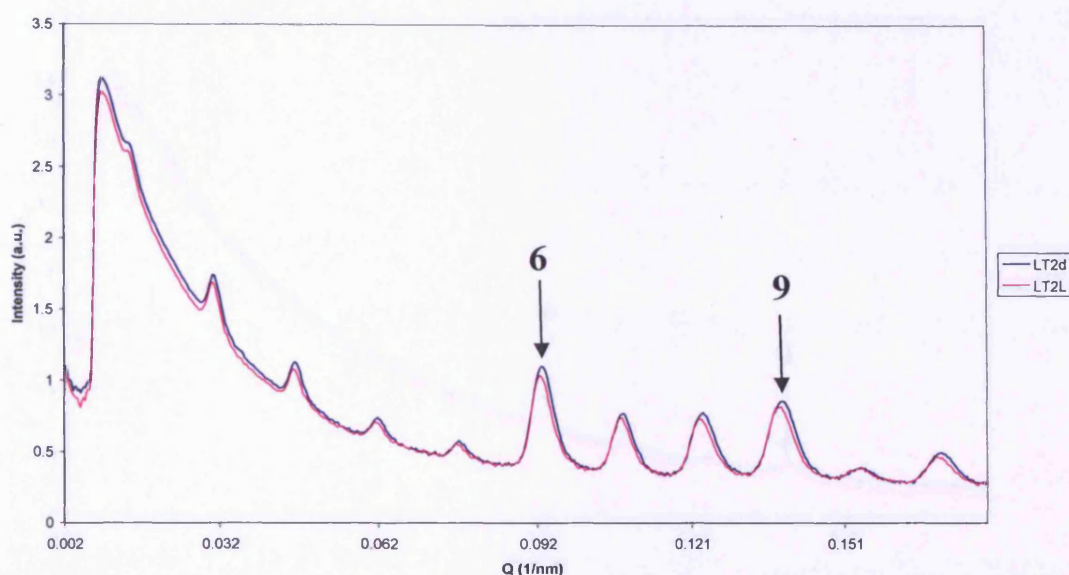
Figure 5.7: Small angle X-ray diffraction one-dimensional linear trace for samples LT2d and LT2L. A shift in the D-period (axial periodicity) is visible, from a lower D-period for the parchment kept at constant conditions (LT2d) to a higher D-period value for the parchment kept at fluctuating conditions (LT2L). The sixth and ninth orders of diffraction are indicated.

Figure 5.7 shows the reflections to a lower D-period for the parchment kept at constant conditions and a higher D-period for the parchment kept at fluctuating conditions (30%-60%RH). This indicates that the sample subjected to the humidity cycling (LT2L) has a higher D-period than the sample kept under constant conditions (LT2d). One-dimensional linear traces of samples LT3d and LT3L are shown in Figure 5.8 where the sixth and ninth orders of diffraction are indicated.
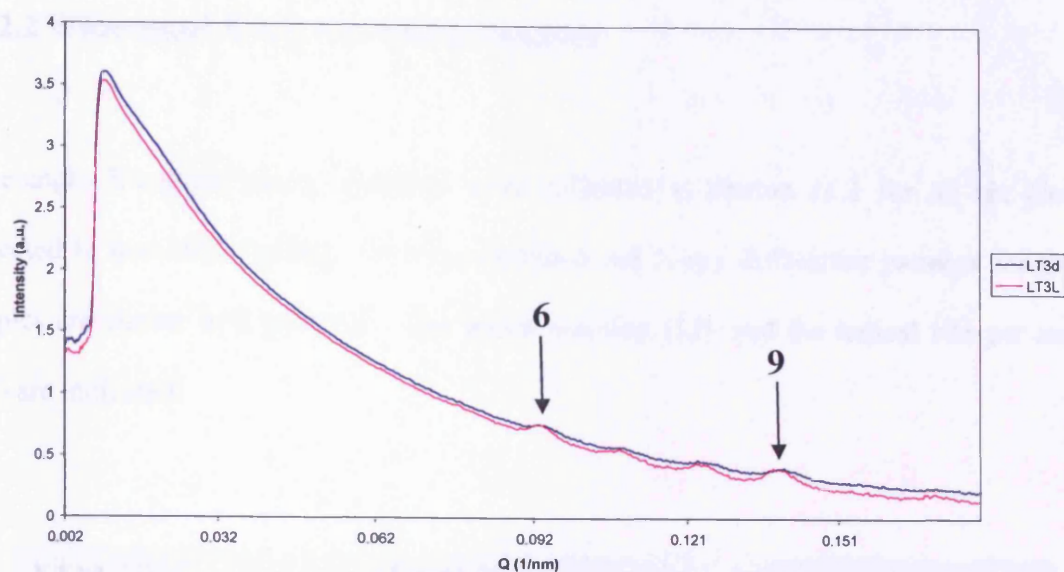
Figure 5.8: **Small angle X-ray diffraction one-dimensional linear trace for samples LT3d and LT3L. The sixth and ninth orders of diffraction are indicated.**

A shift in the D-period is also seen in the samples from scroll LT3 indicating that the sample subjected to the humidity cycling (LT3L) has a higher D-period than the sample kept under constant conditions (LT3d). Samples LT3d and LT3L demonstrated weaker orders of collagen axial diffraction than both the samples taken from scrolls LT1 and LT2. Table 5.5 shows the calculated D-period values for each sample.

Sample Code	Average D-period (nm) (± 0.2nm)	Std dev
LT1d	65.2	0.20
LT1L	64.7	0.12
LT2d	64.8	0.25
LT2L	65.2	0.06
LT3d	63.6	0.32
LT3L	64.4	0.17

Table 5.5: **The calculated values for the average D-period from all six scroll samples, where LT1d, LT2d and LT3d were stored at constant humidity. LT1L, LT2L and LT3L were subjected to fluctuations in humidity. All the parameters are calculated from the linear traces using PeakFit software.**

5.3.2.2 Wide-angle X-ray scattering Analysis

Wide-angle X-ray diffraction patterns were collected at Station 14.1 for all six samples subjected to humidity cycling. The two-dimensional X-ray diffraction patterns for the six samples are shown in Figure 5.9. The lateral packing (LP) and the helical rise per residue (HR) are indicated.
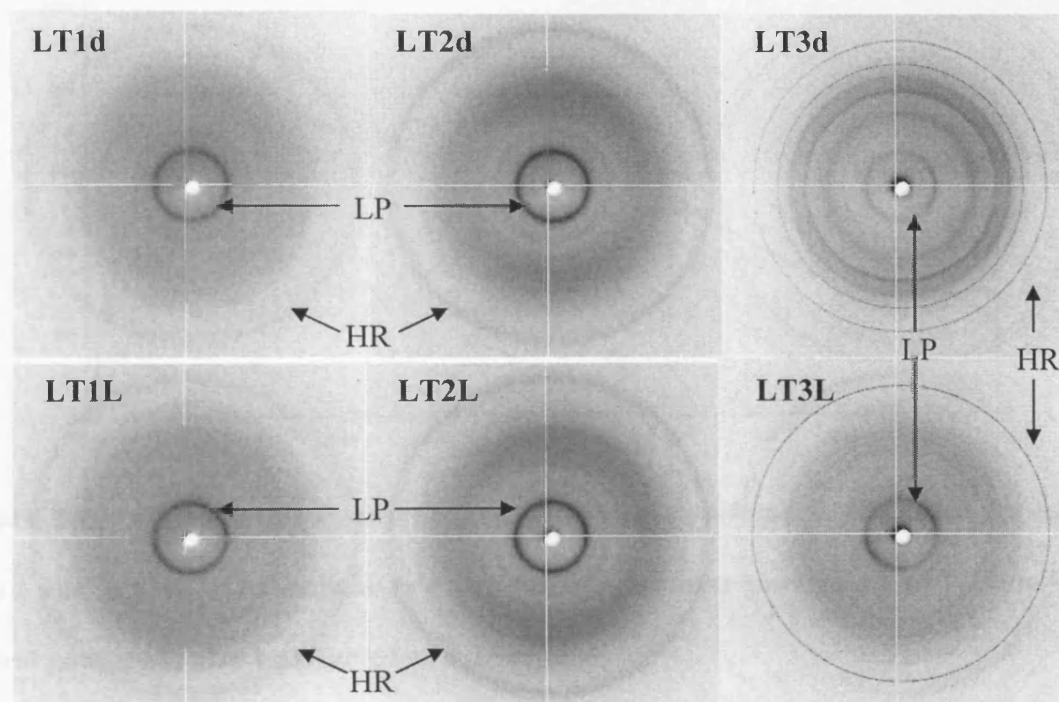
Figure 5.9: Two-dimensional Wide-angle X-ray diffraction images collected on all samples at SRS Daresbury station 14.1 at a sample to detector distance of 140cm. LT1d, LT2d and LT3d (top row from left to right). LT1L, LT2L and LT3L (bottom row from left to right). The lateral packing (LP) and the helical rise per residue (HR) are indicated.

All samples show the presence of reflections at 1.2nm and 0.29nm, corresponding to the lateral packing of the collagen molecules and the helical rise per residue respectively. Samples LT3d and LT3L show the presence of mineral in the sample, with a strong calcite reflection present at 0.3nm in real space.

One-dimensional linear traces of samples LT1d and LT1L are shown in Figure 5.10 where the lateral packing reflection and the helical rise per residue reflection are indicated.
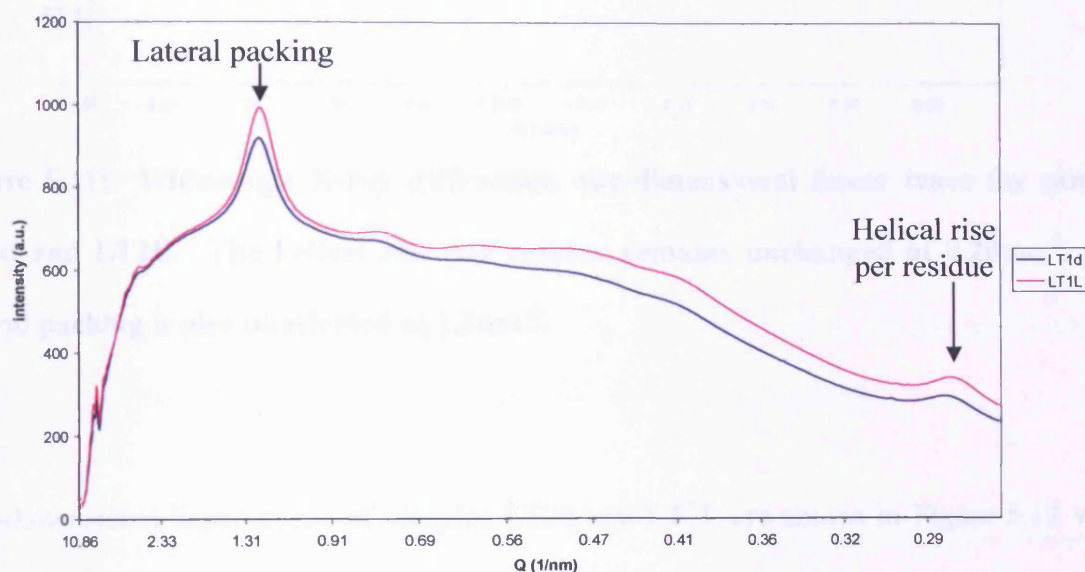
Figure 5.10: Wide-angle X-ray diffraction one-dimensional linear trace for samples LT1d and LT1L. The helical rise per residue remains unchanged at 0.28nm^{-1}. The lateral packing is also unaffected at 1.2nm^{-1}.

One-dimensional linear traces of samples LT2d and LT2L are shown in Figure 5.11 where the lateral packing reflection and the helical rise per residue reflection are indicated.
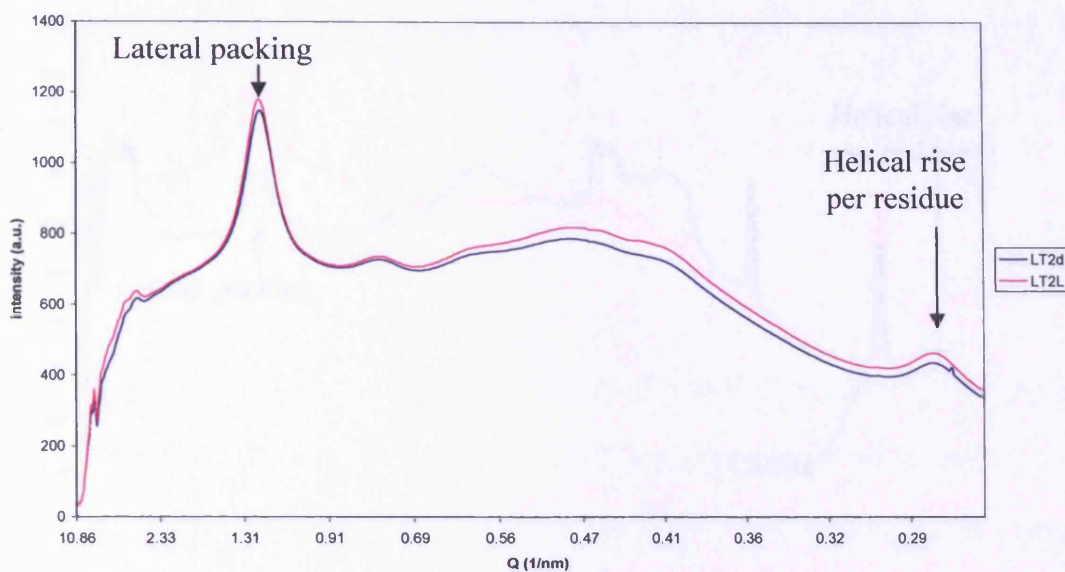
Figure 5.11: **Wide-angle X-ray diffraction one-dimensional linear trace for samples LT2d and LT2L. The helical rise per residue remains unchanged at $0.28nm^{-1}$. The lateral packing is also unaffected at $1.2nm^{-1}$.**

One-dimensional linear traces of samples LT3d and LT3L are shown in Figure 5.12 where the lateral packing reflection and the helical rise per residue reflection are indicated.
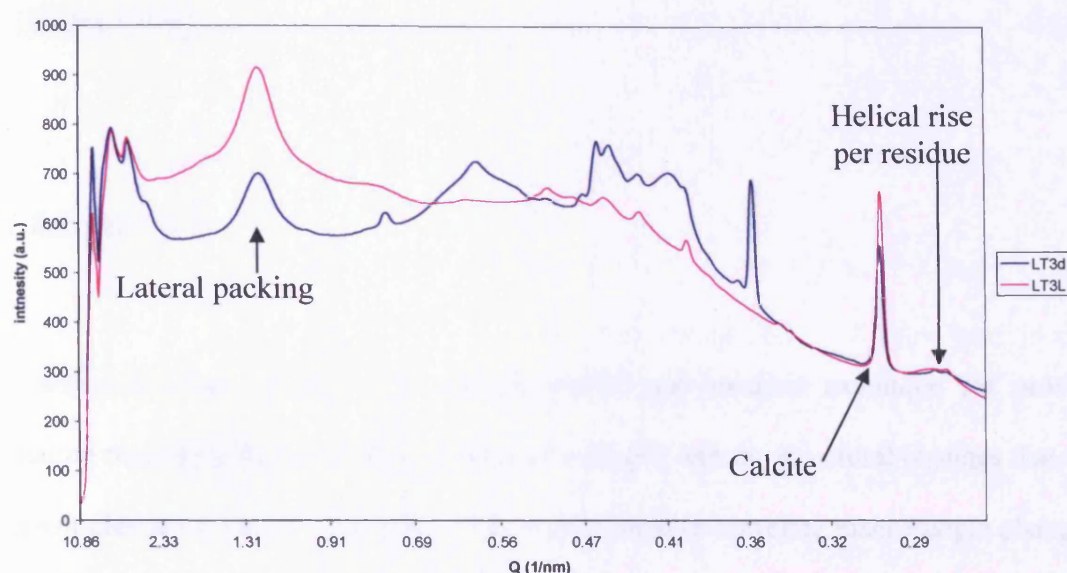
Figure 5.12: **Wide-angle X-ray diffraction one-dimensional linear trace for samples LT3d and LT3L. The helical rise per residue remains unchanged at 0.28nm^{-1}. The lateral packing is also unaffected at 1.2nm^{-1}. A reflection due to the mineral calcite is observed at 0.3nm^{-1}. The other samples show no presence of calcite.**

Across all samples there was a variation in the D-period, whereas the calculated values for the lateral packing distance remained unchanged at 1.2nm, and the helical rise per residue remained constant at 0.28nm.

5.4 Discussion

5.4.1 Introduction

X-ray diffraction has proven an extremely useful non-invasive technique for providing information regarding the molecular packing of collagen and the structural changes that occur within samples at varying RH values. This work aimed to correlate macroscopic changes in the visible appearance of parchment with the alterations seen in the nanoscopic structure of collagen. The structural studies on parchment were conducted at the Synchrotron Radiation Source (SRS), Daresbury and used the in-house NanoStar facility, where X-ray diffraction images were collected from a series of parchment samples of varying condition.

5.4.2 The effect of relative humidity on untreated modern parchment

The modern untreated parchment exhibited visual alterations at a macroscopic level but displayed no visible change in the small-angle or the wide-angle X-ray diffraction data. This implies that although the parchment stored at levels of high and low humidity had visually degraded, no significant alterations occurred at a nanoscopic level. It is proposed that additional changes to the parchment upon humidification were occurring at a different structural level to that observed.

5.4.3 The effect of relative humidity on artificially degraded modern parchment

Changes were observed in both the visual appearance of the parchment and the X-ray diffraction data. The parchment subjected to higher humidities was more flexible to the touch than the control parchment, while the opposite was found for the parchment subjected to lower humidities. By storing the modern artificially degraded parchment in a moist environment with 84%RH, the addition of water molecules into the parchment structure was allowed to take place. We propose that this addition of water molecules caused swelling of the parchment structure and movement of the collagen molecules.

As water is removed from the system, it is proposed that the collagen molecules undergo structural rearrangement. The structural rearrangement seen in dry collagen has been previously discussed by a number of studies (Wess and Orgel, 2000; Buehler, 2006). Three possible mechanisms have been suggested to occur in parchment upon drying; these are outlined in Figure 5.13.

(A) Shearing **(B) Breaking** **(C) Tilting**

Overlap   Gap   Overlap   Gap   Overlap   Gap
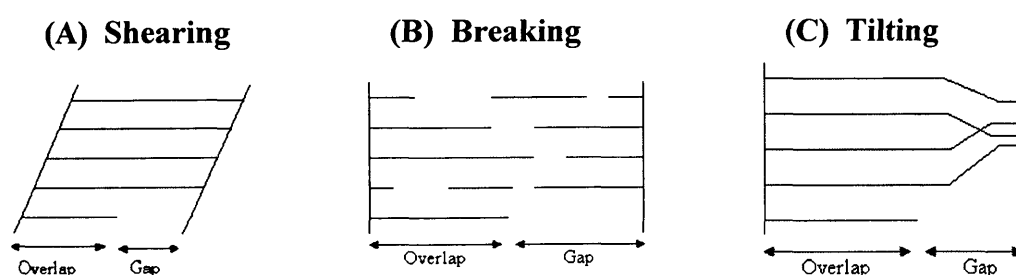
Figure 5.13: Three proposed degradative mechanisms of fibrillar collagen that possibly occur in parchment upon drying, (A) the shearing of laterally adjoined molecules relative to each other, (B) breakages in the amino acid chains of the collagen molecules and (C) the induction of molecular tilting within the staggered array of collagen molecules.

When hydrated collagen is allowed to air dry the water that exists between the fibres migrates to the surface of the parchment and evaporates (Haines, 1999). It has been proposed that significant structural alterations occur within parchment due to the shortening of collagen fibres and their subsequent collapse, although there is no quantitative data to support this argument. It is these large structural changes that make repairing water damage to parchment extremely difficult and time consuming (Hingley, 2001). One of the major effects of water damage is the distortion and rippling of the parchment. Humidification is the most commonly used technique to correct for this surface distortion.

By storing the artificially degraded parchment in a relatively dry environment with 11%RH, the removal of water molecules from the parchment structure was allowed. The D-period for the artificially degraded parchment shows a greater change from the control at higher humidities rather than lower humidities. Therefore it is suggested that the addition of water to the system beyond equilibrium is more harmful to the collagen integrity than the removal of water.

The results have demonstrated that parchment samples of poor condition (considered by X-ray diffraction to be degraded at the outset) show significant changes within the X-ray diffraction patterns under different levels of humidity. In contrast, humidification of parchment samples in good condition (considered intact at the outset as judged by X-ray diffraction) has very little effect on the X-ray diffraction. It is therefore suggested that the presence of degraded collagen within the parchment sample allows further degradation by extreme levels of humidification, which is detrimental to the structural integrity of the parchment.

5.4.4 The effect of relative humidity on degraded parchment

The parchment investigated was artificially degraded using microwaves. To conclusively assess the effect of relative humidity on parchment then historically degraded parchment is required. Two historical degraded parchment samples were investigated, 'Bodleian a' and 'Bodleian b'. The samples exhibited visual alterations at a macroscopic level but displayed no visible change in the wide-angle X-ray diffraction data. There were no visible alterations at a molecular level or in the molecular interactions. The small-angle X-ray diffraction data demonstrated a change in the diffraction peaks for the low levels of humidity as well as the high levels of humidity. Both samples when stored at low humidities exhibited a decrease in the D-period when compared with the control sample. The reverse was found when stored at high humidities, the D-period increased. This is in agreement with the data collected on the artificially degraded modern parchment samples.

5.4.5 The effect of relative humidity cycling on historical parchment

Six parchment samples were sourced from three different scrolls and were investigated using small-angle and wide-angle X-ray diffraction. One sample from each scroll was kept in constant environmental conditions whereas the other samples from each scroll were subjected to humidity cycling.

Samples from all three scrolls were found to react differently to humidity cycling. Samples taken from scroll LT1 showed a small difference in the X-ray diffraction patterns after humidity cycling for a 6-month period. The sample that was subjected to humidity cycling (LT1L) was found to have a smaller D-period than the sample kept under constant conditions

(LT1d). Samples taken from scroll LT2 showed a change in the axial D-period in the small-angle X-ray diffraction patterns after humidity cycling for 6 months. The sample that was subjected to humidity cycling (LT2L) was found to have a larger D-period than the sample kept under constant conditions (LT2d). Samples taken from scroll LT3 showed a difference in the X-ray diffraction patterns after humidity cycling for 6 months. The sample that was subjected to humidity cycling (LT3L) was found to have a larger D-period than the sample kept under constant conditions (LT3d).

This study has reinforced the theory that each parchment sample reacts differently under humidity cycling. This has indicated the need for a larger study to be completed and for each parchment sample to be treated as a heterogeneous material.

5.4.6 Conclusions

The effect of relative humidity on parchment is of great importance in document conservation and storage in a variety of locations including libraries and archives. This study has shown that under extreme levels of humidity structural alterations occur in the collagen structure. A variation in the axial D-period is observed in samples considered in a degraded state upon humidification whereas little or no alteration is seen in the axial D-period in samples considered in an intact state upon humidification. This may be due to the presence of partially degraded collagen within the samples that accelerates the effect of humidity upon the collagen present. However not all the changes observed in the macroscopic properties can be described at structural levels amenable to X-ray diffraction. There is therefore a vital need to relate changes to visual and macroscopic structural properties to the changes in the fibrillar/suprafibrillar architecture. Consequently, there is a need to find a technique that will relate the changes observed in the mesostructure of parchment, where it is proposed that

change is occurring.

Overall, findings have shown that relative humidity has an extremely varied effect on parchment and greatly depends on the integrity of the collagen present within the parchment. This indicates that the need for a comprehensive mechanism of humidity control of the environment in which parchment samples are kept is exceedingly important, particularly those that are believed to be in a more degraded state.

Chapter 6: Molecular Modelling of Changes in Fibrillar Collagen

6.1 Introduction

Collagen is a fibrous structural protein that plays an essential role in many biological tissues, including tendon, cornea, bone and skin (Traub and Piez, 1971). The mechanical properties of collagen are highly dependent on the hierarchical architecture at the nano and micron length scale, where it is vital to understand the structural response to deformation at each level in the structural hierarchy.

The use of X-ray diffraction is a valuable non-invasive technique that allows us to investigate the structural, chemical, and physical properties of materials, and has proven itself as an excellent technique to investigate the structure and molecular packing within collagen fibrils. Structural models have been created that sufficiently account for the X-ray fibre diagram collected from native, hydrated collagen (for example, tendon and skin) (Wess et al., 1998ab; Wess and Orgel, 2000; Cameron et al., 2002). Although a model has been proposed for the native state of collagen, no model has satisfactorily explained the X-ray diffraction patterns collected from collagen that has been altered from its native structure by sources such as drying, X-ray radiation damage and mechanical deformation. While significant research has been conducted on the native structure of collagen, recent studies have also begun to focus on deformation of collagen hierarchical structures (Mosler et al., 1985; Folkhard et al., 1987; Sasaki and Odajima, 1996a; Wess and Orgel, 2000; Buehler, 2006). Structural models of subfibrillar arrangements have been suggested to account for the deformation of collagen

resulting from drying and mechanical deformation, however, they do not give an adequate explanation of the changes observed in the X-ray fibre diagram. The structural changes observed in collagen that has been damaged by an intense dose of X-ray radiation have not previously been explored, and no models have been produced to explain the X-ray diffraction patterns observed. Therefore, more rigorous models are needed in order to understand the changes that can occur in fibrillar collagen upon structural deformation and chemical modification.

6.1.1 Changes in Fibrillar Collagen as Observed by X-ray Diffraction

This section discusses the changes seen in X-ray diffraction patterns collected after deformation resulting from drying, X-ray radiation damage and mechanical testing of collagen based tissues. The possible explanations for the observed changes in the X-ray diffraction patterns will be discussed in section 6.1.2, and structural models that can be constructed in order to account for these will be demonstrated later in this Chapter.

6.1.1.1 Changes in Fibrillar Collagen resulting from Drying

The structure and molecular packing within fibrils is well documented in the native hydrated state, but less is understood in relation to the structural alterations that occur when drying. To appreciate the underlying mechanics of collagen deformation, it is essential to understand the changes in collagen structural order that occur through drying. Figure 1.11 (Chapter 1, page 38) shows two-dimensional small-angle X-ray diffraction patterns from hydrated and air-dried collagen fibres from rat-tail tendon.

Figure 1.11 demonstrates the difference seen in the meridional features of the X-ray fibre diagram between native hydrated collagen and air-dried tendon collagen. The principle effect visible in X-ray diffraction patterns for dry rat-tail tendon collagen is the shortening of the D-period from the characteristic 67nm to around 65nm (Stinson and Sweeny, 1980; Wess and Orgel, 2000). A further difference observed is a decrease in the number of meridional reflections visible in the diffraction series: up to 140 meridionals are observed in the hydrated state, while only up to 40 meridionals are visible in the dry state (Wess and Orgel, 2000). The meridional reflections also display a widening or fanning of the meridionals in dry collagen at angles of up to 20 degrees (Rougvie and Bear, 1953). In a few cases, the meridional reflections are more intense at the outer edges than in the central regions (observed in the 25th and 28th reflections for dry tendon (a) seen in Figure 1.11). Some reflections are split into three areas of intensity parallel to the equator. This phenomenon is observed more easily at the higher orders of X-ray diffraction of collagen than the lower orders.

In summary, the drying of collagen causes large structural changes at a molecular level; there are four main changes seen in the two-dimensional X-ray diffraction pattern of rat-tail tendon collagen on drying:

- A shortening of the D-period from the characteristic 67nm D-period to around 65nm.

- A decrease in the number of visible meridional reflections from approximately 140 visible reflections in the hydrated state compared with approximately 40 reflections in the air-dried state.

- A widening or fanning of meridional reflections producing angles of up to 20 degrees from the meridian.

- A redistribution of intensity of some meridional reflections in the direction parallel

to the equator: in some cases the meridional reflections are more intense at the outer edges than in the central regions.

6.1.1.2 Changes in Fibrillar Collagen resulting from X-ray Irradiation

X-rays are extensively used in medicine for imaging, diagnosis and treatment. It has been suggested that an intense dose of synchrotron X-ray radiation may be beneficial for the treatment of cancer (Blattmann et al., 2005). It is important to understand the effect of X-rays on the structure of collagen for future fast dynamic and coherent studies of proteins where the proposed X-ray dose will be very intense in order to capture transient structures. Very few studies have investigated the possible molecular rearrangements within collagen structure in response to X-ray radiation. Work by the Wess research group has investigated the induction of local strain defects in collagen axial structure resulting from an intense X-ray dose applied to rat-tail tendon. A partially coherent X-ray beam used for X-ray photon correlation spectroscopy (XPCS) was applied in order to deliver an extremely intense X-ray dose (flux was $\sim 10^{13}$ ph/sec/mm^2) at the sample. Rat-tail tendon in its native, unaltered state has a characteristic regular axial D-period of 67±0.5nm (Stinson and Sweeny, 1980). The small-angle meridional X-ray diffraction patterns produced after exposure to an intense dose of X-rays showed an alteration in the D-period (from 67 nm up to 79 nm and from 67nm to 61nm). Figure 6.1 shows the production of the new axial periodicities in addition to the standard 67nm D-period, and the broadening of diffraction peaks in the direction parallel to the meridian of the diffraction peaks. Figure 6.1 shows two-dimensional X-ray diffraction patterns collected from collagen fibrils for (a) unaltered fibrils (1st frame) and (b) fibrils exposed to an intense X-ray dose for 20 minutes.
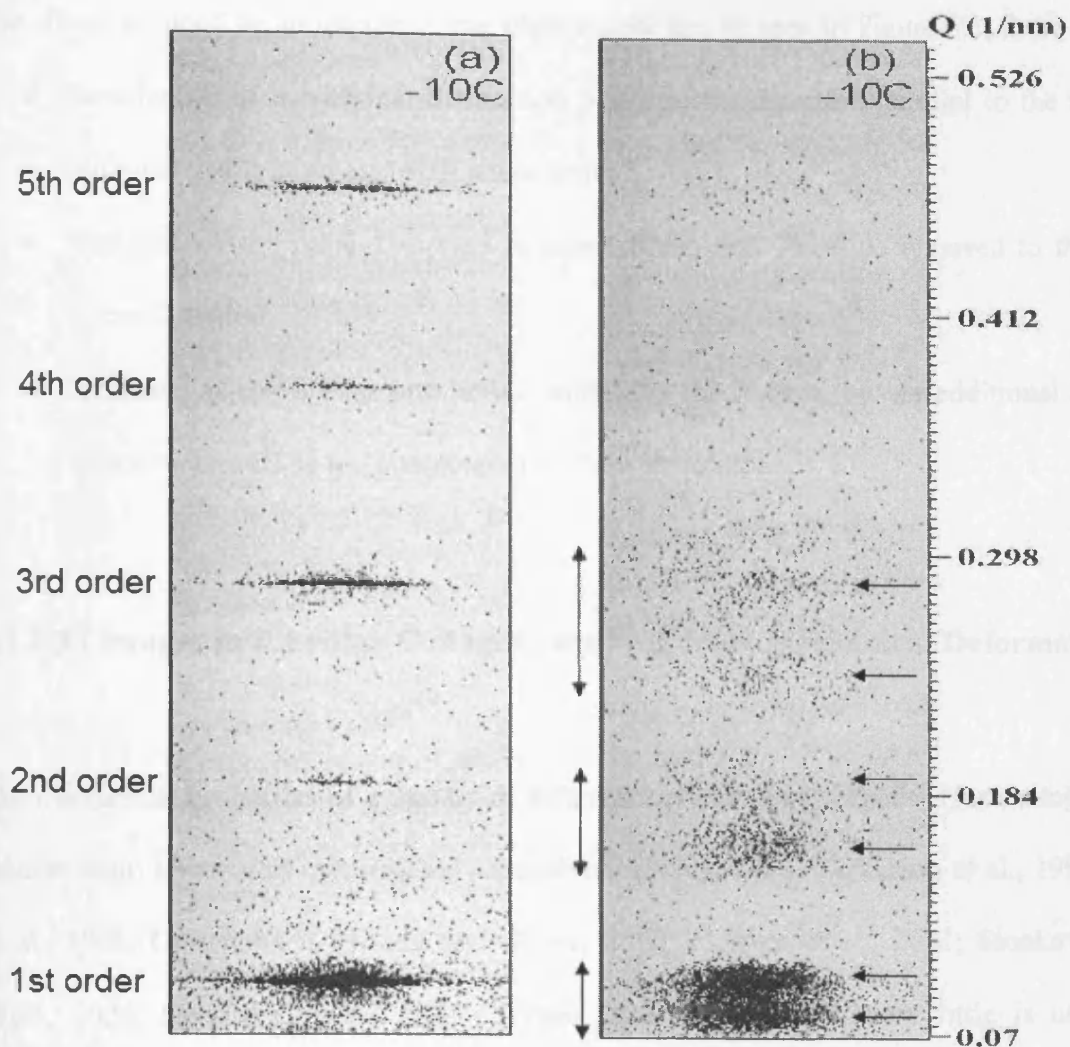
Figure 6.1: Low angle X-ray diffraction pattern of collagen fibrils for (a) unaltered fibrils (1st frame) and (b) fibrils exposed to an intense X-ray dose for 20 minutes. The region of the diffraction space corresponding to the 1st to 5th orders of collagen axial diffraction are shown. The vertical arrows (on 1st, 2nd and 3rd orders) demonstrate the broadening of the reflections in the direction parallel to the meridian of the diffraction peaks. The horizontal arrows (on 1st, 2nd and 3rd orders) mark the presence of additional reflections at new D-period values.

The effects induced by an intense X-ray photon dose can be seen in Figure 6.1, these include:

- Broadening of meridional diffraction peaks in the direction parallel to the meridian with increasing dose and diffraction order.

- Variance of the axial D-period between 61nm and 79nm as opposed to the native 67nm D-period.

- Evidence of more than one lattice bathed by the X-rays (i.e. an additional D-period structure as well as the characteristic 67nm structure).

6.1.1.3 Changes in Fibrillar Collagen resulting from Mechanical Deformation

The mechanical properties of a variety of different collagen-based tissues (for example, bone, tendon, skin) have been investigated extensively (Parry, 1988; Parkinson et al., 1997; Fratzl et al., 1998; Christiansen, Huang and Silver, 2000; Holmes et al., 2001; Sionkowska and Wess, 2004; Hendriks et al., 2005; Screen, 2008). However, very little is understood regarding the deformation mechanisms at the fibrillar and subfibrillar level. The application of tension has been demonstrated to increase the fibrillar D-period from its characteristic 67nm to approximately 68.8nm, with failure occurring after this point (Mosler et al., 1985). Figure 6.2 shows the meridional peaks as a function of stress on the tendon measured using SAXS.
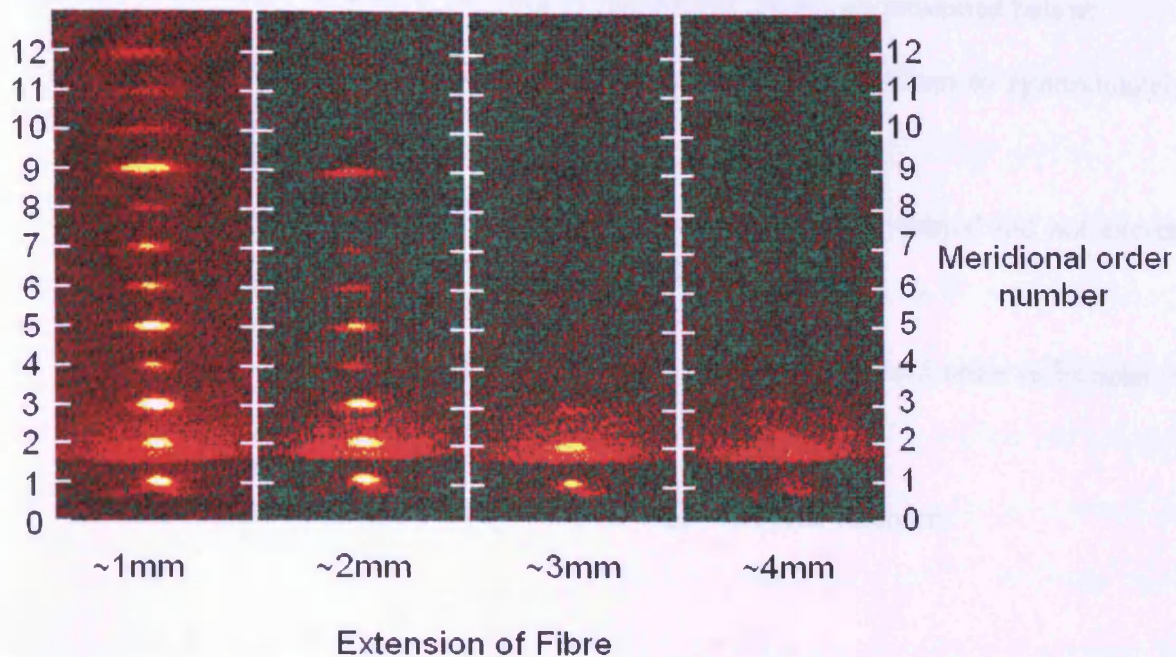
Figure 6.2: Two-dimensional X-ray diffraction patterns for rat-tail tendon collagen subjected to an extension of approximately 1mm, 2mm, 3mm and 4mm. The meridional reflections of collagen are numbered (Fratzl et al., 1997). The first diffraction order has been attenuated by a factor of 10 in order to prevent saturation.

It has been demonstrated that the change in the D-period by the induction of stress is reversible as long as the final D-period does not exceed 68.4nm (Folkhard et al., 1987). The application of stress also caused an alteration in the relative intensities of the meridional reflections. Many studies have shown that there is a change in the intensities of the second and the third order reflections in the meridional diffraction patterns of stretched tendon fibres (Mosler et al., 1985).

A summary of the observed effects induced by mechanical loading is presented below:

- An increase in the fibrillar D-period from its characteristic 67nm to approximately 68.8nm.

- The induction of stress was reversible as long as the final D-period did not exceed 68.4nm.

- An observed change in the intensities of the second and the third order reflections in the meridional diffraction patterns of stretched tendon fibres.

- An observed attenuation of the intensity of higher diffraction orders.

6.1.2 Proposed Explanations for the Changes in Fibrillar Collagen as Observed by X-ray Diffraction

This section discusses the possible theories for the changes at the fibrillar level in the two-dimensional X-ray diffraction patterns of collagen shown in section 6.1.1. Three external factors that are shown to affect the fibrillar structure of collagen have been outlined: drying, X-ray irradiation and mechanical damage; this section will discuss the proposed explanations for these changes.

6.1.2.1 Proposed Explanations for the Changes in Fibrillar Collagen resulting from Drying

The key alteration seen in the fibre diagram for dry rat-tail tendon collagen is the shortening of the D-period from the characteristic 67nm D-period to around 65nm (Stinson and Sweeny, 1980; Wess and Orgel, 2000). It was reported that this shortening in the D-period was not

entirely dependent on the pitch shortening of the collagen helix because this would only alter the position of meridional reflections but no their intensity; it could also arise due to the relative axial sliding of the collagen molecules within a fibril (Wess and Orgel, 2000).

Previous studies have suggested that the overlap region from the Hodge-Petruska model increases on drying from approximately 0.4D to 0.78D, where D is the D-period (Bear and Morgan, 1957; Chandross and Bear, 1973). The mechanism for this is unclear; but it was suggested that an 8% contraction in the D-period could produce this effect (Bear and Morgan, 1957). It has been proposed that the increase in overlap region could be due to a shortening and compaction of the gap region on drying (Chandross and Bear, 1973). Although many explanations have been presented to date, no satisfactory structural model that explains the changes observed in the X-ray diffraction patterns has been produced.

6.1.2.2 Proposed Explanations for the Changes in Fibrillar Collagen resulting from X-ray Irradiation

The major effect observed upon the application of an intense X-ray dose to tendon collagen was a broadening of the reflections in the direction parallel to the meridian of the diffraction peaks. Also seen was a splitting of the Bragg reflections, producing two discrete reflections with different D-periodic values. It is proposed that this may result from an alteration in the lattice structure as opposed to a variation in the finite lattice size; this is because the effect of broadening increases with diffraction angle, corresponding to the accumulation of various different D-periods in real space. Furthermore, the alteration of the diffraction peak integrated intensity indicates a change in the electron density profile of the periodic structure i.e. an alteration of the number and relative position of amino acids in the D-period. Therefore, it is postulated that the variation in the D-period between 61nm and 79nm occurs

due to a change in lattice strain, as opposed to a systematic increase in the axial rise per residue along the collagen helix. The total diffraction intensity within a region of diffraction space was also seen to decrease as a function of the scattering angle, indicating a reordering of the supramolecular structure that can be represented by the relative shearing of molecular structures within individual fibrils; this would result in the decrease of the projected scattering contrast variation within each axial repeat.

6.1.2.3 Proposed Explanations for the Changes in Fibrillar Collagen resulting from Mechanical Deformation

The key effect observed upon mechanical deformation is the increase in the D-period, implying that a lengthening of the fibrils occurs with strain (Mosler et al., 1985). However, the observed change in the relative intensities of the meridional reflections infers that there is a change in the relative length of the gap and overlap regions (i.e. the axial electron density profile). Mosler et al. (1985) proposed that the fibril strain does not arise solely from the homogeneous molecular elongation of the axial rise per residue in the helix (which would keep the gap and overlap region constant) but is also a result of sliding between the triple helical molecules (Mosler et al., 1985). Calculations have shown that the initial deformation from 67nm to 67.6nm relates to the stretching of the triple helices. For the application of larger strains to 68.8nm and breakage, sliding of the triple helices relative to each other is relevant (Folkhard et al., 1987).

Deformation of both the fibril and the triple helix has also been considered (Sasaki and Odajima, 1996a; Sasaki and Odajima, 1996b). A model was constructed to separate the effect of the molecular elongation from the effect of molecular slippage; the conclusion was that molecular elongation is a more dominant mechanism than molecular slippage. However,

174

no specific model can account for what is a critical aspect of molecular behaviour in stress bearing tissues.

6.1.3 Proposed Alterations for the Changes in Fibrillar Collagen as Observed by X-ray Diffraction

The previous sections have demonstrated the ability of collagen to undergo many structural changes from a variety of factors. Attempts have been made to explain these structural changes although no definitive model has been made and there is clearly room for improvement. The following key structural changes have become apparent in the deformation of collagen architectures within fibrils:

- The induction of local strain and lattice distortion.

- The shearing of laterally adjoined molecules relative to each other.

- Breakages in the amino acid chains of the collagen molecules.

- The induction of molecule tilting within the staggered array of collagen molecules.

- A change in the axial rise per residue.

Figure 6.3 shows cartoons of the proposed deformation mechanisms of collagen that may occur and the corresponding projected electron densities. The projected electron densities for the structures shown in (e) and (f) are complex and involve more than one axial repeat; and cannot therefore be represented in a single D periodic description. The structure shown in (e) illustrates a variation in the gap region between longitudinally adjoining molecules resulting in a shorter D-period than 67nm. The model constructed in this chapter induces tilting within the gap region only (and not within the overlap region). The structures in (e) and (f) differ from unit cell to unit cell unlike other proposed structures in Figure 6.4; this is illustrated in
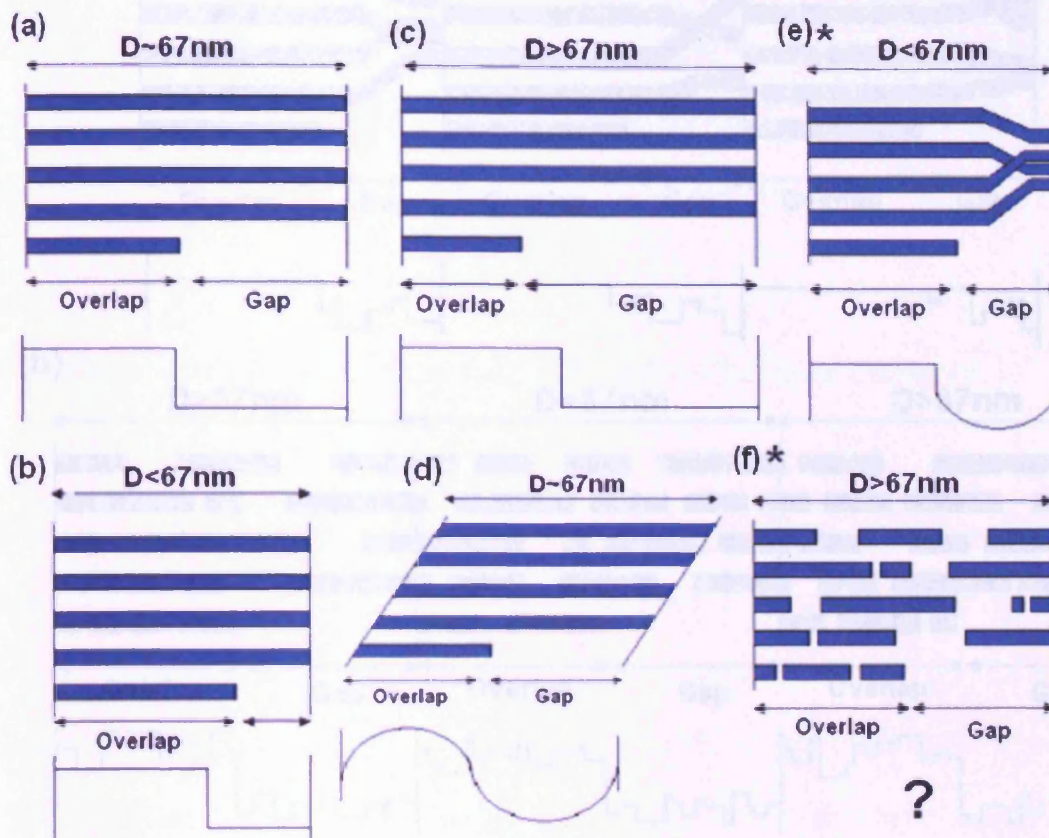
Figure 6.4.

Figure 6.3: Proposed possible deformation mechanisms of collagen with the theoretically projected electron density step function below. (a) Represents the standard Hodge-Petruska quarter-stagger model with a D-period of approximately 67nm. (b) and (c) Demonstrate molecular elongation or compression resulting in a change in the D-period to a value shorter or longer than 67nm. (d) Illustrates a deformation change due to sliding of the collagen molecules relative to one another. (e) Shows a variation in the gap region between longitudinally adjoining molecules resulting in a shorter D-period than 67nm. (f) Represents the fracture of molecules resulting in a longer D-period than 67nm.
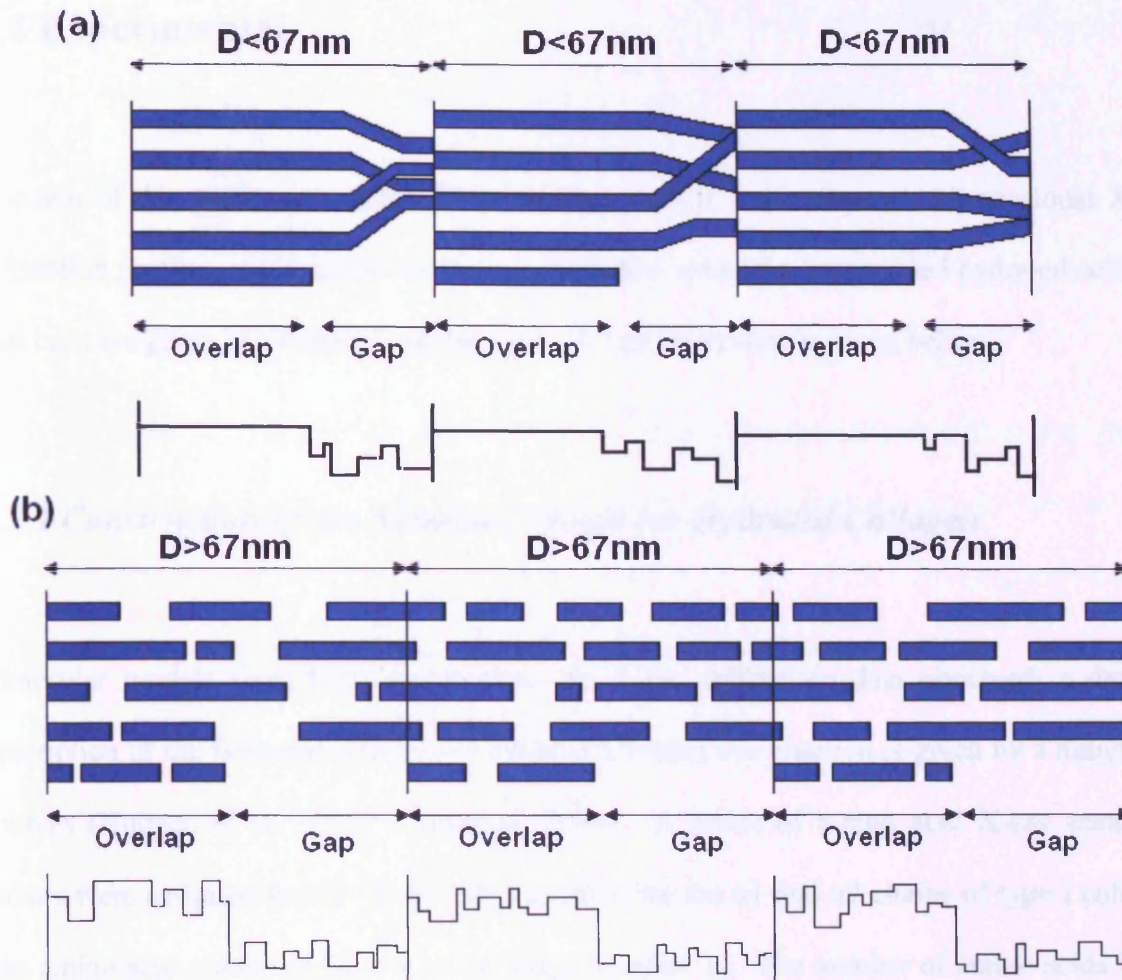
Figure 6.4: Illustrates two structures from Figure 6.4 where the structures are different for every unit cell with the theoretically projected electron density step function below. (a) Shows a variation in the gap region between longitudinally adjoining molecules and (b) represents the fracture of molecules.

A suitable way forward in explaining these changes in fibrillar collagen is the use of X-ray diffraction in combination with computer-aided molecular models. Each model of distortion from the standard gap and overlap arrangement can be constructed by simulating diffraction using the amino acid sequence and corresponding scattering factors, which can then be compared with experimental diffraction patterns and their intensities.

6.2 Experimental

The aim of this study is to construct molecular models to simulate one-dimensional X-ray diffraction profiles. Full details on how the standard model for unmodified hydrated collagen was built are given in Chapter 3, section 3.5. A brief overview is given below.

6.2.1 Construction of the Standard Model for Hydrated Collagen

Molecular models were built to simulate the X-ray diffraction data observed; a detailed description of the fundamentals of the molecular model construction is given by a number of sources (Hulmes et al., 1977; Cameron, 2004). A series of amino acid X-ray scattering factors were assigned for the molecular sequence for the $\alpha 1$ and $\alpha 2$ chains of type I collagen (the amino acid scattering factors are given in Chapter 3). The number of amino acids in the repeating D-periodic unit were produced, and when projected onto a one-dimensional profile exhibited the characteristic gap and overlap features (Hodge and Petruska, 1963). The models also accounted for the non-helical conformation of the telopeptide regions (Wess et al., 1998ab; Orgel et al., 2000). The C terminal telopeptide is 25 residues long and is arranged in a folded conformation while the N terminal telopeptide is positioned in the first 16 residues and is axially contracted (Orgel et al., 2000). The resultant structure was then Fourier transformed to give a set of structure factors represented as complex conjugate terms that were further combined to simulate the scattering of a fibrillar group of fibrils containing a specific or varied molecular configuration. This structure was then compared to the observed linear profile of the meridional X-ray diffraction data. The model intensity terms were represented graphically as a linear profile of the intensity at the corresponding

reciprocal lattice point with a convolved Gaussian profile that is indicative of the Bragg peak profile broadening due to the X-ray beam breadth.

6.2.2 Construction of the Theoretical Models

A series of theoretical models have been constructed to simulate the proposed change mechanisms suggested in section 6.1.3. These mechanisms include an induction of local strain, shearing laterally adjoined molecules relative to each other, breaking the collagen molecule amino acid chains and the induction of molecule tilting within the gap region of the staggered array of collagen molecules.

6.2.2.1 The induction of local strain

One proposed mechanism which may result in a change in the collagen fibrillar structure is the induction in local strain. Figure 6.5 shows a cartoon of five segments of the molecules from native collagen, and the corresponding electron density profiles for structures with (a) a 67nm D-period, (b) a 65nm D-period and (c) a 69nm D-period.
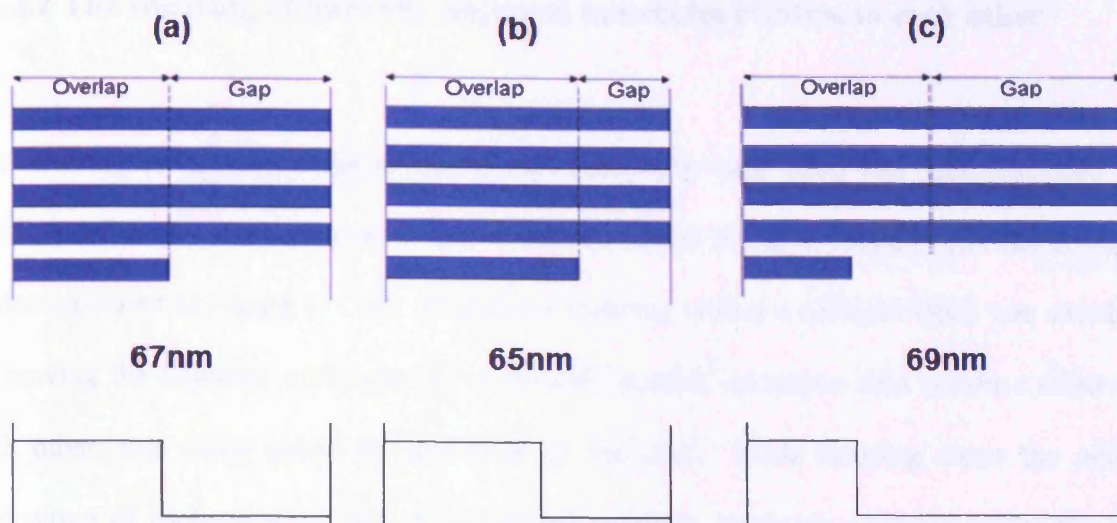
Figure 6.5: Cartoons illustrating the effect of an induction in local strain within a collagen fibril. Shown are the five segments of the molecules from collagen with (a) a 67nm D-period, (b) a 65nm D-period and (c) a 69nm D-period. Also shown for the three structures with a different D-period are the corresponding electron density profiles for these structures.

The model to account for local strain was produced using a number of structures with different D-period values, by varying the number of amino acids per repeat, assuming the axial rise per residue is fixed at 0.286nm. For example, a 67nm D-period structure has 234 amino acids per repeat (67/0.286); a 65nm D-period structure has 227 amino acids per repeat (65/0.286); and a 69nm D-period structure has 241 amino acids per repeat (69/0.286). The model produces each individual structure which has a different electron density profile and lattice length. Each structure is Fourier transformed individually and the intensity factors mapped onto the scattering vector; resulting in broader peaks.

6.2.2.2 The shearing of laterally adjoined molecules relative to each other

The shearing of laterally adjoined molecules relative to each other has been proposed as a possible deformation mechanism that may cause changes in the structure of fibrillar collagen; as demonstrated in Figure 6.4 (d). Molecular shearing within a collagen fibril was simulated by moving the adjacent molecules by a variable number of amino acid residues relative to each other; this value could be specified by the user. Such shearing alters the relative disposition of molecules so that the projected electron density is smeared whilst the axial length of the D period remains constant.

6.2.2.3 Breakages in the amino acid chains of the collagen molecules

A further mechanism proposed to cause an alteration in the fibrillar structure of collagen is the induction of breaks in the collagen molecules within a fibril. The model to simulate breaks in the amino acid chains of the collagen molecules was created through the modification of the model for native collagen. The standard model constructs the amino acid chains to be 1170 amino acids long; this was modified to include a series of breaks in the amino acid chain. Random positions for breaks and a value to displace the amino acid chains relative to its original position were chosen using a random number generator. These breaks provide a mechanism for the elongation of the molecules and thence the axial repeat to be extended. The extension in the axial repeat length is shown in Figure 6.6.

(a)

(b)
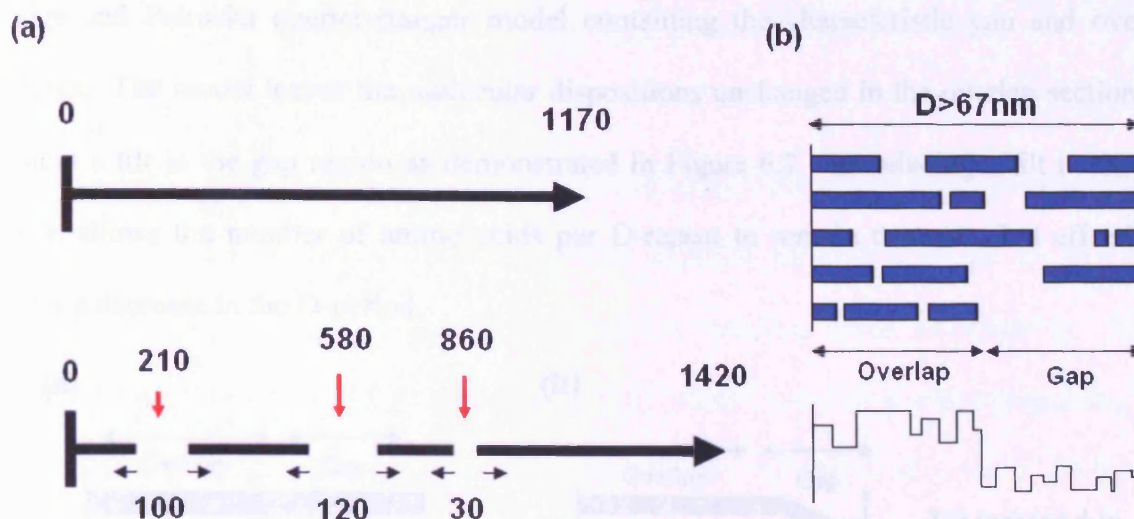
Figure 6.6:   Graphical representation of simulated amino acid chain breaking.   The amino acid chain is randomly broken (at 210, 580 and 860 amino acid residues along the chain for this case).   The random number generator is used once again to decide on how much the chain is displaced by (100, 120 and 30 amino acid residues in this case).   This would allow the molecules to be extended to produce axial repeat lengths observed in the data.

6.2.2.4 The induction of molecule tilting within the staggered array of collagen molecules

It has been suggested that a decrease in the axial periodicity could be brought about by the tilting of molecules within a fibril which would produce an apparent shortening of the lattice in projection on to the fibre axis (Wess and Orgel, 2000).   Due to differences in molecular density in the D period, it is more likely that the molecular tilting rearrangements occur in the lower density gap region.   Molecular tilting at an angle to the fibril axis can be induced within the gap regions of the axially staggered model, which is constructed with the standard

182

Hodge and Petruska quarter-stagger model containing the characteristic gap and overlap features. The model leaves the molecular dispositions unchanged in the overlap section but induces a tilt in the gap region as demonstrated in Figure 6.7. Introducing a tilt in the gap region allows the number of amino acids per D-repeat to remain the same but effectively causes a decrease in the D-period.
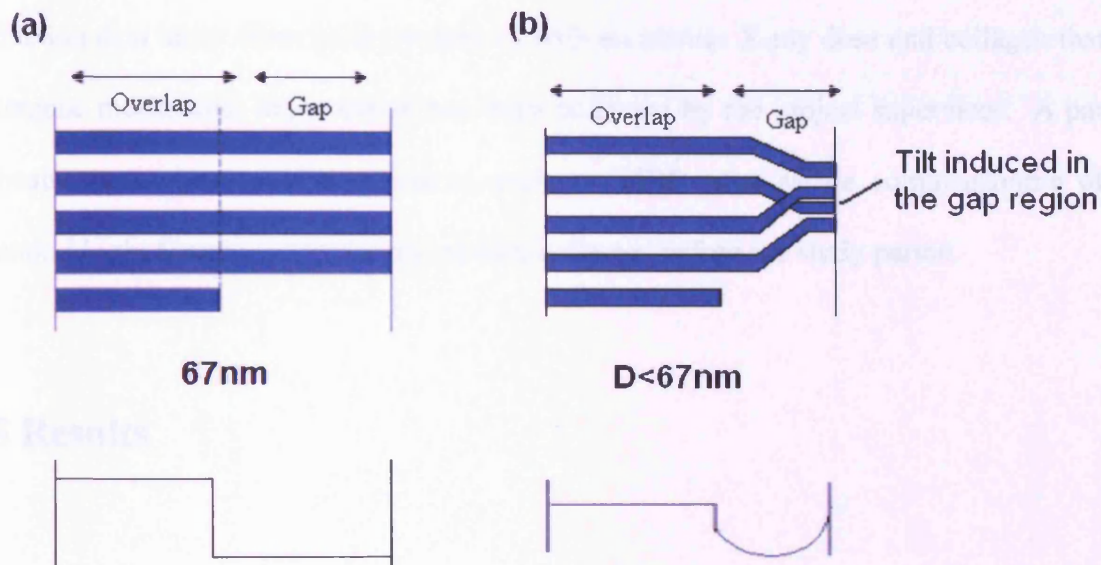
Figure 6.7: Demonstrates (a) the standard model for native collagen and (b) model for the inclusion of tilting of the molecules in the gap region. Tilting in the gap region results in a decreased D-period relative to the standard model.

If the changes in tilt direction and magnitude are not identical within each unit cell bathed by the X-ray beam, this will lead to a loss of diffraction intensity with scattering angle due to incoherence between cell contents. This model only considers tilting within the gap region due to evidence from foregoing research of other groups, although the possibility of tilting within the overlap cannot be discounted.

6.2.3 Collection of Experimental X-ray Diffraction Data

Experimental X-ray diffraction data has been collected for comparison with the models from collagen in a range of states; hydrated; dry and air-dried collagen (Chapter 4); and from collagen subjected to a variety of different relative humidity levels (Chapter 5). X-ray diffraction data taken from collagen treated with an intense X-ray dose and collagen that has undergone mechanical deformation has been collected by the project supervisor. A paucity of beamtime at intense X-ray sources such as ESRF prior to the commissioning of the Diamond Light Source led to the use of data collected before the study period.

6.3 Results

6.3.1 Analysis of the Standard Model for Hydrated Collagen

Before the X-ray diffraction images for the changes in the fibrillar structure of collagen can be modelled, the X-ray diffraction image for the native, unchanged, hydrated structure of collagen must be reproduced as a benchmark to validate the final models. Figure 6.8 (a) shows the first five meridional X-ray diffraction experimental reflections for hydrated rat-tail tendon collagen with the characteristic 67nm D-period. Figure 6.8 (b) shows the first five meridional X-ray diffraction computer-simulated reflections for a 67nm D-period structure corresponding to 234 amino acid residues per repeat. The comparison of the experimental and computer-simulated meridional X-ray diffraction reflections for hydrated collagen shows that the created model produces a good fit.

(a)

(b)
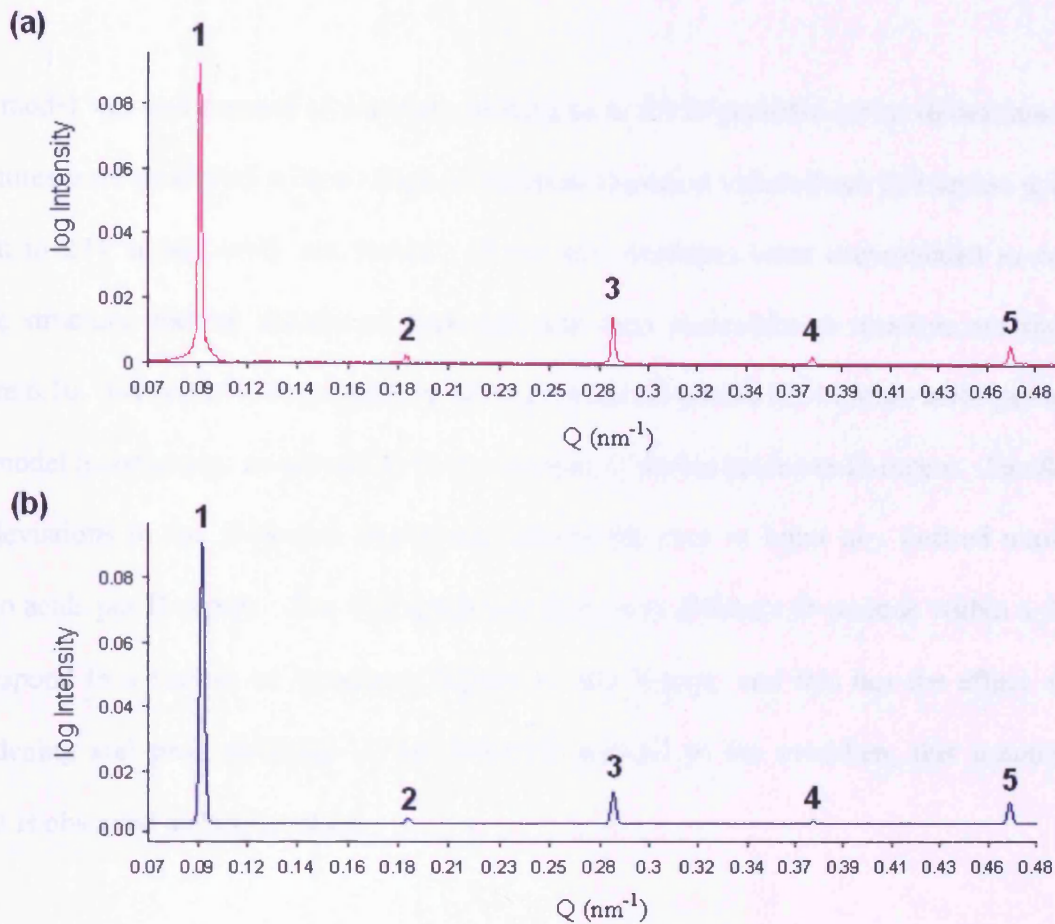
Figure 6.8: **(a) An experimental meridional X-ray diffraction pattern for a 234 amino acid structure (D=67nm) and (b) a simulated meridional X-ray diffraction pattern for a 234 amino acid structure showing the first five orders of diffraction.**

6.3.2 Analysis of the Theoretical Models

Through successfully simulating the intensity terms corresponding to the hydrated structure of collagen it is possible to model further changes in fibrillar collagen. This forms a platform from which changes can be simulated and effects compared to experimental data.

6.3.2.1 The induction of local strain

This model was constructed to simulate deviations in the D-periodic lattice dimensions. Ten structures were produced with a range of different D-period values from 234 amino acids per repeat to 274 amino acids per repeat. These ten structures were accumulated to create a single structure; the ten individual structures and their accumulative structure are shown in Figure 6.10. Instead of every structure having a 67nm D-period (234 amino acids per repeat), this model incorporates an alteration in the number of amino acids per D-repeat. To allow for the deviations in the D-period, the model allows the user to input any desired number of amino acids per D-repeat. The accumulation of various different D-periods within a data set correspond to a variety of structures bathed by the X-rays, and this has the effect of peak broadening and peak splitting in the direction parallel to the meridian; this accumulative effect is observed as lattice strain.
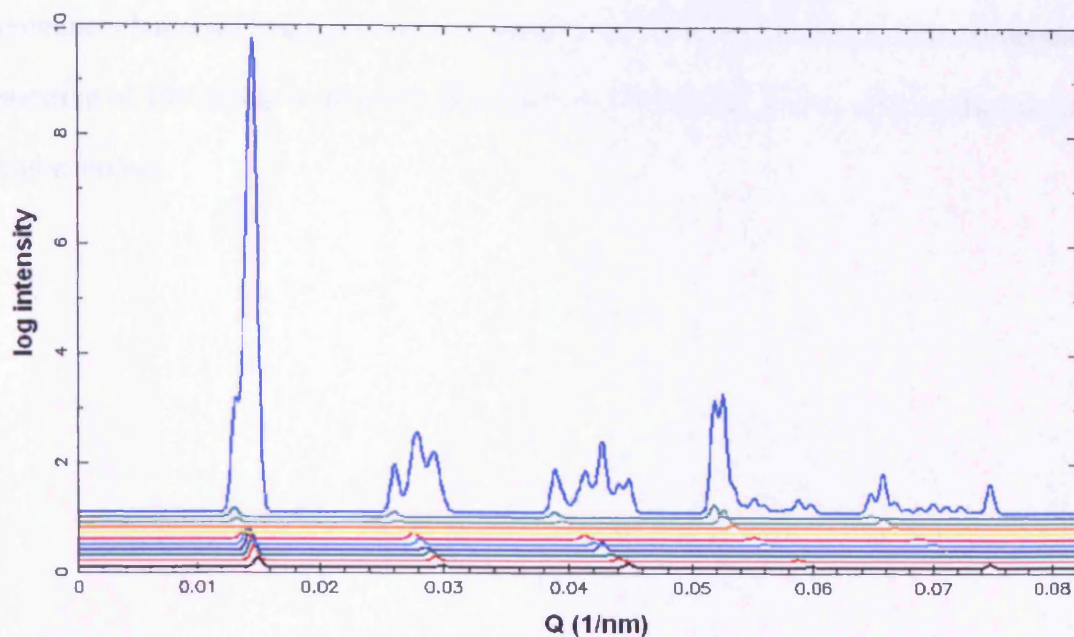
Figure 6.9: **Simulated meridional X-ray diffraction pattern for ten different structures from 234 amino acids to 274 amino acids at an increment of four amino acids per structure. This shows the first five orders of collagen axial diffraction and the accumulative structure.**

6.3.2.2 The shearing of laterally adjoined molecules relative to each other

Molecular shearing within a collagen fibril is simulated by moving the molecules by a variable number of amino acid residues, a value that can be specified by the user. This shear value is used to change the position of the next molecule within a fibril. If no shear value is applied, the next collagen molecule is positioned the standard D-period apart (where D=67nm for a 234 amino acid repeating structure). The introduction of an amino acid shearing causes a decrease in the peak intensities due to the loss of contrast in the repeating objects and the eventual loss of peaks at large values of shearing, while the position of the peaks remains unchanged. At a shear value of 50 amino acid residues (Figure 6.10a) the first order is still

187

prominent but significantly lower in intensity, while the higher orders have disappeared. At a

shearing of 100 amino acid residues (Figure 6.10b) further loss is seen in the intensity of the

higher orders.
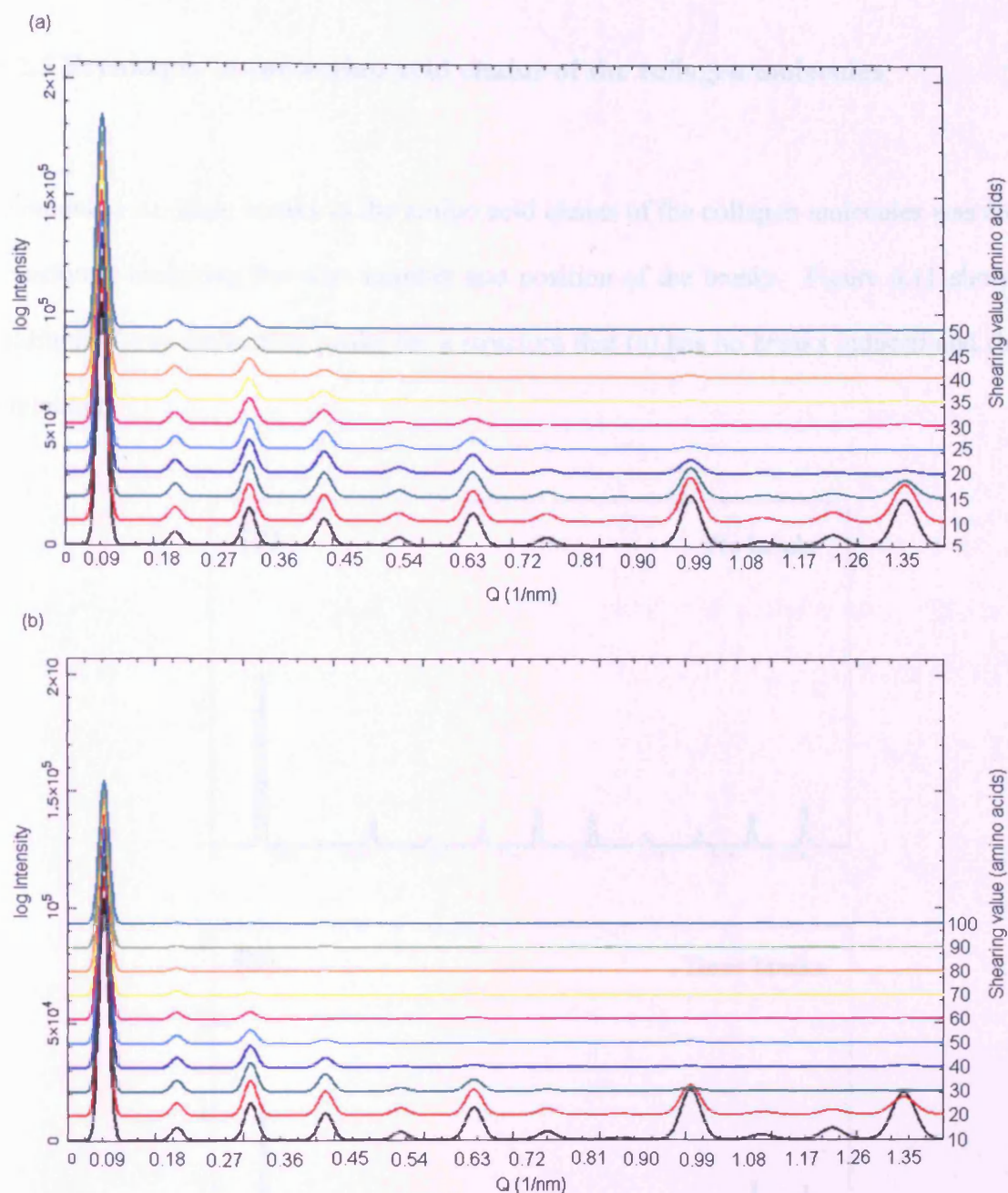
Figure 6.10: Simulated meridional X-ray diffraction profiles for 234 amino acid structures showing the first 12 orders of diffraction. (a) Shearing of 50 amino acid residues is applied. The bottom profile corresponds to a 5 amino acid shear while the top profile relates to a 50 amino acid shear. Each profile is incremented at a 5 amino acid shear. (b) Shearing of 100 amino acid residues is applied. The bottom profile corresponds to a 10 amino acid shear while the top profile relates to a 100 amino acid shear. Each profile is incremented at a 10 amino acid shear.

6.3.2.3 Breakages in the amino acid chains of the collagen molecules

The model to simulate breaks in the amino acid chains of the collagen molecules was created by randomly assigning the size, number and position of the breaks. Figure 6.11 shows the meridional X-ray diffraction peaks for a structure that (a) has no breaks induced and (b) has been broken.
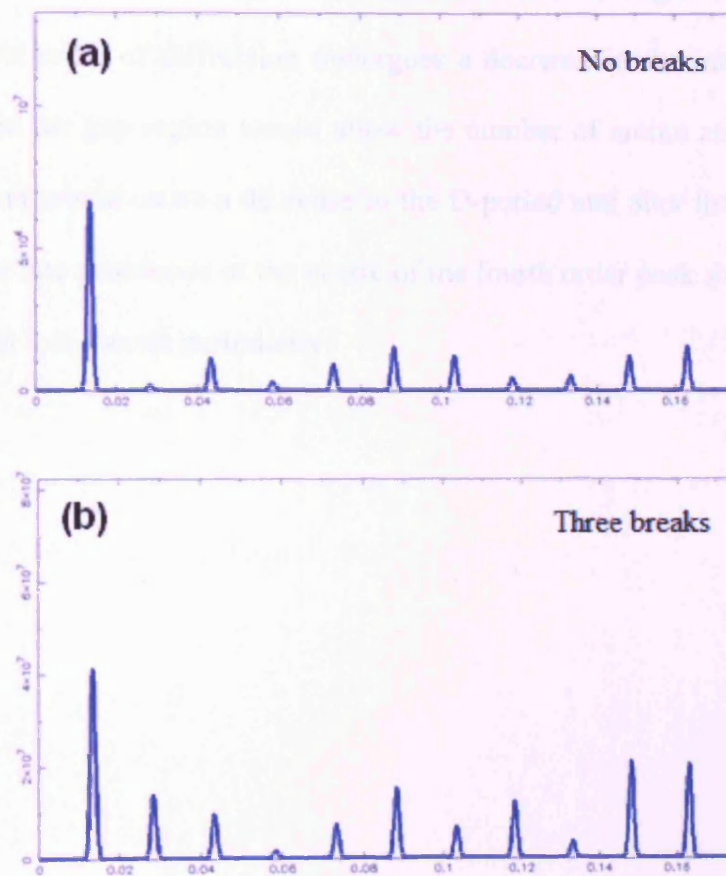
Figure 6.11: (a) Shows the meridional X-ray diffraction peaks for a structure that has no breaks induced and (b) a structure that has been broken in three places. The broken structure shown in (b) includes three breaks positioned at 10, 745 and 858 amino acids along the chain. These three breaks where displaced by 35, 84 and 4 amino acids respectively.

6.3.2.4 The induction of molecule tilting within the staggered array of collagen molecules

An angle increment can be induced within the gap regions of the axially staggered model which is constructed with the standard Hodge and Petruska quarter-stagger model containing the gap and overlap characteristic features. Figure 6.12 shows the meridional X-ray diffraction peaks for 10 structures tilted between 5° and 50° at angle increments of 5° per structure. The first order of diffraction undergoes a decrease in the intensity of the peak. Introducing a tilt in the gap region would allow the number of amino acids per D-repeat to remain the same but would cause a decrease in the D-period and alter the projected electron density. The black line positioned at the centre of the fourth order peak shows the movement in the peak position to a shorter periodicity.
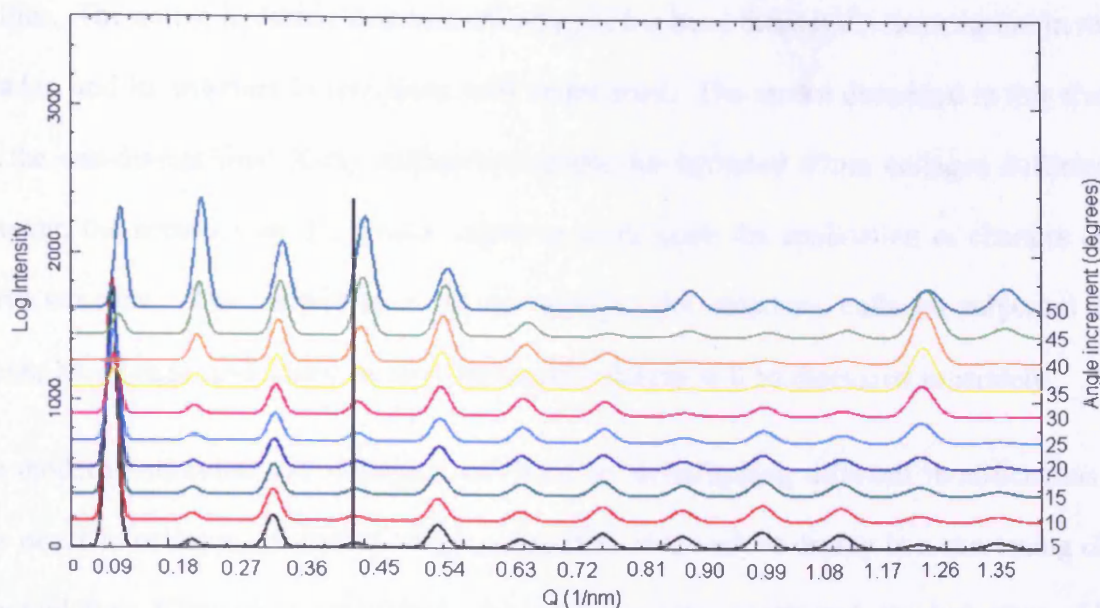
Figure 6.12: A simulated meridional X-ray diffraction peak for 10 different structures with a different angle introduced to the gap regions of the 10 structures. All structures have a length fixed at 234 amino acids and the first 12 orders of diffraction are shown. The first structure (bottom profile) includes an angle of 5° with further structures produced by tilting at angle increments of 5°. The final structure (top profile) demonstrates the effect of an angle of 50° in the gap region.

6.4 Discussion

Structural modifications were applied to the standard structure of collagen to simulate the changes seen in the fibrillar structure of collagen. This chapter has shown the versatility and value of constructing computer simulated molecular models to evaluate structural changes in native fibrillar collagen, and demonstrated the adaptability of the models, helping to explain the structural changes to collagen on drying, intense X-ray dose and mechanical deformation. It is important to note that the computer-simulated models provide only one possible explanation for the changes seen in the experimental one-dimensional X-ray diffraction

profiles. The native hydrated structure of collagen has been thoroughly investigated in recent decades, and its structure is relatively well understood. The model described in this chapter fits the one-dimensional X-ray diffraction profile for hydrated 67nm collagen sufficiently; however, the accuracy of the model begins to wane upon the application of changes to the native structure. The comparisons for the collagen dry structure, collagen subjected to an intense X-ray dose, and mechanically deformed collagen will be discussed separately.

The model to stimulate dry collagen was built by investigating different modifications that may occur in collagen on drying. The main effect observed on drying is a shortening of the D-period from 67nm to around 65nm. From the models constructed, the induction of local strain or the introduction of tilting within the gap region can be used to simulate this effect. A decrease in the number of visible meridional reflections was observed in the diffraction pattern upon drying, from approximately 140 visible reflections in the hydrated state, to approximately 40 reflections in the air-dried state, which may be explained by the shearing of laterally adjoined molecules relative to each other. The structural model to account for shearing resulted in a decrease in the number of visible reflections at higher orders in the meridional series (shown in Figure 1.11). On an individual basis, none of these modifications can sufficiently explain all the structural changes that occur during the drying of collagen. It is proposed that the dry structure of collagen could be explained by a combination of these modifications (tilting, shearing and the induction of local strain).

Many features present in the X-ray diffraction pattern for dry collagen have been unexplored; one such feature is the strong fluctuations of intensity that corresponds to a damped sinusoidal wave with an oscillating periodicity that covers four meridional peaks. This indicates that the fidelity of the molecular transform has been compromised whilst the lattice remains intact. Although it is beyond the scope of this thesis, it is attractive to speculate that the changes in the tilt of the gap region could produce a D periodic function with a length of

around 0.25D. However with sufficient variation between unit cells bathed by the X-ray beam, this feature is poorly defined and causes the molecular transform to contain little detail and hence presents in the molecular transform with relatively few detailed harmonic components.

The molecular models constructed in this Chapter have begun to explain many of the alterations in the diffraction pattern of collagen exposed to an intense dose of X-rays. One observation in the X-ray diffraction pattern for X-ray irradiated collagen is a broadening and splitting of the diffraction peaks, which could be explained by the induction of local strain within the lattice. The decrease in the diffraction intensity as a function of the scattering angle observed may be a result of the shearing of laterally adjoined molecules relative to each other, which would produce an effect of attenuation. The molecular model constructed was able to fit reasonably all of these alterations, simulating the general factors of the diffraction peaks observed. In conclusion the diffraction peaks observed appear to result from a variation in lattice strain and the shearing of laterally adjoined molecules relative to each other.

In the simulated X-ray diffraction patterns for mechanically strained collagen, an overall lowering in the intensity values of the reflections takes place with respect to scattering angle, possibly due to the shearing of laterally adjoined molecules relative to each other. However, this does not account for the increase in D-period, which could be attributed to the introduction of breaks within the amino acid chains of the collagen molecules.

6.4.1 Conclusion

Many structural changes occur at a molecular level of collagen fibrillar packing upon deformation. X-ray diffraction is a useful non-destructive technique for investigating changes at a molecular level in collagen and in combination with molecular modelling can begin to explain the structural changes and the causal factors. X-ray diffraction and molecular modelling have been found to complement each other and when combined assist in furthering our understanding of the variations at the molecular level in collagen. Although the work here goes a long way to show that the real space deformations suggested can account in a large part for the changes observed in the fibre diagram the future work required here is the combination of these modifications to produce an accurate and quantitative fit with the data. Due to the paucity of the diffraction data available there are probably many combinations of deformations that will provide an adequate fit with the data collected, therefore other supporting evidence will be required to be sourced in order to produce a robust estimation of the various contribution of physical changes to molecular structure.

Chapter 7: Determining the Nanostructural Integrity of the Domesday Book

7.1 Introduction

7.1.1 Background of the Domesday Book and historical significance

The Domesday Book was a land survey commissioned by William the Conqueror in 1086 and is a valuable part of English heritage. William commissioned the text in response to a threat of invasion from Denmark. The book included information collected on the land and resources of the land held by the King and his tenants. The exact purpose of the Domesday inquisition was not recorded, but contemporaries believe that the primary object was the collection of taxes (Forde, 1986).

The information collected was recorded onto parchment and compiled into two separate volumes: 'Great Domesday' and 'Little Domesday' which are shown in Figure 7.1 (Forde, 1986).
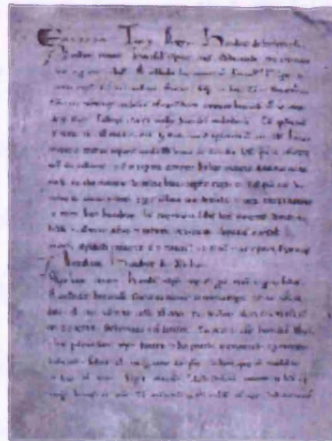
| Great Domesday and Little Domesday | Little Domesday (Catalogue reference E 31/1) | Great Domesday (Catalogue reference E 31/2) |

Figure 7.1: Images of the two volumes of the Domesday Book, Great Domesday and Little Domesday including two sample pages (www.nationalarchives.gov.uk/domesday).

Great Domesday contains information about all counties except the four northern counties, some large towns and the eastern part of the country, which is covered by Little Domesday. The counties of Essex, Norfolk and Suffolk are covered in further detail in Little Domesday, which was meant to be the penultimate version of the text for these counties before inclusion in Great Domesday. The writing itself provides a wealth of knowledge and in addition the parchment it is written on can also supply us with vitally important information. Preservation of these documents for future generations through prevention of degradation is therefore of great importance. This degradation may occur due to a wealth of different external factors, including inappropriate temperature levels, relative humidity mis-use, radiation damage (in particular UV light), mechanical damage (from excessive handling or general wear and tear) and microbiological growth (resulting from elevated temperatures and relative humidity). The two volumes: 'Great Domesday' and 'Little Domesday' have survived over 900 years of English history and are currently held in a specially made chest at The National Archives in Kew, London (http://www.nationalarchives.gov.uk/domesday/). In 1986 to mark the 900th

anniversary of the volumes, further investigation and study was carried out on both volumes, documenting their condition. This investigation focused on evaluating and improving upon previous conservation work carried out in 1952, a time when knowledge and access to materials was limited. During this study further repair work was performed and the books were photographed (to produce a facsimile) and rebound (Forde, 1986). The 1986 campaign included extensive visual documentation, but due to the restricted range of techniques available at the time and the quantity of sample that would have been required, no scientific analysis was completed.

A further study into the condition of the books was proposed in 2006, twenty years after the initial study to investigate how the volumes had degraded over this period. Since the investigation in 1986 there have been a number of significant advances in non-invasive and micro-invasive analysis, creating an opportunity for further examination to be conducted. This allowed, for the first time, a structural survey of the molecular structure to be completed using X-ray diffraction on samples sourced from both Great Domesday and Little Domesday. This study also included visual and biochemical analysis conducted by the School of Conservation in Denmark. This chapter outlines the work conducted on the Domesday Book using X-ray diffraction.

A number of previous studies have been conducted on parchment using conventional X-ray diffraction as a technique (Wess and Orgel, 2000; Wess et al., 2001; Kennedy et al., 2003; Kennedy et al., 2004c; Maxwell et al., 2006; Gonzalez and Wess, 2008b). Conventional X-ray diffraction generally involves the alignment of the sample perpendicular to the direction of the X-ray beam, with a beam size in the region of 200μm producing an image consisting of the composite diffraction features from the entire thickness of the sample. Microfocus X-ray diffraction uses a smaller beam of approximate size 2μm × 6μm to allow for surface-to-surface transmission analysis of parchment samples including the internal stratigraphy and

microtexture, where up to 200 images can be taken in a cross-sectional scan of a ~300μm thick parchment sample. A microdiffraction study on a Central Mexico style pictograph demonstrated the scope and versatility of the technique where it was shown that microdiffraction of a 10μm thick sample was able to produce scattering of sufficient intensity during a short timescale of one minute (Wess et al., 2001). It also provides information about the structure of collagen and its hierarchical arrangements from the molecular structure to the organisation of fibres in a tissue. The advantages of microfocus X-ray diffraction are its non-invasive manner and its ability to examine the structure of exceptionally small samples measuring a few microns in size. This makes the technique of microfocus X-ray diffraction extremely practical for the investigation of historically valuable artifacts including the Domesday Book. This chapter outlines the X-ray diffraction work conducted as part of this large-scale international collaborative report on the Domesday Book.

7.2 Experimental

7.2.1 Sample Preparation

The National Archives has entrusted us with nine samples taken from 'Little Domesday' and 'Great Domesday'. Extensive sampling was not possible from the Domesday Book due to its valuable and irreplaceable nature, so surface scrapings (weighing less than 0.1mg) were therefore taken from the corium (flesh side) throughout the volumes. Samples were taken from both volumes of the Domesday Book as well as the verso (left hand) and recto (right hand) sides of both volumes. The samples were sourced as scrapings from the surface of the parchment and were sub-millimeter in size and approximately 50 microns in thickness. Table

7.1 provides information regarding the Domesday Book samples used in this chapter. In addition to these samples, a control sample, sourced in a similar manner to the Domesday Book, was also subjected to investigation. The control sample was a legal document gifted by the National Archives of Scotland, the age was estimated from the date inscribed on the parchment sheet at the time of use, 1792.

Sample code	Book taken from	Position in book	Side of page used
GD1V*	Great Domesday	Page 1	Verso
LD1V*	Little Domesday	Page 1	Verso
LD109V*	Little Domesday	Page 109	Verso
LD183V*	Little Domesday	Page 183	Verso
LD412V*	Little Domesday	Page 412	Verso
GD203V*	Great Domesday	Page 203	Verso
GD202r*	Great Domesday	Page 202	Recto
GD382r*	Great Domesday	Page 382	Recto
LD449r*	Little Domesday	Page 449	Recto
1792[+]	Legal document,1792	N/A	N/A

Table 7.1: Table of the Domesday parchment samples gifted by the National Archives (*). The control sample was a legal document dating 1792 gifted by the National Archives of Scotland ([+]).

7.2.2 Microfocus X-ray Diffraction, ESRF ID18F

Microfocus X-ray diffraction was used to study the parchment samples due to its micron sized, intense flux X-ray beam. All microfocus experiments were carried out at the high

Parchment samples were scanned horizontally and vertically across the sample, collecting over 100 images in a region measuring a few microns in size. The size of the scanned region and number of images collected varied depending on the size of the sample sourced. Table 7.2 outlines sample information including the size of the scan area and the number of scans collected in this region.

Sample code	Number of images collected	Size of scan area (μm x μm)
GD1V*	102	0.4 x 0.4
LD1V*	126	1.2 x 1.2
LD109V*	108	0.2 x 0.2
LD183V*	201	0.4 x 0.4
LD412V*	100	0.4 x 0.4
GD203V*	110	0.2 x 0.2
GD202r*	101	0.2 x 0.2
GD382r*	101	0.4 x 0.4
LD449r*	100	0.2 x 0.2
1792 control+	100	0.8 x 1.4

Table 7.2: Table documenting the number of scans and the size of the scan area for all nine Domesday samples and the control sample. All scans were conducted in a grid like orientation (mesh scan).

The two-dimensional microfocus X-ray diffraction patterns were analysed using FibreFix software (see section 3.4.1). Using FibreFix, two-dimensional X-ray diffraction images were converted into one-dimensional linear traces.

brilliance synchrotron source at the European Synchrotron Radiation Facility in Grenoble, France on beamline ID18F. Further details of the beam station set up at ID18F are given in section 3.3.1.3. Compound refractive lenses (CRL) were used to generate a microbeam of size 2µm × 6µm (Snigirev et al., 1996). The wavelength of the X-rays was 0.086nm and the sample-to-detector distance was fixed at 213mm. To absorb the direct beam a tungsten backstop of diameter 500µm was used. The extremely small beam size allowed scans to be completed on all nine Domesday samples and a control parchment sample (dated 1792). The parchment samples were mounted on a goniometer, attached to a computer controlled motorised stage. Using the defocused beam and a high-resolution camera, an X-ray transmission image was recorded for each sample to observe the microscopic features. Images were taken of all ten samples using the high-resolution camera prior to starting the microfocus X-ray diffraction scans. A high-resolution camera was used to locate the sample and region due to be scanned. An image of sample GD382r taken with the high-resolution camera is shown in Figure 7.2 with the scan region highlighted as a red-boxed region. This region was scanned using a "mesh scan" which involves the collection of a series of images at points on a raster corresponding to specific movement of the sample in both horizontal and vertical directions in relation to the X-ray beam.
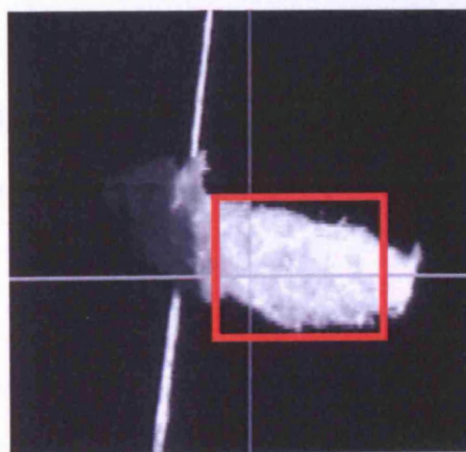
Figure 7.2: Image of sample GD382r mounted on a capillary in the beam. A mesh scan was carried out on the boxed region where over 100 images were collected.

Parchment samples were scanned horizontally and vertically across the sample, collecting over 100 images in a region measuring a few microns in size. The size of the scanned region and number of images collected varied depending on the size of the sample sourced. Table 7.2 outlines sample information including the size of the scan area and the number of scans collected in this region.

Sample code	Number of images collected	Size of scan area (μm x μm)
GD1V*	102	0.4 x 0.4
LD1V*	126	1.2 x 1.2
LD109V*	108	0.2 x 0.2
LD183V*	201	0.4 x 0.4
LD412V*	100	0.4 x 0.4
GD203V*	110	0.2 x 0.2
GD202r*	101	0.2 x 0.2
GD382r*	101	0.4 x 0.4
LD449r*	100	0.2 x 0.2
1792 control+	100	0.8 x 1.4

Table 7.2: Table documenting the number of scans and the size of the scan area for all nine Domesday samples and the control sample. All scans were conducted in a grid like orientation (mesh scan).

The two-dimensional microfocus X-ray diffraction patterns were analysed using FibreFix software (see section 3.4.1). Using FibreFix, two-dimensional X-ray diffraction images were converted into one-dimensional linear traces.

7.3 Results

7.3.1 Analysis of the presence of meridional diffraction

The two-dimensional X-ray diffraction patterns for all nine Domesday Book samples were 'cleaned' using a specially designed computer program. The weak signal images were enhanced by multiplying pixel intensity by the distance from the beam centre. This allowed the creation of clearer two-dimensional X-ray diffraction patterns and simplified the identification of meridional reflections. Figure 7.3 shows two diffraction images taken from the Domesday Book, where one image has undergone modifification and the other image has not. The main difference between the two images is the region surrounding the beamstop. In the image that has not been enhanced (A) the area surrounding the backstop is close to the saturation point of the detector whereas in the cleaned image (B) the intensity of the scatter is far lower.

Beamstop
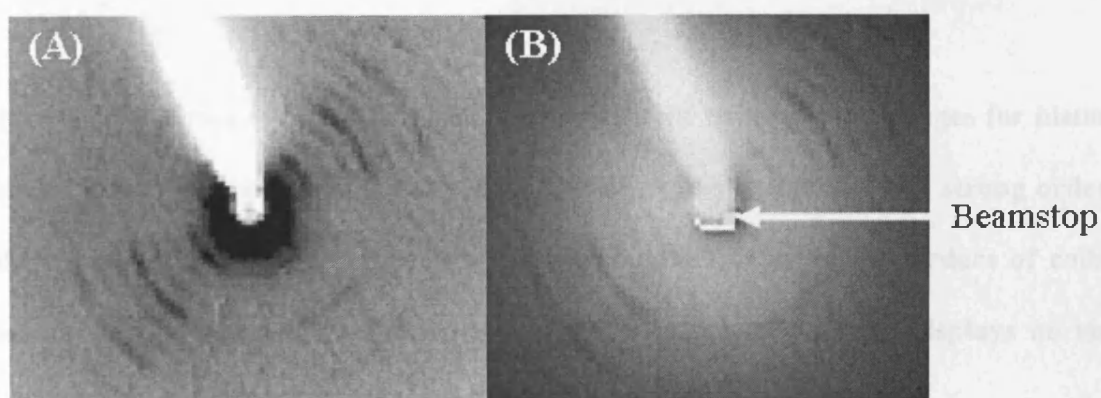
Figure 7.3: Two diffraction images taken from sample GD1V scan 66 where the one image has been cleaned and the other image has not. (A) Shows the diffraction image that has not been cleaned. (B) Shows the diffraction image that has been cleaned using the specially designed computer program.

Due to the micron-sized samples used in this experiment, collection and subsequent analysis was extremely challenging, so the majority of the study was therefore based on visual analysis of the two-dimensional X-ray diffraction patterns. The patterns were assessed for the presence of meridional diffraction orders resulting from collagen axial diffraction. The samples from the Domesday Book gave a variety of different diffraction images, where a good diffraction image generally displayed a strong sixth and ninth order of collagen axial diffraction, and samples that diffracted poorly displayed weak diffraction images or no detectable order of collagen axial diffraction. An X-ray diffraction image for a sample considered intact and a sample considered degraded is shown in Figure 7.4.
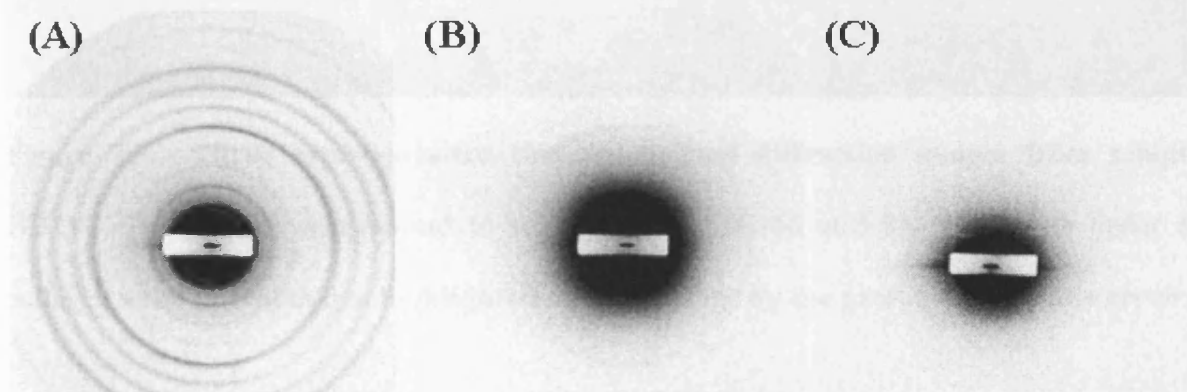
Figure 7.4: A series of Small-angle X-ray diffraction transmission images for historical samples in a variety of different states. (A) Diffraction image displays strong orders of collagen axial diffraction. (B) Diffraction image displays weaker orders of collagen axial diffraction when compared with (A). (C) Diffraction image displays no visible orders of collagen axial diffraction when compared with (A) and (B).

7.3.1.1 Sample GD1V

Sample GD1V was sampled from the verso side of page 1 in Great Domesday. Figure 7.5 shows three representative two-dimensional diffraction images from sample GD1V where the meridional diffraction orders are clearly visible. The sixth order of collagen axial diffraction is highlighted on each image by the presence of a white arrow.
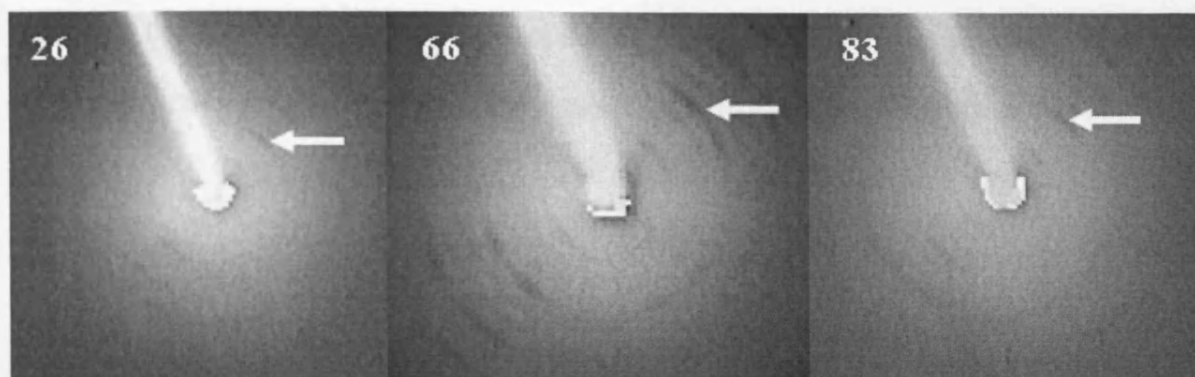
Figure 7.5: **Three representative two-dimensional diffraction images from sample GD1V. The images correspond to scan numbers 26, 66 and 83. The sixth order of collagen axial diffraction is highlighted on each image by the presence of a white arrow.**

7.3.1.2 Sample LD1V

Sample LD1V was sampled from the verso side of page 1 in Little Domesday. Figure 7.6 shows three representative two-dimensional diffraction images from sample LD1V where very weak meridional diffraction orders are seen (as highlighted by the white arrows).
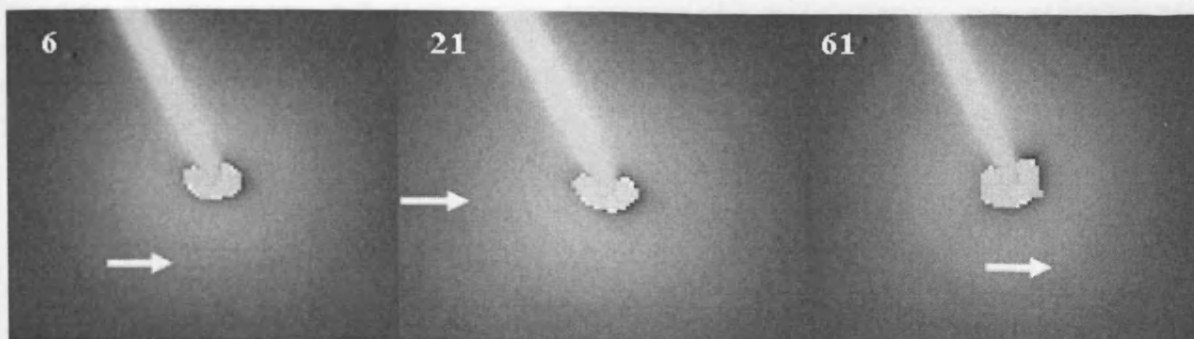
Figure 7.6: Three representative two-dimensional diffraction images from sample LD1V. The images correspond to scan numbers 6, 21 and 61. The presence of collagen axial diffraction is highlighted on each image by the presence of a white arrow.

7.3.1.3 Sample LD109V

Sample LD109V was sampled from the verso side of page 109 in Little Domesday. Figure 7.7 shows three representative two-dimensional diffraction images from sample LD109V where weak meridional diffraction orders are seen.

Figure 7.7: Three representative two-dimensional diffraction images from sample LD109V. The images correspond to scan numbers 3, 73 and 97. The presence of collagen axial diffraction is highlighted on each image by the presence of a white arrow.

7.3.1.4 Sample LD183V

Sample LD183V was sampled from the verso side of page 183 in Little Domesday. Figure 7.8 shows three representative two-dimensional diffraction images from sample LD183V where the meridional diffraction orders are seen.
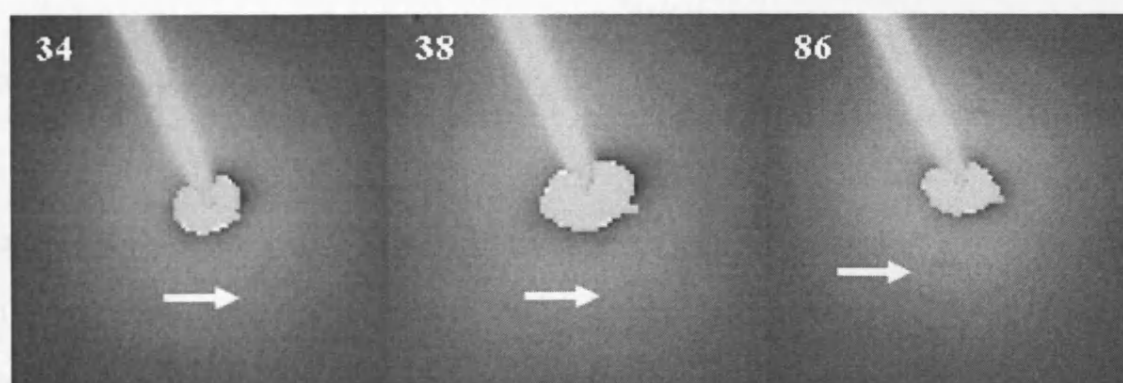
Figure 7.8: Three representative two-dimensional diffraction images from sample LD183V. The images correspond to scan numbers 34, 38 and 86. The presence of collagen axial diffraction is highlighted on each image by the presence of a white arrow.

7.3.1.5 Sample LD412V

Sample LD412V was sampled from the verso side of page 412 in Little Domesday. Figure 7.9 shows three representative two-dimensional diffraction images from sample LD412V where weak meridional diffraction orders are seen.
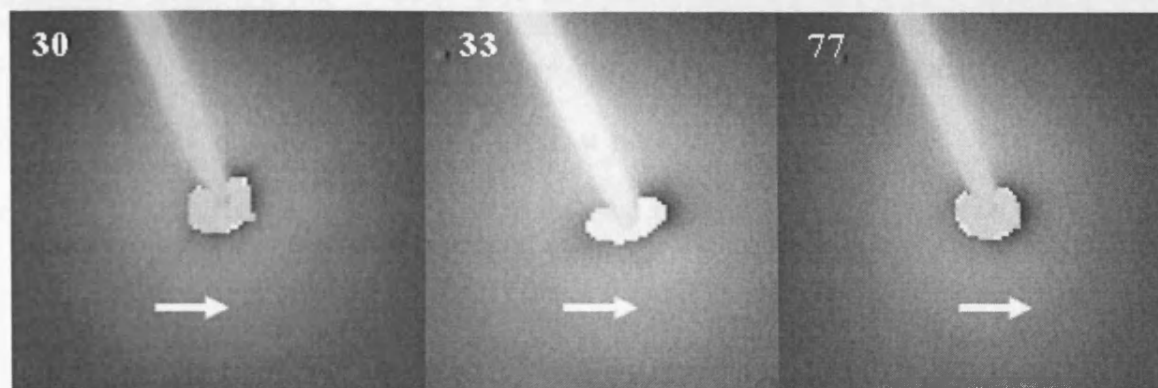
Figure 7.9: Three representative two-dimensional diffraction images from sample LD412V. The images correspond to scan numbers 30, 33 and 77. The presence of collagen axial diffraction is highlighted on each image by the presence of a white arrow.

7.3.1.6 Sample GD203V

Sample GD203V was sampled from the verso side of page 203 in Great Domesday. Figure 7.10 shows three representative two-dimensional diffraction images from sample GD203V where the meridional diffraction orders are seen.
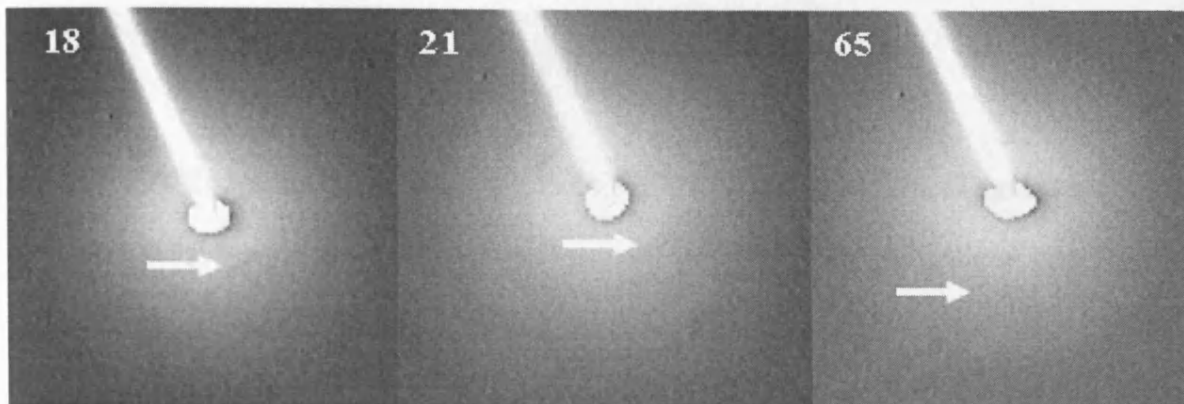
Figure 7.10: Three representative two-dimensional diffraction images from sample GD203V. The images correspond to scan numbers 18, 21 and 65. The presence of collagen axial diffraction is highlighted on each image by the presence of a white arrow.

7.3.1.7 Sample GD202r

Sample GD202r was sampled from the recto side of page 202 in Great Domesday. Figure 7.11 shows three representative two-dimensional diffraction images from sample GD202r where weak meridional diffraction orders are seen.

Figure 7.11: Three representative two-dimensional diffraction images from sample GD202r. The images correspond to scan numbers 9, 51 and 86. The presence of collagen axial diffraction is highlighted on each image by the presence of a white arrow.

7.3.1.8 Sample GD382r

Sample GD382r was sampled from the recto side of page 382 in Great Domesday. Figure 7.12 shows three representative two-dimensional diffraction images from sample GD382r where the meridional diffraction orders are seen.
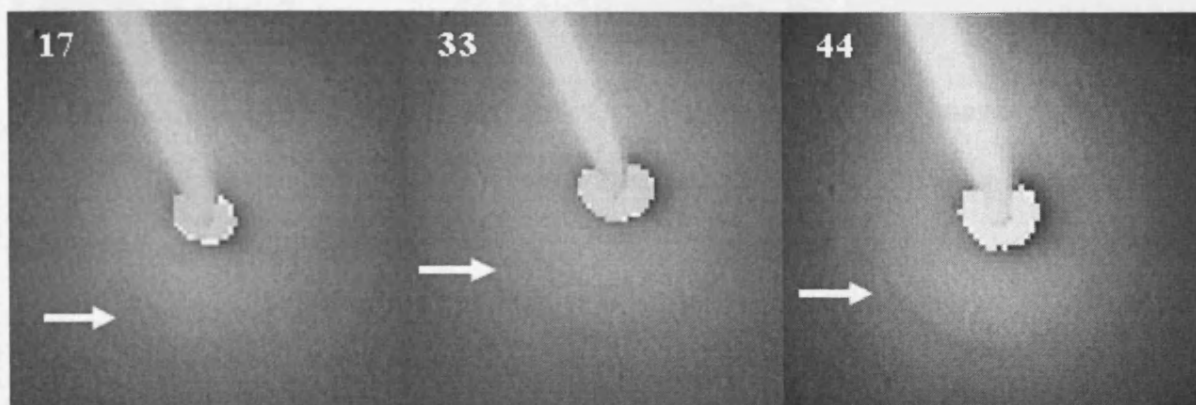
Figure 7.12: Three representative two-dimensional diffraction images from sample GD382r. The images correspond to scan numbers 17, 33 and 44. The presence of collagen axial diffraction is highlighted on each image by the presence of a white arrow.

7.3.1.9 Sample LD449r

Sample LD449r was sampled from the recto side of page 449 in Little Domesday. Figure 7.13 shows three representative two-dimensional diffraction images from sample LD449r where no meridional diffraction orders are seen.
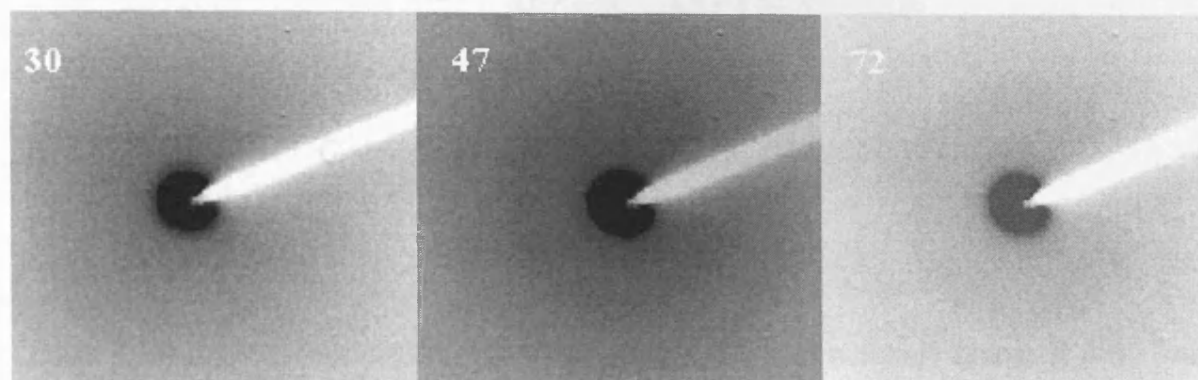
Figure 7.13: Three representative two-dimensional diffraction images from sample LD449r. The images correspond to scan numbers 30, 47, 72. No presence of collagen axial diffraction was observed.

Sample LD449r showed no presence of meridional reflections from collagen axial diffraction. Figure 7.14 shows reflections seen at $2.6nm^{-1}$, $3.3nm^{-1}$, $4.1nm^{-1}$ and $4.5nm^{-1}$. This was the only sample that displayed any reflections at wide-angles. X-ray diffraction has confirmed that there is no evidence of collagen molecular structure in sample LD449r. Further analysis on the Domesday Book conducted by the School of Conservation, Copenhagen, Denmark has confirmed that sample LD449r is cellulose (paper).
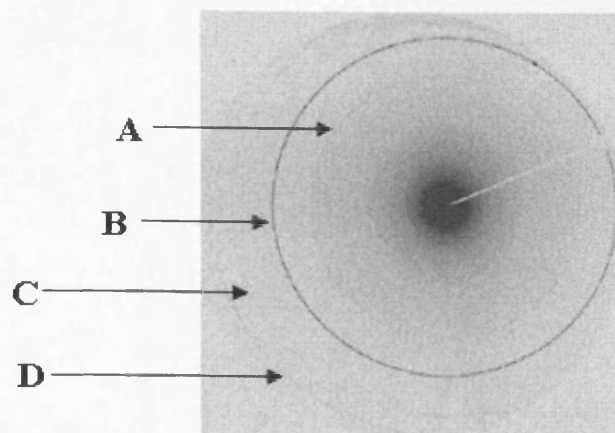
Figure 7.14: A representative two-dimensional diffraction image (zoomed out) from sample LD449r taken at a high angle. The image corresponds to scan number 30. Reflection seen at A, B, C and D correspond to 2.6nm^{-1}, 3.3nm^{-1}, 4.1nm^{-1} and 4.5nm^{-1} respectively.

7.3.2 Evaluation of the axial integrity (D-period)

Evaluation of the D-period for all nine Domesday samples was challenging due to the low pixel resolution encountered when observing the central region of images with visible meridional reflections of collagen axial diffraction. A low pixel resolution results in linear traces with less information in the area of interest. Figure 7.15 shows a linear trace for sample GD1V which contained the strongest meridional reflections. The meridional reflections for the sixth to the ninth orders of collagen axial diffraction only cover an area that is approximately 15 pixels. Figure 7.16 shows a full size two-dimensional X-ray diffraction pattern taken from the Domesday Book and the size of the scan region used to create the linear trace seen in Figure 7.15. This is too coarse to evaluate accurately the D-period of the samples. SAXS can not be conducted due to beam divergence after microfocus.
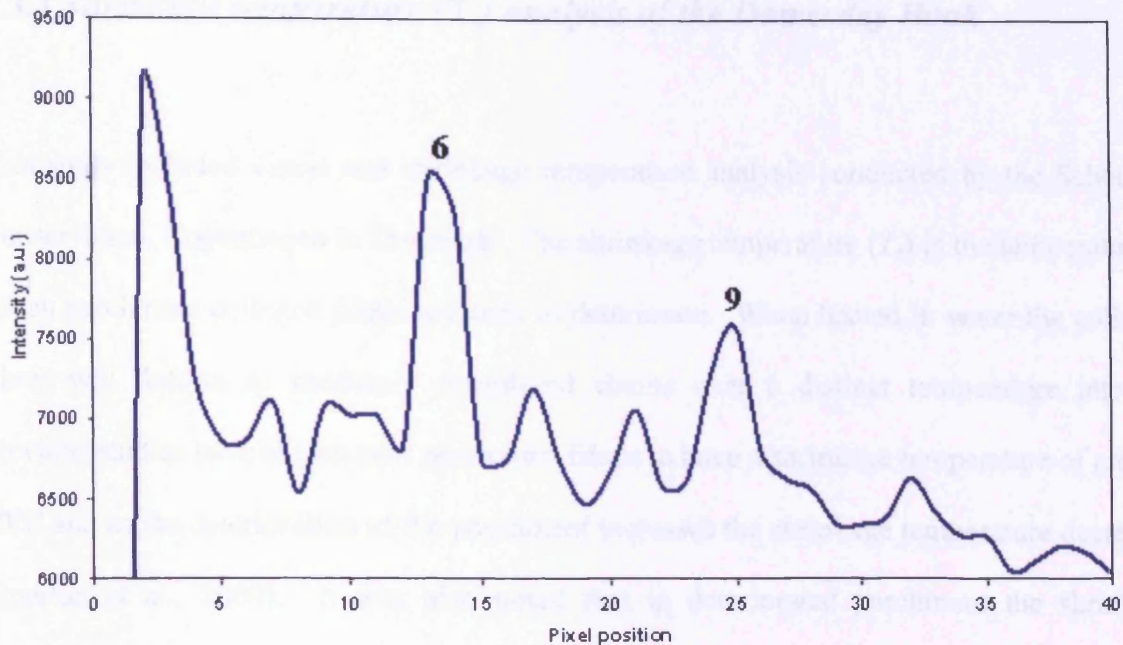
Figure 7.15: A one-dimensional linear trace for sample GD1V scan 66 that contained the strongest meridional reflections. The sixth and ninth orders of collagen axial diffraction are highlighted as 6 and 9 respectively.
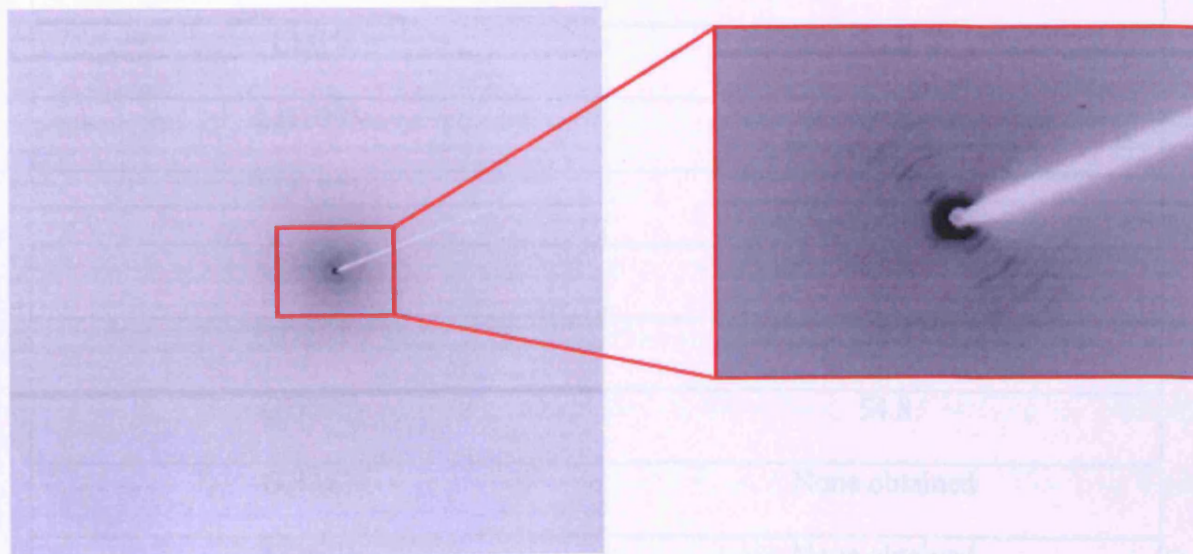
Figure 7.16: A full size two-dimensional X-ray diffraction pattern taken from the Domesday Book and the size of the scan region used to create the linear trace seen in Figure 7.15.

7.3.3 Shrinkage temperature (T_s) analysis of the Domesday Book

This study included visual and shrinkage temperature analysis conducted by the School of Conservation, Copenhagen in Denmark. The shrinkage temperature (T_s) is the temperature at which parchment collagen fibres are seen to deteriorate. When heated in water the collagen fibres will deform to randomly disordered chains over a distinct temperature interval. Previous studies have shown new parchment fibres to have a shrinkage temperature of around 60°C and as the deterioration of the parchment increases the shrinkage temperature decreases (Sportun et al., 2000). It was also noted that in deteriorated parchment the shrinkage temperature would be nearer to 30°C. Table 7.3 shows the shrinkage temperature measurements for seven of the nine Domesday Book samples.

Domesday Book Sample Code	Shrinkage temperature (°C)
GD1V	60.0
LD1V	53.9
LD109V	60.8
LD183V	49.6
LD412V	61.0
GD203V	58.6
GD202r	54.8
GD382r	None obtained
LD449r	None obtained

Table 7.3: The shrinkage temperature measurements for all nine Domesday Book samples collected by the School of Conservation, Copenhagen in Denmark.

7.4 Discussion

Analysis of these historically significant samples on beamline ID18F at ESRF has given a clearer picture of the condition of the Domesday Book. Due to the value of the Domesday Book sampling was restricted to micron-sized samples scraped from the surface of the parchment. This created an issue for collection of X-ray diffraction data using a standard beamline at a synchrotron. An extremely small beam was needed in order to collect X-ray diffraction images from a sample a few microns in size. The use of the microfocus beamline ID18F at ESRF allows the use of a micron size beam measuring $2\mu m \times 6\mu m$. The use of scrapings also created a challenge as only the surface of the parchment was subjected to X-ray diffraction as opposed to the entire cross section of the parchment. It has been proposed that the surface of the parchment is found in a higher state of degradation than the central regions of the parchment (Gonzalez and Wess, 2008a). Sampling only the surface layer has allowed the assessment of the level of degradation of the surface layer alone, without providing an insight into the degradation state of the more intact central parchment regions. Therefore, any conclusions proposed on the state of degradation of the Domesday Book may be weighted towards a higher state of degradation.

The samples studied show a variety of different degradation states with the presence of intact collagen due to the occurrence of axial diffraction in some samples. Samples GD1V, LD183V, GD203V and GD382r showed clearly visible collagen axial diffraction. Samples LD109V, LD1V, LD412V and GD202r contained very weak collagen axial diffraction, while sample LD449r contained no visible collagen axial diffraction.

7.4.1 Comparison of Little Domesday with Great Domesday

Both volumes of the Domesday Book, Great Domesday and Little Domesday were compared to see if any differences were visible at a structural level. Both volumes have always been stored together, so it is therefore assumed that they have both been subjected to identical environmental conditions, such as temperature, relative humidity and UV light exposure. Both volumes have been shown to be made predominately from sheepskin, although the geographical areas from which the animals were sourced are likely to differ (Forde, 1986). Although the provenance of the animal skin may have differed, the method of preparation of the parchment would have been the same. Great Domesday is visually more yellow in colour than Little Domesday. This may be due to more frequent handling of Great Domesday than Little Domesday.

These differences between the two volumes provide an excellent study in which to observe any changes at a structural level between the parchments in both volumes. X-ray diffraction was conducted on four samples from Great Domesday and five samples from Little Domesday. The meridional reflections for all samples from both Great Domesday and Little Domesday were compared. The samples that displayed clear meridional reflections were GD1V, GD203V and GD382r, which were from Great Domesday and LD183V from Little Domesday. The samples that displayed weak meridional reflections were LD109V, LD1V and LD412V from Little Domesday and GD202r from Great Domesday. The ninth sample LD449r from Little Domesday was found to contain no visible meridional reflections. It was later confirmed using biochemical analysis that sample LD449r is cellulose (paper) which is most likely due to earlier conservation work. No clear distinction in meridional reflections is seen between Great Domesday and Little Domesday but the more intact samples appear to be from the Great Domesday Book volume. A larger survey size would be required to

categorically state which volume is in better condition.

7.4.2 Comparison of verso and recto sides

The terms verso and recto are used to describe the left-hand page and the right-hand pages respectively. Many types of degradation may affect the verso and rectos sides in different ways; for example, one side may be more susceptible to mechanical damage resulting from handling and page turning. X-ray diffraction was conducted on six samples from the verso side and three samples from the recto side.

The samples that displayed strong meridional reflections were GD1V, GD203V and LD183V, which were from the verso side and GD382r from the recto side. The samples that displayed weak meridional reflections were LD109V, LD1V and LD412V from the verso side and GD202r from the recto side. The ninth sample LD449r from the recto side was found to contain no visible meridional reflections. As sample LD449r was found to be cellulose the sample set was reduced and contains only two samples sourced from the recto side. One of these samples was found to display strong meridional reflections while the other displayed weak meridional reflections. Therefore, no comparison can be made between the verso and recto sides. For a comparison to be made a larger study is needed with more samples sourced from both the verso and recto side.

7.4.3 Microfocus X-ray Diffraction as a Technique to Investigate Micron Sized Samples

Conventional X-ray diffraction is a valuable technique used to assess the structure of collagen within parchment. The development of micron sized X-ray beams with an intense flux has led to the use of microfocus X-ray diffraction experiments to probe small regions in a sample as well as the investigation of micron-sized samples (Snigirev et al., 1996; Wess et al., 2001; Kennedy et al., 2004b). The valuable and irreplaceable nature of the Domesday Book meant that sampling was limited to surface scrapings of only a few samples. The micron size samples therefore were unable to be investigated using conventional X-ray diffraction. The work conducted on the Domesday Book has highlighted the use of microfocus X-ray diffraction to provide information within a very small sample. Although only several microns thick, the samples were able to produce enough scattering of sufficient intensity for this study. However, an intact sample as opposed to a surface scraping would have produced a greater intensity to analyse. One possible method that could have been used to create a greater scattering from a surface scraping would be to have set the X-ray beam at a slight angle to the sample, thereby creating more material to scatter the X-rays passing through the sample.

7.4.4 Overall view of Collagen Integrity within the Domesday Book

Analysis of these historically significant samples on beamline ID18F at the ESRF has given a clearer picture of the condition of the Domesday Book and allowed a greater understanding of the degradation mechanisms in parchment. The use of microfocus X-ray diffraction has

resulted in the ability to scan minute size samples. The samples studied show the presence of intact collagen due to the occurrence of axial diffraction. However, some samples displayed very weak axial diffraction; this is explained by the use of surface scraping as a technique to supply samples. In taking surface scrapings only the surface on the parchment was investigated instead of the bulk of the parchment. It has previously been proposed that the collagen at the surface of parchment is found to be in an accelerated state of degradation when compared with the underneath (Kennedy et al., 2004b; Gonzalez and Wess, 2008b). Bulk samples instead of surface scrapings would be more beneficial in future experiments. The use of high angle diffraction allows the observation of mineral present in the samples. Very sharp intense mineral reflections were found in sample LD449r, which corresponds to the presence of large amounts of mineral, particularly calcite.

This study allowed the use of microfocus X-ray diffraction on the Domesday Book. To minimize damage to this valuable book, surface scrapings measuring a few microns in size were taken from a limited number of pages. Since the surface layer has undergone greater exposure to damage inducing mechanisms any conclusions proposed on the state of degradation of the Domesday Book may be weighted towards a higher state of degradation. Overall analysis of these historically significant samples on beamline ID18F at the ESRF has given a clearer picture of the condition of the Domesday Book and allowed a greater understanding of the degradation mechanisms in parchment.

Chapter 8: Conclusions

8.1 Introduction

The work presented here represents a detailed investigation into understanding how water and collagen interacts within the scope of parchment conservation and storage at the molecular and supramolecular level. This includes a study into the wetting of parchment in conservation practices to flatten documents, as well as research into the effect of relative humidity variations on the storage of records. The relationship has been studied using both X-ray diffraction and computer-aided molecular models. The combination of these two techniques has enabled an understanding of the interactions with water that may cause damage to collagen structure. This work has resulted in a collaborative project involving an iconic treasure of Great Britain; the Domesday Book.

8.1.1 X-ray Diffraction as a Technique to Understand the Influence of Water on the Structure of Collagen within Parchment

The study on the effect of hydration and air-drying of parchment demonstrated the versatility of X-ray diffraction as a technique to investigate both the dry and hydrated structure of parchment. A number of parchment samples gifted by the National Archives of Scotland were used during this study. These samples were analysed whilst dry, hydrated and air-dried using small-angle and wide-angle X-ray diffraction. One-dimensional linear traces were

produced from the collected two-dimensional X-ray diffraction patterns. From these linear traces a series of different parameters were calculated including the axial rise per residue, intermolecular lateral packing and the axial periodicity (D-period). By calculating these parameters in a number of different states of hydration it is possible to observe if there are any changes in the fibrillar structure of collagen.

When studying parchment it is important to note that we are dealing with an inherently damaged system, unlike investigations using native collagen. Analysis showed that each parchment used in this study reacted in a different manner to hydration and air-drying, indicating the heterogeneous nature of parchment. It is proposed that the heterogeneous nature of parchment results from the use of a variety of animal skins, different techniques used during parchment manufacture and variation in storage conditions. At present conservators treat all parchment as one single homogenous material in both conservation treatment and storage. This study has highlighted the need to evaluate each parchment as an individual document with different needs for preservation and storage.

8.1.2 X-ray Diffraction to Understand the Effect Relative Humidity has on the Structural Integrity of Parchment

This work examined the effect of relative humidity on parchment by utilising X-ray diffraction as a non-destructive technique to assess the structural integrity of collagen within parchment. There are two primary concerns in the preservation of parchment documents; the first is the immediate or short term effects of the environment (relative humidity) in which they are kept, on the collagen molecular structure. The second concern is the long-term effects of the environment, associated with relative humidity. The effect of relative humidity

on parchment is of great importance in the preservation and storage of documents in a variety of locations including libraries and archives.

The work in this thesis has shown the need to consider the amount of water present in the parchment as opposed to the %RH of the environment the parchment is stored under. From a scientific view point it would be more beneficial to consider the amount of water present within parchment although conservators do not measure the water content of their parchment samples, they use %RH. Therefore, an additional future study comparing the accuracy of using %RH as an indication of water content would be advantageous.

This study has shown that under extreme levels of humidity structural alterations are observed in the collagen molecular structure. A variation in the axial D-period is observed in samples considered in a degraded state upon humidification whereas little or no alteration is seen in the axial D-period in samples considered in an intact state upon humidification. This may be due to the presence of partially degraded collagen within the samples that accelerates the damaging effect of humidity upon the collagen present. This implies that there is "resistance" to change in external forces at specific molecular levels. This "resistance" can be overridden by the presence of deformation; a damaged system is more susceptible to external forces than an intact system.

Overall, our findings have shown that relative humidity has an extremely varied effect on parchment and greatly depends on the integrity of the collagen present within the parchment. This study has further highlighted the need to evaluate each parchment document on an individual basis. This indicates that the need for a comprehensive humidity control of parchment samples is exceedingly important in the monitoring and preservation of valuable parchment samples particularly those that are believed to be in a more degraded state.

8.1.3 Molecular Modelling of Changes in Fibrillar Collagen

The overall goal of this chapter was to investigate alterations induced within the molecular structure of collagen by various external factors. This chapter focused on changes in fibrillar collagen by drying, X-ray irradiation and mechanical deformation.

The observed changes in the X-ray diffraction patterns are summarized below:

- Drying

  o Shortening of the D-period from 67nm to approximately 65nm.

  o The visible number of meridional reflections decreases on drying.

  o The meridional reflections display a widening or fanning.

  o A splitting of the meridional reflections is observed.

- X-ray irradiation

  o The meridional reflections broadened with increased dose and diffraction order.

  o New periodicities were observed in addition to the characteristic 67nm D-period for hydrated type I collagen.

- Mechanical deformation

  o Increase in the D-period from 67nm to 68.8nm on mechanical loading.

  o The increase in D-period was reversible as long as the final D-period did not exceed 68.4nm.

  o A change in the intensities of the second and third order reflections.

  o Attenuation of the higher diffraction orders.

A number of mechanisms were proposed that may contribute to the changes observed in the

X-ray diffraction patterns from altered collagen. These were:

- A change in the axial rise per residue.

- The induction of local disorder.

- The shearing of laterally adjoined molecules relative to each other.

- Breakages in the amino acid chains of the collagen molecules.

- The induction of molecule titling within the staggered array of collagen molecules.

X-ray diffraction is a useful non-destructive technique for investigating changes at a molecular and fibrillar level in collagen when differences are identified. Molecular modelling can begin to explain these structural changes and the factors affecting them. X-ray diffraction and molecular modelling compliment each other and when combined help to understand the variations in the fibrillar structure of collagen.

8.1.4 The use of X-ray Diffraction to Study the Structural Integrity of Historical Significant Documents

Sampling of historically significant parchment documents is often heavily restricted due to the valuable and irreplaceable nature of the documents. This creates a dilemma when sampling for scientific investigations as many techniques are destructive and require a large sample size, however data is required to aid the survival of entire collections. Microfocus X-ray diffraction is therefore an ideal method for the investigation of the structure of parchment, as it is micro-destructive and requires sub-micron sized samples.

This study allowed the use of microfocus X-ray diffraction on the Domesday Book. To minimize damage to this valuable book, surface scrapings measuring a few microns in size

were taken from a limited number of pages. Since the surface layer has undergone greater exposure to damage inducing mechanisms any conclusions proposed on the state of degradation of the Domesday Book may be weighted towards a higher state of degradation. Overall analysis of these historically significant samples on beamline ID18F at the ESRF has given a clearer picture of the condition of the Domesday Book and allowed a greater understanding of the degradation mechanisms in parchment.

8.2 Future Direction of Work

This thesis has highlighted many new areas to research further; some of these are discussed below.

8.2.1 Investigation into Parchment as a Stratified Structure using Microfocus X-ray Diffraction

Parchment is a complex material where the degradative assault on the surface is greater than the sub-surfaces; strategies for maintaining the surface integrity are possibly of higher priority than the overall substructure. The assumption that collagen hierarchical behaviour is consistent throughout parchment from flesh to grain is probably invalid. Specific depth-resolved studies that can capture information from different levels of structural organisation are therefore required.

X-ray diffraction has been used in this thesis as a transmission technique where each diffraction pattern collected consists of the composite diffraction features from the entire

thickness of the sample (Kennedy et al., 2004b). In comparison, microfocus X-ray diffraction is a technique that carries out surface-to-surface scans of parchment, presenting the ability to analyse features present in disparate areas (Kennedy et al., 2004b). The use of microfocus X-ray diffraction will allow a detailed investigation into the collagen structure throughout the parchment at both the surface and the sub-surfaces.

Microfocus X-ray diffraction may also be used to assess how different humidity levels affect the surface and sub-surfaces of parchment at the nanoscopic and atomic levels. Since the hierarchical organisation of collagen fibrils and fibres plays a key role in understanding structural fatigue and degradation, these levels of architecture must also be quantified in response to tensors such as humidity.

The use of microfocus X-ray diffraction could help investigate the effect of humidity on all levels of collagen structural hierarchy and distinct layers in the parchment stratum and evaluate how penetrative the effects of humidity are on parchment.

8.2.2 Investigation into the Effect of Long-Term Humidity Cycling on the Structure of Parchment

The work in this thesis has begun to address the immediate or short term effects of variation in relative humidity (RH) on the structure of parchment. A further concern not addressed by this thesis is the long-term effect of relative humidity on parchment stored in museums, libraries and archives. To this end, the next step would be to investigate the effect of humidity cycling on parchment stored for a longer time-scale, for example a ten year period. The organisation of such a long term project could prove to be extremely difficult, relying heavily on the collaboration of a museum, library or archive to house the study. Maintaining

226

a detailed long-term record of the conditions in which the parchment is kept would necessitate a large number of data logging devices to record the relative humidity and temperature of the storage location.

8.2.3 Investigation into the Presence of Water Populations in Parchment using Optical Coherence Tomography (OCT) and Terahertz Spectroscopy (THz)

A catalogue of different techniques is needed in order to investigate the presence, distribution and interaction of different water populations at the microfibril, fibril and fibrous level, as well as to understand the movement of water at all structural hierarchies in parchment. Two techniques that could be utilised are Optical Coherence Tomography (OCT) and Terahertz Spectroscopy (THz). These techniques would provide a detailed depth-resolved analysis of the behavioural changes of collagen fibres when subject to hydration, and provide information regarding the behaviour of water populations within the sample at all different levels of structural hierarchy.

Optical Coherence Tomography (OCT) has been used to examine human skin for several years (Saxer et al., 2000) and has recently been utilised in the examination of parchment degradation; in particular the effect of iron gall ink upon the collagen (Góra et al., 2006). Terahertz (THz) spectroscopy has previously been used to examine low frequency collective vibrational modes of biomolecules. Studies have been completed to assess skin and the dehydration of collagen (Corridon and Wilke, 2007).

8.2.4 Investigation into the Effect of Relative Humidity on Parchment using Fourier Transform Infra Red (FTIR) Spectroscopy

Fourier Transform Infra Red (FTIR) Spectroscopy could be used as a technique to identify any changes in the collagen structure on exposure to a variation in the relative humidity. Work conducted by the Wess Group at Cardiff has shown that the FTIR spectra can be correlated to structural deviations of the collagen helix motif and thence gelatinisation. In addition to FTIR micro Fourier Transform spectroscopy would allow the collection of spectra in micron steps at different depths within the sample, achieved by using a range of different wavelengths (Petra et al., 2005). Micro Fourier Transform spectroscopy could be used as a complimentary technique to microfocus X-ray diffraction.

8.2.5 Investigation into the Use of Different Animal Skins in the Production of Parchment

Previous studies on the effect of humidity on parchment have been focused on a single skin type, often calfskin whereas parchment is manufactured from a range of different animal skins including calfskin, goatskin, sheepskin and deerskin (Haines, 1999). In addition, these studies have assumed uniformity in the collagen throughout all the layers found in skin. Parchment made from calfskin contains a relatively shallow grain layer, fine corium fibres, compacted interweaving and an absence of looseness between the grain and corium layers. In Goatskin, the corium fibres interweave well into the grain layer, so that there is no looseness between the two layers. Unlike calfskin and goatskin, the corium fibres in sheepskin are fine and less compactly interwoven. The interweaving of corium fibres is

limited by the density and curl of the wool fibres within the grain layer, which leads to looseness between the two layers. Deerskin is found to possess coarser corium fibre bundles than calfskin and goatskin. In addition, the weave is more loosely interwoven resulting in a stretchy parchment (Haines, 1999). These differences between the fibre size and the weaving of collagen fibres mean that the structural properties of parchment made from different skins is significantly diverse. We suggest that more tightly woven fibres will be more resistant to humidity than loosely woven fibres. The effect of humidity on a variety of different animal skins used in parchment manufacture could be investigated to establish whether a difference in the fibre size and the weaving of fibres causes humidity to affect the parchment of various species differently.

8.3 Summary

Understanding the molecular alterations in the structure of collagen is important in gaining a comprehensive insight into the degradation of parchment. This thesis has shown that the structural alterations in parchment can be studied using both X-ray diffraction and molecular modelling. Despite extensive X-ray diffraction studies on a number of samples the nanostructure of many parchment samples was found to be unaffected by a variation in the RH. Although the nanostructure of the parchment (as judged by X-ray diffraction) was observed to be unchanged with RH the parchment samples appeared visually different. This implies that any changes within the parchment are occurring at a different structural length scale, for example at a mesoscopic length scale.

Bibliography

Abil E A (2005) Solid-state NMR studies of collagen-based parchments and gelatin. *Biopolymers* 77: 230-245.

Azaroff L V (1968) Elements of X-ray crystallography. McGraw-Hill Education.

Bear R S (1951) X-ray diffraction studies: A review of recent researches which concern collagen. *Journal of the American Leather Chemists Association* 46: 438-445.

Bear R S (1952) The Structure of Collagen Fibrils. *Advances in Protein Chemistry* 7: 69-160.

Bear R S, and Morgan R S (1957) *In Connective Tissue*. Oxford: Scientific Publications Ltd.

Bell N and McPhail D (2007) Managing change: preserving history *Materials Today* 10: 50-56.

Bella J, Brodsky B, and Berman H M (1995) Hydration structure of a collagen peptide. *Structure* 3: 893-906.

Blattmann H, Gebbers J-O, Bräuer-Krisch E, Bravin A, Le Duc G, Burkard W, Di Michiel M et al. (2005) Applications of synchrotron X-rays to radiotherapy. *Nuclear Instruments and Methods in Physics Research Section A: Accelerators, Spectrometers, Detectors and Associated Equipment* 548: 17-22.

Bowden D J, and Brimblecombe P (1999) The Thermal Response of Parchment and Leather to Relative Humidity Changes. *Microanalysis of Parchment.*

Brodsky B, Eikenberry E F, and Cassidy K (1980) An unusual collagen periodicity in skin. *Biochimica et Biophysica Acta (BBA) - Protein Structure* 621: 162-166.

Brodsky B, and Ramshaw J A M (1997) The Collagen Triple-Helix Structure. *Matrix Biology* 15: 545-554.

Buehler M (2006) Nature designs tough collagen: Explaining the nanostructure of collagen fibrils. *Proceedings of the National Academy of Sciences* 103: 12285-12290.

Burgeson R E (1988) New Collagens, New Concepts. *Annual Review of Cell Biology* 4: 551-577.

Burton D, Poole J B, and Reed R (1959) A New Approach to the Dating of the Dead Sea Scrolls. *Nature* 184: 533-534.

Cameron G J (2004) *Structural Features of Heterotypic Collagen Fibrils.* University of Stirling.

Cameron G J, Alberts I L, Laing J H, and Wess T J (2002) Structure of Type I and Type III Heterotypic Collagen Fibrils: An X-Ray Diffraction Study. *Journal of Structural Biology* 137: 15-22.

Chandross R J, and Bear R S (1973) Improved profiles of electron density distribution along collagen fibrils. *Biophysical Journal* 13: 1030-1048.

Choi H U, Johnson T L, Pal S, Tang L H, Rosenberg L, and Neame P J (1989) Characterization of the dermatan sulfate proteoglycans, DS-PGI and DS- PGII, from bovine articular cartilage and skin isolated by octyl- sepharose chromatography. The *Journal of Biological Chemistry* 264: 2876-2884.

Christiansen D L, Huang E K, and Silver F H (2000) Assembly of type I collagen: fusion of fibril subunits and the influence of fibril diameter on mechanical properties. *Matrix Biology* 19: 409-420.

Clark R J H, and Curri M L (1998) The identification by Raman microscopy and X-ray diffraction of iron-oxide pigments and of the red pigments found on Italian pottery fragments. *Journal of Molecular Structure* 440: 105-111.

Corridon P M, and Wilke I (2007) Monitoring the dehydration of collagen by time-domain terahertz transmission measurements. *15th International Conference on Terahertz Electronics.*

Creagh D, Lee A, Otieno-Alego V, and Kubik M (2009) Recent and future developments in the use of radiation for the study of objects of cultural heritage significance. *Radiation Physics and Chemistry* 78: 367-374.

Cullity B D (1978) Elements of X-ray diffraction. *Addison-Wesley.*

Dubovikov N I and Podmurnaya O A (2001) Measuring the Relative Humidity over Salt Solutions. *Measurement Techniques* 44: 1260-1261.

Epstein E J and Munderloh N (1978) Human skin collagen. Presence of type I and type III at all levels of the dermis. *The Journal of Biological Chemistry* 253: 1336-1337.

Folkhard W, Mosler E, Geercken W, Knorzer E, Nemetschek-Gansler H, Nemetschek T, and Koch M H J (1987) Quantitative analysis of the molecular sliding mechanisms in native tendon collagen -- time-resolved dynamic studies using synchrotron radiation. *International Journal of Biological Macromolecules* 9: 169-175.

Forde H (1986) Domesday Preserved. Public Record Office, HMSO.

Fratzl P (2008) Collagen: Structure and Mechanics, an Introduction. In: Fratzl P [ed.] *Collagen: Structure and Mechanics*. New York: Springer

Fratzl P, Misof K, SZizak I, Rapp G, Amenittsch H, and Bernstorff S (1997) In-situ Synchrotron X-ray scattering study of the Tensile properties of Collagen. *ELETTRA HIGHLIGHTS* 1: 44-47.

Fratzl P, Misof K, Zizak I, Rapp G, Amenitsch H, and Bernstorff S (1998) Fibrillar Structure and Mechanical Properties of Collagen. *Journal of Structural Biology* 122: 119-122.

Fullerton G D, and Amurao M R (2006) Evidence that collagen and tendon have monolayer water coverage in the native state. *Cell Biology International* 30: 56-65.

Glab J, Wess T, and Thomas K (Due to be published in 2009) X-ray Scattering of Biomolecules. In: Nalwa H S [ed.] *Encyclopedia of Nanoscience and Nanotechnology* American Scientific Publishers.

Glatter O, and Kratky O (1982) *Small Angle X-ray Scattering*. Academic Press.

Gonzalez L, and Wess T (2008a) The Use of Attenuated Total Reflection–Fourier Transform Infrared Spectroscopy to Measure Collagen Degradation in Historical Parchments *Journal of Applied Spectroscopy* 62.

Gonzalez L, and Wess T (2008b) The Use of Attenuated Total Reflection–Fourier Transform Infrared Spectroscopy to Measure Collagen Degradation in Historical Parchments. *Journal of Applied Spectroscopy* 62: 1108-1114.

Góra M, Pircher M, Götzinger E, Bajraszewski T, Strlic M, Kolar J, Hitzenberger C K et al. (2006) Optical Coherence Tomography for Examination of Parchment Degradation. *Laser Chemistry* 1: 1-6.

Grossman J G (2002a) Shape Determination of Biomolecules in Solution form Synchrotron X-ray Scattering. In: Pike R, and Sabatier P [eds.] *Scattering and Inverse Scattering in Pure and Applied Science* Academic Press.

Haines B (1999) *Parchment - The physical and chemical characteristics of parchment and the materials used in its conservation.* The Leather Conservation Centre.

Hansen E F, Lee S N, and Sobel H (1992) The Effects of Relative Humidity on Some Physical Properties of Modern Vellum: Implications for the Optimum Relative Humidity for the Display and Storage of Parchment. *Journal of the American Institute of Conservation.* 31: 325-342.

Hendriks F M, Brokken D, Oomens C W J, Bader D L, and Baaijens F P T (2005) The relative contributions of different skin layers to the mechanical behavior of human skin in vivo using suction experiments. *Medical Engineering & Physics* 28: 259-266.

Hingley M (2001) Success in the Treatment of Parchment and Vellum using a Suction Table. *Journal of the Society of Archivists* 22: 71-77.

Hochleitner B, Desnicaa V, Mantlera M, and Schreinerb M (2003) Historical pigments:next term a collection analyzed with X-ray diffraction analysis and X-ray fluorescence analysis in order to create a database. *Spectrochimica Acta Part B: Atomic Spectroscopy* 58: 641-649.

Hodge A J, and Petruska J A (1963) Recent studies with the electron microscope on ordered aggregates of the tropocollagen molecule. *Aspects of Protein Structure*: 289-300.

Holmes D F, Gilpin C J, Baldock C, Ziese U, Koster A J, and Kadler K E (2001) Corneal collagen fibril structure in three dimensions: Structural insights into fibril assembly, mechanical properties, and tissue organisation. *Cell Biology* 98: 7307-7312.

Horie C V (1990) Deterioration of skin in museum collections. *Polymer Degradation and Stability.* 29: 109-133.

Hukins D W L (1981) X-ray diffraction by disordered and ordered systems. *Pergamon Press.*

Hulmes D J S (2002) Building Collagen Molecules, Fibrils, and Suprafibrillar Structures. *Journal of Structural Biology* 137: 2-10.

Hulmes D J S, Miller A, White S W, and Doyle B B (1977) Interpretation of the Meridional X-ray Diffraction Pattern from Collagen Fibre in Terms of the Known Amino Acid Sequence. *Journal of Molecular Biology* 110: 643-666.

Hulmes D J S, Miller A, White S W, Timmins P A, and Berthetcolominas C (1980) Interpretation of the Low-Angle Meridional Neutron-Diffraction Patterns from Collagen-Fibers in Terms of the Amino-Acid-Sequence. *International Journal of Biological Macromolecules* 2: 338-346.

Kadler K E (1995) Protein Profile: fibril-forming collagens. *Extracellular Matrix 1* 2: 491-553.

Kadler K E, Baldock C, Bella J, and Boot-Handford R P (2007) Collagens at a glance. *Journal of Cell Science* 120: 1955-1958.

Kadler K E, Holmes D F, Trotter J A, and Chapman J A (1996a) Collagen fibril formation. *Journal of Biochemistry* 316: 1-11.

Kadler K E, Holmes D F, Trotter J A, and Chapman J A (1996b) Collagen fibril formation - a review. *Biochemistry Journal* 316: 1-11.

Kennedy C J, Hiller J, Lammie D, Drakopoulos M, Vest M, Cooper M, Adderley W P, Wess T J. (2004) Microfocus X-ray diffraction of historical parchment reveals variations in structural features through parchment cross sections. *Nanoletters* 4: 1373-1380.

Kennedy C J, Nielsen K, Ramsay L, and Wess T J (2003) Analysis of collagen structure in parchment by Small angle X-ray diffraction. *Fibre Diffraction Review* 11: 117-118.

Kennedy C J, Vest M, Cooper M, and Wess T J (2004c) Laser cleaning of parchment: structural, thermal and biochemical studies into the effect of wavelength and fluence. *Applied Surface Science* 227: 151-163.

Kennedy C J, and Wess T J (2003) The Structure of Collagen within Parchment - A Review. *Restaurator - International Journal for the Preservation of Library and Archival Material* 24: 61-80.

Kite M, and Thomson R (2006) *Conservation of Leather and related materials.* Elsevier.

Kjellen L, and Lindahl U (1991) Proteoglycans: Structures and Interactions. *Annual Review of Biochemistry* 60: 443-475.

Labaki L C, Torriani I L, and Grigera J R (1991) Humidity-Dependent Structural Changes in Native Collagen Studied by X-ray Diffractometry. *Brazilian Journal of Medical and Biological Research* 24: 115-122.

Larsen R (2002) *Microanalysis of Parchment.* Archetype.

Lee A S, Mahon P J, and Creagh D C (2006) Raman analysis of iron gall inks on parchment. *Vibrational Spectroscopy* 41: 170-175.

Lees S (1986) Water content in type I collagen tissues calculated from the generalized packing model. *International Journal of Biological Macromolecules* 8: 66-72.

Light N D (1985) Collagen in Skin: Preparation and Analysis. In: Skerrow D, and Skerrow C J [eds.] *Methods in Skin Research*. John Wiley & Sons Ltd, pp. 559-586.

Lodish H, Berk A, Zipursky L S, Matsudaira P, Baltimore D, and Darnell J (2000) *Molecular Cell Biology*. New York: W. H. Freeman.

MacNeil S (2007) Progress and opportunities for tissue-engineered skin. *Nature* 445: 874-880.

Malone J P and Veis A (2004) Heterotrimeric Type I Collagen C-Telopeptide Conformation As Docked to Its Helix Receptor. *Biochemistry* 43: 15358-15366.

Maxwell C A, Wess T J, and Kennedy C J (2006) X-ray diffraction study into the Effects of Liming on the Structure of Collagen. *Biomacromolecules* 7: 2321-2326.

Meek K M, Chapman J A, and Hardcastle R A (1979) The staining pattern of collagen fibrils. Improved correlation with sequence data. The *Journal of Biological Chemistry* 254: 10710-10714.

Meek K M, and Quantock A J (2001) The Use of X-ray Scattering Techniques to Determine Corneal Ultrastructure. *Progress in Retinal and Eye Research* 20: 95-137.

Menon G K (2002) New insights into skin structure: scratching the surface. *Advanced Drug Delivery Reviews* 54: 3-17.

Mogilner I G, Ruderman G, and Grigera J R (2002) Collagen stability, hydration and native state. *Journal of Molecular Graphics and Modelling* 21: 209-213.

Monteiro-Riviere N A, Inman A O, Snider T H, Blank J A, and Hobson D W (1997) Comparison of an in vitro skin model to normal human skin for dermatological research. *Microscopy Research and Technique* 37: 172-179.

Mosler E, Folkhard W, Knorzer E, Nemetschek-Gansler H, Nemetschek T, and Koch M H J (1985) Stress-induced molecular rearrangement in tendon collagen. *Journal of Molecular Biology* 182: 589-596.

Nagan N, and Kagan H M (1994) Modulation of Lysyl Oxidase Activity toward Peptidyl Lysine by Vicinal Dicarboxylic Amino Acid Residues - Implications for Collagen Cross-linking *The Journal of Biological Chemistry* 269: 22366-22371.

Orgel J P, Wess T J, and Miller A (2000) The in situ conformation and axial location of the intermolecular cross-linked non-helical telopeptides of type I collagen. *Structure* 8: 137-142.

Orgel J P R O, Miller A, Irving T C, Fischetti R F, Hammersley A P, and Wess T J (2001) The in situ supermolecular structure of type I collagen. *Structure* 9: 1061-1069.

Parkinson J, Brass A, Canova G, and Brechet Y (1997) The mechanical properties of simulated collagen fibrils. *Journal of Biomechanics* 30: 549-554.

Parry D A D (1988) The molecular fibrillar structure of collagen and its relationship to the mechanical properties of connective tissue. *Biophysical Chemistry* 29: 195-209.

Peters D (1996) Our environment ruined? Environmental control reconsidered as a strategy for conservation. *Journal of Conservation and Museum Studies* 1.

Petra M, Anastassopoulou J, Theologis T, and Theophanides T (2005) Synchrotron micro-FT-IR spectroscopic evaluation of normal paediatric human bone. *Journal of Molecular Structure* 733: 101-110.

Price R I, Lees S, and Kirschner D A (1997) X-ray diffraction analysis of tendon collagen at ambient and cryogenic temperatures: role of hydration. *International Journal of Biological Macromolecules* 20: 23-33.

Prockop D J, and Fertala A (1998) Inhibition of the Self-assembly of Collagen I into Fibrils with Synthetic Peptides. Demonstration that Assembly is Driven by Specific Binding Sites on the Monomers *The Journal of Biological Chemistry* 273: 15598-15604.

Provenzano P P, Hayashi K, Kunz D N, Markel M D, and Vanderby Jr. R (2002) Healing of subfailure ligament injury: comparison between immature and mature ligaments in a rat model. *Journal of Orthopaedic Research* 20: 975-983.

Quandt A B (1996) Recent Developments in the Conservation of Parchment Manuscripts. In: *The American Institute for Conservation 24th Annual Meeting.* Norfolk Virginia.

Quantock A J, Meek K M, and Chakravarti S (2001) An X-ray diffraction Investigation of corneal Structure in lumican-deficient mice. *Investigative Ophthalmology & Visual Science* 42: 1750-1756.

Rajkumar G, AL-Khayat H A, Eakins F, He A, Knupp C, and Squire J M (2005) FibreFix – A New Integrated CCP13 Software Package. *Fibre Diffraction Review* 13: 11-18.

Ramachandran G N (1967) Structure of Collagen at the Molecular level. In: Ramachandran G N [ed.] *Chemistry of Collagen.* Vol. 1. London: Academic Press, pp. 103-183.

Reed R (1973) *Ancient Skins, Parchment and Leathers ([International series of monographs on science in archaeology])* Academic Press Inc.,U.S.

Rhodes G (2000) Crystallography made crystal clear. *Academic Press.*

Riekel C (2000) New avenues in x-ray microbeam experiments. *Reports on Progress in Physics* 63: 233-262.

Rougvie M A and Bear R S (1953) An X-ray diffraction investigation of swelling by collagen *Journal of the American Leather Chemists Association* 48: 735-751.

Sasaki N and Odajima S (1996a) Elongation mechanism of collagen fibrils and force-strain relations of tendon at each level of structural hierarchy. *Journal of Biomechanics* 29: 1131-1136.

Sasaki N, and Odajima S (1996b) Stress-strain curve and young's modulus of a collagen molecule as determined by the X-ray diffraction technique. *Journal of Biomechanics* 29: 655-658.

Saxer C E, Boer J F D, Park B H, Zhao Y, Chen Z, and Nelson J S (2000) High-speed fiber-based polarization-sensitive optical coherence tomography of in vivo human skin. *Optics Letters* 25: 1355-1357.

Scott J, Ritchie M, Glanville R, and Cronshaw A (1997) Peptide sequences in glutaraldehyde-linked proteodermatan sulphate: collagen fragments from rat tail tendon locate the proteoglycan binding sites. *Biochemical Society Transactions* 25: 663

Scott J E, and Haigh M (1985) Proteoglycan-type I collagen fibril interactions in bone and non-calcifying connective tissues. *Bioscience Reports* 5: 71-81.

Scott J E, Orford C R, and Hughes E W (1981) Proteoglycan-collagen arrangements in developing rat tail tendon. *Biochemical Journal* 195: 573-581.

Screen H R C (2008) Investigating load relaxation mechanics in tendon. *Journal of the Mechanical Behavior of Biomedical Materials* 1: 51-58.

Sionkowska A, and Wess T (2004) Mechanical properties of UV irradiated rat tail tendon (RTT) collagen. *International Journal of Biological Macromolecules* 34: 9-12.

Sionkowska A, Wisniewski M, Skopinska J, Kennedy C J, and Wess T J (2004) Molecular interactions in collagen and chitosan blends. *Biomaterials* 25: 795-801.

Smit W J and Porck H J (1995) Guidelines for the conservation of leather and parchment bookbindings. *KB and the Central Research Laboratory for Objects of Art and Science.*

Snigirev A, Kohn V, Snigireva I, and Lengeler B (1996) A Compound Refractive Lens for Focusing High-energy X-rays. *Nature* 384: 49-51.

Somogyi A, Drakopoulos M, Vincze L, Vekemans B, Camerani C, Janssens K, Snigirev A et al. (2001) ID18F: a new micro X-ray fluorescence end-station at the European Synchrotron Radiation Facility (ESRF): preliminary results. *X-ray Spectrometry* 30: 242-252.

Sportun S, Cooper M, Stewart A, Vest M, Larsen R, and Poulsen D V (2000) An investigation into the effect of wavelength in the laser cleaning of parchment. *Journal of Cultural Heritage* 1: 225-232.

Stinson R H, and Sweeny P R (1980) Skin collagen has an unusual d-spacing. *Biochimica et Biophysica Acta* 621: 158-161.

Stout G H, and Jensen L H (1968) X-ray structure determination. *The Macmillan Company.*

Tamura N, Spolenak R, Valek B C, Manceau A, Meier Chang N, Celestre R S, MacDowell A A et al. (2002) Submicron X-ray Diffraction and its Applications to Problems in Materials and Environmental Science *Review of Scientific Instruments* 73: 1369-1372.

Towns-Andrews E, Berry A, Bordas J, Mant G R, Murray P K, Roberts K, Sumner I et al. (1989) Time-resolved x-ray diffraction station: X-ray optics, detectors and data acquisition. *Review of Scientific Instruments* 60: 2346-2349.

Traub W (1978) Molecular assembly in collagen. *FEBS Letters* 92: 114-120.

Traub W, and Piez K A (1971) The Chemistry and Structure of Collagen. *Advances in Protein Chemistry* 25: 243-352.

Van der Rest M, and Garrone R (1991) Collagen family of proteins. *FASEB Journal* 5: 2814-2823.

Weiner S, Kustanovich Z, Gil-Av E, and Traub W (1980) Dead Sea scroll parchments: unfolding of the collagen molecules and racemization of aspartic acid. *Nature* 287: 820-823.

Wess T J, Drakopoulos M, Snigirev A, Wouters J, Paris O, Fratzl P, Collins M, Hiller J, Nielsen K. (2001) The Use of Small-Angle X-Ray Diffraction Studies for the Analysis of Structural Features in Archaeological Samples. *Archaeometry* 43: 117-129.

244

Wess T J, Hammersley A P, Wess L, and Miller A (1998a) A Consensus Model for Molecular Packing of Type I Collagen. *Journal of Structural Biology* 122: 92-100.

Wess T J, Hammersley A P, Wess L, and Miller A (1998b) Molecular Packing of Type I Collagen in Tendon. *Journal of Molecular Biology* 275: 255-267.

Wess T J and Orgel J P (2000) Changes in collagen structure: drying, dehydrothermal treatment and relation to long term deterioration. *Thermochimica Acta* 365: 119-128.

Whitton J T, and Everall J D (1973) The thickness of the epidermis. *British Journal of Dermatology* 89: 467-476.

Woods C (1995) Conservation Treatments for Parchment Documents. *Journal of the Society of Archivists* 16: 221-238.

Path: K:/ASP-ENN-08-0301/Application/ASP-ENN-08-0301-041.3d
Date: 21st February 2009   Time: 19:08   User ID: BlackLining Enabled

Page Number: 1

X-Ray Scattering of Biomolecules

J. Glab, T. J. Wess, K. Thomas

School of Optometry and Vision Science, Cardiff University, Cardiff, Wales, United Kingdom

CONTENTS

1. INTRODUCTION

X-rays are electromagnetic waves with a wavelength (λ) in the range of 10 nm to 0.1 nm (approximately 1,000 times shorter than visible light). The wavelength of visible light is in the order of 6.0×10^{-7} m, whereas X-rays used in scattering and diffraction are approximately 0.2×10^{-11} – 2.5×10^{-10} m [1]. The discovery that X-rays are scattered by matter has been an essential tool in the investigation into the structure of gases, liquids, amorphous solids, and crystalline solids at the molecular and atomic levels. This chapter provides a detailed description of small-angle X-ray scattering and its application in investigating a variety of biological materials.

2. X-RAY DIFFRACTION AND SCATTERING

All matter scatters X-rays. The scattering process can be simplified to a photon colliding with matter and the two interacting with one another. The energy from the incoming photon causes the charged particles within the matter to oscillate with the same frequency as the incident radiation. These oscillations within the matter cause the atom to become unstable, resulting in the eventual release of a photon. This photon is released with the same energy as the incoming incident photon; hence, no energy is lost from the system. This form of scattering is coherent scattering. The other form of scattering is incoherent scattering, but as this is negligible at small angles it will not be considered in this chapter.

Diffraction is a specific type of scattering that leads to large-scale interference effects, where incoming X-rays are scattered by atoms in all directions. The majority of X-rays scattered by matter will interfere destructively; however, in some directions, the scattered X-rays will be in phase, therefore reinforcing each other and forming diffracted beams [1]. It is the constructive interference that creates the observed diffraction pattern. Destructive interference is the result of two waves being exactly out of phase with one another, while constructive interference occurs when two coherent waves combine, increasing the amplitude of the resultant wave.

The ordering of the material leads to the inference of whether diffraction or scattering occurs. Scattering occurs when the electron density changes within the sample; these fluctuations can then be analyzed to provide structural information. The intensity of the scattering corresponds to the number of atoms present and their relative location.

Figure 1 shows the interference of two waves scattered from different points with a path difference of λ and at an angle of 2θ. The incident-wave vector k_i and the scattered-wave vector k_f are in phase with a scattering angle between them of 2θ. The path difference between the X-rays passing through the points A and O is

$$x - y = rk_i - rk_f = -r(k_f - k_i) \tag{1}$$

The phase is defined as

$$\Phi = -qr \tag{2}$$

when the scattering vector is

$$q = (2\pi/\lambda)(k_f - k_i) \tag{3}$$
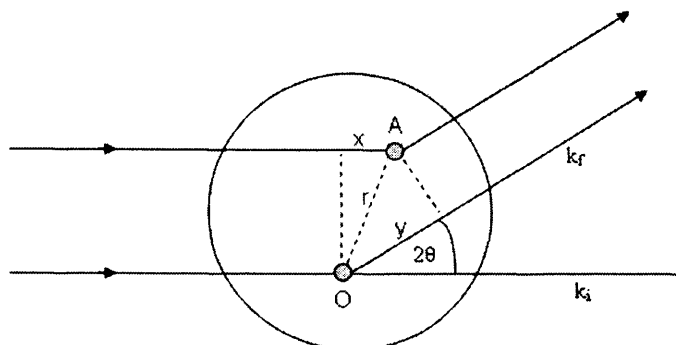
Figure 1. Schematic of the interference between two waves scattered from different points, A and O, with a path difference of λ and at an angle of 2θ.

This scattering vector bisects the angle between the incident and scattered beam and has the following length [2]:

$$q = \frac{4\pi}{\lambda}\sin\theta \qquad (4)$$

The relative distribution of atoms in a sample corresponds in scattering by the relative distances between scattering objects (atoms, in this case); it is often more appropriate to consider the correlation function between scattering centers in a sample as opposed to the sample itself, and thence infer the structure from the correlation function. The correlation function $g(r)$ corresponds to the probability density of having two scatterers in the same sample at a specific length, and its Fourier transform (the spatially inverse relationship) is used to calculate the amplitude of the scattering vector $I(q)$. The scattering of the X-rays within a sample results in a distribution of X-rays continuously over a broad range of angles. If the atomic order within matter tends toward crystallinity, then diffraction occurs where X-rays interact within well-ordered structures, producing a characteristic pattern of sharp peaks collected on a detector due to constructive and destructive interference effects. Many biological samples exhibit both the characteristics of a system which produces both scattering and diffraction.

3. SMALL-ANGLE X-RAY SCATTERING (SAXS)

Small-angle X-ray scattering (SAXS) is observed from almost all kinds of matter, and it is widely used in various fields, such as structural biophysics, soft condensed matter, material science, and for industrial applications. The term small angle corresponds to the scattering at very low angles from the direct beam (typically 0.1–10°). Scattering at low angles allows the examination of large-scale structures from one to several hundred nanometers. Low-angle scattering results from a fluctuation in the electron density. It is the existence of these density inhomogeneities in the sample that is essential in producing characteristic scattering curves which then can be used to explore microstructure on the colloidal length scale.

SAXS is conducted by passing a collimated X-ray beam with a specific wavelength λ through the sample. The intensity changes $I(q)$ are measured as a function of the scattering angle θ. A schematic drawing of the setup is shown in Figure 2.

As well as the large range of length scales covered by the techniques, the other advantages of SAXS are that minimal sample preparation is required and the technique relies on
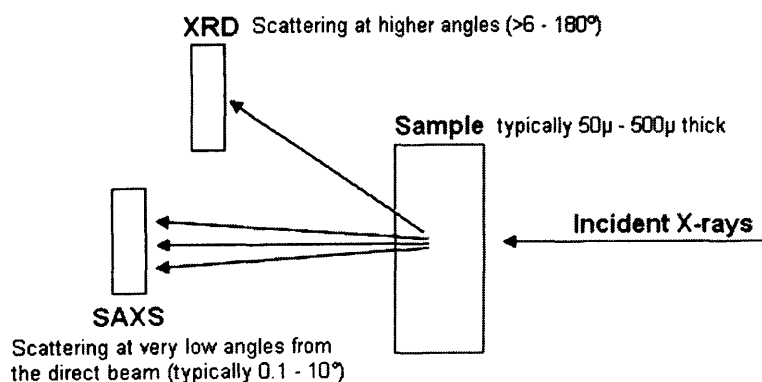
Figure 2. Schematic showing the principles of X-ray diffraction (XRD) and small-angle X-ray scattering (SAXS).

the simultaneous scatter from several scatterers and yields excellent sampling statistics.

In Figure 3a, particles are separated widely enough to make independent contributions to the scattering pattern, and with increasing concentration in the sample, interference effects will occur which produce distinctive reflections (Figure 3c, 3d, and 3e). A single-particle electron density distribution has a finite size; hence, the intensity drops continuously with the increasing scattering vector (Figure 3b). A scattering curve produced from a solid state (Figure 3e) consists of sharp peaks that reflect high regularity in the material lattice.

4. ANALYSIS OF SAXS PATTERNS

Small-angle X-ray scattering is used to determine the structure and organization in a sample at the nanostructural level. The shape and distribution of the scattering at low

Figure 3. Scattering curves generated from various states of matter: (a) gas-type sample, (b) single particle, (c) liquid-type, (d) quasi-crystalline, and (e) solid state.

angles provide information such as size, shape, arrangement, and internal porosity of the scattering particles. In some cases such as liquids, the distribution of scattering is isotropic in terms of its radial distribution; however, samples such as fibers or samples aligned by flow of liquid show preferred orientation in the SAXS signal, and often it is preferable to collect the scattered signal as a two-dimensional (2D) image as opposed to a signal of intensity versus scattering angle.

4.1. Data Collection

The 2D SAXS images are collected using a setup similar to the one shown in Figure 2. It consists of a selected X-ray source that generates radiation, a detector, and a specimen which is mounted between those devices. Emitted X-rays are scattered by electrons in the specimen, and a characteristic pattern is recorded on a selected detector. The most widely used detectors are silicon-based charge-coupled devices (CCDs) where readout takes seconds and can be transferred directly to the computer memory after each exposure. The location of the detector can be varied, resulting in different detector-to-specimen distances. It is the detector-to-sample length that provides information about the specimen at different length scales. A shorter detector-to-specimen distance provides detail about the short-order (higher resolution) structures, while a longer detector-to-specimen distance provides information on the long-range structures.

As most of the X-rays passes through the specimen unscattered, it is necessary to prevent the direct beam from striking the camera. As a result, a lead beamstop is mounted between the specimen and the detector directly in line with the emitted radiation, absorbing the rays from the direct beam. Biological samples can be rapidly damaged by X-ray radiation; one possible way to prevent radiation damage to biological materials is to freeze the specimen.

4.2. Data Correction

Characteristic small-angle scattering patterns are usually accompanied by other scattered radiation which is not due to the interaction with the sample. Before analyzing the data, it is important to subtract this background radiation from the original data to obtain correct intensity values and a clearer scattering image. Usually, it can be done by repeating the same experimental conditions and recording the image of an empty cell without the specimen present. This background image can then be subtracted from the collected data (with a small consideration made for the transmission of the sample) to remove many artifacts introduced to the original image. Once corrected for the background radiation and artifacts, the data can be analyzed.

4.3. Data Reduction and Analysis

The main aim of data analysis is to extract information from the scattering data that relates to physical parameters within the sample; this relates to particle size, crystallinity, orientation, nanoporosity, and so on. Data can be reduced by the conversion of the scattering images into polar plots.
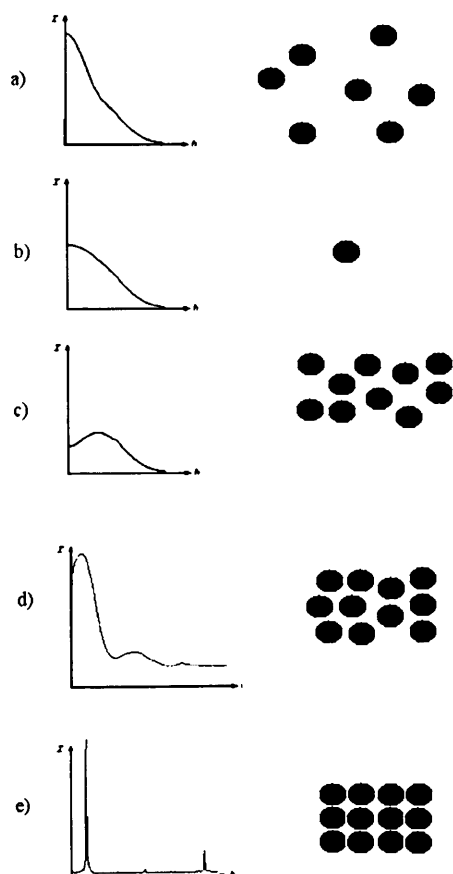
If scattering is isotropic in the azimuthal (angular-dependent) distribution, this is simply a matter of integrating the signal over the whole angular distribution of the detector. Anisotropic scattering calls for more selective regions of integration in order to extract more significant information from specific parts of the scattering signal. Once the 2D data are reduced to a polar plot, it is possible to create a one-dimensional (1D) linear intensity profile from the scattering data. The conversion of Cartesian coordinates to polar coordinates allows the intensity distribution of the scattering to be plotted against an angular position, allowing the estimation of structural parameters.

Various computer programs are currently available for data reduction and processing. These change on almost a year-by-year basis and are frequently updated to account for new modalities of software analysis. The most useful and commonly used of these are as follows.

4.3.1. FibreFix

FibreFix is a Collaborative Computational Project for Fibre Diffraction and Solution Scattering (CCP13) software package created to determine specific parameters from fiber diffraction patterns. This user-friendly program contains various analytical features that allow the raw data to be read in and displayed as a 2D image. It also has many additional features: for example, it allows adjustment of the intensity scale and the contrast of the image, allows estimation and removal of the background radiation, allows calculation of the image center, can calculate any specimen tilt, and finally is able to generate 1D intensity profiles. The user can also choose the type of linear intensity plot to be outputted, for example an intensity profile along a line or a scan around an arc.

FibreFix is available from http://www.ccp13.ac.uk.

4.3.2. Fit2D

Another software program commonly used for analysis of 2D scattering patterns is Fit2D. It performs mathematical operations and geometrical transformations such as intensity scaling, background subtraction, calculation of the 1D plot along the arc, and display of a three-dimensional (3D) surface view. Fit2D can also be used to analyze powder diffraction data and performs such manipulations as center estimation, polar transformation of the data, and generation of a 1D intensity profile as a function of azimuth [3].

Fit2D is available from the European Synchrotron Radiation Facility, http://www.esrf.eu/computing/scientific/FIT2D/.

4.3.3. Peak Fit

Once 1D intensity profiles are obtained from 2D fiber diffraction data, the traces need to be analyzed. The produced 1D intensity profiles consist of series of peaks produced from long-range order and also contain other reflections such as those derived from a uniform fibril radius or an intermolecular distance. However, some peaks in the linear traces can be hidden or shouldered, which may be due to noise and/or a large amount of diffuse scattering. Therefore, detailed determination of the peak parameters is needed. These can be calculated using special computer

programs such as PeakFit (Systat Software Inc.), which is a nonlinear curve-fitting software that can be used to separate all peaks present in the linear plot. It enables the user to fit and subtract the baseline from the traces using different characteristic models for each different data set (e.g., exponential or logarithmic). It also allows the peaks to be mapped and fitted, which allows the calculation of the peak parameters such as the peak position, the peak amplitude, the integral area, and the peak width (full width half maximum, or FWHM). PeakFit also makes it possible to conduct more advanced data manipulation using the software such as Fourier transform, Gaussian convolution, and Loess algorithm for smoothing.

PeakFit is available from http://www.systat.com/products/PeakFit/.

4.3.4. Primus

1D small-angle scattering data obtained from solution scattering from biological macromolecules can be processed by software such as Primus. It performs various manipulation functions such as averaging, background subtraction, and evaluation of parameters: radius of gyration, Porod's volume, zero intensity, and molecular weight from Guinier and Porod plots. A comprehensive guide to Primus is given by Konarev et al. [4].

Primus is available from http://www.ccp13.ac.uk.

4.4. Scattering Analysis

Scattering curves obtained from the interaction of matter with radiation and recorded on a detector contain a vast amount of detailed information about its nanostructure. The next step after generating a linear intensity profile from a 2D detector output is the determination of parameters characteristic for the nanostructural inhomogeneity that produces the scattering. This very often is a macromolecule or a nanoparticulate. The characterization of the physical features is made by two main approaches: (1) the estimation of structural parameters by comparison of relative parts of the scattering curve, where the decay and measured intensity of the scattering curve can be used to indicate size, shape, and interfacial surface area; and (2) the scattering curve is simulated (modeled) from a model system where the shape of the nanofeature and the association between scattering objects are used to modulate the scattering curve (see Section 4.6).

Figure 4 shows a scattering curve with specific regions that can be used to determine the structure of the particle. The scattering intensity is defined as

$$I(q) = I_0 P(q) * S(q) \qquad (5)$$

where the intensity of the incident radiation is I_0, the form factor is $P(q)$, and the structure factor is $S(q)$. They can be used to determine the size and shape of the particle and the interactions present between the particles. The innermost (Guinier) and final (Porod) regions of the scattering curve are used to estimate a radius of gyration and surface area, respectively.

Directly from the scattering pattern, the following parameters can be obtained.
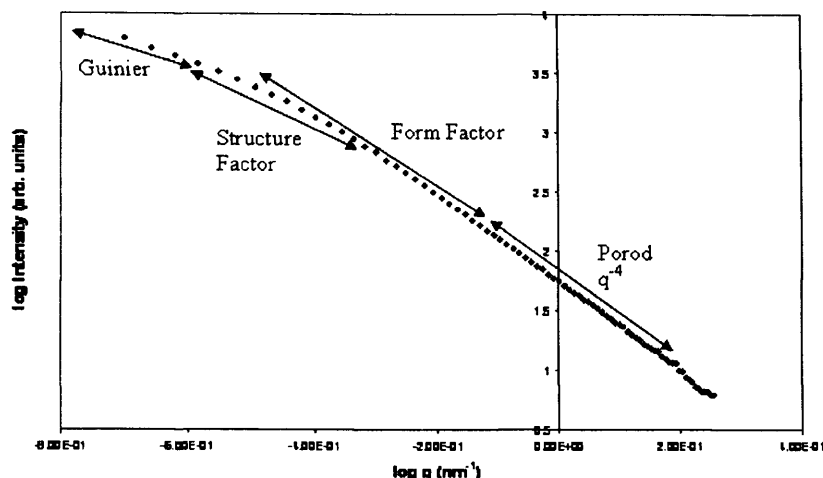
Figure 4. Representation of a scattering curve with the parameters that can be extracted from a scattering pattern labeled. The regions labeled are the Guinier region, the Porod region, the form factor, and the structure factor.

4.4.1. Molecular Weight

Molecular weight of the molecule can be determined from a scattering pattern of its homogeneous solution. For the particles of arbitrary shape, it can be determined from the following equation:

$$M = \frac{I(0)}{P} \cdot \frac{a^2}{\Delta z^2 \cdot d \cdot c \cdot I_e \cdot N_L} = \frac{I(0)}{P} \cdot \frac{2I,0 \cdot a^2}{\Delta z^2 \cdot d \cdot c} \quad (6)$$

where Δz is an electron density difference, P is the integrated intensity, $I(0)$ is an intensity at zero angle, d is sample thickness, c is concentration, I_e is the Thomson factor (effective cross section of the electron), and N_L is the Avogadro number. Corresponding mass per unit length can be determined for cylindrical and flat particles [5].

4.4.2. Radius of Gyration

Radius of gyration is an intuitive measure for the spatial extension of the particle. Its value depends on the distances of all electrons in the particle from their gravity center and can be obtained from the initial (innermost) region of the scattering curve, where scattering data are insensitive to fluctuations in the electron density. The Guinier approximation shows a relationship between integrated scattering intensity and the radius of gyration R_g [6]:

$$I(q) = I(q = 0) \exp(-q^2 Rg^2/3) \quad (7)$$

In a Guinier plot of $\ln I$ vs $(2\theta)^2$, the radius of gyration R_g is proportional to the square root of the slope of the tangent in the limit of $2\theta \to 0$ [2]. Figure 5 shows a Guinier plot where a negative slope gradient is present, and its value can be used to estimate radius of gyration $Rg^2/3$ [7].
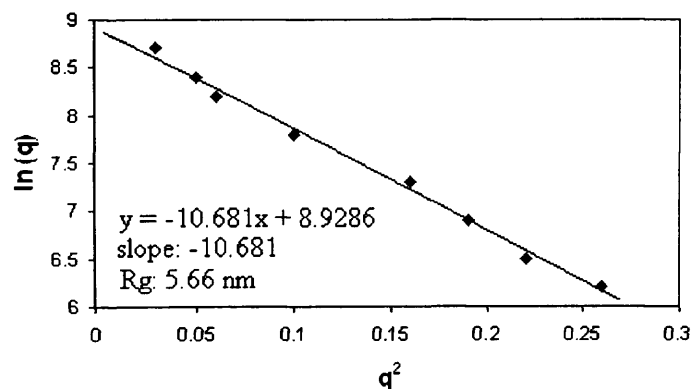
Figure 5. Guinier plot of ln I(q) against q^2. The innermost part of the scattering curve is used to calculate the size of the molecule. The slope from the Guinier plot is directly related to the radius of gyration.

Examples of the studies where radius of gyration has been calculated from the small-angle scattering pattern are those determining the calmodulin changes in the presence of calcium [8], studying the effects of sugars on proteins involved in sugar transport in *Escherichia coli* [9], and, recently, determining fibrillin-1 nanostructure [10].

4.4.3. Volume of the Molecule

The volume parameter can be obtained from the central region of the scattering curve from the particles that contain homogeneous electron density distribution using the following equation:

$$V = K \frac{I_0}{\int_0^\infty I(2\theta) \cdot (2\theta)^2 \cdot d(2\theta)} \qquad (8)$$

where I_0 is the scattered intensity at zero angle and K is the invariant for a given concentration, $K = \frac{\lambda^3 \cdot a^2}{4\pi}$ (a – specimen to detector distance) [2].

4.4.4. Surface Area

The surface area of domains in the nanoscale can be determined from Porod's fourth power law [11]. The scattering intensity distribution results from spatial variations and density fluctuations within the sample. Variations of this kind are often found in colloidal systems, porous media, or suspensions. When two media are separated by a sharp interface, asymptotic scattering occurs in the high q region (Porod region), and scattering intensity can be measured using Porod's law:

$$I(q) = I_e 2\pi\rho^2 S / q^4 \qquad (9)$$

where ρ is the electron density difference, S is the surface interface, and I_b stands for background scattering that is always present in the sample [12].

If a scattering curve is plotted as $I(q)^* q^4$ against q^4, it results in a Porod plot (shown in Figure 6). It is characteristic for a medium made of two phases separated by a sharp interface and contains a curve with a single bump before reaching the Kirste-Porod limit at large q. This limit value can be calculated from the y-intercept and corresponds to a Porod constant that is directly proportional to the surface area [2]:

$$C_P = 2\pi(\Delta\rho)^2 \cdot S \qquad (10)$$

Apart from the position, the width of the bump from the Porod plot can also provide information about the structure of the molecules as it is related to size polydispersity [12].

Porod's law predicts a rapid decay of the scattering intensity as q^{-4}, which leads to usually low intensities in the Porod regime. This may cause difficulties in the separation of the signal from the background scattering and the interpretation of the data. Another disadvantage is various calibration procedures that are applied to the data and may cause up to 20% error of the calculated Porod constant [13]. However, in the appropriate range of Q values and with low values of background scattering, this method is extremely useful and has been widely used to study changes and differences of total surface or interface area in samples such as porous media, colloid suspensions, or microemulsions. As an example, it was used to study silica colloids suspended in water [14], nanofeatures present in an avian eggshell [15], archaeological bones [16], and a surface of a cement paste [13].

4.4.5. Radius of the Cylindrical (Rodlike) Particles

A scattering pattern of uniform rodlike particles can be conveniently described as a first-order Bessel function. A linear plot of intensity vs. scattering vector Q converted from a 2D scattering pattern from a solid cylinder consists
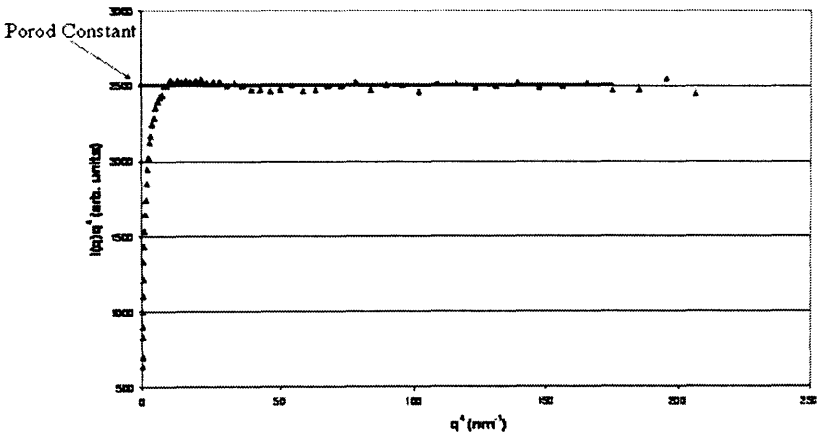
Figure 6. I(q)*q⁴ versus q⁴; a Porod plot obtained from the scattering curve of a medium containing two separated phases. Scattering curve approach a constant (Porod limit) at high q.

of characteristic minima and maxima, which positions are related to its radius (r) and can be used to estimate its value. Intensity of the scattered X-rays is proportional form factor F^2, given by eqn (11):

$$F(Q) = \rho A \frac{2J_1(Qr)}{Qr} \qquad (11)$$

where J_1 is the first-order Bessel function of the first kind and A is a cross-sectional area of the cylinder (πr^2). The scattering intensity of a single or a group of uniformly shaped cylinders is given by

$$I(Q) = b + cr^4 \left[\frac{2J_1(Qr)}{Qr} \right]^2 \qquad (12)$$

and, for the polydisperse system,

$$I(Q) = b + c \sum_{i-1}^{N} r_i^4 w_i \left[\frac{2J_1(Qr_i)}{Qr_i} \right]^2 \qquad (13)$$

where b and c correspond to a baseline correction and scaling factor, respectively, and w_i is a frequency of occurrence of a given radius [2, 12, 17–19].

The majority of biological tissues in terms of global biomass, such as connective tissues or wood, are built from long-chain fibril-forming biological molecules (e.g., collagen, fibrillin, and cellulose). Those fibrils or molecules can be conveniently described as cylinders, often of uniform diameter; hence, they produce characteristic reflections on a scattering pattern. This fact has been used in various connective tissue studies and has given an insight into their molecular structure [17, 19–21].

4.5. Diffraction Analysis

Many biological substances that do not form monolithic crystals still contain long- or short-range order regions and can generate distinctive diffraction patterns characteristic of preferentially aligned polycrystallites. An example can be fibrous materials such as collagen, muscle fibers, or fibrillin. Figure 7 shows a diffraction pattern characteristic for rat tail tendon type I collagen (Figure 7a) and a corresponding linear intensity profile (Figure 7b).

The following parameters can be calculated from the diffraction pattern.

4.5.1. Determination of Intermolecular/ Particulate Distance

When many particles are involved in the scattering process (e.g., a great number of molecules in the solution or fibrils in the biological tissue), an interference effect will occur. Attraction and/or repulsive forces will effect in characteristic ordering of the individual particles, and their strength will depend on the packing density of the molecules. Scattering intensity is correlated with the interference function, and their relationship is given by

$$I(K) = F^2 \cdot G(K) \qquad (14)$$

where F^2 is the scattered intensity for a single particle and $G(K)$ is the interference function characteristic of the interaction *between* the discrete scattering objects.

4.5.2. Particle Size Distribution

When a great number of particles are present in the solution and their size is sufficiently uniform, they will generate a scattering pattern characteristic for a single particle. However, variation of the size still occurs and becomes a parameter that can be determined from the scattering curve. The size distribution can be described as $Dn(R)$, which defines a number of particles of size R. Many analytical methods of size distribution determination have been developed and published [2, 22–25].

4.5.3. Periodicity

Some biological molecules (e.g., collagen and fibrillin) are characterized by a highly ordered long-range structure. As small-angle scattering is highly sensitive to any form of order, it can be used to determine parameters characterizing the structure of those molecules. One of the parameters is axial periodicity, which derives from the electron density distribution along the molecule and gives rise to equidistant Bragg's reflections on the scattering pattern. Periodicity can be easily estimated as a reciprocal value of a measured distance between those reflections. Because the long-range

Figure 7. The conversion of (a) a Cartesian two-dimensional image of rat tail tendon to (b) a linear intensity distribution. The third and ninth orders of diffraction are highlighted.

Path: K:/ASP-ENN-08-0301/Application/ASP-ENN-08-0301-041.3d
Date: 21st February 2009   Time: 19:08   User ID: muralir   BlackLining Enabled

Page Number: 8

order of rat tail tendon collagen gives rise to strong reflections and equidistant peaks, it is often used as a spatial calibration sample in SAXS experiments.

4.6. Data Interpretation

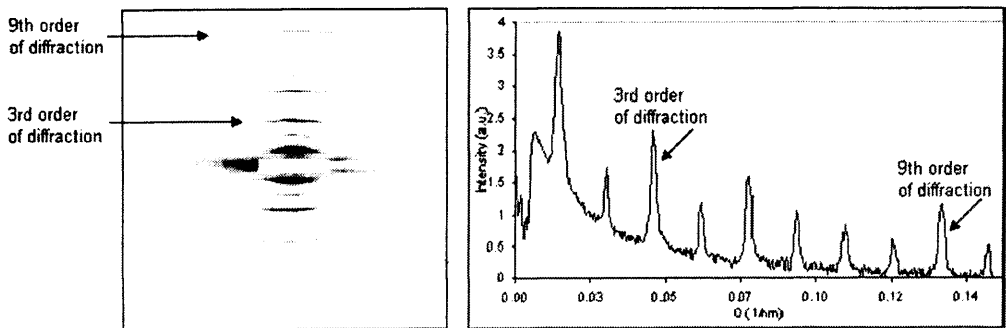The parameters described above characterize the size and shape of the particle and can be directly determined from the scattering curve. Understanding of the scattering process and the reciprocal correlation between particle size and scattering angle enabled scientists to calculate theoretical scattering curves for the particles of any shape and size. To interpret experimental curves and obtain information about the size and shape of the object, very often those simulated computer models were generated and compared with the real data. One approach is to build models of various shapes such as spheres or cylinders, generate corresponding scattering curves, and use simulated annealing (SA) algorithms to fit the data. After obtaining the theoretical curve that best fits the data, one can obtain information about the approximate size and shape of the particle. SA programs generate random "movements" of the elements (here, these are a rearrangement in shape and size of the molecule and corresponding changes on the scattering pattern) and by trial and error anneal the data, which leads to an iterative improvement [26]. After obtaining the theoretical curve that best fits the data, one can obtain information about the approximate size and shape of the particle.

The initial analysis and reconstruction of the size and shape of the molecules used an a priori approach. Information obtained from other methods was used to generate theoretical models on a trial-and-error basis. However, recent modeling studies have shown that an X-ray scattering curve contains sufficient information to use *ab initio* methods. The *ab initio* approach uses bead-modeling methods to reconstruct the most reliable shape. As the total volume of the molecule is known from the scattering pattern, computer programs "fill" the maximum area with beads. The scattering curve is then generated from the model using Debye's formula [27]. Starting from a random distribution, the model is being modified until the best match is obtained [28]. The construction of the average models can be performed by such programs as Damaver [28] or Supcomb. The latter program enables users to match 3D structures using the normalized spatial discrepancy (NSD) algorithm to measure similarity between the objects [29]. Other software packages currently available for *ab initio* structure analysis are Sasha [30], Dammin [31], or Gasbor [32]. Programs such as Credo enable users to add missing fragments (e.g., loops or domains) to existing models. This method becomes useful if the structure of the molecule is already determined by other techniques (such as X-ray crystallography or NMR), but some disorganized regions still remain unknown [33].

The aim of all modeling studies is to recover the 3D structure of the molecule from its 1D scattering curve. A recent development of *ab initio* methods and the availability of sophisticated computer programs enabled scientists to determine the structure of various molecules [34–36].

All the programs described above are available from the CCP13 website (http://www.ccp13.ac.uk).

5. APPLICATION OF SAXS

The advantages of SAXS are that it does not require any specific chemical preparation of the sample prior to measurement (such as electron density enhancement or dehydration); hence, treatments such as fixation and staining, which can introduce artifacts into the final image, can be avoided. This nondestructive technique allows analysis of solid or liquid materials and is commonly used in structural studies of materials such as keratin, collagen, lipids, fibrillin, carbohydrates, bone, and minerals.

5.1. Keratins

Keratin is an abundant fibrous structural protein found in hair, nails, claws, horns, scales, feathers (beta-keratins), and the outermost layer of the skin. The helical molecules that comprise keratin are found to twist around each other to form intermediate filaments. Keratins are tough, fibrous tissues due to their ability to form covalent chemical bonds resulting in a rigid aggregate. Nails are a substructure of the outer layer of skin and are made of the protein keratin, which is formed by amino acids. These proteins are a strong, flexible material made from many layers of dead, flattened cells.

Hair is also composed of keratin: the acidic type I hair keratin, and the basic type II hair keratin. Keratin in hair is softer and more flexible than many of the keratins. The use of small-angle X-ray scattering has allowed the long-range structure of keratins to be summised and, more recently, the growth zones of a hair follicle to be studied [37]. Human hair fiber shows three main regions in cross section. The medulla is the central region, which contains loosely packed cells; the cortex comprises closely packed keratin microfibrils; and the outermost layer is the cuticle, which is composed of intermediate filaments [38, 39].

Figure 8 shows a small-angle X-ray scattering pattern of human hair with an equatorial distribution of scattered intensity highlighted. Using this feature, the structure of alpha-keratin can be revealed, allowing parameters such as

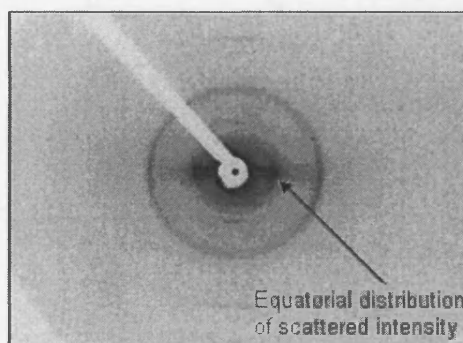Equatorial distribution of scattered intensity

Figure 8. Small-angle X-ray scattering pattern of human hair. The hair axis is vertical, and the equatorial features horizontal. Reprinted with permission from [40], F Briki et al., *Biochim. Biophys. Acta* 1429, 57–68 (1998). © 1998, Elsevier.

Path: K:/ASP-ENN-08-0301/Application/ASP-ENN-08-0301-041.3d
Date: 21st February 2009   Time: 19:08   User ID: muralir   BlackLining Enabled

Page Number: 9

the shape and packing of the keratin microfibrils to be calculated. The intensity of the equatorial scattering is attributed to the lateral packing between the intermediate filaments [39, 40].

5.2. Collagen

Small-angle scattering has proved to be a useful tool to investigate the structure of biological molecules in soft tissues. One example is collagen, which is the most abundant protein of the mammalian body [41]. There are many different forms of collagen; more than 30 types of collagen have been discovered [42]. The most abundant type of collagen and the first discovered was type I collagen, which is found predominately in tendons, skin, breasts, and corneas [43]. Collagen structure is highly ordered, and the molecules are regularly staggered by a fixed distance (tissue-specific D-period); moreover, in some tissues they have a uniform diameter and fixed center-to-center distance. The hierarchical organization of fibrillar collagen is shown in Figure 9.

This high level of organization in tissues, where there is an obvious high-volume fraction of macromolecules (>0.2), can produce scattering of the incoming X-rays and generate characteristic sharp reflections on a scattering pattern. Less organized structures produce a more diffuse scattering pattern. Two distinct forms of scattering occur: meridional and equatorial reflections. Meridional reflections, a series of Bragg reflections parallel to the fiber axis, provide information about the long-range repeating axial structure of fibrillar collagen. The equatorial reflections are found perpendicular to the fiber axis and supply information on the lateral packing of the molecules within a fibril. The fiber diagram of collagen—like that of keratin—is rich and extends to a resolution of about 0.1 nm, where the effect of nearest atoms is approached. The SAXS profile of collagen has proven more difficult to elucidate than the high-angle studies since the fibrillar organization in the wet and dry states is noticeably different, and both are insufficiently explained by current models of molecular organization.

5.2.1. Skin

Skin comprises a specific collagenous-based tissue where SAXS has contributed significantly to our understanding of the organization within the multiple layers of epithelial tissues that guard underlying muscles and organs. Skin is composed of collagen organized into fibrils, which are in turn grouped into bundles or fibers (see Figure 9). A small-angle X-ray scattering pattern of skin is shown in Figure 10.

Small-angle X-ray scattering has been used to investigate skin, which contains both type I and type III collagen, revealing a detailed supramolecular organization of collagen molecules into fibrils and fibers [44]. It was found that the axial periodicity of skin (type I and type III collagen) is 65.5 nm, compared with the 67 nm periodicity of rat tail tendon (type I collagen only) [45–47].

Understanding the structure of skin and its hierarchical arrangements is of great importance for many medical applications such as skin grafting and in postmortem or historical uses of skin such as in parchment, which is made from untanned animal skins. Writing on prepared animal skin has been used for many centuries and is of vital importance as it contains much of our written history. As parchment degrades over time, it loses strength and becomes brittle and unusable [48]; small-angle X-ray diffraction has been used to compile a detailed explanation of how this degradation affects the structural integrity of historical parchment [49]. It has also facilitated a greater understanding of how factors like ultraviolet (UV) rays, hydration, relative humidity misuse, and the presence of lipids affect the structure of parchment and cause irreversible damage [48, 50–52].

Leather is produced from the tanning of animal hides and skins. The leather industry is a vast area with many products ranging from clothing to book bindings. Understanding the structure of leather is considered important in trying to produce better quality leather and aid in the preservation of leather products. SAXS experiments have been carried out on leather to investigate the effects of biaxial stretching on the fiber orientation [53] and the production process of leather and parchment [52].
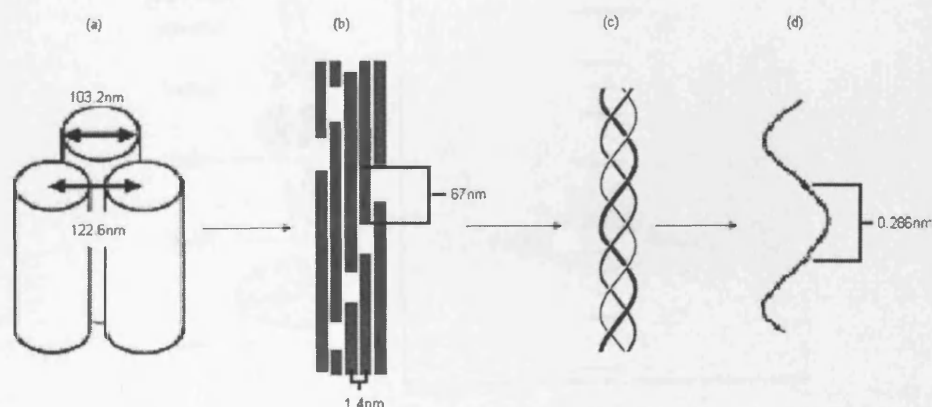

Figure 9. Collagen hierarchy: (a) fibril packing, (b) microfibril packing, (c) collagen triple helix, and (d) the helical rise per residue. Diagram not to scale.

Path: K:/ASP-ENN-08-0301/Application/ASP-ENN-08-0301-041.3d
Date: 21st February 2009   Time: 19:09   User ID: muralir   BlackLining Enabled

Page Number: 10
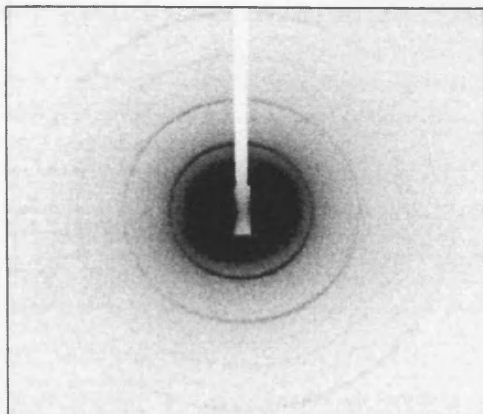
Figure 10. (a) Two-dimensional small-angle X-ray scattering pattern of rat tail skin on a 2 m camera length on beamline ID02 at the European Synchrotron Radiation Facility (ESRF) in Grenoble, France.

5.2.2. Tendon

Rat tail tendon (RTT) consists of >95% type I collagen [54]; hence, it is a useful model tissue to investigate generic molecular properties of collagen structure. Type I is the most abundant collagen type [55]. It has a highly hierarchical structure that is responsible for the viscoelastic properties of connective tissues. Figure 11 shows the hierarchical levels of organization in tendon. Collagen fibrils are almost parallel to the tendon axis and are grouped into primary bundles (fibers), secondary bundles (fascicles), and, in some cases, tertiary bundles.

The small-angle X-ray scattering pattern of tendon exhibits a series of sharp meridional peaks that corresponds to a fundamental periodicity of 67 nm in the hydrated state and 64 nm in the dry state (Figure 11) [45, 46]. One of the great

advantages of SAXS is a possibility to study tissues at different states of hydration. Modifications in the collagen structure upon drying have been investigated using this technique, where X-ray diffraction patterns have been recorded while rat tail tendon was heated up to 200°C [56]. Wess and Orgel also used X-ray diffraction to observe the effects of drying and dehydrothermal treatment on collagen in rat tail tendon and historical parchment [50]. Those studies aimed to simulate the accelerated aging of historic parchment manuscripts and describe structural changes that occur during treatment. The advantage to conducting dynamic studies has been used to describe molecular rearrangements in RTT collagen structure during stretching [55, 57–59]. Those studies required very short exposure times to record time-dependent structural changes; hence, conventional X-ray generators were replaced by a synchrotron radiation, a very bright X-ray source that will be described later. Studying molecular alterations in RTT collagen structure proved useful for understanding viscoelastic behavior and elastic properties of the connective tissues like skin or blood vessels.

5.2.3. Cornea

The cornea, the outer part of the eye, consists of layers containing parallel collagen fibrils whereby the orientation of these collagen fibrils is different for different layers. Structurally ordered fibrils with uniform diameter and fixed intermolecular distance produce scattering patterns similar to the patterns from other collagenous tissues. Small-angle X-ray scattering on corneas has shown that the organization of collagen fibrils is highly specific to the order of position within the cornea and even exhibits mirror symmetry between eye pairs. Small-angle X-ray scattering is used to gain insight into the collagenous structure of the tissue, and has became one of the major techniques used in corneal studies. Understanding parameters such as the size and arrangement of collagen fibrils is important for optimizing corneal and refractive surgery and cornea graft surgery

Figure 11. (a) Levels of organization in tendon, and (b) two-dimensional SAXS pattern of rat tail tendon; vertical reflections correspond to the axial periodicity of type I collagen. Image (b) taken at Daresbury Laboratory (Daresbury, United Kingdom) on station 2.1 using a 5.5 m sample to detector distance.

Path: K:/ASP-ENN-08-0301/Application/ASP-ENN-08-0301-041.3d
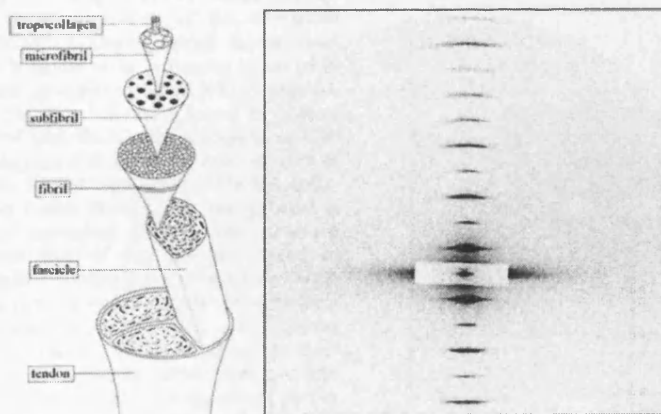Date: 21st February 2009   Time: 19:09   User ID: muralir   BlackLining Enabled
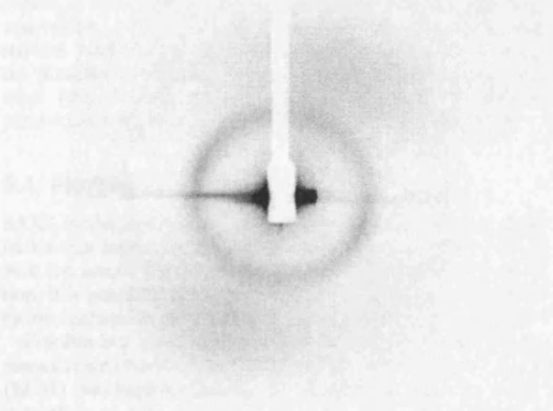
Page Number: 11

Figure 12. Small-angle X-ray scattering pattern of stretched cornea taken on a 10 m camera length on beamline ID02 at the European Synchrotron Radiation Facility (ESRF) in Grenoble, France.

[60, 61]. A small-angle X-ray scattering pattern of a cornea is shown in Figure 12.

Small-angle X-ray scattering has also be used to describe the changes in collagen structure that occur during corneal development [62], aging [63, 64], and corneal wound healing [65]. A review on the use of scattering techniques to determine corneal ultrastructure is given by Meek and Quantock [66].

5.2.4. Breast Tissue

Breast cancer is the leading cause of cancer death among women aged 20–59 years in developed countries [67]. Early-diagnosed cancer is the most treatable; hence, screening and diagnostic tests can considerably reduce its mortality (www.breastcancer.org). The progression of breast carcinomas was observed to cause alterations of the interstitial extracellular matrix (ECM). Collagen, which is the main component of ECM, is believed to be primarily involved in the changes observed during tumor invasion [68]. A putative new form of collagen packing has been found in human breast tissues (onco-fetal laminin-binding collagen, or OF/LB) and was initially suggested to be a potential marker of malignancy [68]. Further studies showed that fibrillar collagen is newly formed in tumor tissues, but the process is deeply deregulated and generates disorganized structure markedly different from that of the collagen found in healthy tissues [69]. Previous studies pointed to a role of collagenases from the matrix metalloproteinases (MMPs) family in tumor growth and metastasis [70]. Collagenases catalyze the degradation of native fibrillar collagen into thermally unstable triple-helical fragments, which denature into gelatin, and in healthy tissues they play an important part in the tissue-remodeling processes such as embryonic development, ovulation, and wound healing [71, 72]. It has been suggested that in tumor-invaded tissues, the collagenase's activity can cause alterations in collagen structure [72, 73]

and can be monitored using SAXS. Scattering patterns from the breast tissues recorded using synchrotron radiation showed a clear difference between normal and malignant samples. Changes in the fundamental axial periodicity were observed to be slightly higher in the invaded region, which was suggested to be due to the change in the crimping angle. Distinctive differences were also reported in the lateral packing, as the collagen found in areas invaded by cancer was poorly ordered. Moreover, the background scattering was stronger from the tumor's regions [74]. Results obtained from X-ray scattering were compared with histological examination and showed a clear correlation [75]. This pointed to a suggestion that SAXS can be used as a diagnostic test to locate regions invaded by cancer. Although most of the studies were conducted using synchrotron radiation, the initial experiments with conventional X-ray sources have also shown distinct differences between normal and malignant tissue samples [76]. This approach would prove to be more useful as a potential diagnostic test in hospitals and clinics. A small-angle X-ray scattering pattern is shown in Figure 13.

5.3. Lipids

Lipids are hydrocarbon-containing organic compounds that form the cell membranes, build compartments and barriers within the cells, and support the proteins in the walls of the cell.

Cell membrane fusion is a common way for molecules to enter or exit cells where the main structural component for the cellular membrane is a double layer of lipid molecules [77]. Understanding cellular membranes may help researchers understand recognition of "self," the basis for signal transduction, and the prevention of infection such as when the body is threatened by viruses (e.g., HIV from entering and infecting the cells). It may also lead to the design of drug delivery systems or gene therapy [77]. Small-angle X-ray scattering has been used to identify the impact that
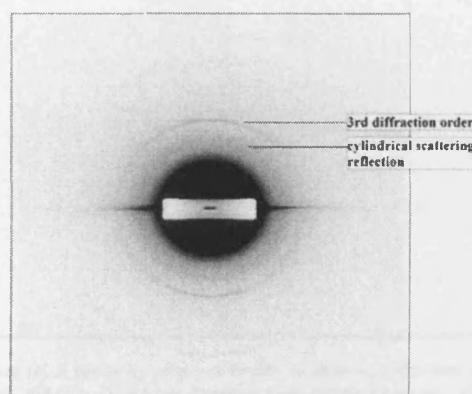

Figure 13. Small-angle scattering image from breast tissue. Rings correspond to a third and fifth diffraction order of collagen. Image was taken at Daresbury Synchrotron Facility (Daresbury, United Kingdom) with a 6.5 m camera length. Figure provided by S. Pearson.

drugs have on the structure and behavior of cells, which is critical in determining the impact of drug loading, stability, and release [78]. It has also been used to understand the stresses found within biological membranes and to study the presence of lipids in materials such as historical parchment [48]. A small-angle scattering pattern of historical parchment with lipid rings present is shown in Figure 14.

5.4. Fibrillin

SAXS is the optimal nanostructural technique to analyze bulk intact tissue samples in the fully hydrated state. Along with the use of the highly intense synchrotron X-ray radiation, it is possible to study biological samples such as fibrillin that exhibit weakly diffracting long-range periodicities.

Fibrillin is a main component of fibrillin-rich microfibrils, essential structural components of the extracellular matrix (ECM) that impart elasticity on all dynamic connective tissues such as skin, muscle, ligaments, and zonular fibers. Microfibrils have a complex ultrastructure resembling beads on a string, with an average periodicity of 56 nm and a diameter of ~10–14 nm measured by electron microscopy (EM). The X-ray diffraction pattern of native hydrated fibrillin-rich microfibrils exhibits a series of meridional Bragg peaks accompanied by a background diffuse scatter, which may suggest a high static disorder [79]. Meridional peaks correspond to a 56 nm axial spacing previously measured by EM.

A wide range of axial periodicities has been observed by STEM (300% variation), which may indicate that microfibrils are highly elastomeric [80]. The unusual elastic behavior of individual microfibrils is predicted to reside within the reversible molecular rearrangements and extension of the bead–interbead repeat. A model for the alignment of

fibrillin molecules within microfibrils suggested by Baldock et al. [81] showed a possible folding of the molecules to form a beaded microfibril. The proposed model would produce ~160 nm microfibrils in the unfolded state, an intermediate state of ~90 nm, and stable 56 nm periodicity-beaded microfibrils [81]. The SAXS technique has been used to monitor the reversible *elastic* response hitherto unrecordable by EM, and the alterations in the axial periodicity in the extended and relaxed states have been described. Here, the scattering pattern of the native microfibrils showed a series of meridional peaks that corresponded to characteristic 56 nm periodicity. A controlled tissue extension to 150% of the rest length resulted in a markedly different diffraction image. The results showed that elongation to 100% and 150% produced an increase in fundamental axial periodicity to 80 nm and 100 nm, respectively [79, 82, 83]. This was also accompanied by a change in the axial intensity distribution of the small-angle scattering position, which suggests a disruption of the characteristic supramolecular array seen in the resting state. As the beads on a string are extended and unravel, the axial contrast density decreases. The increase in the fundamental axial periodicity corresponds to microfibrillar metastable states and may reflect molecular unfolding.

The use of SAXS to study the effects of tissue extension has provided a further insight into the elastic behavior of fibrillin-rich microfibrils. Diffraction patterns of native hydrated microfibrils verified the fundamental axial periodicity previously measured by EM. Images recorded during controlled tissue extension showed intermediate states of an unfolding process that were predicted by an alignment model [81]. A small-angle X-ray scattering pattern of fibrillin is shown in Figure 15.
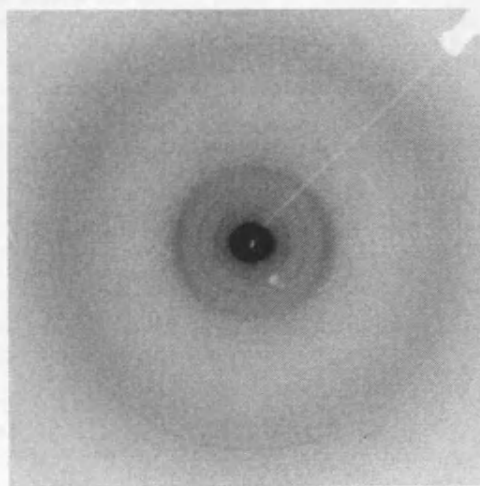
Figure 14. Two-dimensional SAXS pattern of lipid in historical parchment. Image was taken at European Synchrotron Radiation Facility (ESRF), Grenoble, France.
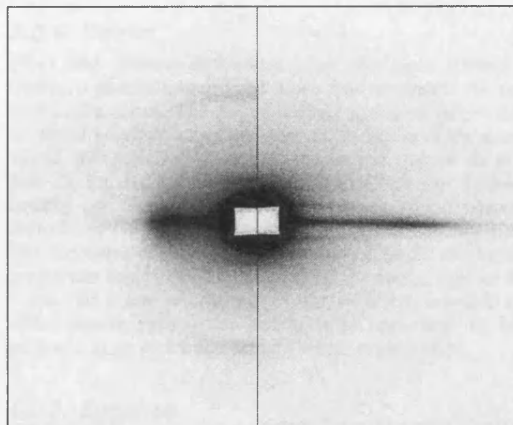
Figure 15. A scattering pattern of fibrillin in an intact native state (left panel) and after 150% tissue extension (right panel). Equatorial reflections are moved to higher angles upon stretching which corresponds to a decrease of fibrils radii, while an increased axial periodicity causes meridional reflections to move to low angles near the beamstop. Images were taken at European Synchrotron Radiation Facility (ESRF), Grenoble, France, using a 5 m camera length.

Path: K:/ASP-ENN-08-0301/Application/ASP-ENN-08-0301-041.3d
Date: 21st February 2009   Time: 19:09   User ID: muralir   BlackLining Enabled

Page Number: 13

5.5. Cellulose

Cellulose is the most abundant naturally occurring organic substance and is the major structural component found in plant cell walls, cotton, linen, viscose, paper, celery, and wood. Cellulose is organized in crystalline domains called microfibrils [84], where the diameter of the microfibrils varies between 2 nm and 25 nm. A small-angle X-ray scattering pattern of celery cellulose is shown in Figure 16.

SAXS has been used to provide detail on the shape and dimensions of the cellulose microfibrils. SAXS images of cellulose consist of a strong equatorial intensity profile where the angularly distributed width of the streak with respect to the fiber axis corresponds to a misalignment of the microfibrils [85]. This misalignment is called the microfibril angle μ and is in part responsible for the mechanical properties of cellulose. Cellulose is arranged in a spiral arrangement which provides the properties of stiffness and extensibility.

Understanding the properties of cellulose microfibrils is essential work in the agricultural field. Until recently, the size of the cellulosic microfibril diameter has been relatively obscure; however, recent studies on celery collenchyma have revealed a more regular fibril diameter and have opened a new avenue for the study of fibrillar interactions.

5.6. Bone and Mineral

Bone tissue is a mineralized form of connective tissue that plays an important supportive role in the vertebrate body. Bones consist of a mineral phase deposited in collagen fibrils, an arrangement that provides the mechanical properties of the tissue. Bone tissues generate diffuse scattering at low angles that contain information about their structure and can be used to interpret the surface region and provide information about the orientation of mineral crystals present in bone samples. As there is a sharp interface between the mineral and organic phases in the bone, the inferface can be analyzed as a SAXS Porod plot to estimate the area
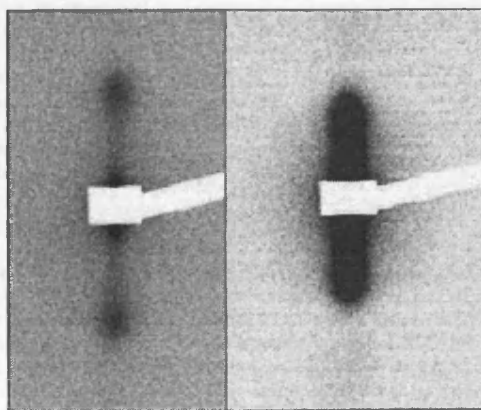
Figure 16. Small-angle X-ray scattering pattern for dry (left panel) and wet (right panel) celery cellulose taken at the European Synchrotron Radiation Facility (ESRF), Grenoble, France, on a beamline ID02 using a 1 m camera length.

of mineral crystals. With other parameters also calculated from the scattering curve, it is then possible to obtain information about the shape of the crystals and the mean thickness, a parameter difficult to obtain by other methods.

To understand the calcification process, SAXS has been used to investigate those parameters for samples dissected from differently aged animals, and it has shown the pattern of crystal nucleation and growth [86, 87].

Application of the microbeam small-angle scattering technique, which allows study of the nanostructure of the materials with a few micrometers' scanning resolution, has enabled scientists to investigate the mineralization front with high precision. Studies had shown an alteration in mineral crystals' shape and arrangement in the first stage of the biomineralization process [88]. A comparative study has also been performed on the molecular arrangement of collagen fibrils between mineralized and unmineralized turkey leg tendon. It showed the irregularity in the collagen lateral packing, which authors described as a 2D fluid structure [89]. The study gave a detailed insight into the process of crystal deposition inside collagen fibrils. SAXS has also been used to describe mineral crystals formed in different types of calcified tissues. It has been reported that the turkey leg tendon contains mainly plate-shape crystals and its mineral microstructure differs from that of bone, where needle-shaped crystals were found [90].

Many studies have been carried out using SAXS to correlate micro- and nanostructural properties within bone and to investigate diseases such as osteogenesis imperfecta (OI). OI is a genetic bone disorder caused by a mutation of type I collagen and characterized by fragility of bone [91]. SAXS studies showed clear differences between the mineral crystals in healthy and OI bones [87] that can be used as a diagnostic tool of the disease. Figure 17a shows a small-angle X-ray scattering pattern of bone.

5.6.1. Dentin

Fiber and mineral architecture has also been studied in dentin, a porous mineralized tissue that surrounds the pulp cavity of a tooth. The SAXS studies provided information on tissue microstructure and showed variation in the mineralized collagen fiber's architecture depending on its position in the tooth [92, 93], and the differences between healthy and altered dentin (for example, in dentinogenesis imprefecta [94] or in age-related transparent dentin [95]). The structure of dentin is directly related to its mechanical properties and hence the strength of the tooth. Age or diseases can cause alterations in the collagen network and affect dentin properties; hence, it is important to fully understand its molecular structure and organization.

5.6.2. Eggshell

The avian eggshell is a highly ordered bioceramic composite, with both organic and inorganic composites [15]. The complete process of shell formation takes approximately 24 hours and is one of the fastest calcification processes known in biology [96]. SAXS has been used to investigate structures on the nanometer scale such as size, shape, arrangement, and internal porosity. In addition to SAXS,

Figure 17. Small-angle scattering pattern of cow's bone (left panel) and an eggshell (right panel). Bone image was taken using a NanoSTAR X-ray source, and the eggshell image was taken at European Synchrotron Radiation Facility (ESRF), Grenoble, France, using a microfocus beamline with a sample-to-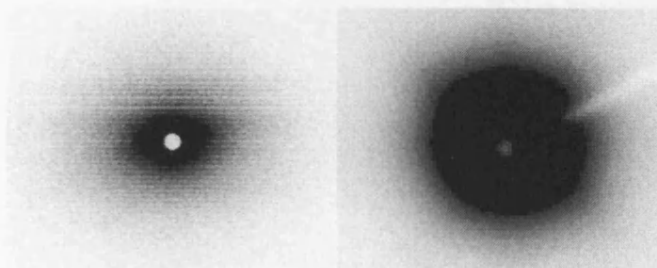detector distance of 20 cm. Figures courtesy of J. Hiller, Diamond Synchrotron Light Source; and D. Lammie, Cardiff University, Wales.

microfocus small-angle X-ray scattering (μSAXS) has been utilized to resolve different aspects of the shell growth process and to investigate structural changes at different layers within the eggshell. It showed nanofeatures which have not been identified by previous electron microscopy and wide-angle diffraction studies and a variation within the nanostructure of different shell layers [15].

The nanostructure and nanotexture of the eggshell are closely related to its function as a mechanical protection and a source of calcium for the developing embryos. This structure–function relationship is a subject of studies aimed at improving the quality of eggshells, an important factor in the poultry industry. Figure 17b shows a small-angle X-ray scattering pattern of an avian eggshell.

5.6.3. Archaeological Samples

The nondestructive nature of the SAXS technique becomes an advantage in analyzing rare and irreplaceable samples such as archaeological bones. The structure of mineral and collagen components can provide information on specific processes that affect bones after death, such as cremation, cooking, or geological and biological degeneration (diagenesis reviewed by Hedges [97]). The analysis of SAXS patterns from archaeological bones showed alterations of the crystallites as an effect of various diagenetic changes [98]. To gain a further insight into specific changes of bone mineral, the studies have been conducted to simulate diagenesis processes (for example, experimental heating as a simulation of cremation [16]).

5.7. Chromatin

Chromatin is a complex of DNA and proteins where genetic information is stored and expressed. It is found in eukaryotic cells nuclei and characterized by a hierarchically organized structure. The basic structural unit of chromatin is the nucleosome, which is composed of DNA wrapped in a left-handed superhelix. This is often referred to as beads on a string, with an 11 nm nucleofilament [99]. The nucleosomes are arranged into a compact array forming a 30 nm chromatin fiber by the presence of the histones and other proteins. The next structural level is the densely packed

DNA, which allows the attainment of the metaphase chromosome.

Chromatin structure is an important factor in DNA repair and replication [100]. It has been studied using electron microscopy; however, dehydration of the fibers and the fixation process, a part of the sample preparation, were found to be responsible for inducing alterations into chromatin fibers. The SAXS technique has also been applied as it does not require any chemical preparation and can give detailed information about the chromatin nanofeatures [101–103]. The experiments were conducted on the isolated chromatin fibers, and very often nonspecific reflections were recorded on the diffraction pattern. It was suggested that the isolation process of chromatin from the living cell may induce disorder into the structure; hence, the studies have been conducted in vivo, where the intact structure can be monitored [104, 105]. Diffraction patterns from the living cell can be difficult to interpret as they contain reflections produced by other structures than the one that is being studied. However, the experiments gave a great insight into the structure of chromatin fiber in vivo and showed a variation in its packing in different cells and nuclei [104, 105]. SAXS has also been used to study the changes that occur in chromatin structure during the cell cycle [104, 105]. Figure 18 shows two small-angle X-ray scattering patterns from chromatin.

The structural order of chromatin has been of great scientific interest, and it is believed that the understanding of chromatin may lead to a number of therapeutic applications against main diseases, for example cancer and HIV.

5.8. Muscles

Muscle is a specialized, contractile tissue of the vertebrate body. It is built by muscle cells that contain myofibrils, cylindrical organelles composed of myosin, and actin proteins. Myosin molecules found in myofibrils consist of the tail and head domain that binds to a filamentous actin. Both compounds enable cell movements and are responsible for a muscle contraction. Understanding of the transformation of chemical to mechanical energy during muscle contraction has been an important goal of many research studies. It is known now that the process involves a cyclical
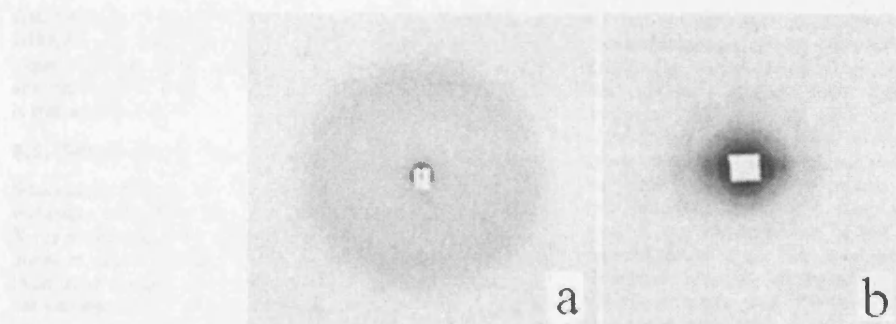
Figure 18. Small-angle patterns of chromatin taken from living cells. (a) Living rabbit erythrocytes, and (b) living whole sea urchin sperm *Echinus esculentus* in semen. Reproduced with permission from [104], J. P. Langmore and J. R. Paulson, *J. Cell Biol.* 96, 1120–1131 (1983). © 1983, Rockefeller University Press.

movement of myosin heads called the cross-bridge cycle [106]. Since muscles can produce characteristic small-angle scattering, the technique has been used to describe structural changes that occur during contraction. The scattering pattern obtained from the muscle contains sharp peaks and a large amount of diffuse background scattering, which are generated by characteristic myosin layers and an arrangement of myosin heads [107, 108]. Changes in both Bragg and diffuse scattering have been investigated to describe the contractile cycle, usually using a time-resolved approach with a millisecond time scale [107, 109, 110]. Frog sartorius muscle and insect flight muscle have often been used as material in many studies [111–113]; however, interpretation of experimental data was difficult due to a statistical disorder present in the tissue. A use of alternative tissues has been proposed, such as bony fish muscle with more crystalline structure of myosin filaments [114]. Small-angle scattering has also been used to study the disorder introduced by temperature in the arrangement of the myosin filaments. Studies showed that at lower temperatures (below 10°C), sharp lines on the scattering pattern that are due to a myosin layer become very weak, which is accompanied by an increase in diffuse scattering [115, 116]. This leads to a suggestion that the helical arrangement of the myosin heads can be very sensitive to temperature.

Recent studies on muscle contraction use an advantage of high-resolution systems, which enables scientists to view the movements of the myosin heads with subnanometer-level resolution [117, 118]. A third-generation synchrotron radiation facility has also been used to conduct time-resolved studies using 0.53 msec time resolution and to study the effects of a single electrical impulse on the skeletal muscles [119, 120]. Figure 19 shows a small-angle X-ray scattering pattern for muscle.

6. COMPLEMENTARY TECHNIQUES TO SAXS

Standard SAXS has been exemplified by the previous studies described in detail; the following examples describe the use of techniques allied to SAXS that probe aspects beyond the conventional scattering volume.

6.1. Grazing Incidence Small-Angle X-Ray Scattering (GISAXS)

Traditionally, SAXS is used for measuring bulk materials and is unable to measure the surface or near surface of thin films. Grazing incidence small-angle X-ray scattering (GISAXS) combines two techniques: grazing incidence diffraction (GID), which uses reflection geometry to obtain surface and near-surface X-ray scattering; and SAXS, which measures structures on a nanometer scale. GISAXS is a versatile tool for characterizing nanoscale density correlations and is principally used to characterize nanoscopic particles, pores, or thin films [121]. GISAXS is able to provide detailed information on particle geometry, size
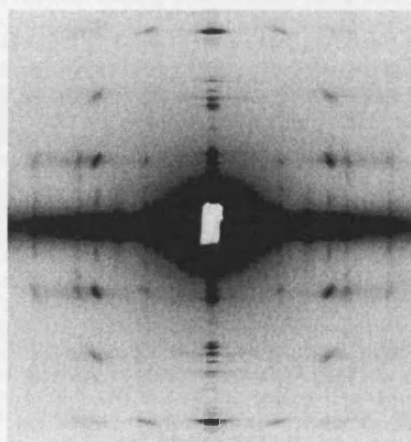

Figure 19. Small-angle diffraction pattern from fish muscle recorded at European Synchrotron Radiation Facility (ESRF), Grenoble, France, using a beamline ID02. The reflection indicated with the arrow corresponds to 1/143 A-1. Courtesy of Professor John Squire.

distributions, and spatial correlations. Advantages to GISAXS are that like SAXS it is a nondestructive technique which requires little or no sample preparation, in situ and real-time studies can be carried out, and the technique is statistically robust.

6.2. Small-Angle Neutron Scattering

Small-angle neutron scattering (SANS) is a complementary technique to SAXS which uses neutron scattering instead of X-ray scattering. Scattering of neutrons is caused by differences in the scattering power of different nuclei and has been used to study many materials, substances, and biological systems. SANS enables the observation of the internal structure of microparticles and allows the investigation of the size, shape, and distribution of scattering inhomogeneities found in the microstructure. Unlike X-rays, neutrons interact weakly with matter, resulting in a relatively small amount of the highly penetrating neutrons being absorbed by the matter. The major advantage of SAXS is twofold: first, the radiation damage to a sample is reduced; and, second, the negative scattering cross section of hydrogen can be counterbalanced by deuterium. In the latter case, the selective deuteration of macromolecules can be used to contrast match specific molecular components. This has enabled specific molecular interactions between macromolecules to be inferred.

There are two approaches to harnessing neutron radiation. The first neutron radiation source is available at neutron-scattering facilities around the world; one such facility is the Institut Laue-Langevin (ILL) in Grenoble, France. The second approach is the use of spallation neutron sources, which use synchrotrons to produce high-energy proton beams that can then be directed toward a heavy metal target. The bombardment of heavy nuclei with highly energetic protons causes the neutrons to be forced from the nuclei, resulting in an intense neutron pulse. The ISIS facility in Oxford, United Kingdom, is an example of a spallation neutron source. A more comprehensive review of SANS is given by Pethrick and Dawkins [122].

6.3. Microfocus Small-Angle X-Ray Scattering (μSAXS)

Microfocus small-angle X-ray scattering (μSAXS) provides a powerful tool capable of probing nanostructural textural differences in a sample at a micron-scale resolution. Microfocus provides small focal spots for the diffraction and small-angle X-ray scattering (SAXS) of single crystals and for the use of scanning diffraction experiments. A broad range of materials can be investigated with μSAXS such as single crystals and fibers. Microfocus has been used to investigate a range of biological materials including bone [123], skin [124], starch [125], and eggshell [15]. Microfocus beamlines can be found at many synchrotron facilities, including the beamline ID13 at the European Synchrotron Radiation Facility (ESRF), Grenoble, France.

6.4. Solution SAXS

Minimal sample preparation becomes a great advantage in solution-scattering experiments where processes such

as the assembly and (un)folding of proteins or conformational transitions during effectors' binding can be studied [126]. The technique gives an insight into a quaternary and tertiary structure and the shape of the native biological molecules in their nearly physiological states [32]. It can also prove the existence of the intermediate states that may occur during unfolding or other conformational changes of the protein. In this approach, data are recorded during the (un)folding process. The next step is the determination of the particle size, which can be calculated from the scattering pattern. Then many different random configurations are built within the known volume, and different simulated scattering patterns are generated. Simulated annealing algorithms are then used to fit the computer-generated pattern with the obtained data. This approach was used to investigate the thermally induced unfolding of the protein neocarzinostatin [127] and the Mg^{2+}-dependent folding of nucleic acids [128]. Solution SAXS also proved useful to determine the shape of nucleic acids [129], to determine the effects of ligand binding by analyzing the ligand-induced changes in the conformation of the protein receptors [130], and to describe large conformational changes in viruses [131]. A review on the use of small-angle scattering to analyze the structure of biological macromolecules is given by Svergun and Koch [126].

7. PRODUCTION OF X-RAYS

X-rays are produced when accelerated electrons collide with a metal target (usually copper or molybdenum). As a result of the electrons' deceleration, the X-rays photons are emitted and radiate in all directions. Most of the electron kinetic energy, however, is transformed into heat, and less than 1% is converted into X-rays. This kind of radiation (*Bremsstrahlung*, German for braking radiation; also called white radiation) is made up of all possible wavelengths. Yet the most desirable source of X-rays is the one that generates a monochromatic radiation that can be used for crystallography.

If the electrons collide with the target with very high velocity (hence, high energy), their energy enables them to remove the electron from the inner shell of the target metal atom. As a result, electrons from the higher energy levels will drop into the vacancy made up by knocked-up electrons, and, if the gap between two energy levels is big enough, the X-ray photons are emitted. Generated X-rays have a specific wavelength that depends on the differences between the energy levels in the target atom. For the elements of higher atomic number Z, the X-ray photons' wavelength will be shorter, which would correspond to the higher energy values. This kind of radiation is called characteristic radiation, as it contains precisely fixed energies.

To obtain radiation that can be used in crystallography, every X-ray source must therefore contain an electron source, high accelerating voltage, and a target metal. There are two main types of X-ray sources: gas tubes, which are obsolete, and filament tubes, which are the most widely used in laboratories. The most recent and yet most powerful X-ray source is synchrotrons, giant rings where the

Path: K:/ASP-ENN-08-0301/Application/ASP-ENN-08-0301-041.3d
Date: 21st February 2009   Time: 19:09   User ID: muralir   BlackLining Enabled

Page Number: 17

particles are accelerated close to the speed of light and travel in the circular trajectory.

The *filament* X-ray source contains two electrodes placed in the two ends of the tube, the anode and the cathode, with a high voltage between them. The electrons are produced by a current-heated cathode (tungsten filament), and then are accelerated by the high voltage maintained between two electrodes in the tube. Accelerated electrons hit the target metal atoms (anode), and in the process of knocking out the electron from the inner shell and replacing it with one from the higher energy level, the X-rays of characteristic wavelength are emitted. The emitted electrons are focused inside a tube by a focal spot, and therefore they hit a narrow region of the target. Generated radiation is emitted in all directions and emerges from the tube through vacuum-tight and X-ray-transparent windows, usually made of beryllium.

As 99% of the electron kinetic energy is converted into heat, the anode must be constantly water cooled. The heat dissipation is one of the great limitations in obtaining high-intensity radiation. This problem can be solved by using rotating anodes, where the fresh target metal is continuously being brought into the focal-spot region so the heat is spread onto the larger area. Better heat dissipation leads to an increased intensity of the X-ray radiation, and such tubes are at least ten times more powerful than tubes with fixed anodes.

Because the intensity of the X-ray beam corresponds to the exposure time that is needed to detect all diffracted X-ray beams, the rotating-anode tubes allow its reduction. These types of detectors are commonly used in radiography. The focal spot, a small metal cup that concentrates the electrons on a very small area of the target metal, determines the X-ray image resolution and hence its quality. The small size of the focal spot is a key element in microfocus tubes, which are used to produce an extremely fine X-ray beam and are used for special studies (e.g., of very small crystals).

7.1. Synchrotron Radiation

There are many ways to utilize and produce X-rays, for example using synchrotron radiation. A synchrotron is a specific type of cyclic particle accelerator in which a magnetic and an electric field are used to circulate and accelerate particles. Synchrotron facilities have the ability to emit electromagnetic radiation at wavelengths from X-rays to the far infrared. Synchrotrons consist of (1) an electron source (electron gun), (2) a linear accelerator which accelerates electrons close to the speed of light (LINAC), (3) a booster ring where electrons' intensities are enhanced, and (4) an outer storage ring (shown in Figure 20).

The electrons travel in ultrahigh vacuum. They are emitted from the cathode heated to $\sim1100^\circ$C and then accelerated by the radio frequency electric fields. From the LINAC, the electrons are transferred to the booster ring that consists of bending and focusing magnets. From the booster ring, they travel to the outer storage ring, where they are forced to travel in the nearly circular trajectory. In the straight sections of the ring, there are two types of insertion devices, wigglers and undulators, which are used to increase the beam intensity. They consist of a complex array of magnets with alternating polarity. When a bunch of electrons passes through one of the devices, the electrons start to wiggle. Their undulating movement causes the interference effect, and as a result a beam of much higher intensity is created. The difference between the two insertion devices is the deviation angle, which is smaller in undulators.

The beam of light is produced when the electrons are deflected through the magnetic field generated by the bending magnets in the storage ring. When electrons travel at relativistic velocities (near the speed of light), photons are emitted in a narrow cone in a forward direction. Emitted beams can then be focused so the beam is kept small and well defined and is used for the appropriate technique in the beamlines (e.g., a SAXS beamline), straight tubes that depart from the storage ring and lead to the stations. Synchrotron radiation consists of a wide energy spectrum, and it is possible to obtain radiation of any selected wavelengths for a specific purpose. X-rays generated using synchrotron radiation sources are hundreds of thousands of times more intense than conventional X-ray tubes, so the exposure times are reduced to several minutes or even
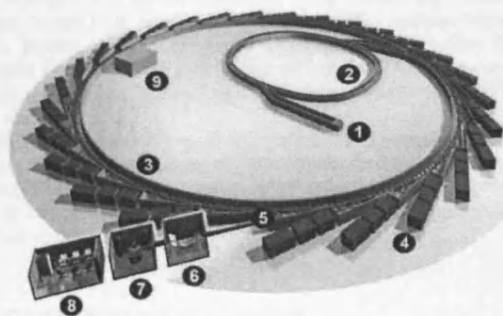

Figure 20. (a) A schematic plan of a synchrotron: (1) electron source, (2) booster ring, (3) storage ring, (4) experimental station, and (5, 6, 7, 8) optics and experimental hutches and control cabin, which together make a beamline. (b) Diamond Synchrotron Light Source, Oxfordshire, United Kingdom. © Diamond Light Source Ltd.

seconds. Apart from the extreme intensity and brightness, synchrotron radiation is also highly collimated and polarized.

At present, there are over 50 synchrotron facilities world-wide. The first synchrotrons were built back in the 1930s to investigate the particles that comprise atoms by accelerating particles to extremely high speeds. These accelerated particles caused atoms to break up into their constituent parts when they collided, hence allowing physicists to investigate the atom. These first synchrotrons were known as first-generation synchrotrons, and although initially radiation was just an unwanted by-product, it soon became a useful property to utilize. Synchrotrons have developed vastly over the last few decades with the introduction of synchrotrons built for the principle application of producing a source of radiation. Second-generation synchrotron facilities are used to solely to produce radiation of relatively low flux. They were usually built as a circular ring with ports located at points around the ring. An example of a second-generation synchrotron is the Synchrotron Radiation Source (SRS) in Daresbury, United Kingdom. Over the last few years, synchrotron radiation has reached a new level with the introduction of the third-generation synchrotron sources that create radiation with a higher flux than second-generation synchrotrons. A third-generation synchrotron uses an undulator and wigglers to produces radiation of a high flux. These synchrotrons differ from previous ones as they use magnets located around the ring, causing the accelerated electrons to oscillate and hence creating a higher intensity beam. An example of a third-generation synchrotron is the Diamond Synchrotron Source in the United Kingdom, the Advanced Photon Source (APS) in the United States, and ESRF in France.

Synchrotron radiation has become an indispensable tool in a wide range of different research fields, even though a major disadvantage is the necessity to travel to the giant storage rings.

7.2. Laboratory-Based X-Ray Facilities

Although synchrotrons are excellent sources for the production of high-intensity, bright, collimated, polarized X-rays, the use of laboratory X-ray facilities is also feasible. An example of a laboratory-based X-ray scattering system is the NanoSTAR facility, which is available commercially from Bruker ASX (Karlsruhe, Germany). This facility is capable of both SAXS and X-ray diffraction (XRD) measurements and can be used to investigate a wealth of different materials.

The high demand in synchrotron time and lengthy application time for beamtime at synchrotrons means that the NanoSTAR system is a viable alternative, although it produces less intense images, which results in much longer collection times.

8. DETECTION OF X-RAYS

Generated and then diffracted X-ray beams must be eventually measured to obtain the characteristic reflection pattern. Obtaining good-quality data still highly depends on the performance of the X-ray detector. High sensitivity is needed for precise measurements of reflection intensities as low-quality detectors might limit usefulness of even the brightest X-ray source. The most important parameters are absorption efficiency (high absorption coefficient), spatial resolution (large area), bandwidth (wide frequency range), energy resolution, and a high speed.

X-ray detectors use the fact that X-rays can interact with matter and cause ionization that can be detected and measured. The simplest X-ray detector is photographic film (or plate). It is sensitive to X-rays in the same way as it is sensitive to visible light, and it has been used since the discovery of X-rays. This type of detector has many disadvantages: it can absorb only about 1% of the radiation, and it needs chemical development. However, photographic plates are still used in medicine, but in crystallography studies they have been almost completely replaced by image plates and more recently by digital detectors.

Image plate detectors consist of plastic sheets coated with small, photostimulable phosphor crystals (e.g., $BaF:Eu^{2+}$). After X-ray photons' absorption, electrons are ejected from the crystal and are trapped in the F^- layer that contains electron vacancies created during the manufacturing process. The layer is then stimulated by a visible light which excites the trapped electrons. While electrons are dropping back to the Eu layer, the visible light photons are produced and released. After conclusion of the experiment, the plate is scanned, allowing the light photons produced during the exposure to be recorded and the data to be transferred to the computer that generates the corresponding diffraction image. The intensity of the emitted visible light corresponds to the intensity of the absorbed X-rays. A major advantage to image plate detectors is that they are reusable. After the exposure, the plate has to be erased so all electron vacancies (often called the F-centers) are depopulated. This can be accomplished by exposing the plate to the bright visible light. To minimize the time of the data collection, it is possible to use three independent plates where exposure, readout, and erasure take place simultaneously (e.g., as found in synchrotrons).

Proportional counters consist of the chamber filled with gas that can react with X-rays. Windows of the chamber are designed to stop visible light photons penetrating and allowing only X-rays to enter the detector. Incoming X-rays interact with gas atoms, which results in the ejection of the electrons. The number of emitted electrons is proportional to the incoming X-ray energy. As a result of this photoionization process, a cloud of electrons is created inside the chamber. The cloud passes through the arrangements of electrodes where it is being amplified and then reaches the anode. The signal is then measured, and with the known electron charge the energy of the incoming X-rays can be calculated.

Proportional counters are large-area detectors, which means that with the large surface they can capture more incoming X-rays; hence, they do not require focusing of the electron beam.

Another type of large-area detector is the microchannel plate, which consists of a large number of independent narrow channels (usually about 10^7 channels with 10 microns in diameter). Channels are made of a reactive material, so when X-rays strike the surface, the photoelectric effect

Path: K:/ASP-ENN-08-0301/Application/ASP-ENN-08-0301-041.3d
Date: 21st February 2009   Time: 19:09   User ID: muralir   BlackLining Enabled

Page Number: 19

X-Ray Scattering of Biomolecules   **19**

causes ejection of the electron. The ejected electron is then accelerated using an electric field, and while passing through the channel walls it interacts with the material and cause the electron cascade. Released particles travel to the end of the channel, where their charge is measured.

The most recently designed detectors are silicon-based charge-coupled devices (CCDs) that can detect up to 80% of incoming photons. CCDs contain arrays of pixels that can accumulate electrical charges generated by the interaction of X-rays with the detector surface. Each pixel can emit visible light in response to an incoming X-ray photon. Generated charge is stored during the exposure, and in a similar way to gas-proportional counters it corresponds to the amount of photons that hit the surface (i.e., the intensity of the X-rays). Silicon in CCD detectors is doped with impurities which enable it to conduct electricity. Electric impulse can then be transferred to the end of the chip where it is measured. Accumulated charge is stored during the exposure, and after a certain collection time the readout takes place. Readout is carried on in parallel for all stored charges, and the measurements are transferred directly to the computer memory. CCD detectors usually have a small area to collect the data (the most common detectors currently used contain 1024 × 1024 or 2048 × 2048 pixels); hence, they require focusing mirrors. This disadvantage of a long readout time is compensating by very accurate measurements of the energy and high precision. Recently, a fast CCD-based area detector has been developed that contains three CCD chips [132]. This unique design enables a reduction of detector readout to a millisecond, and the detector has been used to conduct time-resolved scattering experiments at microsecond to millisecond time resolution.

An alternative design to widely used CCD detectors is monolithic pixel sensors. Pixel detectors consist of thick silicon wafers with very small area rectangular pads that are used as readout cathodes. Unlike in CCD, circuitry in each pixel in pixel detectors is active only during the readout; pixels are also directly addressed for readout. An advantage of minimal pixel size is that it allows high spatial resolution. One type of pixel detector is the monolithic active pixel sensor (MAPS), which is a highly specialized application-specific integrated circuit (ASIC). This device can detect a wide range of radiation and convert it into an electronic signal. Detailed information about monolithic silicon detectors is provided by many different sources [e.g., 133–135]. The hybrid pixel detector is another type of device often used in high-energy physics studies. An advantage of using these detectors is not only excellent spatial resolution and a high signal-to-noise ratio but also a possibility of producing large-area detectors by tiling the modules. Hybrid detectors contain thick silicon pixellated semiconductor and collection electrodes which are bump-bonded to a pixellated readout chip (ASIC).

Recently a new class of detectors has been developed that is based on a gas technology. Gas microstrip detectors (GMSDs) are a type of micropatterned detector where incoming X-rays generate ionization of the gas inside the device which is then amplified through an electron avalanche. The created electric charge is then captured on the microscopic metal stripes and further processed. The GMSD detectors provide high spatial and time resolution, and have been developed for the use of the synchrotron light sources [136]. A type of GMSD device, HOTSAXS, is currently being developed for the small-angle scattering studies at the third-generation Diamond Synchrotron Facility (United Kingdom). Another example of gas-based detectors is the refined ADC per input detector system (RAPID), developed by the Central Laboratory of the Research Councils (CCLRC), to study dynamic processes in biological tissues using SAXS [136]. This gas wire device allows monitoring molecular changes on a microsecond scale and is characterized by a high time resolution and low noise levels. This type of detector has been used in synchrotron facilities such as SRS (Daresbury, United Kingdom), the European Synchrotron Radiation Facility (Grenoble, France), and Spring-8 (Japan). With the purpose of studying real-time dynamic processes, another type of detector has also been developed based on silicon microstrip technology. The Xstrip device is fabricated from thick silicon and contains an electronic chip called the XCHIP. Its special design allows high-speed readout, and the output signal from the XCHIP is then transferred to a PC-based data acquisition system [137].

9. CONCLUSIONS

Small-angle X-ray scattering (SAXS) is a useful technique for investigating nanostructural features of biological materials. This review has shown that SAXS can be used to study various biomolecules, for example collagen, keratin, lipid, muscle, chromatin, and cellulose. As well as biological materials, SAXS is a valuable technique for examining other materials areas such as metals [138, 139], plastics [140], the pharmaceutical industry [141], and the food industry [142]. SAXS allows the determination of particle size, particle shape, and other nanostructural characteristics.

Advances in computer software design and development have allowed simpler and more precise analysis of SAXS images. The collection of SAXS images has also been made easier by the recent growth in synchrotron radiation facilities. The addition of synchrotrons such as those at ESRF, Spring 8, APS, Diamond, and Soleil, and lab-based devices such as NanoSTARs have made SAXS readily available to the entire scientific community.

ACKNOWLEDGMENTS

REFERENCES

1. B. D. Cullity, Addison-Wesley, 1978.
2. O. Glatter and O. Kratky, "Small Angle X-Ray Scattering," San Diego, CA: Academic Press, 1982.

Path: K:/ASP-ENN-08-0301/Application/ASP-ENN-08-0301-041.3d
Date: 21st February 2009   Time: 19:09   User ID: muralir   BlackLining Enabled

Page Number: 20

3. A. P. Hammersley, "ESRF Internal Report," no. ESRF97HA02T, Grenoble, France: European Synchrotron Radiation Facility, 1997.

4. P. V. Konarev, V. V. Volkov, A. V. Sokolova, M. H. J. Koch, and D. I. Svergun, *J. Appl. Cryst.* 36, 1277–1282 (2003).

5. O. Glatter, *J. Appl. Cryst.* 13, 7–11 (1980).

6. A. Guinier, *Ann. Phys.* (Paris), 12, 161–237 (1939).

7. K. Butter, K. Kassapidou, G. J. Vroege, and A. P. Philipse, *J. Coll. Interf. Sci.* 287, 485–495 (2005).

8. B. A. Seaton, J. F. Head, D. M. Engelman, and F. M. Richards, *Biochemistry* 24, 6740–6743 (1985).

9. M. E. Newcomer, B. A. Lewis, and F. A. Quiocho, *J. Biol. Chem.* 256, 13218–13222 (1981).

10. C. Baldock, V. Siegler, D. V. Bax, S. A. Cain, K. T. Mellody, A. Marson, J. L. Haston, R. Berry, M.-C. Wang, J. G. Grossmann, M. Roessle, C. M. Kielty, and T. J. Wess, *PNAS*, 103, 11922–11927 (2006).

11. G. Porod, *Kolloid Z* 124, 83–114 (1951).

12. L. Auvray and P. Auroy, "Scattering by Interfaces: Variations on Porod's Law," Amsterdam: North-Holland, 1991.

13. J. J. Thomas, H. M. Jennings, and A. J. Allen, *Cement Concr. Res.* 28, 897–905 (1998).

14. M. A. V. Axelos, D. Tchoubar, and J. Y. Bottero, 1186–1190 (1989).

15. D. Lammie, M. M. Bain, and T. J. Wess, *Nanobioscience* 12, 721–726 (2005).

16. J. C. Hiller, T. J. U. Thompson, M. P. Evison, A. T. Chamberlain, and T. J. Wess, *Biomaterials* 24, 5091–5097 (2003).

17. M. Muller, C. Czihak, G. Vogl, P. Fratzl, H. Schober, and C. Riekel, *Macromolecules* 31, 3953–3957 (1998).

18. G. Oster and D. P. Riley, *Acta Cryst.* 5, 272–276 (1952).

19. K. L. Goh, J. C. Hiller, J. L. Haston, D. F. Holmes, K. E. Kadler, A. Murdoch, J. R. Meakin, and T. J. Wess, *Biochim. Biophys. Acta* 1722, 183–188 (2005).

20. H. F. Jakob, P. Fratzl, and S. E. Tschegg, *J. Struct. Biol.* 113, 13–22 (1994).

21. D. J. Hulmes, T. J. Wess, D. J. Prockop, and P. Fratzl, *Biophys. J.* 68, 1661–1670 (1995).

22. J. Riseman, *Acta Cryst.* 5, 193–196 (1952).

23. I. S. Fedorova and P. W. Schmidt, *J. Appl. Cryst.* 11, 405–411 (1978).

24. D. Tatchev and R. Kranold, *J. Appl. Cryst.* 37, 32–39 (2004).

25. G. Walter, R. Kranold, T. Gerber, J. Baldrian, and M. Steinhart, *J. Appl. Cryst.* 18, 205–213 (1985).

26. S. Kirkpatrick, C. D. Gelatt, and M. P. J. Vecchi, *Science*, 220, 671–680 (1983).

27. P. Debye, *Ann. Physik* 46, 809–823 (1915).

28. V. V. Volkov and D. I. Svergun, *J. Appl. Cryst.* 36, 860–864 (2003).

29. M. B. Kozin and D. I. Svergun, *J. Appl. Cryst.* 34, 33–41 (2001).

30. D. I. Svergun, V. V. Volkov, M. B. Kozin, and H. B. Stuhrmann, *Uniqueness. Acta Cryst.* A52, 419–426 (1996).

31. D. I. Svergun, *Biophys. J.* 76, 2879–2886 (1999).

32. D. I. Svergun, M. V. Petoukhov, and H. J. Koch, *Biophys. J.* 80, 2946–2953 (2001).

33. M. V. Petoukhov, N. A. J. Eady, K. A. Brown, and D. I. Svergun, *Biophys. J.* 83, 3113–3125 (2002).

34. M. Bada, D. Walther, B. Arcangioli, S. Doniach, and M. Delarue, *J. Mol. Biol.* 300, 563–574 (2000).

35. D. J. Scott, J. G. Grossmann, J. R. Tame, O. Byron, K. S. Wilson, and B. R. Otto, *J. Mol. Biol.* 315, 1179–1187 (2002).

36. D. I. Svergun, V. V. Volkov, M. B. Kozin, H. B. Stuhrmann, C. Barberato, and M. H. J. Koch, *J. Appl. Cryst.* 30, 798–802 (1997).

37. M. E. Rafik, F. Briki, M. Burghammer, and J. Doucet, *J. Struct. Biol.* 154, 79–88 (2006).

38. L. Kreplak, C. Merigoux, F. Briki, D. Flot, and J. Doucet, *Biochim. Biophys. Acta* 1547, 268–274 (2001).

39. Y. Kajiura, S. Watanabe, T. Itou, K. Nakamura, A. Iida, K. Inoue, N. Yagi, Y. Shinohara, and Y. Amemiya, *J. Struct. Biol.* 155, 438–444 (2006).

40. F. Briki, B. Busson, and J. Doucet, *Biochim. Biophys. Acta* 1429, 57–68 (1998).

41. R. S. Bear, *Adv. Prot. Chem.* 7, 69–160 (1952).

42. K. E. Kadler, *Extracell. Matrix* 1 2, 491–553 (1995).

43. W. Traub and K. A. Piez, *Adv. Prot. Chem.* 25, 243–352 (1971).

44. T. J. Wess, *Adv. Prot. Chem.* 70, 341–374 (2005).

45. B. Brodsky, E. F. Eikenberry, and K. Cassidy, *Biochim. Biophys. Acta - Prot Struc.* 621, 162–166 (1980).

46. R. H. Stinson and P. R. Sweeny, *Biochim. Biophys. Acta* 621, 158–161 (1980).

47. G. K. Menon, *Adv. Drug Deliv. Rev.* 54, S3–S17 (2002).

48. C. Ghioni, J. C. Hiller, C. J. Kennedy, A. E. Aliev, M. Odlyha, M. Boulton, and T. J. Wess, *J. Lipid Res.* 46 (2005).

49. C. J. Kennedy, K. Nielsen, L. Ramsay, and T. J. Wess, *Fibre Diffract. Rev.* 11, 117–118 (2003).

50. T. J. Wess and J. P. Orgel, *Thermochimica Acta* 365, 119–128 (2000).

51. C. J. Kennedy, M. Vest, M. Cooper, and T. J. Wess, *Appl. Surf. Sci.* 227, 151–163 (2004).

52. C. A. Maxwell, T. J. Wess, and C. J. Kennedy, *Biomacromolecules* (2006).

53. E. J. Sturrock, C. Boote, G. E. Attenburrow, and K. M. Meek, *J. Mater. Sci.* 39, 2481–2486 (2004).

54. L. S. Bass, N. Moazami, J. Pocsidio, C. Mehmet, P. LoGerfo, and M. R. Treat, *Lasers Surg. Med.* 12, 500–505 (1992).

55. R. Puxkandl, I. Zizak, O. Paris, J. Keckes, W. Tesch, S. Bernstorff, P. P. Purslow, and P. Fratzl, *Philos. Trans. R. Soc. Lond.* (2002).

56. A. Bigi, A. M. Fichera, N. Roveri, and M. H. J. Koch, *Intl. J. Biol. Macromol.* 9, 176–180 (1987).

57. E. Mosler, W. Folkhard, E. Knorzer, H. Nemetschek-Gansler, T. Nemetschek, and M. H. J. Koch, *J. Mol. Biol.* 182, 589–596 (1985).

58. W. Folkhard, E. Mosler, W. Geercken, E. Knorzer, H. Nemetschek-Gansler, T. Nemetschek, and M. H. J. Koch, *Intl. J. Biol. Macromol.* 9, 169–175 (1987).

59. N. Sasaki and S. Odajima, *J. Biomech.* 29, 1131–1136 (1996).

60. T. J. Gyi, K. M. Meek, and G. F. Elliott, *Intl. J. Biol. Macromol.* 10, 265–269 (1988).

61. K. M. Meek and D. W. Leonard, *Biophys. Soc.* 64, 273–280 (1993).

62. A. J. Quantock, S. Kinoshita, M. S. Capel, and D. J. Schanzlin, *Biophys. J.* 74, 995–998 (1998).

63. N. S. Malik, S. J. Moss, N. Ahmed, A. J. Furth, R. S. Wall, and K. M. Meek, *Biochim. Biophys. Acta* 1138, 222–228 (1992).

64. A. Daxer, K. Misof, B. Grabner, A. Ettl, and P. Fratzl, *Invest. Ophthalmol. Vis. Sci.* 39, 644–648 (1998).

65. I. M. Rawe, K. M. Meek, D. W. Leonard, T. Takahashi, and C. Cintron, *Biophys. J.* 67, 1743–1748 (1994).

66. K. M. Meek and A. J. Quantock, *Prog. Retin. Eye Res.* 20, 95–137 (2001).

67. A. Jemal, R. C. Tiwari, T. Murray, A. Ghafoor, A. Samuels, E. Ward, E. J. Feuer, and M. J. Thun, *CA Cancer J. Clin.* 54, 8–29 (2004).

68. I. Pucci-Minafra, C. Luparello, M. Andriolo, L. Basiricb, A. Aquino, and S. Minafra, *Biochemistry*, 32, 7421–7427 (1993).

69. I. Pucci-Minafra, M. Andriolo, L. Basirico, R. Alessandro, C. Luparello, C. Buccellato, R. Garbelli, and S. Minafra, *Carcinogenesis* 19, 575–584 (1998).

70. E. J. Bernhard, S. B. Gruber, and R. J. Muschel, *Proc. Natl. Acad. Sci. USA* 91, 4293–4297 (1994).

71. R. Ala-Aho and V.-M. Kahari, *Biochimie* 87, 273–286 (2005).

72. M. J. Duffy, T. M. Maguire, A. Hill, E. McDermott, and N. O'Higgins, *Breast Canc. Res.* 2, 252–257 (2000).

73. A. R. Round, S. J. Wilkinson, C. J. Hall, K. D. Rogers, O. Glatter, T. Wess, and I. O. Ellis, *Phys. Med. Biol.* 50, 1–10 (2005).

74. M. Fernandez, J. Keyrilainen, R. Serimaa, M. Torkkeli, M.-L. Karjalainen-Lindsberg, M. Tenhunen, W. Thomlinson, V. Urban, and P. Suortti, *Phys. Med. Biol.* 47, 577–592 (2002).

75. M. Fernandez, J. Keyrilainen, M.-L. Karjalainen-Lindsberg, M. Leidenius, K. V. Smitten, S. Fiedler, and P. Suortti, *Spectroscopy* 18, 167–176 (2004).

76. M. E. Poletti, O. D. Goncalves, and I. Mazzaro, *X-Ray Spectrom.* 31, 57–61 (2002).

77. L. Yang and H. W. Huang, *Science* 297, 1877–1879 (2002).

78. A. Illing, T. Unruh, and M. H. J. Koch, *Pharmaceut. Res.* 21, 592–597 (2004).

79. T. J. Wess, P. P. Purslow, and C. M. Kielty, *Fed. Euro. Biochem. Socs.* 413, 424–428 (1997).

80. M. J. Sherratt, D. F. Holmes, C. A. Shuttleworth, and C. M. Kielty, *Int. J. Biochem. Cell Biol.* 29, 1063–1070 (1997).

81. C. Baldock, J. K. Abraham, U. Ziese, M. J. Rock, M. J. Sherratt, K. E. Kadler, C. A. Shuttleworth, and C. M. Kielty, *J. Cell Biol.* 152, 1045–1056 (2001).

82. T. J. Wess, P. P. Purslow, and C. M. Kielty, *J. Struct. Biol.* 122, 123–127 (1998).

83. J. L. Haston, S. B. Engelsen, M. Roessle, J. Clarkson, E. W. Blanch, C. Baldock, C. M. Kielty, and T. J. Wess, *J. Biol. Chem.* 278, 41189–41197 (2003).

84. A. M. C. Emons and B. M. Mulder, *Trends Plant Sci.* 5, 35–40 (2000).

85. M. Muller, C. Czihak, M. Burghammer, and C. Riekel, *J. Appl. Cryst.* 33, 817–819 (2000).

86. P. Fratzl, N. Fratzl-Zelman, K. Klaushofer, G. Vogl, and K. Koller, *Calcif. Tiss. Int.* 48, 407–413 (1991).

87. P. Fratzl, S. Schreiber, and K. Klaushofer, *Connect Tiss. Res.* 34, 247–54 (1996).

88. H. S. Gupta, P. Roschger, I. Zizak, N. Fratzl-Zelman, A. Nader, K. Klaushofer, and P. Fratzl, *Calcif. Tiss. Int.* 72, 567–576 (2003).

89. P. Fratzl, N. Fratzl-Zelman, and K. Klaushofer, *Biophys. J.* 64, 260–266 (1993).

90. P. Fratzl, M. Groschner, G. Vogl, H. Plenk, J. J. Eschberger, N. Fratzl-Zelman, K. Koller, and K. Klaushofer, *J. Bone Miner. Res.* 3, 331–336 (1992).

91. H. Kuivaniemi, G. Tromp, and D. J. Prockop, *FASEB J.* 5, 2052–2060 (1991).

92. J. Kinney, J. Pople, C. Driessen, T. Breunig, G. Marshall, and S. Marshall, *J. Dent. Res.* 80, 1555–1559 (2001).

93. W. Tesch, N. Eidelman, P. Roschger, F. Goldenberg, K. Klaushofer, and P. Fratzl, *Calcif. Tiss. Int.* 69, 147–157 (2001).

94. J. H. Kinney, J. A. Pople, G. W. Marshall, and S. J. Marshall, *Calcif. Tiss. Int.* 69, 31–37 (2001).

95. J. H. Kinney, R. K. Nalla, J. A. Pople, T. M. Breunig, and R. O. Richie, *Biomaterials* 26, 3363–3376 (2005).

96. I. Lavelin, N. Meiri, and M. Pines, *Poult. Sci.* 79, 1014–1017 (2000).

97. R. E. M. Hedges, *Archaeometry* 44 (2002).

98. T. J. Wess, M. Drakopoulos, A. Snigirev, J. Wouters, O. Paris, P. Fratzl, M. Collins, J. Hiller, and K. Nielsen, *Archaeometry* 43, 117–129 (2001).

99. E. Maccioni, L. Vergani, A. Dembo, G. Mascetti, and C. Nicolini, *Mol. Biol. Rep.* 25, 73–86 (1998).

100. L. Perez-Grau, J. Bordas, and M. H. J. Koch, *Nucl. Acids Res.* 12 (1984).

101. J. P. Baldwin, P. G. Boseley, and E. M. Bradbury, *Nature* 253, 245–249 (1975).

102. H. Damaschun, G. Damaschun, V. A. Pospelov, and V. I. Vorobiev, *Mol. Biol. Rep.* 6, 185–191 (1980).

103. B. Richards, J. Pardon, D. Lilley, R. Cotter, J. Wooley, and D. Worchester, *Cell. Biol. Int. Rep.* 1, 107–116 (1977).

104. J. P. Langmore and J. R. Paulson, *J. Cell Biol.* 96, 1120–1131 (1983).

105. J. R. Paulson and J. P. Langmore, *J. Cell Biol.* 96, 1132–1137 (1983).

106. A. F. Huxley, *Prog. Biophys. Biophys. Chem.* 7, 255–318 (1957).

107. J. Lowy and F. R. Paulsen, *Nature* 299, 308–312 (1982).

108. J. Lowy and F. R. Paulsen, *Biophys. J.* 57, 977–985 (1990).

109. H. Huxley, A. Faruqi, M. Kress, J. Bordas, and M. Koch, *J. Mol. Biol.* 158, 637–684 (1982).

110. H. Iwamoto, T. Kobayashi, Y. Amemiya, and K. Wakabayashi, *Biophys. J.* 68, 227–234 (1995).

111. K. C. Holmes, R. T. Tregear, and L. J. Barrington, *Proc. R. Soc. Lond. Ser. B, Biol. Sci.* 207, 13–33 (1980).

112. F. R. Paulsen and J. Lowy, *Nature* 303, 146–152 (1983).

113. K. Wakabayashi, Y. Sugimoto, H. Tanaka, Y. Ueno, Y. Takezawa, and Y. Amemiya, *Biophys. J.* 67, 2422–2435 (1994).

114. J. Harford and J. Squire, *Biophys. J.* 50, 145–155 (1989).

115. J. Lowy, D. Popp, and A. A. Stewart, *Biophys. J.* 60, 812–824 (1991).

116. S. Malinchik, S. Xu, and L. C. Yu, *Biophys. J.* 73, 2304–2312 (1997).

117. H. Huxley, M. Reconditi, A. Stewart, and T. Irving, *J. Mol. Biol.* 363, 743–761 (2006).

118. H. Huxley, M. Reconditi, A. Stewart, and T. Irving, *J. Mol. Biol.* 363, 762–772 (2006).

119. N. Yagi, *Biophys. J.* 84, 1093–1102 (2003).

120. N. Yagi, *Biophys. J.*, Epub ahead of print. (2006).

121. J. R. Levine, J. B. Cohen, Y. W. Chung, and P. Georgopoulos, *J. Appl. Cryst.* 22, 528–532 (1989).

122. R. A. Pethrick and J. V. Dawkins, "Modern Techniques for Polymer Characterisation," New York: John Wiley, 1999.

123. T. Wess, I. Alberts, J. Hiller, M. Drakopoulos, A. T. Chamberlain, and M. Collins, *Calcif. Tiss. Int.* 70 (2002).

124. C. J. Kennedy, J. C. Hiller, D. Lammie, M. Drakopoulos, M. Vest, M. Cooper, W. P. Adderley, and T. J. Wess, *Nano Lett.* 4, 1373–1380 (2004).

125. T. A. Waigh, A. M. Donald, F. Heidelbach, C. Riekel, and M. J. Gidley, *Biopolymers* 49, 91–105 (1999).

126. D. I. Svergun and M. H. J. Koch, *Curr. Opin. Struct. Biol.* 5, 654–660 (2002).

127. J. Perez, P. Vachette, D. Russo, M. Desmadril, and D. Durand, *J. Mol. Biol.* 308, 721–743 (2001).

128. X. Fang, K. Littrell, X. Yang, S. J. Henderson, S. Siefert, P. Thiyagarajan, T. Pan, and T. R. Sosnick, *Biochemistry* 39, 11107–11113 (2000).

129. S. S. Funari, G. G. Rapp, M. Perbandt, K. Dierks, M. Vallazza, C. Betzel, V. A. Erdmann, and D. I. Svergun, *J. Biol. Chem.* 275, 31283–31288 (2000).

130. P. F. Egea, N. Rochel, C. Birck, P. Vachette, P. A. Timmins, and D. Moras, *J. Mol. Biol.* 307, 557–576 (2001).

131. M. A. Canady, H. Tsuruta, and J. E. Johnson, *J. Mol. Biol.* 311, 803–814 (2001).

132. N. Yagi, K. Inoue, and T. Oka, *J. Synchrotron Rad.* 11, 456–461 (2004).

133. G. Anelli, S. C. Commichau, M. Despeisse, G. Dissertori, P. Jarron, C. Miazza, D. Moraes, A. Shah, G. M. Viertel, and N. Wyrsch, *Nucl. Instrum. Met. Physics Res. A* 518, 366–372 (2004).

134. A. Bulgheroni, M. Caccia, K. Domanski, P. Grabiec, M. Grodner, B. Jaroszewicz, T. Klatka, A. Kociubinski, M. Koziel, W. Kucewicz, K. Kucharski, S. Kuta, J. Marczewski, H. Niemiec, M. Sapor, M. Szelezniak, and D. Tomaszewski, *Nucl. Instrum. Met. Physics Res. A* 535, 398–403 (2004).

135. R. Turchetta, J. D. Berst, B. Casadei, G. Claus, C. Colledani, W. Dulinski, Y. Hu, D. Husson, J. P. L. Normand, J. L. Riester, G. Deptuch, U. Goerlach, S. Higueret, and M. Winter, *Nucl. Instrum. Met. Physics Res. A* 458, 677–689 (2001).

136. CCLRC, CCLRC Engineering and Instrumentation Highlights.

137. J. Headspith, G. Salvini, S. L. Thomas, G. Derbyshire, A. Dent, T. Rayment, J. Evans, R. Farrow, C. Anderson, J. Cliche, and B. R. Dobson, *Nucl. Instrum. Met. Physics Res. A,: Accel., Spectrom., Detect. Assoc. Equip.* 512, 239–244 (2003).

138. P. Fermo, F. Cariati, C. Cipriani, M. Canetti, G. Padeletti, B. Brunetti, and A. Sgamellotti, *App. Surf. Sci.* 185, 309–316 (2002).

139. K. Tamura, M. Inui, T. Matsusaka, D. Ishikawa, M. Huq Kazi, X. Hong, M. Isshiki, and Y. Oh'ishi, *J. Non-Cryst. Solids* 312–314, 269–273 (2002).

140. M. Rabeony, H. Shao, K. S. Liang, E. Siakali-Kioulafa, and N. Hadjichristidis, *J. Reinf. Plast. Compos.* 18, 642–650 (1999).

141. B. Y. Shekunov, P. Taylor, and J. G. Grossmann, *J. Cryst. Growth* 198–199, 1335–1339 (1999).

142. A. López-Rubio, P. Hernandez-Muñoz, R. Catala, R. Gavara, and J. M. Lagarón, *Food Add. Contam.* 22, 988–993 (2005).